NUWC-NPT Technical Report 10,223
12 August 1993

(2

Relation Between the Fluctuating Wall Pressure and the Turbulent Structure Of a Boundary Layer on a Cylinder In Axial Flow

Stephen R. Snarski
Submarine Sonar Department

Naval Undersea Warfare Center Detachment
New London, Connecticut

PREFACE

This report was prepared as a dissertation for the degree of Doctor of Philosophy in Mechanical Engineering awarded July 1992 by Northwestern University. The project was supported by Dr. D. A. Hurdis (NUWC Code 2141), with funding provided by the Office of Naval Research, Program Manager J. A. Fein. Additional funding was received from the Amoco Foundation Doctoral Fellowship Program in Mechanical Engineering.

The technical reviewer for this report was Dr. Richard M. Lueptow of Northwestern University.

The author gratefully acknowledges the following individuals for their contribution to the completion of this study: Dr. Richard M. Lueptow, thesis advisor, for his direction, support, and constructive advice; Michael Goodwin and Norman Wells of the Mechanical Engineering Machine Shop for their expert assistance during the design and development of the wind tunnel and experimental apparatus; Drs. Alan L. Kistler, Seth Lichter, and Siavasch H. Sohrab for their helpful suggestions and review of the final manuscript.

REVIEWED AND APPROVED: 12 AUGUST 1993

F.J. Kingsbury

F. J. Kingsbury
Head, Submarine Sonar Department

REPORT DOCUMENTATION PAGE

Form Approved
OMB No. 0704-0188

1. AGENCY USE ONLY (Leave blank)

2. REPORT DATE
12 August 1993

3. REPORT TYPE AND DATES COVERED
Ph.D Dissertation

4. TITLE AND SUBTITLE
Relation Between the Fluctuating Wall Pressure and the Turbulent Structure of a Boundary Layer on a Cylinder in Axial Flow

5. FUNDING NUMBERS
PE N0014-89-J-1439

6. AUTHOR(S)
Dr. Stephen R. Snarski

7. PERFORMING ORGANIZATION NAME(S) AND ADDRESS(ES)
Naval Undersea Warfare Center
Division Newport Detachment New London
New London, CT 06320

8. PERFORMING ORGANIZATION REPORT NUMBER
TR 10,223

9. SPONSORING/MONITORING AGENCY NAME(S) AND ADDRESS(ES)
Office of Naval Research
Arlington, VA 22217-5000

10. SPONSORING/MONITORING AGENCY REPORT NUMBER

11. SUPPLEMENTARY NOTES

12a. DISTRIBUTION/AVAILABILITY STATEMENT
Approved for public release; distribution is unlimited.

12b. DISTRIBUTION CODE

13. ABSTRACT (Maximum 200 words)

The turbulent flow structures responsible for the fluctuating wall pressure in the turbulent boundary layer on a cylinder in axial flow ($\delta/a = 5.04$, $Re_\theta = 2870$) have been investigated. Simultaneous measurements of the fluctuating wall pressure and turbulent stream wise velocities have been performed throughout a large volume of the boundary layer ($y^+ = 14$ to $y/\delta = 1.91$, $0 \le x/\delta \le 1.52$, azimuthal angle $\phi = 0°, 20°, 40°$) with a subminiature electret microphone ($d^+ = 25.9$) and hotwire velocity probe ($l^+ = 18.5$).

Pressure-velocity cross-spectra and cross-correlation measurements indicate that two primary groups of pressure fluctuations exist in the cylindrical boundary layer: (1) small-scale, high-frequency disturbances concentrated close to the wall associated with the burst-sweep cycle and (2) large-scale, low-frequency disturbances extending from the wall to the turbulent/potential-flow interface that are consistent with a large

14. SUBJECT TERMS
Cylindrical Boundary Layer
Transverse Curvature
Turbulence Structure
Turbulent Boundary Layer
Wall Pressure Fluctuation

15. NUMBER OF PAGES
268

16. PRICE CODE

17. SECURITY CLASSIFICATION OF REPORT	18. SECURITY CLASSIFICATION OF THIS PAGE	19. SECURITY CLASSIFICATION OF ABSTRACT	20. LIMITATION OF ABSTRACT
UNCLASSIFIED	UNCLASSIFIED	UNCLASSIFIED	SAR

NSN 7540-01-280-5500

Standard Form 298 (Rev. 2-89)
Prescribed by ANSI Std. Z39-18
298-102

13. ABSTRACT (Cont'd)

spanwise-oriented 'vortex' in close contact with and inclined to the wall. Because the large- and small-scale motions coexist near the wall and an overlap occurs in the frequencies over which their energy is concentrated, the two motions appear to be interrelated.

Conditionally sampling by pressure-peak and VITA detection schemes indicates a distinct bidirectional relationship between both positive and negative large-amplitude wall pressure fluctuations and the temporal derivative of u in the near-wall region, suggesting that both types of processes are equally important to the physics of the near-wall flow. No explicit relationship exists between the sign of p and the sign of u, and the turbulent sources generating the large-amplitude negative pressure peaks are concentrated closer to the wall than those responsible for the positive pressure peaks.

The power spectral density of the wall pressure in a cylindrical boundary layer compared with a planar boundary layer contains less energy at low frequencies (outer variables) but is unaffected at high frequencies (inner variables). This indicates that transverse curvature reduces the energy content of the larger eddies but does not affect the smallest scales near the wall. Even so, the character of the near-wall flow structures may be altered as evidenced by variations in the statistics for the large-amplitude wall pressure fluctuations.

TABLE OF CONTENTS

LIST OF TABLES

LIST OF ILLUSTRATIONS

NOMENCLATURE

English Symbols

a	radius of cylinder (radius of transverse curvature) (m)
a^+	cylinder radius scaled on inner variables = au_τ/ν
$a(t)$	acoustic input to microphone for calibration (Pa)
d^+	transducer diameter scaled on inner variables = du_τ/ν
d^*	transducer diameter scaled on modified inner variables = d^+u_τ/U_∞
E[ ]	expected value operation
f	frequency (Hz)
f_c	lowpass cutoff frequency (Nyquist frequency) = $f_s/2$ (Hz)
f_s	digital sampling frequency (Hz)
f^+	frequency scaled on inner variables = $f\nu/u_\tau^2$
i, j	vector indices (1=streamwise, 2=wall-normal, 3=spanwise), summation indices
k	wavenumber (1/m)
K	flatness (kurtosis)
l_ν	viscous length = ν/u_τ
l^+	hot-wire length scaled on inner variables = lu_τ/ν
N	number of data points
n_d	number of subrecords in ensemble average
p, p_w	fluctuating wall pressure (Pa)
p_{rms}	root mean square wall pressure level (Pa)
$\langle p \rangle$	conditionally averaged wall pressure (Pa)
P	total pressure = $\overline{P}+p$ (Pa)
$\overline{P}$	mean pressure (Pa)
q_∞	free-stream dynamic pressure (Pa)
Q	quadrapole source term for the fluctuating pressure
r	radial coordinate (m)
Re_b	Reynolds number, based on length scale b, = $U_\infty b/\nu$, b = {a, X_P, δ^*, δ}
Re_θ	momentum thickness Reynolds number = $U_\infty\theta/\nu$
R_{pu}	cross correlation between wall pressure and streamwise turbulent velocity
s	circumferential separation distance between wall pressure transducer and velocity measurement location at some (specified) distance above the wall (m)

S	skewness
t	time (s)
t^+	time scaled on inner variables = tu_τ^2/ν
t_ν	viscous time unit = ν/u_τ^2
t_i	detection time of event for conditional sampling (s)
T	averaging time, record length, ensemble window duration (s)
T^+	averaging time for VITA detection scaled on inner variables = Tu_τ^2/ν
Δt	time between samples = $1/f_s$ (s)
Δt^+	time between samples scaled on inner variables = $\Delta tu_\tau^2/\nu$
ΔT^+	average event duration scaled on inner variables = $\Delta Tu_\tau^2/\nu$
u	streamwise turbulent velocity (m/s)
$\langle u \rangle$	conditionally averaged streamwise turbulent velocity (m/s)
u_i	fluctuating velocity component i (m/s)
u_{rms}	root mean square streamwise velocity (m/s)
u_τ	friction velocity = $\sqrt{\tau_w/\rho}$ (m/s)
$\overline{U}$	streamwise mean velocity (m/s)
u^+	streamwise mean velocity scaled on inner variables = $\overline{U}/u_\tau$
U_c	convection velocity (m/s)
U_i	velocity component i = $\overline{U_i}+u_i$ (m/s)
$\overline{U_i}$	mean velocity component i (m/s)
U_∞	free-stream velocity (m/s)
v	wall-normal turbulent velocity (m/s)
V	volume (m^3)
w(x)	probability density function for variable x(t)
x	streamwise (axial) coordinate measured from origin at pressure transducer (m)
x^+	streamwise coordinate scaled on inner variables = xu_τ/ν
x_i, x_j	spatial coordinate i, spatial coordinate j
x(t)	stationary random variable (fluctuating quantity)
$\overline{x_p}$	vector position of fluctuating pressure measurement
$\overline{x_s}$	vector position of quadrapole source
X_p	axial distance between boundary layer trip and wall pressure station (m)
y	wall-normal coordinate (m)
y^+	wall-normal coordinate scaled on inner variables = yu_τ/ν
z	spanwise coordinate measured from x-y plane through microphone (m)

Greek Symbols

$\gamma^2(f)$	coherence function
$\Gamma_{pu}(\omega)$	coherence function between pressure and velocity = $\gamma_{pu}{}^2(\omega)$
δ	boundary layer thickness (m)
δ^*	boundary layer displacement thickness (m)
κ	fluctuation level normalized by rms value, event detection threshold level
λ_e	eddy size/wavelength (m)
ν	fluid kinematic viscosity (m^2/s)
ω	angular frequency = $2\pi f$ (rad/s)
$\varnothing$	cylindrical coordinate polar angle from x-y plane (deg, °)
$\varnothing_{em}(\omega)$	phase response of microphone (deg)
$\varnothing_{pu}(\omega)$	phase function between p and u (negative implies p leads u) (deg)
$\Phi_{xx}(\omega)$	single-sided autospectral density (V^2/Hz)
$\Phi_p(\omega)$	single-sided autospectral density of p (Pa^2/Hz)
$\Phi_u(\omega)$	single-sided autospectral density of u [$(m/s)^2$/Hz]
$\Phi_{pu}(\omega)$	single-sided cross-spectral density between p and u (mPa/s/Hz)
ρ	fluid density (kg/m^3)
$\rho_{pu}(\tau)$	cross-correlation coefficient between wall pressure and streamwise velocity
σ	standard deviation (V, m/s, Pa)
τ	time delay (s)
τ_w	wall shear stress (Pa)
θ	boundary layer momentum thickness (m)
< >	conditional (ensemble) average

Superscripts

$\overline{}$	(over-bar) time-averaged quantity
$\widehat{}$	statistical estimate
+	nondimensionalized on inner length and time scales, t_ν and l_ν (or ν and u_τ)

Subscripts

∞	free-stream conditions
rms	root mean square value (= standard deviation for zero mean quantity)

CHAPTER 1

INTRODUCTION

The relationship between the fluctuating wall pressure beneath and streamwise turbulent velocities within a turbulent boundary layer on a cylinder in axial flow is investigated in this study. Since the work of Kraichnan (1956), it has been understood that the fluctuating pressure at the wall is intimately linked to the turbulent velocity fluctuations in the boundary layer. Because these fluctuating velocities are produced by turbulent structures or "eddies" that exist throughout the flow field, the aim has been to relate the unsteady pressure at the wall to turbulent structures in the flow. Although a general understanding of the character of the fluctuating wall pressure and its relation to the flow has evolved over the last 35 years of research, many details concerning the underlying mechanisms have remained inconclusive. Furthermore, nearly all of the work that has been performed has concentrated on the canonical flat plate boundary layer. The present study is an extension of these previous investigations but is aimed at relating the fluctuating pressure at the wall to turbulent structures in a boundary layer with transverse wall curvature.

The motivation behind most wall pressure studies is related to the problem of fluid-structure interaction and the need to better understand the mechanisms responsible for turbulence-induced structural vibrations. These vibrations can lead to radiated acoustical

noise or structural damage if the oscillations are large. A second motivation derives from the use of wall-mounted microphones for the measurement of far-field sound. In this scenario, the fluctuating wall pressure interferes with the acoustical measurement because it is not possible to distinguish between the far-field acoustic sound and the near-field hydrodynamic pressure fluctuations. Such a scenario occurs in an ocean towed sonar array where a number of hydrophones are mounted in a long towed submerged cylinder. Because of the cylindrical geometry of the wall, however, information from planar turbulent boundary layers is of limited value in efforts to reduce, control, or account for the "self-noise" caused by the turbulent pressure fluctuations. Consequently, there is a need to investigate the sources of the fluctuating wall pressure in the turbulent boundary layer on a cylinder in axial flow.

To provide a physical basis for the problem being investigated, the next Section reviews the physical features and turbulence structure of planar turbulent boundary layers, the relationship between the fluctuating wall pressure and organized structures in the flow, and the present level of understanding of the effect of transverse curvature on the structure of boundary layer turbulence. This is followed by a statement of the research objectives for the present investigation.

1.1 Physics of the Problem

1.1.1 The Structure of Boundary Layer Turbulence

When a viscous fluid flows adjacent to a solid surface, the no-slip condition at the wall and the viscous shear forces between the fluid and the surface cause the relative speed of the fluid to vary from zero at the wall to the free-stream value U_∞ at some

distance from the surface. At some distance downstream, this boundary layer region becomes unstable due to the growth of initially small random disturbances in the flow. This condition progresses with downstream distance until the boundary layer becomes fully turbulent as evidenced by highly irregular and complicated fluctuations in velocity and pressure in both space and time and the presence of coherent fluid structures or eddies of varying form across the entire boundary layer. Historically, the turbulent flow has been viewed as a random fluid motion resulting from the highly agitated and apparently unpredictable motion of the eddies. Over the last 25 years, however, this perspective has changed due to the realization that the turbulent boundary layer contains organized, coherent fluid motions that are random in occurrence in space and time but similar in character and whose dynamics strongly influence the evolution of the flow. Because these organized fluid motions possess spatio-temporal randomness, the phrase "quasi-coherent" is frequently used to describe these structures.

In general, terms two types of coherent structures or organized motions can be defined in the turbulent boundary layer. The first is a quasi-cyclical ordered sequence of events in the near-wall region that is responsible for the majority of turbulence production in the boundary layer. The second is a large-scale motion in the outer portions of the boundary layer with a scale on the order of the boundary layer thickness, δ. These two scales of motion are consistent with the two-scale character of boundary layer flows.[1] Although this overall classification is straightforward, many types of coherent structures have been

---

[1] The turbulent boundary layer is traditionally divided into an inner and an outer region to differentiate the portion of the boundary layer dominated by viscous effects associated with the wall (inner region) and that controlled by the global features of the boundary layer (outer region). The outer region length and velocity scales are the boundary layer thickness δ (or δ^*) and the free-stream velocity U_∞, respectively. For the inner region, the scales are ν/u_τ for the length and u_τ for the velocity, where ν is the kinematic viscosity and $u_\tau = \sqrt{\tau_w/\rho}$ is the friction velocity. The outer region is generally considered to extend from $y/\delta \sim 0.2$ to the edge of the boundary layer. The near-wall region is generally defined as $y^+ = yu_\tau/\nu < 100$.

observed in turbulent boundary layers over the last 30 years of research. The result is very little consensus on the exact character of the large- and small-scale motions or the role of each in the dynamics of the turbulent boundary layer. Recently, Kline and Robinson (1990) have provided some order to the confused state of affairs by classifying all of the turbulent structures, events, and motions observed in the turbulent boundary layer into an eight category classification. Their taxonomy of boundary layer turbulence structures is presented below.

Classification of Quasi-Coherent Structures Observed in the Turbulent Boundary Layer on a Flat Plate and in a Channel (Kline and Robinson 1990)

---

1. Low-speed streaks near the wall
2. Ejections of low-speed fluid outward from the wall
3. Sweeps of high-speed fluid toward the wall
4. Vortical structures of various forms near the wall
5. Near-wall inclined shear layers
6. Near-wall "pockets"
7. Large (δ-scale) inclined discontinuities in streamwise velocity, or "backs"
8. Large (δ-scale) motions capped by bulges in the outer turbulent/potential interface

<u>Near-Wall Turbulence Structure</u>

Categories (1) through (6) are associated with coherent motions in the near-wall region that have been either directly observed, measured, or computed through numerical simulations.

(1) Low-speed streaks. Low-speed streaks (Kline et al. 1967) consisting of regions of low-speed fluid ($u < 0$) have been found to form in the immediate vicinity of the wall ($y^+ < 7$).[2] Although they occur randomly in both space and time, they have an average spanwise spacing of $\sim 100\nu/u_\tau$. Between the low-speed streaks exist regions of high-speed fluid ($u > 0$) referred to as high-speed streaks. Because of the alternating regions of high- and low-speed fluid and their close proximity to the wall, they are often referred to as the sublayer streaky structure. The streamwise extent of low-speed streaks has been found to vary from ~ 100 to $\sim 1500\nu/u_\tau$. High-speed streaks are somewhat shorter, with maximum lengths of $\sim 800\nu/u_\tau$. The near-wall streaks are believed to play a passive role in the overall dynamics of the boundary layer.

(2) Ejections. The low-speed streaks observed near the wall migrate slowly outward as they move downstream (often referred to as lift-up), where at some critical distance they turn sharply and move rapidly away from the wall in what is referred to as an ejection-type motion (Kline et al. 1967). By marking the fluid in the low-speed streak near the wall, the ejection process has been observed to be followed by a rapid oscillation and subsequent disintegration of the low-speed streak into very fine scales of turbulence. The entire process of low-speed streak formation, lift-up, ejection, and breakdown was called 'bursting' by Kline et al. (1967), and it is believed to be a primary source of turbulence production in the boundary layer. The entire process is confined to the region $y^+ < 40$.

(3) Sweeps. Sweeps of high-speed outer fluid towards the wall are evident in the near-wall region (Corino and Brodkey 1969). The details of these motions are not as well understood, however, due to the difficulties in marking high-speed fluid. Even so, they

---

[2] All variables superscripted with "+" have been nondimensionalized using the inner length and velocity scales ν and u_τ, e.g., $y^+ = yu_\tau/\nu$.

have been found to be responsible for the majority of turbulence production in the very near-wall region $y^+ < 12$ (Willmarth and Lu 1972). Ejections are the primary contributors above this point. Because sweeps and ejections have been found to occur in close streamwise proximity to one another (Corino and Brodkey 1969), the bursting process has come to be referred to as the burst-sweep cycle. However, the details and sequencing of events are not completely certain nor universally agreed upon. New evidence from a numerically simulated turbulent boundary layer (Robinson, Kline, and Spalart 1990) suggests that sweeps and ejections actually occur simultaneously with a spanwise separation between them rather than sequentially in the streamwise direction as initially suggested.

(4) Vortical Structures. Defined as connected vortices with more than one spatial orientation, vortical structures of various forms have been observed in the near-wall region. They are generally believed to be the cause of the other coherent motions near the wall (categories 1-3) and thus the underlying mechanism for the production of turbulence in the near-wall region. Conclusions on the shape of the vortical structures believed to be responsible for the bursting phenomenon cannot be resolved from the experimental results due to inherent difficulties in making complete vortical structures visible and distinguishing between ensemble averages and individual realizations. Many investigators have proposed that the sequence of events related to bursting is intimately linked to quasi-streamwise hairpin-shaped vortical structures in the near-wall region (Willmarth and Tu 1967; Kline et al. 1967; Hinze 1975; Wallace 1982, 1985) while others report (not necessarily conflicting) ring-shaped vortices (Falco 1974, 1983) or inclined roller eddies (Townsend 1976). Recent numerically simulated turbulent boundary layer results (Robinson, Kline, and Spalart 1990), however, have provided evidence that a strong association exists between hairpin-like vortical structures near the wall and both ejections

and sweeps.

An illustration of the quasi-streamwise vortex structure and its relationship to the coherent motions observed near the wall is shown in Figure 1-1. The presence of the vortex structure is physically consistent with all the observed behavior in the wall region. It is assumed to form from an initially spanwise vortex near the wall that becomes kinked due to some random perturbation in the flow and subsequently stretched by the mean flow into a U-shaped loop. As the loop is stretched as it is convected downstream, it lifts from the wall due to the self-induction of the legs of the vortex structure. Because the vortex structure is inclined to the wall, an outward flow of fluid against the mean flow is experienced between the counter-rotating legs of the structure reminiscent of ejections. The outward flow creates a localized region of low-speed fluid beneath the structure that lifts from the wall with the structure as it convects downstream, consistent with the behavior of low-speed streaks. Along the outboard sides of the legs and head of the vortex structure, a wallward flow of fluid in the direction of the mean flow results, which is consistent with the appearance of sweeps and high-speed streaks at the wall. As the structure moves away from the wall due to the self-induction of the rotating legs, it experiences a higher mean velocity, which acts to stretch the structure even more rapidly. This causes the vortex to rotate even faster due to the conservation of angular momentum that, in turn, causes it to move more rapidly away from the wall and into regions of even higher mean velocity. The process is highly nonlinear and leads to a rapid destabilization and disintegration of the structure reminiscent of bursting.

(5) Near-wall shear layers. Regions of locally high shear evidenced by rapid changes in streamwise velocity are observed in the near-wall region $y^+ < 80$ (Corino and Brodkey 1969). The shear layers are typically inclined to the wall by an angle of $\leq 20°$. The shear layer instabilities are believed to play a dominant role in the production of turbulence in the

near-wall region and have been used as a trigger to detect the presence of bursting in the near-wall region.

(6) Near-Wall Pockets. Pockets or roughly circular regions in the sublayer that are swept clear of marked fluid particles have been observed in flow visualization studies (Falco 1983). They are believed to be an impression of some outer structure that induces fluid towards the wall. Other investigators, however, have suggested that they are merely an artifact of the marking technique and not of dynamical significance to the turbulent flow.

Outer-Region Turbulence Structure

Categories (7) and (8) in the taxonomy of structures are the two types of coherent motions observed in the outer portions of the boundary layer. Although they are referred to as outer flow structures, they have often been found to extend very close to the wall.

(7) Large (δ-scale) discontinuities in u. Shear layers or sharp jumps in the streamwise velocity (not to be confused with the small-scale high-shear layers observed in the near-wall region) are observed to extend across the full thickness of the boundary layer (Brown and Thomas 1977; Brodkey, Wallace, and Lewalle 1984). The angle of inclination of these large-scale shear layers, or 'backs' as they are called, is between 12° and 30°. Some results suggest that they are related to bulges in the turbulent/potential-flow interface and high-production events near the wall (Brown and Thomas 1977, Praturi and Brodkey 1978, Thomas and Bull 1983). It has even been suggested that they are phase-linked to the bursting process. In general, the phase relationship between δ-scale backs and near-wall flow structures and events remains unclear based on the available experimental results.

(8) Large-scale motions. At the edge of the boundary layer is a highly contorted and

undulating surface that separates the turbulent and nonturbulent (potential) flows (Corrsin and Kistler 1955). This interfacial region contains bulges of low-speed fluid from within the boundary layer that have dimensions of δ in both the streamwise and spanwise directions. In addition, deep and narrow crevices of free-stream fluid extending downward, in some cases very near the wall, have been observed (Kovasznay et al. 1970). Beneath this surface exists large-scale fluid motions, the precise form of which is a subject of controversy. The large-scale structures that have been reported take one of two (not necessarily conflicting) forms: a δ-scale spanwise vortex that rotates in the direction of the mean shear (Willmarth and Wooldridge 1963, Willmarth 1975, Fiedler 1986, Kobashi and Ichijo 1986) and a δ-scale horseshoe-shaped vortical structure (Theodorsen 1952, Brown and Thomas 1977, Thomas and Bull 1983). The large-scale structures appear to be inclined to the wall; however, angles of both 12-30° and 45° are reported. This has introduced some controversy as to the relationship between the large-scale structures and the δ-scale backs. Falco (1974) has reported that the average large-scale eddy structure assumes the form of a cochlear spiral similar to that of a breaking wave with a mushroom-like appearance when viewed on end.

The form of the large-scale structures, as well as their relationship to the backs, bulges, and crevices in the turbulent/nonturbulent interface, is not entirely clear from the existing body of results. This is presumably related to the inherent difficulties in making the complete structure visible and distinguishing between ensemble averages and individual realizations.

Inner-Flow/Outer-Flow Interaction

The major issue in the study of the structure of boundary layer turbulence concerns the spatio-temporal relationships and/or interactions between the various flow structures and

whether the various flow structures are separate entities or part of a larger process. Some investigators feel that the outer flow structures are merely outwardly diffused wall turbulence, while others feel it is the large-scale outer structures that are responsible for the turbulence in the inner layers. Still others feel that the inner and outer layers interact, with both contributing equally to the collection of events in the boundary layer. At present, very little is understood about these possible interactions.

1.1.2 Relation Between the Wall Pressure and Organized Flow Structures

<u>Origin of the Fluctuating Wall Pressure</u>

The quasi-coherent structures that are distributed throughout the turbulent boundary layer produce turbulent velocity fluctuations that, in turn, generate a fluctuating pressure field in the turbulent flow and at any boundary surfaces. For an incompressible flow, the pressure field is related to the velocity field through Poisson's equation, obtained from the divergence of the momentum equation (Kraichnan 1956):

$$\frac{\partial^2 P}{\partial x_i^2} = -\rho \frac{\partial^2 U_i U_j}{\partial x_i \partial x_j} \ . \tag{1.1}$$

The Poisson equation for the fluctuating component of pressure can be obtained by substituting for the pressure and the velocity in equation (1.1) sums of a mean and fluctuating component (i.e., $P=\overline{P}+p$, $U_i=\overline{U_i}+u_i$) and subtracting off the mean of the resulting equation (Reynolds decomposition). The resulting Poisson relation for the fluctuating wall pressure becomes

$$\frac{\partial^2 p}{\partial x_i^2} = -\rho Q \ . \tag{1.2}$$

where Q is the source term for the fluctuating wall pressure given by the following expression:

$$Q = \frac{\partial^2}{\partial x_i \partial x_j} (u_i u_j + u_i \overline{U_j} + u_j \overline{U_i} - \overline{u_i u_j}) \qquad (1.3)$$

Considering a two-dimensional wall-bounded flow, where $\overline{U_2} \approx 0$, $\overline{U_3}=0$, $\overline{U_1}=\overline{U_1}(x_2)$, and employing the usual boundary layer assumptions, the expression for the source term becomes (see Lilley and Hodgson 1960)

$$Q = 2\frac{d\overline{U_1}}{dx_2}\frac{\partial u_2}{\partial x_1} + \frac{\partial^2}{\partial x_i \partial x_j} (u_i u_j - \overline{u_i u_j}) \; . \qquad (1.4)$$

This equation for the source term shows that there are two types of processes responsible for the fluctuating pressure in equation (1.2). The first term represents an interaction of the mean shear with the wall-normal turbulent fluctuations and is linear in the turbulent velocity fluctuations. The second term represents an interaction of the turbulent fluctuations with themselves and is quadratic in the turbulent velocity fluctuations. It is generally assumed that the contribution of the nonlinear quadratic terms to the wall pressure can be neglected since the velocity fluctuations are small compared to the mean shear. Even though Panton and Linebarger (1974) have shown that the turbulence interaction terms contribute minimally to the wall pressure (~6 percent), neglecting them is still a subject of much debate since small-scale, large-amplitude disturbances observed very near the wall (see Section 1.2.2) suggest the existence of strong nonlinear processes. Nevertheless, with this assumption the equation for the fluctuating pressure after setting $u_2 = v$, $\overline{U_1}=\overline{U}$, $x_1 = x$, and $x_2 = y$ becomes

$$\frac{\partial^2 p}{\partial x^2} = -2\rho \frac{d\overline{U}}{dy}\frac{\partial v}{\partial x}\,. \tag{1.5}$$

A solution to equation (1.5) is obtained by integrating over the boundary layer sources (Lilley and Hodgson 1960). The resulting integral representation for the pressure fluctuation experienced at a point $\overline{x_p}$ due to the velocity fluctuations at points $\overline{x}_s$ in the entire half-space above the wall containing the flow is then

$$p(\overline{x_p},t) = \frac{\rho}{\pi}\int_V \frac{d\overline{U}}{dy}\frac{\partial v}{\partial x}\frac{dV(\overline{x_s})}{|\overline{x_s}-\overline{x_p}|}\,. \tag{1.6}$$

Because contributions to the wall pressure from surface integrals are at least two orders of magnitude less than contributions from volume integrals (Lilley and Hodgson 1960), the surface integral has been neglected in equation (1.6). Finally, the expression for the wall pressure is obtained by setting the point at which the pressure is evaluated equal to the origin on the wall, $\overline{x_p}=0$, such that

$$p_w(t) = p(0,t) = \frac{\rho}{\pi}\int_V \frac{d\overline{U}}{dy}\frac{\partial v}{\partial x}\frac{dV(\overline{x_s})}{|\overline{x_s}|}\,. \tag{1.7}$$

Any reference to fluctuating pressures or use of the term p(t) throughout this dissertation refers exclusively to the fluctuating pressure at the wall.

Character of the Wall Pressure Field

Because equation (1.7) is a volume integral over the entire half-space containing the flow, the fluctuating pressure at any single point on the wall is not highly correlated with the velocity fluctuations at any single point in the flow but is instead associated with turbulent velocity fluctuations throughout the entire flow. As a result, the fluctuating wall pressure is made up of contributions from turbulent structures (or pressure sources) throughout the boundary layer. Because the contributions of the various velocity fluctuations to the wall pressure in equation (1.7) are weighted by r^{-1}, where $r = |\overline{x_s}|$ is the distance between the wall pressure and turbulent source locations, contributions to the wall pressure from coherent structures in the boundary layer should diminish with increased distance from the wall. By examining the spectral solution to equation (1.7) and the potential turbulent sources from various regions of the boundary layer contributing to the fluctuating wall pressure, the character of the wall pressure field has been investigated (Bradshaw 1967, Panton and Linebarger 1974, Blake 1986).

The solution suggests that three separate spectral regions exist for the wall pressure fluctuations corresponding to three separate turbulent source regions in the boundary layer. Turbulent sources in the innermost portions of the boundary layer ($y^+ < 30$) contribute to the high-frequency portion of the wall pressure spectrum and lead to an ω^{-5} frequency dependence for the spectral energy. Sources in the log portions of the boundary layer (including the inner portion of the wake region ($y^+ > 30$ to $y/\delta < 0.6$)) contribute to the intermediate spectral frequencies and result in an ω^{-1} frequency dependence for the spectrum. Finally, the solution suggests that sources located in the outermost portions of the boundary layer ($y/\delta > 0.6$) (including the turbulent/nonturbulent interface) and in the portion of the potential flow outside of the boundary layer that experiences irrotational velocity fluctuations due to the undulating turbulent/nonturbulent

interface contribute to the low-frequency portion of the wall pressure spectrum and lead to an ω^2 frequency dependence.

Experimental and numerically simulated planar wall pressure spectra are in general agreement with these suggested spectral trends (Willmarth and Wooldridge 1962, Bull 1967, Schloemer 1967, Blake 1970, Emmerling 1973, Panton et al. 1980, Schewe 1983, Farabee and Casarella 1991, Choi and Moin 1990, and others). The mid- and high-frequency regions of ω^{-1} and ω^{-5} frequency dependence are observed in nearly all the results. The low-frequency ω^2 frequency dependence is not characteristic of all the measurements, however, because of contamination of the wall pressure measurements from facility noise and vibration at low frequencies. Identification of the turbulent source regions in the boundary layer contributing to the various spectral regions has been accomplished by examining the scaling relationships necessary to collapse the various regions of the experimental and numerical wall pressure spectra (Choi and Moin 1990; Farabee and Casarella 1991; Leith, Hurdis, and Abraham 1991). The scaling behavior of the measured spectra is consistent with the multilayer structure suggested from equation (1.7) (see Section 4.2.2).

Further evidence for the multilayer structure of the wall pressure field has been provided by directly probing the turbulent source regions of the boundary layer responsible for the wall pressure fluctuations through simultaneous pressure velocity measurements. Although turbulence source contributions to the wall pressure diminish with distance from the wall due to the r^{-1} term in equation (1.7), these measurements have revealed a definitive link between the wall pressure and flow structures throughout the entire boundary layer.

Turbulent Source Contributions to the Wall Pressure

The fluctuating wall pressure has been found to be correlated to turbulent velocities in the flow from very near the wall ($y^+ = 4$, Johansson et al. 1987) to distances of over 2.5δ from the wall (Panton et al. 1980). Because the length scales and coherent structures that exist in the flow change with distance from the wall, the character of the pressure-velocity relationships also change. In overall terms, the relationship between the wall pressure and turbulent velocities takes two general forms: large-scale, low-frequency associations presumably related to large-scale outer-flow structures and small-scale, high-frequency associations confined primarily to the near-wall region, presumably related to the burst-sweep cycle of events (Kobashi and Ichijo 1986).

Outer-region turbulent sources. The large-scale pressure-velocity relationships have been observed to take two forms. Measurements of the low-frequency, large-scale contributions to the wall pressure from the outermost portions of the boundary layer, the turbulent/potential-flow interface, and the irrotational velocity fluctuations in the potential flow ($0.5 \leq y/\delta \leq 2.6$) have been examined in the noise-free, low free-stream turbulence environment of the boundary layer on the fuselage of a sailplane (Panton et al. 1980). Although some of these velocity measurements were made well outside of the boundary layer, they still retained a strong correlation with the wall pressure. For $y/\delta > 1$, the correlations R_{pu} and R_{pv} indicate that the u and v components of velocity for the large-scale, pressure-producing structure are 90° out of phase (where u leads v). Panton et al. explained this observed phase relation between the velocities and the wall pressure by considering a potential flow over a wavy wall and Bernoulli's equation for the associated pressure. This model was originally proposed by Bradshaw (1967) to describe the low-frequency, large-scale contributions to the wall pressure spectrum (i.e., region of ω^2 dependence) originating in the outer irrotational flow.

For $y/\delta < 1$, the form of the pressure-velocity correlations changes reflecting an out-of-phase relationship between the u and v velocity components. This relationship has been found to be generally true throughout the bulk of the boundary layer where almost all the R_{pu} and R_{pv} correlations are of opposite sign (Willmarth and Wooldridge 1963). This led Willmarth (1975) to suggest that a rotating spanwise-oriented vortex was responsible for the observed flow behaviors in the outer region of the boundary layer. At the downstream side of the vortex, one can imagine a flow towards the wall ($v < 0$) of high-speed fluid ($u > 0$) from the outer portion of the boundary layer, while at the upstream side of the vortex, there would be a flow away from the wall ($v > 0$) of low-speed fluid ($u < 0$) from the inner portions of the boundary layer. For the conceptual model to be consistent with the observed signs of R_{pu} and R_{pv}, it was assumed that the passage of the vortex structure produced a reduced pressure at the wall. The physical basis for this, however, is unclear. By computing the contributions to p and v with an arbitrary displacement of a hot-wire probe with respect to a pressure probe, an R_{pv} correlation was produced qualitatively comparable to the actual measurements. No mention was made of the form of the streamwise velocity component.

Kobashi and Ichijo (1986) also computed pressure-velocity correlations for a large-scale rotating vortex in a boundary layer in an attempt to model the average large-scale structure that contributes to the low-frequency pressure-velocity correlations. Although their computed R_{pv} correlations are comparable to their measurements as Willmarth (1975) found, their computed R_{pu} correlations only appear similar to the measurements very near the wall and past the edge of the boundary layer, indicating some deficiency in the assumed form of the model. Because they did not state their assumptions, it is difficult to deduce the cause for the discrepancy between the computed and measured results.

Near-wall turbulent sources. Near-wall contributions to the wall pressure have been found to be of fundamental importance to the overall character of the fluctuating wall pressure signal. Very small-scale, large-amplitude wall pressure fluctuations with magnitudes as large as $9p_{rms}$ have been detected (Emmerling 1973, Schewe 1983, Karangelen et al. 1991). Although these large-amplitude wall pressure fluctuations only occur a small percentage of the time, they contribute significantly to the total rms wall pressure level. Schewe (1983) found that pressure fluctuations of magnitude $p \geq |3p_{rms}|$ occur 1 percent of the time but contribute 40 percent to the rms wall pressure level. Because these large-amplitude fluctuations have an average propagation velocity that is consistent with that for flow structures in the buffer region ($y^+ \approx 30$) (Emmerling 1973, Schewe 1983), it appears that they are related to the bursting process in the near-wall region. Further support for this has been provided by correlation measurements between p and all three components of velocity in the near-wall region (Willmarth and Wooldridge 1963, Willmarth and Tu 1967). The isocorrelation pressure-velocity contours that result produce a picture consistent with the presence of a quasi-streamwise vortex structure (Figure 1-1) if the lower loop of the vortex line is aligned with the pressure transducer—the configuration for which an optimum effect on the wall pressure by these randomly passing vortex structures would occur. It should be kept in mind that the vortex structure is convected at the local mean velocity so that the correlations are derived from the ensemble of a number of realizations.

Investigations of these high-amplitude wall pressure peaks and their relationship to flow structures in the near-wall region through the use of conditional sampling techniques on the pressure and velocity signals have revealed that positive high-amplitude wall pressure peaks are related to streamwise shear layers [accelerations in u(t)] in the near-wall region (Thomas and Bull 1983; Johansson, Her, and Haritonidis 1987; and

Haritonidis, Gresko, and Breuer 1990). Johansson, Her, and Haritonidis (1987) found that a bi-directional relationship (i.e., one-to-one correspondence) exists between these large-amplitude positive wall pressure peaks and accelerating streamwise velocity events and concluded that buffer region shear-layer structures related to the bursting process are to a high degree responsible for the generation of large positive wall pressure peaks. Such a bi-directionality would imply that detection of burst events could be triggered by monitoring the wall pressure. Results indicating that the frequency of occurrence of large-amplitude ($|p/p_{rms}| \geq 2.5$) wall pressure events (Karangelen et al. 1991) is consistent with that measured for bursting events in the buffer region (Blackwelder and Haritonidis 1983) appear to lend support to this prospect. From direct numerical simulation of a turbulent channel flow, Kim (1989) has concluded that the large-amplitude wall pressure fluctuations are a 'footprint' of the bursting phenomenon.

Johansson, Her, and Haritonidis (1987) also reported that the large-amplitude negative wall pressure peaks are related to periods of high streamwise velocity ($u > 0$). In a subsequent investigation, however, Haritonidis, Gresko, and Breuer (1990) constructed the joint probability density function $w(u,v)$ of u and v weighted by the pressure (i.e., $p^*w(u,v)$) and arrived at the conclusion that positive pressures are primarily associated with sweep-type events ($u > 0$, $v < 0$) while negative pressures are associated with both ejections ($u < 0$, $v > 0$) and inward interactions ($u < 0$, $v < 0$). They also reported that the primary coupling mechanism between the wall pressure and flow structures in the buffer layer is the normal component of velocity. The cause for the contradictions between their two sets of measurements is difficult to interpret at this time.

Interdependency between inner and outer contributions. A possible relationship between these near-wall, high-amplitude pressure peaks and the large-scale structures in the outer portions of the flow was investigated by Thomas and Bull (1983) by separating

their pressure signal into low-frequency and high-frequency portions. By correlating the low- and high-frequency portions of the signal and conditional sampling the low-frequency portion of the signal on the high-amplitude pressure peaks in the high-frequency portion of the signal, they concluded that the low- and high-frequency disturbances were interdependent. They also proposed that the large-scale structures are phase linked to the bursting process. The phase relation and causality between large-scale structures and high turbulence production events near the wall, however, is a subject of much controversy (Kline and Robinson 1990).

1.1.3 The Structure of Turbulence in a Cylindrical Boundary Layer

The Axisymmetric Turbulent Boundary Layer

The equations of motion for an axially symmetric flow, such as the axial flow over a cylinder,[3] retain the same form as for the two-dimensional planar boundary layer case only if the boundary layer thickness is much smaller than the radius of the contour of the body (Schlicting 1979). For the boundary layer on a cylinder in axial flow, this condition is not satisfied if the the cylinder is sufficiently long and thin since the growth of the boundary layer can cause its thickness to approach or exceed the radius of the cylinder. As a result, the ratio δ/a serves to characterize the degree of transverse curvature of the cylinder and the extent to which the fundamental two-dimensional character of the

[3]A boundary layer on a cylinder in axial flow is not strictly axisymmetric if the cylinder is yawed with respect to the mean flow. However, the overall character of an "axisymmetric turbulent boundary layer" and a "turbulent boundary layer on a cylinder in axial flow" that is nearly axisymmetric is likely to be very similar. In this dissertation, the phrases "boundary layer on a cylinder in axial flow," "boundary layer with transverse curvature," and "cylindrical boundary layer" are used synonymously.

boundary layer is altered[4].

A transverse curvature ratio of zero ($\delta/a = 0$) corresponds to the limiting case of a two-dimensional planar boundary layer. As δ/a approaches infinity, the limiting case of a cylindrical wake flow is obtained. Lueptow, Leehey, and Stellinger (1985) and Lueptow and Haritonidis (1987) have shown that the point at which transverse curvature begins to affect the flow is $\delta/a \approx 1$, evidenced by a fuller mean velocity profile and increased coefficient of friction from that observed in a planar boundary layer (see Section 3.3.2). For $\delta/a < 1$, the effect of transverse curvature is thus minimal and the boundary layer is similar to a planar boundary layer. For $\delta/a > 1$, however, the boundary layer can be much thicker than the radius of the cylinder and, as a result, the outer flow becomes increasingly independent of the wall. Denli and Landweber (1978) suggest that the cylinder may be considered as a small vorticity- and turbulence-producing disturbance, making the flow similar to a cylindrical wake flow with a modified inner boundary condition. Considering the diminished role of the wall in the cylindrical boundary layer, differences can be expected to exist in the turbulence structure.

The Effect of Transverse Curvature on the Structure of Boundary Layer Turbulence

Although research on the cylindrical boundary layer has been going on for nearly 40 years, most of the investigations have concentrated on the effect of transverse curvature on the mean properties of the flow field. Only a handful of investigations over the last 20 years have considered the effect of transverse curvature on the turbulence structure. For a detailed account of all these studies, the reader is referred to the exhaustive review of

---

[4]Other parameters utilizing the additional length scale "a" have been introduced to characterize the degree of transverse curvature of the boundary layer (Lueptow 1988). The ratio of δ/a, however, is the most common and the most intuitive.

Lueptow (1988). All the investigations into the structure of turbulence in the cylindrical boundary layer have considered the fluctuating wall pressure and the turbulent velocity field separately. The turbulent velocity field in the cylindrical boundary layer has been investigated the most extensively, covering the range of δ/a of 1 to 40. The only wall pressure measurements made in a cylindrical boundary layer were performed by Willmarth and Yang (1970) and Willmarth et al. (1976) with $\delta/a = 2$ and 4, respectively.

Velocity measurements in a cylindrical boundary layer have revealed that the distances from the wall for the maximum turbulence intensity and the ensemble-averaged events detected using VITA are similar to those found in planar boundary layers and other wall-bounded flows. This led Lueptow et al. (1985) and later Lueptow and Haritonidis (1987) to suggest that the burst-sweep cycle is the underlying mechanism responsible for the generation of turbulence at the wall in the cylindrical boundary layer as it is for a planar boundary layer and other wall-bounded flows. A near-wall streaky structure similar to that in a planar boundary also appears to be present in the cylindrical boundary layer (Lueptow and Jackson 1991). Even so, significant differences concerning the global structure of the boundary layer have been observed.

Eddy length scales. From computed wall pressure convection velocities from streamwise-separated pressure transducers, Willmarth and Yang (1970) and Willmarth et al. (1976) found that the convection velocity for the pressure-producing eddies in the cylindrical boundary layer was the same as that for a planar boundary layer. However, since the mean velocity profile convecting the eddies in the cylindrical boundary layer is fuller due to the effect of transverse curvature, they asserted that the pressure-producing eddies in the cylindrical boundary layer are necessarily nearer to the wall where the velocity is lower and therefore smaller than those in a planar boundary layer. This conjecture was strengthened by their space-time correlation measurements of the wall

pressure, which illustrated that constant wall pressure correlation contours were compressed in the spanwise direction as compared to those observed in a planar boundary layer, indicating a reduction in the transverse scale of the turbulent eddies.

Because the cylindrical boundary layer has a limited lateral extent (which is equal to 2δ as 'a' approaches zero), Willmarth pointed out that the peripheries of the larger eddies whose dimensions approach or exceed that of the cylinder extend in the transverse direction into regions where the mean velocity is higher. As a result, Willmarth attributed the transverse reduction in scale of the eddies to the transverse shearing action that results from the limited lateral extent of the cylindrical boundary layer. This effect is clearly not present in the planar boundary layer where no constraints are imposed on the lateral extent of the boundary layer and all portions of an eddy at a given distance from the wall experience the same mean velocity. Willmarth and Yang (1970) and Willmarth et al. (1976) provided further support for the presence of a larger percentage of small eddies by finding that for the cylindrical boundary layer the two-point pressure correlation decays more rapidly in the streamwise direction[5] and that the wall pressure spectra contain less energy at low frequencies and more energy at high frequencies than is observed in a planar boundary layer.

Unconstrained outer flow. For large δ/a, the size of the larger eddies can exceed the dimension of the cylinder. Consequently, only a portion of the eddy is actually bounded by the cylinder wall and, as a result, the structure and evolution of these large-scale structures should not depend directly upon the presence of the wall (Willmarth et al. 1976). This is clearly not the case in a planar boundary layer where even the largest eddies are completely bounded by the wall on one side. Flow visualization experiments performed in a cylindrical boundary layer indicate that large-scale structures actually move

[5] An eddy of any size decays after a distance proportional to its size (Willmarth and Wooldridge 1962).

from one side of the cylinder to the other (Lueptow and Haritonidis 1987). Reynolds stress and turbulence intensity profiles are also markedly different from the respective planar profiles (Lueptow et al. 1985). Although the cylindrical boundary layer profiles drop off much more rapidly with distance from the wall than the planar profiles indicating less turbulent energy throughout the bulk of the boundary layer (presumably related to the smaller turbulent eddies), the profile magnitudes exceed the planar boundary layer values for $y/\delta > 0.8$. This illustrates that the turbulent eddies are more energetic in the outer portions of the cylindrical boundary layer, presumably due to the lack of constraint on the eddies by the wall of the cylinder. Intermittency levels measured by Lueptow and Haritonidis (1987) indicate that the mean location of the turbulent/nonturbulent interface is 25 percent farther from the wall than that in a planar boundary layer. They attributed the difference to the more energetic eddies in the outer portion of the cylindrical boundary layer "filling out" the boundary layer more fully before being dissipated.

Outer-flow/inner-flow interaction. Since the wall does not constrain the motion of eddies in a cylindrical boundary layer as much it does in the planar case, there is the possibility for substantial interaction between the inner (near-wall) and outer (large-scale) structures of the boundary layer. Lueptow and Haritonidis (1987) suggest that these large-scale outer structures may trigger turbulence at the wall as they wash or sweep by the surface of the cylinder. Although the inner and outer flows for a planar boundary layer are generally believed to interact only weakly (Kline and Robinson 1990), it appears that the interaction is much stronger for the cylindrical boundary layer (Lueptow and Haritonidis 1987).

Circumferentially coherent structures. Velocity correlations measured between spanwise and streamwise separated probes near the wall ($y^+ = 8$) and in the outer region ($y^+ = 77$) by Lueptow and Haritonidis (1987) indicate a negative correlation for all spatial

separations used. Similar correlations for a planar boundary layer by Favre et al. (1957, 1958), however, were positive. Lueptow and Haritonidis (1987) suggested that the difference could be due to the splitting of a high-speed sweep of fluid around each side of the cylinder as it approaches the wall, although it may have been related to the specific choice of spanwise separation. This sort of circumferentially coherent flow structure does not occur in a planar boundary layer, where little spanwise motion is experienced by wallward moving fluid. Considering the periodic condition in the spanwise direction in a cylindrical boundary layer, it remains unclear what effect this circumferential constraint may impose on coherent structures near the wall.

1.2 Research Objectives

The relationship between the fluctuating wall pressure and turbulent structures in the flow have been studied extensively in a planar boundary layer. Although research has been performed to examine the fluctuating wall pressure and turbulent structure of a boundary layer on a cylinder in axial flow, this work has considered the fluctuating wall pressure and turbulent velocity field separately. These studies have indicated that although the mechanism of turbulence production near the wall in the cylindrical boundary layer is similar to that for other wall-bounded flows, there appear to be significant differences in the size, distribution, and motion of coherent structures in a cylindrical boundary layer compared to a planar boundary layer. To understand the relationship between the organized motions in the cylindrical boundary layer and the fluctuating pressure at the wall, simultaneous wall pressure and turbulent velocity measurements have been made in a cylindrical boundary layer in this investigation. The goal is to deduce the character of the flow structures that contribute to the fluctuating wall pressure in a

turbulent boundary layer on a cylinder in axial flow.

The investigation to be undertaken is primarily experimental and entails simultaneous measurements of the fluctuating wall pressure beneath and streamwise turbulent velocities within the turbulent boundary layer that develops on a cylinder in axial flow with $\delta/a = 5$. To be able to fully elucidate the global character of the cylindrical boundary layer and the various flow phenomena known to contribute to the wall pressure in a planar boundary layer, the velocities were measured throughout a relatively large portion of the boundary layer. In relation to the wall pressure transducer, the measurements spanned a distance of nearly 2δ in the wall-normal and streamwise directions and a circumferential extent of 40°. In order to investigate the turbulent sources that contribute to the fluctuating wall pressure, several data analysis techniques were employed. They include the statistical and spectral properties of the fluctuating wall pressure and turbulent streamwise velocities, conditional sampling of the pressure and velocity measurements using VITA and pressure-peak detection methods, pressure-velocity cross spectra (coherence and phase), and pressure-velocity cross correlations.

The results of this study are ultimately aimed at efforts to reduce, control, or account for the "self-noise" caused by turbulent pressure fluctuations at the cylindrical surface of a towed hydrophone (sonar) array. Of equal interest is the fundamental understanding to be gained on the structure of turbulence in a boundary layer flow with transverse wall curvature. A final motivation is to provide an experimental data base for comparison with direct numerical simulations of a turbulent cylindrical boundary layer conducted by Neves, Moin, and Moser (1991) at the NASA Ames Research Center.

The remainder of this dissertation is organized as follows. The wind tunnel facility, cylindrical model, measurement instrumentation, data acquisition, and data analysis

techniques will be described in Chapter 2. Factors related to the experimental environment that can affect the accuracy of the measurements performed, including extraneous flow disturbances, transducer resolution, and the mean properties of the turbulent boundary layer, are discussed in Chapter 3. Individual record analyses of the pressure and velocities (statistics and spectra) are presented in Chapter 4. Joint record analyses of the pressure and velocity measurements are presented in Chapter 5 (conditional sampling) and Chapter 6 (cross spectra and cross correlations). Finally, all significant findings and developed understandings derived from the analyses in Chapters 4 through 6 will be summarized and discussed in Chapter 7.

CHAPTER 2

EXPERIMENTAL INVESTIGATION

This chapter provides information pertaining to the experimental equipment and techniques used to acquire the data and results presented throughout this dissertation. This includes a description of the wind tunnel facility in which the investigation was conducted, the cylindrical flow model on which all boundary layer measurements were made, and all instrumentation required to perform the measurements. Also included are details of the experiments conducted for this investigation, the data acquisition and storage systems used to record the measurements, and the analysis methods used to examine the data.

2.1 Experimental Apparatus

In order to address the effect of transverse wall curvature on the fluctuating wall pressure and structure of boundary layer turbulence, several experimental requirements needed to be met. The first requirement concerned the need to generate an axisymmetric boundary layer on the cylinder by eliminating cylinder sag, obtaining precise alignment of the cylinder with the mean flow, and obtaining a straight cylinder with a uniform cross

section. Willmarth et al. (1976) found that a cylinder yaw angle of 1 degree (due to misalignment, sag, or a bend in the cylinder) could result in rms wall pressure differences of up to 20 percent from one side of the cylinder to the other. Lueptow et al. (1985) found that a similar difference existed for the boundary layer thickness for yaw angles as small as 0.1 degree. The second requirement involved the need to produce a low-turbulence, low-noise flow environment for the wall pressure and hot wire measurements. Such disturbances can have pronounced effects on the character of sensitive boundary layer measurements. The third experimental requirement was to generate a thick cylindrical boundary layer ($\delta/a > 1$) so that the effect of transverse curvature on the fluctuating wall pressure and turbulent flow field could be appropriately studied. The final experimental requirement was to minimize transverse cylinder vibration due to the transmission of low-frequency floor and building vibrations into the wind tunnel and ultimately the cylindrical model. Such vibrations can produce spurious low-frequency pressure signals and affect velocity measurements performed close to the wall.

In answer to the experimental requirement to generate a highly axisymmetric cylindrical boundary layer, a vertical wind tunnel was designed and built for this research. With the test section in a vertical orientation, gravity effects leading to cylinder sag were eliminated. The overall design and layout of the wind tunnel, as well as specific design features incorporated into the wind tunnel to satisfy the remaining experimental requirements, are discussed in Section 2.1.1. The cylindrical model and model support system designed and built for these experiments, as well as the additional design features implemented to fulfill the experimental requirements, are discussed in Sections 2.1.2 and 2.1.3.

2.1.1 Vertical Wind Tunnel Facility

A low-speed, open-circuit indraft wind tunnel was designed and built for these experiments. The wind tunnel consists of six separate sections. These are the settling chamber, contraction section, test section, diffuser, blower and motor, and silencer section. A schematic of the wind tunnel and its orientation in the laboratory appears in Figure 2-1. The overall dimensions of the tunnel were 24.5 ft high by 12.5 ft long and 5 ft wide. Because of the large vertical dimension, a portion of the wind tunnel passed through a 6-ft by 4-ft passage in the first floor laboratory ceiling and into a 12-ft by 12-ft by 12-ft inlet room with acoustical wall treatment on the second floor. The wind tunnel was designed to operate at a maximum speed of 45 m/s using an 8-hp motor. For the experiments discussed herein, the blower was powered by a 3-hp dc motor resulting in a maximum speed of 20 m/s.

The settling chamber directs the ambient air into the wind tunnel and acts to condition the flow before it enters the contraction section. It is the primary source responsible for the production of a low-turbulence flow environment. It has a 45.25-in.-square cross section and an overall length of 42.5 in. It consists of nine separable sections made from 3/4-in.-thick plywood with a formica inner surface. The first four sections each support an 18-mesh aluminum window screen while the last five sections each support a 30-mesh stainless steel screen. The section containing the fourth 18-mesh screen also houses a 25,000-cell aluminum honeycomb element (0.25-in. cell size, 2-in. length). Each screen was contained in a separate removable box to allow interchangeability and access for cleaning of the screens.

The purpose of the screens is to produce a uniform mean velocity profile through the imposition of a large pressure drop across the screen. In addition, the screens break up large-scale structures (eddies) in the inlet flow so that they can dissipate prior to entering

the test section, thus reducing axial velocity fluctuations (u). The purpose of the honeycomb is to axially align the flow, remove swirl, and suppress lateral turbulent velocity fluctuations (v and w). The flow conditioning elements were selected and arranged to achieve a maximum turbulence reduction in a minimum streamwise length. The minimum length was necessary due to the constraints imposed by the dimensions of the laboratory space and the need to avoid the generation of excessively thick wall boundary layers that are susceptible to separation in the contraction section. Downstream of the final 30-mesh screen is a 10-in.-long, formica-surfaced plywood settling region attached directly to the inlet of the contraction section. It serves to allow any small-scale, screen-generated turbulence to dissipate prior to the flow entering the contraction section. The primary references used for the design of the settling chamber flow conditioning and turbulence management devices were Wieghardt (1953), Loehrke and Nagib (1976), Mehta and Bradshaw (1979), Tan-Atichat et al. (1982), Batill et al. (1983), Nagib et al. (1984), Rae and Pope (1984), and Batill and Nelson (1989).

The contraction section accelerates the flow and provides additional turbulence suppression by increasing the mean flow velocity relative to the existing level of turbulence, thus decreasing the turbulence intensity. The contraction has a 45.25-in.-square inlet cross section and a 13.8-in.-square outlet cross section, resulting in a contraction ratio of 10.8:1. The total length of the contraction section is 54.5 in. The contraction geometry was a third-order matched spline polynomial (Batill et al. 1983, Batill and Nelson 1989) with a match point at $x/L = 0.6$. This geometry and match point were chosen because they generated the most uniform outlet flow without any apparent boundary layer separation at the outlet based on a two-dimensional numerical flow simulation using NEKTON. The contraction section was custom built from plywood and fiberglass with a formica inner surface. As can be seen from Figure 2-1, because of the

large vertical length of the wind tunnel, the settling chamber and contraction section actually resided on the second floor above the laboratory space. A vibration isolated beam system on the second floor landing was used to support the contraction section and the settling chamber. It was designed to reduce the transmission of low-frequency floor and building vibrations to the settling chamber or contraction section and ultimately into the flow.

The test section, or the working section of the wind tunnel, has a total length of 118 in. and a 13.8-in.-square inlet cross section. The maximum possible test section length within the constraints of the building and other wind tunnel component dimensions was incorporated into the design so that a long cylindrical model (to be discussed in section 2.1.2) could be used to promote the development of a thick boundary layer (and thus a large δ/a). The walls of the test section were set at a divergence angle of approximately 0.13 degrees with respect to the centerline to counteract the test section wall boundary layer displacement thickness growth and to minimize the streamwise pressure gradient in the test section. This results in a square outlet of 14.3 in. The divergence angle was selected because it provided the smallest overall pressure gradients in the test section across the full range of design flow speeds of the tunnel. The test section was constructed from 3/4-in.-thick plywood with a formica inner surface and an aluminum external frame. One wall of the test section contained three 36-in.-long by 12-in.-wide clear plexiglass (0.5-in.-thick) access windows mounted flush with the inside surface of the test section. Each of the windows was hinged and latched enabling both visual and physical access to the entire test section and model. The interior surfaces of the test section along with the settling chamber and contraction section were covered with the polished formica laminate to reduce excessive boundary layer growth.

A second vibration isolation beam system mounted on the second floor landing was

used to support the test section. Initially, this support system was designed to allow the test section to be free hanging and thus not in contact with any other wind tunnel components. However, because of a tension device that was subsequently required to appropriately support the cylinder in the test section (see Section 2.1.3), the test section and contraction section were in hard contact and thus coupled.

Following the test section is a diffuser-elbow section that serves to decelerate the flow and turn the flow 90 degrees into a horizontal direction. The diffuser is constructed of a 14-gauge-steel exterior case with a perforated 22-gauge, galvanized-steel interior flow surface and a fiberglass acoustical wool lining inserted between the two. Because blower noise has been responsible for the contamination of fluctuating wall pressure measurements at low frequencies in previous wind tunnel investigations, the 90-degree bend and the perforated steel/acoustical lining were incorporated into the design to reduce the blower noise from propagating upstream into the test section. The diffuser section was custom built by VAW (Vibro-Acoustics® Western) Systems. The diffuser plus support stand dimensions are 69 in. high, 98.25 in. long, and 40 in. wide. The inlet to the diffuser has a 14.3-in.-square cross section that connects to the outlet of the test section by means of a flexible couple (latex rubber). The flexible couple served to prevent blower vibrations, which pass through the diffuser, from entering the test section and cylinder. The outlet to the diffuser has a 32-in. circular cross section that connects directly into the circular inlet of the blower.

The blower is an airfoil vane centrifugal fan blower (type 27 SQA) by Chicago Blower Corporation. It is rated at 10,500 ft^3/min at 1349 rpm, 3.5 in. of water static pressure, and 8.78 bhp (5124 ft^3/min at 696 rpm, 1 in. water, 1.21 bhp). This particular type of blower was selected because of its low sound power output. The blower is driven by means of a dual belt drive and a Minarik 180-V, 3-hp permanent magnet dc motor,

model number 504-36-043A, with a speed range of 30-1800 rpm. The speed control is provided by a General Electric rheostat controlled ac-motor/dc-generator set. The motor shaft speed and, hence, blower rpm are measured using a Minarik magnetic pickup device in conjunction with a 60-tooth gear mounted to the motor shaft. The desired test section flow velocity was obtained by calibrating the blower rpm against Pitot tube measurements of the mean velocity at the centerline of the test section.

The flow exiting the blower is directed through a silencer section designed to reduce the low-frequency acoustic blower noise from entering the lab space and ultimately the pressure measurements. It is constructed in the same manner as the diffuser and has a vertical dimension of 84 in. The cross section is rectangular with outlet dimensions of 39 in. by 31.5 in. Air exiting the silencer is recirculated to the inlet of the settling chamber by passing through the second floor opening through which the wind tunnel passed as indicated in Figure 2-1.

2.1.2 Cylindrical Model

A 10-ft 3-in. long, 0.375-in.-diameter cylindrical model suspended along the centerline of the test section was used for all the experiments. This is shown in a cutaway view of the wind tunnel in Figure 2-2. The cylinder was fabricated from 0.375-in.-diameter, 18-gauge brass tubing (0.295-in. I.D., 0.040-in. wall thickness). The brass tubing was selected because it provided the best available O.D. tolerance (±0.002-in., or ±0.005-diameters)—a key factor in establishing an axisymmetric boundary layer. A large cylinder length-to-diameter ratio, $L/(2a)$, is necessary to establish a large ratio of δ/a, since a long streamwise length is required to generate a large boundary layer thickness, δ. Consequently, it is desirable to use small cylinder diameters when investigating the effect of transverse curvature. The 0.375-in.-diameter tube used for the present investigation

was the smallest diameter tubing available that would allow internal mounting of miniature wall pressure and vibration transducers (see Section 2.2).

The cylindrical model consists of three sections that are joined to produce one continuous 10-ft. 3-in. model, as shown in Figure 2-2. The first section is an 8-ft-long section of 0.375-in. brass tube with 5/16-24 internal threading on both ends. The next section is the cylinder instrumentation section that housed the wall pressure transducer (Section 2.2.1). Also shown in the figure is a vibration transducer installed in the instrumentation section to monitor the oscillations of the cylinder. This will be discussed in Section 3.1.2. The relative positioning of the instrumentation section in the model and a blowup view of this portion of the model is shown in Figure 2-2. The instrumentation section consists of three parts as shown in an exploded view in Figure 2-3. The first part is a 3.55-in.-long, 0.295-in.-O.D., 0.219-in.-I.D. support frame machined from a piece of 0.3125-in.-diameter brass rod. Both ends of this frame were machined with 5/16-24 external threading. The next two parts are 3.000-in.-long interlocking brass half shells machined from the 0.375-in. tubing. They snapped together over the 3.050-in.-long, 0.295-in.-O.D. center portion of the support frame forming a continuous 0.375-in.-O.D. shell. One end of this section was then threaded into the 8-ft-long, 0.375-in. section. A 0.025-in. external step machined onto the edge of both half shells combined with a 0.025-in. internal relief machined into the trailing edge of the 8-ft section locked the leading edges of the half shells in place. The third and final section of the cylinder was a 2-ft-long section of the 0.375-in. tubing machined in exactly the same manner as the 8-ft section. This 2-ft piece threaded onto the bottom end of the support frame, locking the lower halves of the half shells in place. The two transitions between each of the three cylinder sections were flush to within less than 0.001 in. (~0.003 cylinder diameters, or ~ 1 viscous wall unit).

2.1.3 Model Support and Alignment Assembly

The cylindrical model was supported in the test section by a 0.04-in.-diameter, 150-lb tensile strength polyurethane-coated steel cable attached to aerodynamically-shaped brass cones threaded into the nose and tail of the model. The suspended model is shown in Figure 2-2. The upper cable extended to the center of a structural airfoil located in the settling chamber. The airfoil was mounted in the second last downstream 30-mesh screen frame by means of two adjustable flanges. The structural airfoil was fabricated by covering a 52-in.-long rectangular steel bar (1.5 in. by 0.25 in.) with a 45-in.-long laminar airfoil (NACA 63_4-021 profile) constructed from a balsa wood frame covered by a layer of mylar film (2.75-in. chord length, 0.6-in. chord thickness). It was positioned upstream of the last screen so that any large-scale structures shed from it had a chance to pass through a fine-mesh screen prior to entering the contraction section. The position of the airfoil and, hence, the attachment point of the support cable were adjustable along the airfoil axis. The cable leading from the tail of the cylindrical model extended downward to structural airfoil tubing located in a square wood frame (14.3-in. inside dimension) mounted at the outlet of the test section. This airfoil had specially designed flanges at either end that enabled it to be adjusted in the plane of the test section cross section. The combined adjustability of the upper and lower airfoils allowed for precise alignment of the cylindrical model with the mean flow (see Section 3.2.1).

Following the lower structural airfoil, the cable passed through the wall of the 14.3-in. square frame and into a ratchet torque tension device that was used to place the cylinder under 75 lb of tension. This device was needed to eliminate the bow in the cylinder due to the inherent non-straightness of the tubing and thus improve the axisymmetry of the boundary layer (see Section 3.2.1). The tension apparatus did, however, act to couple the settling chamber, contraction section, test section and

cylindrical model. Because of the use of the brass support frame in the cylinder instrumentation section, the shell of the instrumentation section that housed the pressure transducer (see Section 2.2.1) did not experience any stress from the tensile loading.

2.2 Instrumentation and Calibration

2.2.1 Fluctuating Wall Pressure Measurements

Measurements of the fluctuating wall pressure were made in the instrumentation section of the cylinder at a distance of 97.5 in. downstream from the boundary layer trip (see Figure 2-2). The boundary layer tripping device is discussed in Section 3.3.1. An experimental requirement of this investigation was to use a wall pressure transducer with an effective diameter small enough to resolve the smallest scales of the turbulent pressure fluctuations (see Section 3.2). To this end, a Knowles model number EM-3068 subminiature electret condenser microphone with integral FET amplifier was used to make the fluctuating wall pressure measurements. The microphone and all significant dimensions are shown in Figure 2-4. The microphone is of the pinhole variety. The pressure port has a 1.00-mm (0.039-in.) O.D. and a 0.70-mm (0.0295-in.) I.D. This inside diameter across which the wall pressure acts scaled on inner wall variables is $d^+ = du_\tau/\nu = 25.9$ for the measurement flow conditions. Because of the very small volume enclosed by the pinhole cap and diaphragm case, the Helmholtz resonance frequency for the pinhole system was greater than 10,000 Hz and therefore above the frequency range of interest to this investigation. The EM-3068 microphone also utilizes a special construction to give low vibration sensitivity.

The microphone was mounted in the instrumentation section of the cylinder as shown

in Figure 2-3. A 0.040-in. hole was drilled through the center of one of the half shells. Three 30-gauge wire leads were soldered to the three microphone terminals and strain relieved via shrink tubing to avoid detachment. The microphone was then placed inside the half shell with the 0.039-in.-diameter stem protruding though the drilled hole. The microphone was epoxied in place from the inside of the half shell, making sure the microphone stem was seated squarely in the hole. Epoxy was allowed to protrude through the annular gap between the stem and the hole. The stem and epoxy were later sanded flush with the surface of the half shell. A Knowles BU-1771 ceramic vibration transducer (accelerometer) was also incorporated into the frame of the cylinder instrumentation section so that any influence of cylinder vibration on the wall pressure or near-wall velocity measurements could be assessed (see Section 3.1.2).

The EM-3068 microphone was powered by a Kikusui Electronics, Model PAB 70-1, 1.3-V dc power supply connected to the positive and ground terminals. A 6-ft-long, four pair, 22-AWG multiconductor individually shielded cable was used to conduct the microphone output signal and the 1.3-V power input between the microphone and the input of an external junction box. The BU-1771 accelerometer was connected in parallel to the 1.3-V source. A schematic of the microphone and accelerometer measurement systems is shown in Figure 2-5. The output signals from the microphone and the accelerometer were passed through two battery-powered EPAC Model 60/10 LN amplifiers. The amplifiers had a flat bandwidth (±0.1 dB) from 1 to 100 kHz and a selectable gain of 0 to 60 dB in 10-dB increments (gain from 1 to 1000). From the amplifiers, the signals passed through a TTE Filters, Inc., Model LE1161-10K-FSB, three-channel anti-aliasing filter with 60-dB attenuation and a shape factor of 1.10. The signals were then carried to a MacAdios II data acquisition card in a Macintosh IIcx computer for digital sampling. The data acquisition system is discussed in Section 2.3.2.

The EM-3068 microphone's nominal sensitivity response is relatively flat in the frequency range of 1000 to 6000 Hz. The nominal sensitivity level at 1000 Hz is 15.8 mV/Pa (-56 dB re 1V/μbar). The two ends of the response curve drop off to 7.1 mV/Pa (-63 dB) by 100 and 10000 Hz, respectively. No information was provided by the manufacturer on the nominal phase characteristics of the microphones. The manufacturer indicates that the frequency response characteristics for the Knowles EM-3068 are highly stable and insensitive to ambient conditions (e.g., temperature, pressure, and humidity).

Microphone Calibration

The calibration of the Knowles EM-3068 electret microphone required establishing the complex frequency response for the microphone over the frequency range covered by the present investigation, $f < 10000$ Hz. The complex frequency response is given by

$$H_{em}(f) = |H_{em}(f)|\, e^{j\varnothing_{em}(f)} \,, \tag{2.1}$$

where $|H_{em}(f)|$ is the sensitivity response or gain factor for the microphone giving the amplitude ratio of the output (voltage) to the input (pressure) as a function of frequency. The phase response or phase factor, $\varnothing_{em}(f)$, is the phase angle by which the output leads the input at a particular frequency. If the phase angle is negative, the output lags the input.[1] Without knowledge of the complex frequency response (i.e., both magnitude and phase) at all frequencies present in the signal, it is impossible to predict the input

[1] Another definition for the phase uses -j rather than +j in equation (2.1). This definition is often preferred because it makes $\Theta(f)$ positive when the output lags the input. This agrees with the physical requirement that it takes a positive time delay for a signal to propagate from input to output (Bendat and Piersol 1980). The +j in equation 2.1 was utilized because it was consistent with the references used to design the dynamic microphone calibration for the present investigation (Bruel and Kjaer 1982, Doeblin 1983, and Beranek 1988).

waveform (i.e., pressure) from the output electrical signal. This type of dynamic microphone calibration in which both the magnitude and phase characteristics of the microphone transfer function are sought has received only limited attention in the acoustics (or turbulent wall pressure) literature—presumably because of the inherent difficulties in measuring phase and the relative lack of value of phase information for many applications. Such dynamic microphone calibrations can take one of essentially three forms (Schweppe 1963): impulse tests (such as with a spark gap device), step tests (such as with a shock tube), or frequency-response tests. For the present investigation, the complex frequency response was determined by performing a frequency-response comparison calibration between the EM-3068 microphone and a calibrated Bruel and Kjaer standard reference microphone.

Although there are many factors to consider in the design of an effective comparison calibration (Beranek 1988), two considerations of primary importance are the acoustical nature of the calibration environment and the location in the sound field of the microphones with respect to each other and the sound source. Generally, the acoustic environment in which the microphone calibration is to be performed must consider the type of measurements the microphone was designed for (i.e., free-field response, random incidence response, or pressure response). In this way, diffraction/reflection effects resulting from the acoustic impedance of the microphone (a function of frequency, sound propagation direction, and microphone size and shape) can be appropriately taken into account. However, these diffraction effects only become important as the acoustic wavelengths approach the diameter of the microphone (Bruel and Kjaer 1982). For this investigation, the smallest acoustic wavelength considered is 1.3 in., corresponding to a frequency of 10000 Hz. Because this is two and a half times the largest microphone diameter to be used in the calibrations, free-field (anechoic), pressure, and diffuse-field

(random incidence) calibrations should all provide the same result for the frequencies considered in this investigation.

The location of the microphones in the sound field with respect to the sound source must be considered because it can cause magnitude and phase differences to exist between the sound waves impinging on the diaphragms of the two microphones. This is simply a result of the fact that the microphones are not at the same spatial location in the sound field. Because sound intensity varies as the inverse of distance from the source squared, differences between the sound pressure levels at the two microphones can be neglected if the source to microphone distance is kept large and the separation distance between the microphones is kept small. Phase differences or time lags between the two microphones result from differences in the path lengths between each of the microphones and the acoustic source. Reflections in the sound field can produce the same effect with the time lag between the two microphones being a function of the angle of incidence of the sound wave and the microphone separation distance. If the two microphones are kept equidistant from the sound source and no reflections are present (as with a free-field calibration in a large anechoic chamber), phase difference can be eliminated.

Initially a free-field comparison calibration was performed in a 4-ft cubic anechoic chamber (plywood box lined with Sonex acoustical foam). However, the overall chamber dimensions were too small, resulting in low-frequency near-field source effects and strong standing waves that interfered with the calibration for frequencies less than about 2000 Hz. Consequently, a diffuse-field calibration was performed in the laboratory space instead. By definition, a diffuse sound field is composed of reflected sound waves that travel in all directions with equal magnitude and probability. Although a reverberant chamber is usually used for these purposes, large rooms with a large number of solid reflecting objects and surfaces have been shown to be a suitable alternative (Beranek

1988). The diffuse-field calibration configuration and associated instrumentation are shown in Figure 2-6. The calibration was performed by projecting 'white noise' produced by a GenRad Random Noise Generator, Model No. 1390-B, and Harmon Kardon stereo amplifier through an 8-in. full-range (57-16000 Hz) speaker at an oblique angle into the 25-ft by 25-ft by 16-ft lab space. The Bruel and Kjaer reference microphone was placed adjacent to the EM-3068 inlet sound port in the cylinder instrumentation section with a separation distance between the microphone diaphragms of 15/16 in. and a separation distance between the speaker and the microphones of 20 ft.

Two separate reference microphones were used to perform the calibrations. These were the Bruel and Kjaer type 4138 1/8-in. and type 4134 1/2-in. pressure-response microphones. The Bruel and Kjaer microphones were used in conjunction with a type 2639 1/2 in preamplifier and UA 0036 Adapter and a type 2804 Power Supply. The sensitivity response for the 1/8-in. and 1/2-in. microphones is flat (±0.1 dB) for frequencies less than 20,000 Hz and 3000 Hz, respectively. The nominal sensitivity response for the preamp is flat for frequencies less than 100,000 Hz. The sensitivities for the Bruel and Kjaer microphones and preamp become frequency dependent generally below frequencies of 20 Hz. The absolute sensitivity level for the Bruel and Kjaer microphone system (microphone plus preamp) is obtained by calibrating the microphone system against a Bruel and Kjaer type 4220 Pistonphone that generates a fixed sound pressure level at a frequency of 250 Hz. The calibrated sensitivities were 0.788 mV/Pa and 10.624 mV/Pa for the 1/8- and 1/2-in. systems, respectively.

Bruel and Kjaer only provides nominal phase characteristics for the microphones and preamp used in this investigation (Bruel and Kjaer 1982). For the frequencies covered by this investigation, the microphone phase angle decreases slightly with increasing frequency to values of -4° and -40° at 10000 Hz for the 1/8- and 1/2-in. microphones,

respectively. The decreases were assumed to be linear. The low-frequency phase response of the microphones was estimated from the dynamics of capacitance microphones (Bruel and Kjaer 1982, Doeblin 1983) and from information provided by Bruel and Kjaer on the pressure equalization lower-limiting frequency and the capacitance-resistance characteristics of their microphones. The low-frequency response is positive for frequencies less than 100 Hz and approaches 180° as frequency approaches zero. The nominal phase response of the preamplifier is zero in the frequency range of 100 to 10000 Hz and slightly positive for frequencies less than 100 Hz. The combined microphone-preamplifier phase angle is less than 15° except at frequencies less than 10 Hz.

The diffuse-field comparison calibration in Figure 2-6 can be modeled as a single-input/two-output constant-parameter linear system (Bendat and Piersol 1980, 1986) as shown in Figure 2-7. In the figure, a(t) is the acoustic input to both microphones, x(t) is the output electrical signal of the reference Bruel and Kjaer microphone, and y(t) is the output electrical signal of the EM-3068 test microphone. For this configuration, the complex frequency response for the EM-3068 microphone, $H_{em}(f)$, is computed from

$$H_{em}(f) = H_{xy}(f)\, \frac{H_{bk}(f)\, H_{pa}(f)\, H_{Gx}(f)}{H_{d_{xy}}(f)\, H_{Gy}(f)} \quad . \tag{2.2}$$

The transfer functions $H_{bk}(f)$ and $H_{pa}(f)$ are the complex frequency responses of the Bruel and Kjaer microphone and preamplifier, respectively. The complex frequency responses of the two EPAC amplifiers are denoted by $H_{Gx}(f)$ and $H_{Gy}(f)$. The transfer function $H_{d_{xy}}(f)$ accounts for factors related to the spatial separation of the microphones, d_{xy}.

The term $H_{xy}(f)$ is computed from the autospectral densities of the microphone signals

$S_{xx}(f)$ and $S_{yy}(f)$ and the cross-spectral density $S_{xy}(f)$ in one of three ways:[2]

$$H_{xy}(f) = \frac{S_{xy}(f)}{S_{xx}(f) - S_{mm}(f)} , \tag{2.3a}$$

$$H_{xy}(f) = \left(\frac{S_{yy}(f) - S_{nn}(f)}{S_{xx}(f) - S_{mm}(f)}\right)^{1/2} e^{j\theta_{xy}(f)} , \tag{2.3b}$$

$$H_{xy}(f) = \frac{S_{yy}(f) - S_{nn}(f)}{S_{yx}(f)} , \tag{2.3c}$$

where

$$S_{xy}(f) = |S_{xy}(f)| e^{j\theta_{xy}(f)} = S^*_{yx}(f) .$$

The terms $S_{mm}(f)$ and $S_{nn}(f)$ are the autospectral densities of extraneous noise present at the output of the reference and test microphones, respectively. Although these spectral noise terms are generally quite small and can be neglected, their neglect should cause equations (2.3a) and (2.3c) to under and overestimate, respectively, the sensitivity at frequencies where the signal-to-noise ratios, $S_{xx}(f)/S_{mm}(f)$ and $S_{yy}(f)/S_{nn}(f)$, are small . If $S_{mm}(f) \approx S_{nn}(f)$, equation (2.3b) should provide a better estimate of the sensitivity at these frequencies since noise terms exist in both the numerator and denominator. By computing the sensitivity with each of the three expressions, this was found to be the case. At high frequencies ($f > 1000$ Hz), where the signal-to-noise ratios diminish, (eq. 2.3a) $\leq$ (eq. 2.3b) $\leq$ (eq. 2.3c) as would be expected. Consequently, the error resulting from the use of equation (2.3b) due to neglecting the extraneous noise terms should be negligible.

The transfer function $H_{d_{xy}}(f)$ in equation (2.2) models any phase differences between

[2]The auto- and cross-spectral densities are defined in Sections 4.2.1 and 6.1.1, respectively. The use of the double-sided spectrum, $S(f) = \Phi(f)/2$, defined for $-\infty \leq f \leq \infty$ in equation (2.3) is the standard convention.

the two microphones due to time lags resulting from reflections in the sound field and the spatial separation of the microphones, d_{xy}. If there are no primary or preferred directions for the reflected waves, $H_{d_{xy}}(f)$ can be neglected since the phase difference is uniformly zero for such a purely diffuse sound field (Bendat and Piersol 1980). If preferred directions exist, a time lag, $\tau_{d_{xy}}$, will exist between the two microphones that will produce a phase angle that is a linear function of frequency, $\O_{d_{xy}}(f) = 2\pi f \tau_{d_{xy}}$. By comparison of the measured coherence between the two microphones to that predicted for the diffuse sound field, it is possible to determine if $H_{d_{xy}}(f)$ can be neglected for the present measurements. The coherence is a measure of the linear dependence between two signals as a function of frequency. It is defined in terms of the autospectra and the cross spectrum as (see Section 6.1.1)

$$\gamma_{xy}^2(f) = \frac{|S_{xy}(f)|^2}{S_{xx}(f)\, S_{yy}(f)} \tag{2.4}$$

and is bounded by the inequality $0 \leq \gamma_{xy}^2(f) \leq 1$. The coherence between two microphone signals in a purely diffuse sound field is given by (Bendat and Piersol 1980)

$$\gamma_{xy}^2(f) = \left(\frac{\sin(k_o d_{xy})}{k_o d_{xy}}\right)^2 , \tag{2.5}$$

where $k_o = \frac{2\pi f}{c}$ and c = 340 m/s is the speed of sound.

A comparison of the coherence functions for the diffuse sound field with d_{xy} = 15/16 in. and that determined for a typical measurement in the laboratory space is shown in Figure 2-8(a). The two curves agree quite well for frequencies in the band of approximately 40 to 4000 Hz. The larger coherence values for the calibration sound field

for $f > 4000$ Hz are caused by correlated electrical noise in the two microphone signals. Although the lower coherence values for the calibration sound field for $f < 40$ Hz could be due to a number of factors, the phase correction at these acoustic wavelengths is negligible. The similarity between the two coherence functions illustrates that the calibration sound field was sufficiently diffuse to allow phase effects related to spatial separation (i.e., $H_{d_{xy}}(f)$) to be neglected at least for frequencies less than approximately 4000 Hz.

The final equations used to compute the sensitivity and phase response for the EM-3068 microphone, obtained from equations (2.1), (2.2), and (2.3b) with noise at the microphone outputs and the effect of their spatial separation neglected (i.e., $S_{mm}(f) \approx S_{nn}(f) \approx 0$, and $H_{d_{xy}}(f) \approx 1$, respectively), are

$$|H_{em}(f)| = \left(\frac{S_{yy}(f)}{S_{xx}(f)}\right)^{1/2} \frac{|H_{bk}(f)|\,|H_{pa}(f)|\,|H_{Gx}(f)|}{|H_{Gy}(f)|} , \tag{2.6}$$

$$\varnothing_{em}(f) = \varnothing_{xy}(f) + \varnothing_{bk}(f) + \varnothing_{pa}(f) , \tag{2.7}$$

where

$$\varnothing_{xy}(f) = \tan^{-1}\left[\frac{\mathrm{Im}\{S_{xy}(f)\}}{\mathrm{Re}\{S_{xy}(f)\}}\right] . \tag{2.8}$$

By simultaneous monitoring of the output of both amplifiers resulting from a single electrical input, it was determined that the EPAC amplifiers were phase matched for frequencies less than 10000 Hz. As a result, only the EPAC amplifier gains need be considered.

Typical sensitivity and phase responses are shown in Figures 2-8(b) and 2-8(c), respectively. As stated previously, the coherence function shown in Figure 2-8(a) is

bounded by the inequality $0 \leq \gamma^2_{xy}(f) \leq 1$. A coherence value of 1 means both microphone signals are linearly related (i.e., receiving the same inputs) while a coherence value of 0 means the two microphone signals are totally uncorrelated. Hence, the computed sensitivity and phase responses shown in Figures 2-8(b) and 2-8(c) are only reliable estimates of the microphone response at frequencies where the coherence remains fairly large. If a value of $\gamma^2_{xy}(f) = 0.5$ is taken as the cutoff (a conservative value), the computed sensitivity and phase responses can be considered as reliable estimates of the actual microphone response for frequencies in the range of approximately 20 to 3000 Hz. Shown in Figure 2-9 is the power spectral density of the fluctuating wall pressure measured in this investigation indicating the energy content of the turbulent wall pressure fluctuations as a function of frequency (see Section 4.2.2). The bold line in the figure is the fractional contribution to the total energy (area under the wall pressure spectrum) as a function of frequency. Because 99 percent of the turbulent wall pressure energy is contained in the band 80 to 3000 Hz, the uncertainty in the sensitivity and phase response estimates at low and high frequencies due to the low coherence between the microphones will have a negligible effect on the results.

The final sensitivity and phase calibrations for the Knowles EM-3068 microphone were taken as the average of seven separate calibrations performed over a period of 2 months. Polynomial curve fits to these magnitude and phase calibration responses were used as the calibration curves for subsequent data analysis (see Section 2.3.3).[3] These final sensitivity and phase response curves are shown in Figures 2-10(a) and 2-10(b), respectively, along with error bars taken as the standard deviation of the seven calibrations. The nominal sensitivity provided by Knowles is included with the calibrated

[3]Several curves of varying orders were used for each response to ensure the best possible fit. Three separate polynomials were used to fit the magnitude response: a 4th-order for $0 < f < 700$ Hz, a linear for $700 < f < 3800$ Hz, and a second linear for $3800 < f < 10000$ Hz. The phase response was fitted with two polynomials: a 4th-order for $0 < f < 1000$ Hz and a linear for $f > 1000$ Hz.

sensitivity curve in Figure 2-10(a). No nominal phase information was available. The increased scatter above 3000 Hz and below 20 Hz is consistent with the smaller coherence between the two microphones at these frequencies (Figure 2-8(a)).

2.2.2 Velocity Measurements

Mean velocity profiles and streamwise turbulent velocities were measured using constant temperature hot-wire anemometry. The anemometry system consisted of a Dantec anemometer (Main Frame model 56B10 with a CTA 56C01/56C17 bridge plug-in unit) and a home-built hot-wire probe. The hot wire itself was a 2.5-µm diameter, 0.5-mm- (0.02-in.) long platinum-rhodium wire. The wire supports consisted of two jeweler's broaches with a 0.0015-in.-diameter tip cut to a length of 0.013 m (0.5 in.). The hot-wire length corresponds to 18.5 viscous wall units for the flow conditions used, with a length-to-diameter ratio of 200. The time constant for the wires determined from a square-wave test at the operating flow speed was approximately 1 µs. This results in a phase response for the wires that is essentially zero for the frequencies considered in this investigation; consequently, no correction was necessary for the time lag of the wires. The hot-wire signal from the Dantec anemometer was fed into a home-built offset and gain box. The offset and gain were set so that the output voltage made maximum use of the full ±10-V range of the MacAdios II A/D card. From the gain box, the signal passed through the TTE anti-aliasing filter and then into the MacAdios II A/D card in the Macintosh IIcx computer (see Section 2.3.2). The hot wire velocity measurement instrumentation is shown schematically in Figure 2-5.

Mean velocity profiles and the turbulent velocity measurements were made by mounting the hot-wire probe to a streamlined strut that was attached to an external traversing mechanism. This permitted positioning of the hot-wire probe within the

boundary layer. The traverse assembly was mounted on two guide rails that ran the full length of the test section. The probe was positioned by a SLO-SYN M062-CF-402 microstep stepping motor that drove a rack attached to the strut. The stepping motor was controlled by a SLO-SYN 3180-PT125 stepping motor controller connected by means of a digital bus line to the MacAdios II A/D card in the Mac IIcx computer. This is shown in a block diagram format in Figure 2-5. The strut passed through a foam-lined slot centered between the two guide rails in the test section wall. The stepping motor could increment the probe by 0.00018 in., with a maximum traverse range of 5 in.

The position of the velocity probe with respect to the wall was set by positioning the probe at a specified position very near the wall (as measured using a microscope) and then traversing the probe outward a desired distance. Although the digital voltage input to the stepping motor could be used as a measure of the traversed distance, this was inaccurate due to a large error for small stepping-motor increments. Consequently, a probe position sensing technique was employed that utilized one sensing device for the near-wall region ($y < 0.18$ in, $y/\delta < 0.191$, $y^+ < 169$) and a second for the outer portions of the boundary layer. The near-wall device was an Edmund Scientific No. 72469 10X microscope/telescope with a resolution of 0.0005 in. that mounted on an external optical stand. The sensing device for the outer portions of the boundary layer was an Enco vernier caliper that was mounted to the external traverse in such a way as to follow the motion of the strut and probe. The caliper resolution was also 0.0005 in. Although the caliper was mounted in such a way as to follow the motion of the strut and probe, it only did this accurately after the strut had moved far enough (~0.1 in.) because of backlash in the system. The 10X telescope was used for the inner portion of the boundary layer.

Hot Wire Calibration

The hot-wire calibration curve was obtained by calibrating the hot-wire output voltage against a total head tube at eight flow speeds from 0 to 20 m/s. The dynamic pressure and, hence, flow speed was obtained from a 0.063-in. diameter total head tube located in the free stream between the test section wall and cylinder and the average of two static pressure ports located on the test section wall 6 in. upstream and downstream of the cylinder instrumentation section. The pressure was measured by means of a Baratron-223-B ±1 torr (±0.54 in. H_2O) differential pressure transducer with 0.001 torr resolution. The analog output from the pressure transducer was connected to the Macintosh IIcx A/D card to permit simultaneous dynamic pressure and anemometer voltage measurements. The resulting eight calibration points were then fitted to a fourth-order polynomial. The implementation of this calibration will be described in more detail in Section 2.3.3.

2.2.3 Wall Shear Stress Measurements

The wall shear stress was measured using a Preston Tube (Preston 1954) by computing the shear stress from a measured dynamic pressure within the wall region of the boundary layer. The Preston tube constructed for use in this investigation to measure the total pressure in the wall region of the boundary layer is shown in Figure 2-11. It consists of a 0.022-in. O.D. stainless steel tube (0.006-in. wall thickness) inserted through a hole drilled into a brass half-ring. The brass half-ring was machined such that its inner radius matched the 0.1875-in. outer radius of the cylindrical model. A 3/8 in. O-ring was then used to hold the Preston tube assembly in place on the cylindrical model such that the upstream end of the stainless steel (total head) tube remained firmly in contact with the cylinder wall. The upstream end of the stainless steel tube, which

measured the total pressure, extended 1 in. beyond the upstream edge of the brass half-ring in order to avoid any flow interference effects caused by half-ring. A 0.0625-in. outside diameter tube was then soldered to the downstream end of the stainless steel tube, which was connected to one side of the Baratron differential pressure transducer with 1/16-in.-diameter Tygon tubing. The static pressure, connected to the opposite side of the pressure transducer, was taken as the average of two static pressure-port measurements on the test section wall located 6 in. upstream and downstream of the total pressure measurement location.

The method of using a Preston tube to measure the mean wall shear stress in planar boundary layers has been well established in the literature (Winter 1977). Preston (1954) first developed the method when he utilized a hypodermic needle aligned parallel with the flow and in contact with the wall to measure the local wall shear stress in a planar boundary layer. If the main portion of the tube lies within the log region of the wall flow, the dynamic pressure measured by the tube, ΔP, depends only on the local velocity distribution close to the wall. With this velocity distribution for planar turbulent boundary layers being the universal velocity distribution known as the law of the wall, it can be shown through dimensional analysis that

$$\frac{\tau_w d_0^2}{\rho v^2} = F\left(\frac{\Delta P d_0^2}{\rho v^2}\right), \tag{2.9}$$

where d_0 is the outside tube diameter. The function F is then obtained by calibration (ΔP versus τ_w), so that measurement of ΔP enables a determination of τ_w. Patel (1965) determined the function F valid for a wide range of flow conditions and sizes of Preston tubes. As long as the ratio d_i/d_0 is kept close to 0.6 (where d_i is the inside tube diameter), the function is universal for all planar boundary layer flows. Patel presents his calibration

by the following empirical relations:

$$0<p^*<1.5 \text{ and } d_o^+<11.2: \qquad \tau_w^*=0.0357+0.5p^* \qquad (2.10a)$$

$$1.5<p^*<3.5 \text{ and } 11.2<d_o^+<110: \qquad \tau_w^*=0.8287-0.1381p^*+0.1427p^{*2}-0.0060p^{*3} \qquad (2.10b)$$

$$3.5<p^*<5.3 \text{ and } 110<d_o^+<1600: \qquad p^*=\tau_w^*+2.01\log_{10}(1.95\tau_w^*+4.1) \qquad (2.10c)$$

where

$$p^* = \log_{10}\left(\frac{\Delta P d_o^2}{4\rho\nu^2}\right) ,$$

$$\tau_w^* = \log_{10}\left(\frac{\tau_w d_o^2}{4\rho\nu^2}\right) .$$

To be able to use Preston's method for a boundary layer with transverse curvature, the flat plate calibration data of Patel (1965) must be assumed to be valid for the cylindrical boundary layer. Since the planar calibration data are obtained with the Preston tube immersed in the law of the wall region of the planar boundary layer, this requires that the outer diameter of the Preston tube used for the shear stress measurement on the cylinder to fall within the region where the cylindrical boundary layer velocity profile can be approximated by the flat plate law of the wall. If the transverse curvature is small, the cylindrical velocity profile will coincide with the planar law of the wall so the use of the Preston tube is perfectly valid. However, as transverse curvature increases, the velocity profile for the cylindrical boundary layer drops below the planar profile and error is introduced into the computed wall shear stress. More will be said about the use of the Preston tube for the present measurements in Section 3.2.2.

Because of the relative inconvenience of equations (2.10), particularly (2.10c) which is in an inverse format, the tabulated version of Patel's results produced by Head and Ram (1971) are used in this investigation.

2.3 Experimental Method

2.3.1 Conducted Experiments

The experiments performed in this investigation entailed simultaneous measurements of the fluctuating wall pressure beneath and the turbulent streamwise velocity within the turbulent boundary layer that develops on a 0.375-in.-diameter cylinder in axial flow. The flow geometry and a typical measurement configuration of the wall pressure transducer and hot-wire probe are shown in Figure 2-12. The figure is drawn to scale and the boundary layer thickness to cylinder radius, δ/a, at the wall pressure station is representative of the measured value of 5.04. All measurements were carried out at fixed experimental and flow conditions. These conditions are discussed in conjunction with the mean flow field in Section 3.1.

Wall pressure was measured at a single fixed position on the surface of the cylinder while the turbulent streamwise velocity was measured at 216 locations in the boundary layer. Figure 2-13 illustrates the boundary layer distribution of the 216 locations at which velocity measurements were made in relation to the pressure transducer. The measurements entailed nine wall-normal, eight axial, and three circumferential separation distances between the pressure transducer and the velocity measurement location. The absolute and nondimensional spatial separation distances of the wall pressure and velocity measurements in the three orthogonal directions are presented in Table 2-1. The spatial extent of the measurement points was chosen so that the pressure-velocity correlations would span a distance of at least one boundary layer thickness in all three coordinate directions (at the farthest position from the wall for the circumferential extent). The spatial extent in the wall-normal direction was made nearly two boundary layer thicknesses so that contributions to the fluctuating wall pressure from the irrotational portions of the

boundary layer could be investigated. Similar measurements were made in a planar boundary layer by Panton et al. (1980) and Kobashi and Ichijo (1986).

The data were taken by traversing the hot-wire probe through the 9 wall-normal boundary layer positions at each of the 24 axial-circumferential positions. Each of these 24 wall-normal traverses was taken as a series. Series were done sequentially at each of the eight axial separation distances for each of the three circumferential positions of the probe. For each series, the wind tunnel was turned on after the probe was aligned in the axial and circumferential directions. A calibration of the hot wire was then performed with the hot wire centered between the cylinder and test section wall (see Section 2.2.2). The hot-wire probe was then traversed in towards the cylinder and microstepped until it was at the initial wall-normal position of 0.015 in. as measured by the microscope.[4] The simultaneous wall pressure and velocity data were then taken. The probe was next stepped out to the second wall-normal position where the simultaneous data were taken again. This process was repeated until the probe reached its final position from the wall. At this point, the probe was moved back out into the free stream between the cylinder and the test section wall and recalibrated. In all cases, the two calibrations agreed to within less than 1 percent. The final calibration curve was taken as the average of the two curves. The average elapsed time between calibrations for a series was approximately 1 hour. Because of the high stability of the EM-3068 electret microphone frequency response, calibrations were only performed periodically throughout the course of all 216 series. The final calibration curves (magnitude and phase) were taken as the average of several calibrations performed over a period of about 2 months (see Section 2.2.1 and Figure 2-10).

---

[4] Because the access window needed to be opened for this microscope measurement, subtle cylinder oscillations that occurred during this process placed a limitation on the closest probe position to the wall of 0.015 in. ($y^+ = 14$) because of the possibility of hot wire breakage.

The circumferential and axial alignment of the hot-wire probe with respect to the wall pressure transducer was checked via the 10X telescope (0.0005-in. resolution) discussed in Section 2.2.2. The circumferential position was established by rotating the cylinder through the appropriate angular displacement as observed through the 10X scope. The cylinder was premarked with etch-lines at an angular displacement of 20 and 40 degrees relative to the Ø = 0 degree position. The uncertainty in the angular displacement was less than 0.5 degrees. This corresponds to uncertainties in the circumferential direction of approximately 1 viscous length at the surface of the cylinder and 11 viscous lengths at the farthest position from the wall. The axial position was first set globally by manually moving the externally mounted traverse mechanism on the two guide rails mounted to the test section. Once the probe was in close proximity to the desired position as observed with the 10X scope, an optical stand with a micro-adjustment screw was installed under the traverse mechanism. This allowed for a precise setting of the final position with an uncertainty of less than 0.001 in., or approximately 1 viscous length.. The wall-normal traversing was controlled by the stepping motor on the external traverse mechanism and a stepping motor controller tied in with the Macintosh IIcx computer. The uncertainty in the wall-normal distance was also less than 0.001 in., or 1 viscous length.

2.3.2 Data Acquisition and Storage

The data acquisition system used for all the measurements is a Macintosh IIcx computer equipped with a GW Instruments, Inc., MacAdios II data-acquisition board. The MacAdios II board interfaced with the computer's microprocessor through the Nubus interface by means of an internal Nubus expansion slot. The computer contained a 32-bit, 16-MHz MC68030 microprocessor, an MC68882 floating-point coprocessor, 5 Mbytes of RAM, a 40-Mbyte internal hard drive, a 1.4-Mbyte internal floppy disk drive, and an

RGB color monitor. In addition, an external 45-Mbyte removable cartridge hard disk drive and 40-Mbyte cartridge tape drive were used for data storage.

MacAdios II is a multi-function data acquisition board with analog I/O, digital I/O, and time-related digital I/O functions that can be expanded, with up to three optional daughterboards. All MacAdios II and daughterboard activities are synchronized with a master clock. Analog-to-digital conversion is performed by a single 12-bit A/D converter chip (AD7572) configured to receive analog input voltages within the range of ±10 V (with a software-selectable input gain of 1). The board provides sample-rate throughputs up to 142 kHz (conversions per second). Installed on the main MacAdios II board are two 1-channel, 12-bit A/D converter daughterboards, also with maximum sampling rates of 142 kHz. This allowed simultaneous sampling and conversion of three channels at a sampling rate of up to 142 kHz. The MacAdios II board also contains an 8-bit TTL-compatible digital output port. This was used to drive the motor controller that drove the hot-wire traverse (see Section 2.2.2).

All data measured for this investigation was sampled at 20 kHz. All signals passed through a multichannel (TTE Filters, Inc., Model LE1161-10K-FSB) anti-aliasing filter with a cutoff frequency of 10 kHz. The filter has 60-dB attenuation with a shape factor of 1.10. Each channel of data consisted of 82000 samples, which translates to a sampling duration of 4.1 s. The data from each channel were written in integer binary format to a separate sequential, unformatted compressed file. The first two lines of each file contained the sampling frequency and the number of data points. In this format, each channel's data file required 160 kbytes of storage space, which amounted to 480 kbytes per data set (three channels of data for the wall pressure, velocity, and accelerometer signals). Additional data were also taken in which the pressure and velocity signals were sampled independently for a duration of 50 s (10^6 samples). This was done to enable

more accurate statistical analyses of the fluctuating wall pressure and turbulent streamwise velocity signals. Each of these data sets required 2 Mbytes of storage. All data were initially recorded onto the 40-Mbyte internal hard drive. After each series, the data were transferred to the external 45-Mbyte removable cartridge hard disk drive and the 40-Mbyte tape cartridge as a backup.

2.3.3 Data Reduction and Analysis

All data reduction and analysis were performed on a Macintosh IIsi computer. The computer contains a 32-bit, 20-MHz MC68030 microprocessor, 5 Mbytes of RAM, a 40-Mbyte internal hard drive, a 1.4-Mbyte internal floppy disk drive, and an RGB color monitor. A NuBus adapter card with a built-in MC68882 floating-point coprocessor was also installed in the internal expansion slot. As with the Macintosh IIcx, the external 45-Mbyte removable cartridge hard disk drive and 40-Mbyte cartridge tape drive were used for raw data storage. An additional 200-Mbyte external hard drive was used to facilitate storage during data processing and analysis.

Before the raw data could be analyzed, they needed to be conditioned. Because the pressure and velocity data were written to file as integers, the first step involved converting the integer values to voltages from knowledge of the 12-bit resolution and ±10 V range of the A/D converter. The second step involved applying the calibrations to the velocity and pressure voltage signals. The hot-wire calibration for the velocity data was implemented in the time domain immediately following the conversion to volts. This involved converting volts to meters/second by the following calibration equation:

$$u(m/s) = P_o + P_1(v_u) + P_2(v_u)^2 + P_3(v_u)^3 + P_4(v_u)^4 \ , \tag{2.11}$$

where P_o, P_1, etc., are the coefficients for the fourth-order least-squares polynomial curve fit to the hot-wire calibration data (see Section 2.2.2).

The pressure calibration needed to be implemented in the frequency domain since the microphone sensitivity and phase information are functions of frequency (see Section 2.2.1). As a result, the pressure voltage data were Fourier transformed into the frequency domain. The finite Fourier transform of a fluctuating variable x(t) is defined as

$$X(f) = \frac{1}{T}\int_0^T x(t)\, e^{-j2\pi ft}\, dt \; . \tag{2.12}$$

The discrete form is given by

$$X(f_k) = \frac{1}{N}\sum_{n=0}^{N-1} x_n\, e^{-j\frac{2\pi kn}{N}}, \quad k=0,1,\ldots, N-1 \; . \tag{2.13}$$

Because equation (2.13) is computed by fast Fourier transform (FFT) methods, a constraint for all the analyses was that the total number of data points used had to be a power of 2. The relationship between the input pressure and the output voltage of the calibrated microphone neglecting noise at the input or output is given by

$$V_p(f) = H_{em}(f)P(f) \; , \tag{2.14}$$

where $H_{em}(f)$ is the complex frequency response for the EM-3068 microphone, and P(f) is the frequency domain representation of the desired fluctuating wall pressure signal. The microphone calibration was implemented by the equation

$$P(f) = \frac{V_p(f)}{H_{em}(f)} = \frac{V_p(f)}{|H_{em}(f)|\, e^{j\phi_{em}(f)}} \,, \tag{2.15}$$

where $|H_{em}(f)|$ and $\phi_{em}(f)$ are the calibrated sensitivity and phase responses shown in Figure 2-10 (see Section 2.2.1).

The third and final step of the data conditioning process involved digital bandpass filtering the pressure and velocity signals. Filtering was implemented in the frequency domain with a rectangular window function, W(f), and low- and high-frequency cutoffs of 58.59 and 5332.00 Hz, such that

$$P'(f) = W(f)P(f) \tag{2.16}$$

$$U'(f) = W(f)U(f) \tag{2.17}$$

where

$$W(f) = \begin{cases} 1, & 59 < f < 5332 \text{ Hz} \\ 0, & \text{elsewhere} \end{cases} \,.$$

Because filtering was implemented in the frequency domain, it was necessary to Fourier transform the velocity data (equation (2.13)) prior to the application of equation (2.17). The low-frequency cutoff rejected frequencies corresponding to $\omega\delta^*/U_\infty < 0.138$ or $\omega\nu/u_\tau^2 < 0.019$. This was done to remove the influence of any extraneous wind-tunnel-generated large-eddy turbulence or acoustic disturbances in the test section. The low-frequency cutoff also serves to eliminate the portion of the microphone calibration for which the coherence was low and the uncertainty was unacceptable (see Section 2.2.1 and Figure 2-10) and to remove the dc component of the signals. The high-frequency cutoff

rejected frequencies corresponding to $\omega\delta^*/U_\infty > 12.5$ or $\omega\nu/u_\tau^2 > 0.271$.[5] The cutoff was selected to remove correlated output signal noise observed to exist above 5500 Hz in all the measured signals.

At this point, the Fourier transforms P'(f) and U'(f) were either further processed in the frequency domain or inverse Fourier transformed back into the time domain depending upon the type of analysis to be executed. The inverse finite Fourier transform is defined as

$$x(t,f_s) = \int_0^{f_s} X(f)\, e^{j2\pi ft}\, df \ . \tag{2.18}$$

The discrete form is given by

$$x_n = \sum_{k=0}^{N-1} X(f_k)\, e^{j\frac{2\pi kn}{N}}, \quad n=0,1,\ldots, N-1 \ . \tag{2.19}$$

Separate Fortran programs were developed for each type of analysis undertaken. The various analysis procedures implemented and the subsequent chapter in which the technique and results are discussed are shown in Table 2-2. All individual record pressure and velocity results are presented in Chapter 4. The joint record analyses of the simultaneous wall pressure and turbulent velocity signals are presented in Chapters 5 and 6. Each program generated at least two output files. One file recorded the computational details and intermediate results of the particular analysis for verification purposes. The remaining output file(s) contained tab-delimited output for importing into Deltagraph® Professional.

---

[5]The values of $\omega\delta^*/U_\infty$ and $\omega\nu/u_\tau^2$ associated with both the low- and high-frequency cutoffs for the present investigation are comparable and in some cases identical to values used in other fluctuating wall pressure investigations (Bull 1967, Willmarth and Wooldridge 1963, Willmarth and Yang 1970, Willmarth et al. 1976, Karangelen et al. 1991).

CHAPTER 3

EXPERIMENTAL ENVIRONMENT

The character of the fluctuating wall pressure and streamwise turbulent velocity measurements as well as the relationships between them are affected by factors related to the flow environment in which the experiments are conducted. This includes extraneous disturbances present in the wind tunnel and cylindrical model due to the free-stream turbulence and ambient sound field in the test section, vibration of the cylindrical model, and aerodynamic interaction between the hot-wire probe and the pressure transducer. Also of fundamental importance is the limited spatial resolution resulting from the finite size of the wall pressure transducer and hot-wire probe. Finally, the measurements are strongly influenced by the character of the turbulent boundary layer in which the measurements are performed. The properties of primary interest include the turbulent development of the boundary layer, the streamwise pressure gradient, and the mean flow conditions in the boundary layer. By examining these factors, the nature of the flow environment in which the present measurements were taken can be established, enabling valid comparisons of the present results to those from previous turbulent boundary layer measurements on both flat plates and cylinders.

3.1 Extraneous Disturbances

3.1.1 Free-Stream Turbulence and Ambient Sound Field

Turbulence in the Test Section

The combined turbulence suppression effects of the settling chamber and contraction section resulted in a free-stream turbulence level of $\sqrt{\overline{u'^2}}/U_\infty = 0.001$ at the operating speed of 11.4 m/s used for this investigation. This value was measured at the centerline of the test section without any model or model support mechanisms installed.

With the introduction of the cylindrical model into the test section, turbulence resulting from the wakes of the support wires became a primary consideration. Initially, 0.009-in.-diameter horizontal wires at the inlet and outlet of the test section were used to support the cylindrical model. Because an independent vibration isolation beam system supports the test section, the test section was 'free hanging' and not in contact with any other components of the wind tunnel. Consequently, supporting the cylindrical model entirely within the test section allowed the model to be isolated from everything but the test section to reduce the number of transmission paths for disturbances into the model. However, from preliminary testing, it was discovered that the upper horizontal support wire generated a wake that had a width at the axial location where measurements were to be taken of the order of the cylinder boundary layer thickness. In addition, the shedding vortices generated large-amplitude audible aeolian tones and transverse oscillations of the cylindrical model that created a high-energy spike in the wall pressure spectra at the Strouhal shedding frequency of 3 to 9 kHz, depending upon flow speed. Consequently, after extensive experimentation, a structural airfoil was mounted in the low-speed settling chamber section where vortex shedding and overall disruption of the flow could be minimized. A second structural airfoil at the exit of the test section was also used (see

Section 2.1.3). With this configuration, free-stream turbulence levels measured between the cylinder and test section wall were $\sqrt{\overline{u'^2}}/U_\infty = 0.0015$ at the operating speed of 11.4 m/s.

Ambient Sound Field in the Test Section

The ambient sound field in the test section was measured in the free stream adjacent to the cylinder instrumentation section at the centerline between the cylinder and the test section wall. The measurement was made with a Bruel and Kjaer UA 0436 Turbulence Screen in conjunction with a Bruel and Kjaer 1/2-in. pressure response microphone consisting of a 1/2-in. pressure response Condenser Microphone Cartridge, Type 4134, mounted on a 1/2-in. Microphone Preamplifier, Type 2639, powered by a Type 2804 Power Supply. The Turbulence Screen is a microphone attachment specifically designed for the measurement of airborne noise in ducts. It consists of a 20-in.-long, 0.8-in.-diameter tube with a 16.3-in. axial slit covered with a specially selected damping material to control the flow resistance of the slot. A streamlined nose cone is attached at the front end of the tube while the tail end contains a clamping device to secure the 1/2-in. Bruel and Kjaer microphone. The combined effect of the slit width and damping material enables the Turbulence Screen to distinguish between flow noise resulting from turbulent pressure fluctuations along the length of the tube and acoustic noise in the duct by suppressing the turbulent flow noise. As a result, the Turbulence Screen provides a means by which to measure essentially only the acoustic pressure fluctuations present in the flow.

Because of the noise suppression capabilities of the Turbulence Screen, the measured power spectrum is a direct indication of the ambient sound pressure level in the test section. The power spectral density of the ambient sound field, $\Phi_{p_{amb}}(f)$, measured by

the Turbulence Screen at an operating speed of 11.4 m/s is shown in Figure 3-1(a). The bold line in the figure is the fractional contribution to the total ambient sound field energy (area under $\Phi_{pamb}(f)$) as a function of frequency. Ninety percent of the ambient energy is below 20 Hz, and nearly all the ambient sound energy occurs below 60 Hz.[1] If it is assumed that the ambient sound field in the test section consists of plane waves propagating in the streamwise direction through the test section, streamwise velocity fluctuations will be generated by the acoustic wave. However, because nearly all of the acoustic energy exists below 60 Hz, the bandpass filtering operation ($59 < f < 5332$ Hz) should eliminate all contributions to the wall pressure and velocity signals from acoustic pressure fluctuations in the test section. As a result, pressure-velocity relationships resulting from the ambient sound field in the test section need not be considered in this investigation.

Also shown in Figure 3-1(a) is the power spectral density of the fluctuating wall pressure measured on the cylindrical model by the EM-3068 microphone, $\Phi_p(f)$, as well as the fluctuating wall pressure spectrum corrected for the ambient sound field, $\Phi_p'(f) = \Phi_p(f) - \Phi_{pamb}(f)$. Nearly all the correction to the fluctuating wall pressure spectrum from the ambient sound field occurs below 125 Hz. Below 70 Hz, the ambient sound pressure level exceeds the measured wall pressure spectral level resulting in negative values for $\Phi_p'(f)$ that do not appear in Figure 3-1(a) because of the log scaling. This result indicates that either the wall pressure transducer is not detecting the ambient sound energy below 70 Hz or that the large uncertainty in the calibrated sensitivity response of the EM-3068 microphone at these frequencies is producing artificially low values for the wall pressure spectrum. Shown in Figure 3-1(b) is the coherence between the Turbulence Screen and

---

[1]The small hump that occurs in the ambient sound spectrum near 400 Hz is coincident with the frequency at which a maximum in the wall pressure spectrum occurs. Consequently, it is most likely a contribution to the Turbulence Screen signal from the suppressed turbulent pressure fluctuations.

the EM-3068 wall pressure signals. The nonzero coherence values below 70 Hz indicate that the EM-3068 microphone does detect the low-frequency acoustic pressure fluctuations in the test section. However, because the coherence values are less than one, the two microphone signals are not completely related due either to the uncertainty in the calibrated sensitivity response of the EM-3068 microphone or the microphones not receiving identical acoustic inputs. Either way, corrections to the wall pressure spectrum for the ambient sound level in the test section are approximate. As a result, ambient sound field corrections are not utilized and portions of the wall pressure spectrum below this point are neglected in this investigation (see Section 4.2.2).

3.1.2 Cylindrical Model Vibration

The vibration of the cylindrical model during the pressure-velocity measurements was measured by a Knowles BU-1771 ceramic vibration transducer (accelerometer) that was incorporated into the frame of the cylinder instrumentation section that contained the wall pressure transducer as shown in Figures 2-2 and 2-3. The vibration measurements were performed so that any influence of cylinder vibration on the wall pressure or near-wall velocity measurements could be assessed. The accelerometer is contained in a small rectangular box with dimensions 7.92 mm (0.312 in.) by 5.59 mm (0.220 in.) by 4.14 mm (0.163 in.). It was mounted and epoxied in place at the front edge of the cylinder instrumentation section, approximately 1 in. upstream of the microphone, as shown in Figures 2-2 and 2-3. The active axis of the accelerometer was oriented so that it had its greatest sensitivity to transverse cylinder oscillations in the plane containing the microphone ($\emptyset = 0°$). The accelerometer was electrically connected in parallel with the EM-3068 microphone, and all power and signal connections were made identical to those for the microphone, as discussed in Section 2.2.1 and shown in Figure 2-5. The BU-

1771 vibration transducer's nominal frequency response is flat from 20 to 2500 Hz. The nominal sensitivity is 5.6 mV/g (-45 dB re 1V per 1g of vibration).

The power spectral density of the cylinder vibration measured by the BU-1771 vibration transducer at an operating speed of 11.4 m/s is shown in Figure 3-2(a). Nearly all the vibrational energy is concentrated in the band of frequencies from 150 to 300 Hz due to a peak in the spectrum at approximately 235 Hz. Although it is difficult to predict natural frequencies of oscillation for the cylinder due to the coupling of the cylinder, support wires, test section, and contraction section under the 75-lb tensile loading, the natural frequency of transverse oscillation for the cylinder and support wires is at least an order of magnitude less than the 220-Hz spectral peak. Because it is this transverse cylinder oscillation that will have the greatest effect on both the wall pressure measurements and the near-wall velocity measurements,[2] the cylinder vibration should not have much of an effect on the results.

This is confirmed from the computed coherence functions between the fluctuating wall pressure and accelerometer and the streamwise turbulent velocity at $y/\delta = 0.016$ ($y^+ = 14$) and accelerometer in Figures 3-2(b) and 3-2(c), respectively. The coherence between the velocity and accelerometer in Figure 3-2(c) is essentially zero at all frequencies, indicating that no relationship exists between the cylinder vibration and the hot-wire probe (i.e., the cylinder is not affecting the flow field and the hot wire presence does not affect the cylinder). The coherence between the wall pressure and accelerometer in Figure 3-2(b) is zero except in the frequency range of approximately 500 to 4000 Hz. This indicates that the cylinder oscillations are not detected by the microphone since the coherence is zero for frequencies less than 300 Hz where nearly 100 percent of the vibrational energy exists.

---

[2] By virtue of their design, condenser microphones are inherently sensitive to vibration in a direction perpendicular to the diaphragm. Because the plane of the diaphragm for the EM-3068 microphone was aligned with the axis of the cylinder, the sensitive direction corresponds to a transverse oscillation of the cylinder.

The nonzero coherence above 5000 Hz is probably a result of correlated output noise. This may be related to the fact that the accelerometer and microphone were electrically connected in parallel in the instrumentation section even though the signals from the two devices were independently shielded.

The nonzero coherence values between 500 and 4000 Hz in Figure 3-2(b) roughly coincide with a small concentration of vibrational spectral energy (relative to the general decay of the spectrum) in Figure 3-2(a) in the range of 1000-2000 Hz. This suggests that the nonzero coherence values in this frequency range are a result of small-scale cylinder oscillations caused by the fluctuating wall pressure along a localized region of the cylinder surface. This appears to be supported by the fact that the measured coherence between the wall pressure and accelerometer with no flow in the test section is zero, except above 5000 Hz (not shown). As a result, the nonzero coherence is not a result of the cylinder vibration affecting the wall pressure signal but both the wall pressure and vibration transducers responding to the same input (wall pressure fluctuations). The relatively small coherence values result because the accelerometer responds to wall pressure fluctuations over the surface of the cylinder, while the wall pressure transducer responds to pressure fluctuations at a 'point' on the wall.

3.1.3 Hot-Wire/Microphone Interference

Two issues that need to be addressed are the effect of the hot-wire probe on the wall pressure measurements and the effect of the pinhole microphone on the near-wall hot wire measurements. Wall pressure spectra measured with the hot wire located at $y/\delta = 0.016$ ($y^+ = 14$), $y/\delta = 0.032$ ($y^+ = 28$), and $y/\delta = 1.91$ are shown in Figure 3-3(a). The spectrum measured with the hot-wire probe at $y/\delta = 0.016$ contains more energy than the spectrum with the probe at $y/\delta = 1.91$ for frequencies less than approximately 800 Hz.

This results in a mean square wall pressure level that is 10 percent larger at the near-wall probe position. The effect still exists at a probe position of $y/\delta = 0.032$ as shown in the figure, although it is considerably reduced. Although not shown, the hot-wire probe does not affect the wall pressure measurements at the third wall-normal probe position of $y/\delta = 0.095$ ($y^+ = 85$) as evidenced by a collapse of the wall pressure spectrum with that measured when no probe is present. The hot-wire interference is only experienced with the probe in the streamwise plane containing the microphone (i.e., $\varnothing = 0°$) and at the streamwise location of the pressure transducer ($x^+ = 0$). Consequently, only the two measurement locations immediately above the pressure transducer were affected.[3]

Velocity spectra at $y/\delta = 0.016$ ($y^+ = 14$) in the streamwise plane of the wall pressure transducer ($\varnothing = 0°$) and in the farthest circumferentially separated streamwise plane ($\varnothing = 40°$, $s^+ = 133$) agree within experimental uncertainty. This indicates that the effect of the pinhole on the flow field is negligible, at least for $y^+ > 14$.

A second effect of the near-wall hot-wire probe measurements was detected during examination of the coherence between the velocity and accelerometer measurements discussed in the previous section. When the hot-wire probe is *not* located immediately above the pressure transducer, the coherence between the near-wall velocity and accelerometer measurements is zero at all frequencies as shown in Figure 3-2(c). The probe was located at $x^+ = 0$, $\varnothing = 40°$ for this figure. When the probe *is* located immediately above the pressure transducer ($x^+ = 0$, $\varnothing = 0°$), as shown in Figure 3-3(b), a nonzero coherence exists between the velocity and accelerometer near 1000 Hz for the first two probe positions from the wall (i.e., the two positions for which the hot wire affects the measured wall pressure spectrum). This indicates that at these two probe

[3]The larger wall pressure energies measured at these two locations is likely caused by a wallward flow component resulting from the adjusted flow upstream of the hot-wire probe impinging upon the wall pressure transducer. This is supported by the positive skewness measured for the wall pressure at these locations as opposed to negative skewness when the probe was not present (see Free-stream 4.1.2).

positions the flow about the hot-wire probe is interacting with the pinhole of the microphone causing subtle small-scale cylinder oscillations. Because the coherence measured between the wall pressure and the accelerometer is independent of probe position, the subtle hot-wire-induced vibrations do not affect the wall pressure measurements.

3.2 Spatial Resolution

3.2.1 Wall Pressure Measurements

Transducer Size Effects

Transducer size is probably the most important consideration in comparisons of wall pressure measurements of various investigators. The size of the transducer diaphragm surface places a limit on its spatial resolution of the pressure field because small-scale pressure fluctuations are averaged across the transducer's pressure sensitive surface. In essence, the transducer cannot resolve pressure scales that are smaller than its effective diameter. This results in low-pass spatial filtering of the pressure field and an attenuation of the wall pressure spectrum at high frequencies. This problem of inadequate spatial resolution was recognized during even the earliest wall pressure studies; however, the problem was not formally addressed until the work of Corcos (1963) and Willmarth and Roos (1965).

Corcos (1963) proposed that a correction be applied to the high-frequency portion of the wall pressure spectrum that depends only upon the quantity $\omega d/U_c$, where d is the transducer diameter and U_c is the convection velocity of the pressure-producing disturbance. The ability of this correction to account for the smallest scales in the flow

was brought into question, however, after measurements with the smallest transducers at that time revealed small-scale, high-intensity wall pressure fluctuations that produced rms wall pressure levels of $p_{rms}/q_\infty = 0.01$, nearly twice as large as what was found previously (Emmerling 1973). Only small-scale pressure-producing eddies very near the wall and close to the pressure transducer where their measured intensity would be large would be expected to produce such a large increase in the measured rms pressure. This suggested that important structural details in or near the sublayer were not being detected by the larger pressure transducers used previously. Because the experimental data Corcos used to construct the correction were from cross correlation measurements with pairs of large transducers not capable of resolving these high-intensity, small-scale fluctuations, the theory cannot predict the sort of increase in the rms wall pressure observed by Emmerling (1973).

Recently, Keith and Bennett (1991) extended the Corcos analysis into the wavenumber domain. They concluded that additional uncertainties associated with the nonuniformity of the pressure transducer sensitivity distribution across the transducer diaphragm combined with incomplete knowledge of the true wavenumber-frequency response of the transducer renders the Corcos correction only approximate in nature. As a result, improved turbulence models are necessary if the true frequency spectrum is to be recovered from pressure measurements that were affected by spatial resolution. To date, no improved correction theories have been formulated.

A quantitative measure of the effect of transducer diameter on the resolution of the turbulent flow was provided when existing values of the rms wall pressure level were compiled as a function of transducer size and it was discovered that the wall pressure level, p_{rms}/q_∞, depends on the microphone diameter scaled on inner variables, $d^+ = du_\tau/\nu$ (Emmerling 1973, Bull and Thomas 1976, Schewe 1983). As shown in Figure 3-4, a

very distinct decrease in the rms wall pressure level occurs with increased transducer diameter. It was not until the work of Schewe (1983), however, that the role of transducer diameter on the resolution of the turbulent pressure field was more completely understood. Schewe performed a systematic analysis of transducer diameter in which he varied the transducer diameter over the range $19 \leq d^+ \leq 333$ at constant Reynolds number. From the probability density distributions, skewness, and flatness of the pressure fluctuations for the various size transducers, Schewe found that as the diameter of the transducer increases the transducer statistics approach that of a Gaussian distribution, as shown in Figure 3-5. He explained this observation by the central limit theorem of probability, which asserts that a Gaussian distribution will result from the sum of a large number of mutually independent random variables acting together (Bendat and Piersol 1986). If the fluctuating wall pressure produced by a given pressure structure is assumed to be such a random process and the individual pressure structures are assumed to be statistically independent, then the wall pressure averaged over the face of the transducer will yield a Gaussian distribution if the number of structures being averaged is large. Schewe concluded that a pressure transducer of diameter $d^+ \approx 20$ is sufficient to resolve the pressure structures essential to turbulence.

The pressure sensitive diameter for the Knowles EM-3068 microphone used in this investigation corresponds to $d^+ = 25.9$ for the measurement flow conditions.[4] Because this diameter value represents only a 1- to 2-percent reduction in p_{rms}/q_∞ (shown in Figure 3-4) and a 3- to 4-percent variation in the skewness and flatness values, respectively (shown in Figure 3-5), compared to those values that exist at $d^+ \approx 20$ recommended by Schewe (1983), spatial resolution effects should only have a minimal effect on the present

[4]Keith, Hurdis, and Abraham (1991) have shown that other nondimensional scalings of the wall pressure transducer diameter (d/δ^* and d^+u_τ/U_∞) may be more effective at characterizing the attenuation resulting from inadequate spatial resolution. This will be discussed in conjunction with the fluctuating wall pressure spectrum in Section 4.2.2.

measurements. In addition, the only smaller transducers reported in the literature were those of Schewe (1983) [$d^+ = 19$] in air and Lauchle and Daniels (1987) [$d^+ \approx 1$] in glycerine.

Transducer Pinhole Effects

Because of spatial resolution effects associated with large transducers, investigators have sought to make smaller and smaller transducers, generally of a piezoelectric type material. However, with decreased size comes decreased sensitivity. To decrease the effective diameter without losing sensitivity, other investigators have mounted pinhole caps over the diaphragms of highly sensitive condenser microphones (Blake 1970, Emmerling 1973). These results, however, were called into question by Bull and Thomas (1976). By making extensive measurements with flush-mounted piezoelectric and pinhole transducers of the same diameter, they concluded that measurements made with pinhole transducers will be in serious error for $\omega^+ > 0.1$ due to spurious pressure contributions from the pinhole.

Leehey (1988) draws the Bull and Thomas (1976) results into question, however, because of "the difficulty in establishing a physical basis for the interaction caused by the pinhole microphone with the turbulent boundary layer." Leehey supports his conjecture by comparing pinhole and flush piezoelectric wall pressure spectra of a large number of investigators. Leehey concludes that failure of the high-frequency portion of the spectra to collapse on inner wall variables for pinhole and flush transducers with the same d^+ (see discussion in Section 4.2.2) is more likely a result of the transducer protruding above the wall or errors in the measurement of the wall shear stress. Farabee (1986) and Farabee and Casarella (1991) have also made extensive use of pinhole microphones and have concluded that they are effective for wall pressure measurements. Considering the

contradictory conclusions of Bull and Thomas (1976) and those of Farabee (1986) and Leehey (1988), it is clear that the effect of the pinhole is not very well understood.

Because the Knowles EM-3068 microphone used for the present measurements was of the pinhole variety, the possibility of an effect due to the pinhole must be noted when the present results are compared to those of other investigators.

3.2.2 Velocity Measurements

Hot-Wire Probe Length Effects

When velocity measurements are made with a hot-wire probe, spatial averaging of the velocity fluctuations across the length of the hot wire occurs. When the smallest turbulent scales in the flow are less than the length of the hot wire (which is almost always the case), the spatial averaging will affect the turbulence resolution of the measurements. Johansson and Alfredsson (1983) examined the effect of the hot wire length on measurements of the streamwise velocity in the near-wall region of a turbulent boundary layer. By compiling data of several investigations, they found that a strong correlation exists between the measured value of the maximum turbulence intensity and the hot-wire probe length in viscous units ($l^+ = lu_\tau/\nu$), as shown in Figure 3-6. Maximum turbulence intensities (u_{rms}/u_τ) decrease from a value of roughly 2.8 for probe lengths of a few viscous units to 2.1 for probes of 100 viscous lengths—a decrease of 25 percent. The differences between measured turbulence intensities for different probe lengths diminish as wall-normal distance increases, as would be expected since the spanwise scale of turbulence increases with distance from the wall.

Because larger probe lengths act to average out the small-scale, large-amplitude fluctuations in the boundary layer, the skewness and flatness of measured velocities are

affected by probe length in the near-wall region. The general trend observed by Johansson and Alfredsson (1983) is for the measured skewness and flatness values to be closer to the Gaussian values for measurements made with larger probe lengths ($l^+ = 32$ versus 14). They also observed that the detection of bursting events by the VITA method (see Chapter 5) was sensitive to spatial resolution of the probe, with the number of events detected decreasing with increasing hot wire length . Blackwelder and Haritonidis (1983) also found this to be the case and that a significant decrease in the number of events occurs for probe lengths longer than approximately 20 viscous lengths. The effect is most pronounced with small VITA averaging times ($T^+ \sim 5$) and disappears altogether at large averaging times ($T_0 = TU_\infty/\delta > 1$).

The hot-wire probe used in the present investigation was 0.5 mm (0.02 in.) long, which corresponds to 18.5 viscous wall units for the flow conditions used. For this probe length, the reduction in maximum turbulence intensity near the wall due to spatial averaging amounts to approximately 5 percent (see Figure 3-6). Although the reduction is small, the effect of spatial averaging on the small-scale structure near the wall must be noted when the present measurements are compared to those of other investigators.

3.3 Character of the Turbulent Boundary Layer

3.3.1 Development, Symmetry, and Pressure Gradient

Turbulent Boundary Layer Development

The boundary layer used in this investigation developed along a 123-in.-long, 3/8-in.-diameter brass cylinder suspended along the centerline of a vertically oriented test section.

The cylinder was fitted with an aerodynamically smooth brass nose cone, and the cylinder and nose cone were highly polished to provide a smooth surface for the boundary layer to develop. By examining the temporal character and autospectra of the wall pressure and velocity fluctuations as well as the mean velocity distribution in the boundary layer, it was discovered that the boundary layer on the cylinder with natural transition was not fully developed at the axial location of the wall pressure measurements. This was a result of the limited streamwise extent of the cylinder due to the constraint imposed on the vertical wind tunnel dimension by the laboratory space. This necessitated the use of a boundary layer tripping device.

The boundary layer was tripped by a 3/8-in. rubber O-ring (0.065 in. unstressed thickness) around the cylinder at the joint between the nose cone and the cylinder. The stressed O-ring height, h, is approximately 0.05 in. This satisfies the criterion to cause fully effective tripping to turbulent flow at the free-stream velocity of 11.4 m/s given by $h > 826\nu/U_\infty = 0.043$ in. (White 1974). The wall pressure transducer was located 97.5 in. (1950 trip heights) downstream of the boundary layer trip. With the addition of the trip, a fully developed turbulent boundary layer was established at the location of the wall pressure transducer as evidenced by the character of the mean velocity distribution (Section 3.3.2) and the pressure and velocity fluctuations (Chapter 4). It should be pointed out that controversy exists as to the effect of tripping devices upon the evolution and attainment of a universal statistical structure of turbulent fluctuations. Although many feel all effects of the trip disappear at some reasonable distance downstream of the trip, others contend (Willmarth 1975) that the trip has a permanent influence on the character of the boundary layer, particularly the large-scale eddy structures in the outer portions of the boundary layer. The possibility of such an effect in the present measurements cannot be ruled out.

Boundary Layer Axisymmetry

Willmarth et al. (1976) found that a cylinder yaw angle of 1 degree could result in rms wall pressure differences of up to 20 percent from one side of the cylinder to the other. Lueptow et al. (1985) found that a similar difference existed for the boundary layer thickness for yaw angles as small as 0.1 degree. To avoid influences of this nature on the present measurements, it was necessary to establish a boundary layer that was as symmetric as possible. The first step in this process was the elimination of all cylinder sag or bow. This was achieved by designing the wind tunnel to have a vertical test section so that all gravity effects leading to cylinder sag could be eliminated (see Section 2.1.1). To eliminate the bow in the cylinder resulting from the inherent nonstraightness of the tubing, a tension device was incorporated into the cylindrical model support and alignment assembly (see Section 2.1.3) so that the cylinder could be placed under an axial load. Application of various axial tensile loads to the cylinder and comparison of the edge of the cylinder to an adjacent 0.04-in.-diameter plumb bob chord revealed that 50 lb of tension was sufficient to remove all observable deviation from straightness. A tensile load on the cylinder of 75 lb was used for all the measurements. Based on the diameter of the plumb bob chord, the deviation from straightness can be assumed to be less than 0.01 in. (0.03 cylinder diameters).

The second step involved in establishing an axisymmetric boundary layer was eliminating crossflows by ensuring that the cylinder was accurately aligned with the mean flow. Through the combined adjustability of the upper and lower airfoils in the model support and alignment assembly (see Section 2.1.3), the cylinder was centered and aligned to within 0.5 mm over the full 3-m length of the test section, or to within 0.01 degree of the mean flow. To test the axisymmetry of the boundary layer resulting from this cylinder alignment, wall pressure and wall shear measurements were made at 90-

degree increments around the cylinder by rotating the cylinder in the test section. The results from the wall pressure and wall shear stress measurements done at free-stream velocities of 14.4 and 18.5 m/s are shown in Figure 3-7. The measurements revealed maximum variations of 3.7 percent in the rms wall pressure and 2.5 percent in the mean wall shear stress from the average values computed across all circumferential positions. Since these variations are of the order of experimental uncertainty, the boundary layer was assumed to be axisymmetric.

Streamwise Pressure Gradient

Because streamwise pressure gradients alter the character of the mean flow in the boundary layer, the walls of the test section were set at a divergence angle of approximately 0.13 degrees to counteract the test section wall boundary layer displacement thickness growth and to minimize the streamwise pressure gradient in the test section (see Section 2.1.1). At the operating flow speed of 11.4 m/s used in these experiments, a slight adverse pressure gradient of less than 1 Pa/m ($dC_p/dx < 0.013\ m^{-1}$) was measured at the wall pressure transducer location. A pressure gradient of this magnitude has been found to have a negligible effect on the equilibrium boundary layer on a cylinder (Willmarth and Yang 1970). Thus, it can be assumed that the mean flow in the boundary layer does not differ appreciably from the zero pressure gradient case.

3.3.2 Mean Flow Conditions

Mean Velocity Profile

The mean velocity profile in the turbulent boundary layer on a cylinder in axial flow has been investigated extensively by Richmond (1957), Chin et al. (1967), Rao and

Keshavan (1972), Willmarth et al. (1976), and Lueptow et al. (1985). The recent review by Lueptow (1988) provides an excellent summary of the effect of transverse curvature on the mean properties of the flow field. When the transverse curvature is small ($\delta/a \leq 1$), the cylindrical velocity profile coincides with the planar profile. As transverse curvature increases, the coefficient of friction increases and the cylindrical boundary layer velocity profile becomes fuller than that observed in a planar boundary layer. When the velocity profile is plotted in traditional inner variables (u/u_τ vs yu_τ/ν), the boundary layer with transverse wall curvature retains a logarithmic region, however, the slope of the log region becomes a function of transverse curvature δ/a. Lueptow et al. (1985) proposed a mixed-scale log law for this logarithmic portion of the axisymmetric boundary layer of the form

$$u^+=(1/m)\ln y^+ + n \ . \tag{3.1}$$

By compilation of the mean velocity profile results for the existing axisymmetric boundary layer measurements, Lueptow et al. (1985) constructed empirical relations for the coefficients *m* and *n* in equation (3.1) as a function of δ/a, or

$$m = 0.0274(\delta/a) + 0.373 \ , \tag{3.2}$$

$$n = 4.5(\delta/a)^{0.25} \ . \tag{3.3}$$

Very near the wall in the viscous sublayer, the constant shear layer in the planar boundary layer ($\tau = \tau_w$) is replaced by a constant shear moment ($a\tau_w = r\tau$) in the boundary layer with transverse curvature. This results from the requirement that the shear force per unit length on a cylinder of fluid remains constant. This shear relation forces the velocity

profile in the viscous sublayer of the axisymmetric boundary layer to take the form

$$u^+ = a^+ \ln(r/a)$$
$$= a^+ \ln(1 + y^+/a^+) \ . \qquad (3.4)$$

As a^+ approaches infinity, equation (3.4) reduces to the planar sublayer profile $u^+ = y^+$. However, even for the smallest values of a^+ at which measurements have been made (Willmarth et al. 1976) where $a^+ = 33.4$, equation (3.4) does not differ enough from the linear planar boundary relation to verify whether or not it accurately describes the velocity profile in the viscous sublayer of an axisymmetric boundary layer.

The mean velocity profile for the turbulent boundary layer used in the present investigation is shown in traditional inner coordinates in Figure 3-8. The velocity profile was measured with the hot-wire probe at the axial location of the wall pressure transducer and at a free-stream velocity of 11.4 m/s. This flow speed was used for all the measurements performed in this investigation. Also included in the figure is Coles law (Coles 1955) for an equilibrium planar boundary layer. The value for the friction velocity used to scale the mean velocity for the present measurements was $u_\tau = (\tau_w/\rho)^{1/2} = 0.552$ m/s. This value was computed from the measured Preston tube (Section 2.2.3) wall shear stress of 0.369 Pa. To be able to use Preston's method for a boundary layer with transverse curvature, the flat plate calibration data (Patel 1965) must be assumed to be valid for the cylindrical boundary layer. Because the flat plate calibration data is obtained with the Preston tube immersed in the law of the wall region of the planar boundary layer, the Preston tube used for the shear stress measurement on the cylinder must fall within the region where the cylindrical boundary layer velocity profile can be approximated by the flat plate law of the wall. The Preston tube diameter of 0.022 in. used for the present

investigation corresponds to a height of 21 wall units, as indicated in Figure 3-8. Because the cylindrical boundary layer profile agrees with the planar profile well past $y^+ = 21$, the use of the planar Preston tube calibration data is valid for determining the wall shear stress for this investigation. It is worthwhile to point out that Willmarth et al. (1976) used a Preston tube of similar diameter for cylinder diameters as small as 0.25 in. and $\delta/a = 9.4$.

Also included in Figure 3-8 are the axisymmetric viscous sublayer relation (equation (3.4)) with a+ = 177 and the mixed-scale log law for the logarithmic portion of the axisymmetric boundary layer with $\delta/a = 5.04$ (equations (3.1)-(3.3)). The mean velocity profile measured in the present investigation is in good agreement with the previous axisymmetric turbulent boundary layer results with similar transverse curvature according to equation (3.1). This verifies that the cylindrical boundary layer used for the present investigation was a fully developed turbulent flow. Velocity measurements were not made close enough to the wall to illustrate whether the profile followed equation (3.2).

Flow Parameters

The measurement conditions and experimental parameters used for all of the measurements in this investigation are listed in Table 3-1. The boundary layer parameters computed from the measured mean velocity profile in Figure 3-8, flow parameters derived from the measured wall shear stress, and spatial resolution parameters for the wall pressure transducer and hot-wire probe are also listed. The uncertainty in the measured boundary layer thickness δ is ± 0.0005 m, or $\pm$ 2 percent. This corresponds to an uncertainty in δ/a of ± 0.1. The uncertainty in the measured wall shear stress τ_w is ± 0.013 Pa (or $\pm$ 3.5 percent). This results in an uncertainty of $\pm$ 1.8 percent in u_τ, or ± 0.01 m/s.

CHAPTER 4

STATISTICAL AND SPECTRAL CHARACTERISTICS OF THE WALL PRESSURE AND STREAMWISE VELOCITY FLUCTUATIONS

The statistical and spectral properties of the fluctuating wall pressure and the streamwise turbulent velocities measured in this investigation are presented in this chapter. Some of these properties for boundary layers with transverse curvature have been presented and documented elsewhere in the literature; hence, in these instances, the present results primarily serve to verify the quality of the pressure and velocity measurements made in the present investigation. Otherwise, where similar results for the boundary layer with transverse curvature have not been presented in the literature, possible effects of transverse curvature on the turbulent boundary layer properties will be examined through comparison with measurements made in planar boundary layers.

All the results presented in this chapter are individual record analyses of independently sampled 524,288-point pressure and velocity data records. All joint record analyses of the simultaneously acquired wall-pressure/velocity data are presented in Chapters 5 and 6. The independent velocity measurements were made at the axial location of the pressure transducer but adjacent to the surface of the cylinder opposite to that which contained the pressure transducer. This was done to eliminate any possible effect of the pinhole microphone on the near-wall velocity statistics and spectra. At the sampling frequency of

20000 Hz, the total sampling time for the 524,288-point records corresponds to 26.2 s or approximately 12000 δ/U_∞. The total sampling time for the shorter 81920-point simultaneous pressure and velocity measurements used for the analyses in Chapters 5 and 6 corresponds to 4.1 s or 1912 δ/U_∞. Although either data set was sufficiently long to reveal all essential features of the turbulent flow, the longer independently acquired data were utilized to ensure accurate and reliable statistical and spectral estimates of the fluctuating wall pressure and turbulent streamwise velocity signals.

4.1 Statistical Properties

A turbulent fluid motion is by definition an irregular condition of flow in which the various quantities exhibit an apparently random or disordered behavior in both space and time. However, due to the deterministic dynamics governing the fluid system, a high degree of underlying structure is buried in the turbulent fluctuations. Because of this 'deterministically random' nature of turbulence, standard statistical techniques are an effective means to reveal fundamental characteristics on the "randomness" of the turbulent signals.

4.1.1 Definitions

A turbulent quantity is typically separated into mean and fluctuating components according to

$$X(t) = \overline{X} + x(t) \quad . \tag{4.1}$$

Because $\overline{X}$ is the average value of X(t), the fluctuating or turbulent component x(t) has a zero mean by definition. It is the characteristics of these zero-mean turbulence quantities x(t) that are investigated. The statistical properties of primary interest are the probability density function and its associated moments (rms, skewness, and flatness). From the fundamental principles of probability theory (Bendat and Piersol 1980, 1986), the probability that the random process x(t) will fall within a particular window Δx is equivalent to the fraction of time the signal spends in the interval, or

$$\mathrm{Prob}\left[x < x(t) < x+\Delta x\right] = \lim_{T\to 0}\left[\frac{T[x < x(t) < x+\Delta x]}{T}\right] , \tag{4.2}$$

where $T[x < x(t) < x+\Delta x]$ is the accumulative time the signal spends between the amplitudes x and $x + \Delta x$, and T is the total record length. The probability density function w(x) is obtained by dividing by the interval Δx (i.e., a density) and taking the limit as Δx approaches zero, or

$$w(x) = \lim_{\Delta x\to 0}\left[\frac{\mathrm{Prob}[x < x(t) < x+\Delta x]}{\Delta x}\right] . \tag{4.3}$$

Equation (4.3) (with equation (4.2)) is estimated computationally using a histogram approach defined by

$$\widehat{w(x)} = \frac{N_x}{N\Delta x} , \tag{4.4}$$

where N is the total number of data points, Δx is the histogram bin width, and N_x is the number of data points that fall within a band, Δx, about x ("bin x"). The hat (^) in

equation (4.4) signifies that the quantity is an estimate of the true variable w(x). The actual probability that the random process x(t) occupies some specified range of amplitudes between value *a* and value *b* is determined from

$$\mathrm{Prob}[a \leq x(t) \leq b] = \int_a^b w(x)dx \quad \cdot \qquad (4.5)$$

This equation is useful in determining fraction-of-time contributions of specific signal amplitudes to the total record length.

The *n*th moment of x(t) can be computed directly from w(x) by the expected value operation (Bendat and Piersol 1986)

$$E[x^n(t)] = \int_{-\infty}^{\infty} x^n w(x)dx \quad , \qquad (4.6)$$

where n = 1 is the mean value, n = 2 is the mean square, n = 3 is associated with the skewness, and n = 4 is associated with the kurtosis or flatness. By integration of equation (4.6) between specified limits, contributions to the various statistics by specific signal amplitudes can be computed. To compute the moments directly from discrete data, the sample estimate is used:

$$\widehat{E[x^n]} = \overline{x^n} = \frac{1}{N}\sum_{i=1}^{N} x_i^n \quad . \qquad (4.7)$$

This is the method used for this investigation. The first moment (n = 1) of x(t)

corresponding to the mean is zero by definition. The second moment (n = 2) of x(t) corresponds to the mean square value and provides a measure of the power level of the signal. The root mean square (rms) value of x(t) denoted as x_{rms} is obtained from the square root of the second moment, or

$$x_{rms} = \left(\overline{x^2} \right)^{\frac{1}{2}} . \tag{4.8}$$

The rms value of the signal indicates the typical fluctuation level from the mean.

The third and fourth moments are typically normalized by the third and fourth powers of the standard deviation, σ_x. Because the mean is zero, the standard deviation is equivalent to the rms value due to the relationship $\overline{x^2} = \sigma_x^2 + \overline{x}^2$. Consequently, for the zero-mean random process, the skewness S and kurtosis K are defined by the expressions

$$S = \frac{\overline{x^3}}{x_{rms}^3} , \tag{4.9}$$

$$K = \frac{\overline{x^4}}{x_{rms}^4} . \tag{4.10}$$

The skewness is a measure of the direction of excursions from the mean and the kurtosis is a measure of the magnitude of the excursions from the mean. The values are weighted most heavily by the larger amplitude fluctuations because of the 3rd and 4th powers of x(t).

Because of the random character of turbulence, the statistics of turbulent quantities are frequently compared to those for a Gaussian random process. This is because the Gaussian distribution describes the distribution of a variable that varies in a purely random

('normal') fashion about some mean value. Any divergence from the purely random Gaussian distribution is a result of underlying order or structure in the turbulent system. The probability density function for a zero-mean Gaussian random process is given by

$$w(x) = \frac{1}{\sigma_x\sqrt{2\pi}} e^{-\frac{x^2}{2\sigma_x^2}} . \tag{4.11}$$

If the probability density functions for the Gaussian and turbulent processes are computed in terms of $x(t)/x_{rms}$, σ_x in equation (4.11) is unity and the turbulent and Gaussian distributions can be compared directly. A Gaussian distribution has a skewness of 0 and a flatness of 3. For a zero-mean non-Gaussian process, $S < 0$ indicates large-amplitude negative fluctuations are more likely than positive ones, while $S > 0$ indicates large-amplitude positive fluctuations are more likely. A value of $K > 3$ indicates that large-amplitude fluctuations occur more frequently than for a Gaussian signal, while $K < 3$ implies that large-amplitude fluctuations occur less frequently.

The statistical results for the wall pressure and streamwise velocities were computed after digitally filtering the signals to remove low-frequency wind-tunnel-generated large-eddy turbulence and acoustic disturbances in the test section. Low- and high-frequency cutoffs of 59 and 5332 Hz were utilized—consistent with the filtering operation used throughout the remainder of this investigation (see Section 2.3.2). The analysis of the data was performed by the programs PSTATS and USTATS in Table 2-2.

Segments of the temporal records for the fluctuating wall pressure and the streamwise turbulent velocities at all nine wall-normal positions at which data were taken are shown in Figure 4-1. The signals are normalized by their respective rms values. None of the temporal records in Figure 4-1 were taken simultaneously and are therefore completely independent, unsynchronized signals. The temporal records illustrate the overall character

of the turbulent fluctuations measured in this investigation and provide a basis for the statistical results to follow. The high-frequency oscillations in the velocity signals for $y/\delta > 1$ are 5000-Hz electrical noise. The noise is visible because the signals are normalized by their rms values and a small signal-to-noise ratio exists for the hot wire at these low-turbulence wall-normal locations.

4.1.2 Fluctuating Wall Pressure Statistics

The probability density functions for the fluctuating wall pressure measured in the present investigation is compared to that for a zero-mean unit-variance Gaussian random process in Figure 4-2(a). The probability density function was computed by dividing the range between the minimum and maximum fluctuation levels into 101 uniform bins. For the minimum and maximum fluctuations of $-7.3p_{rms}$ and $6.7p_{rms}$, shown in Table 4-1, this corresponds to a bin size of $0.141p_{rms}$. Also included in the figure is the probability density for the fluctuating wall pressure measured in a planar boundary layer by Schewe (1983) with a transducer diameter of $d^+ = 19$[1]. The probability density function for the present measurements in the boundary layer with transverse curvature appears almost identical to the planar boundary layer result of Schewe. Both sets of measurements reveal a higher probability for the occurrence of fluctuations near the mean ($|p/p_{rms}| < 0.5$) and at large positive and negative amplitudes ($|p/p_{rms}| > 3$) than is observed for the Gaussian process. This indicates that the fluctuating wall pressure is an intermittent process characterized by large-amplitude fluctuations separated by relatively long periods of inactivity. This intermittent character is confirmed by the large flatness values of 5.05 for the present measurements and 4.9 for the planar boundary layer measurements of Schewe

[1] The measurements of Schewe (1983) were performed at $Re_\theta = 1400$ with a flush transducer. Because the effects of Reynolds number and microphone type on higher order pressure statistics have not been documented in the literature, their effect is unclear.

(1983) (compared to 3 for a Gaussian distribution), shown in Table 4-1. Adjusted for the transducer spatial resolution effects found by Schewe (1983) (see Figure 3-5), an even larger flatness value of 5.3 is obtained for the present measurements. If this larger value in the present measurements is solely due to transverse wall curvature, large-amplitude wall pressure fluctuations occur more frequently in the cylindrical boundary layer than in the planar boundary layer.[2] As discussed by Schewe (1983), these large-amplitude wall pressure fluctuations are a manifestation of the near-wall, small-scale coherent structures essential to the generation of turbulence in the boundary layer.

To examine more closely the character of the wall pressure fluctuations associated with these near-wall coherent structures, the mean square energy associated with a particular fluctuation level is examined in Figure 4-2(b) for the present measurements and the Gaussian signal. From equation (4.6) with n = 2, the mean square wall pressure level can be computed from the probability density function according to

$$\overline{p^2} = p_{rms}^2 = \int_{-\infty}^{\infty} p^2 w(p) dp \ . \tag{4.12}$$

Consequently, if p/p_{rms} is used in place of p in equation (4.12), the integrand $(p/p_{rms})^2 w(p/p_{rms})$ represents the fractional contribution to the total mean square wall pressure level at a particular fluctuation level. It is this quantity that is plotted in Figure 4-2(b). It represents a 'mean-square energy density function' and is simply the mean square

[2]The unfiltered wall pressure statistics in the present investigation were contaminated by low-frequency acoustic noise; hence, the highpass filter acted to increase the flatness from 4.57 to 5.05 due to removal of low-frequency oscillations near the mean. Because contributions to the rms wall pressure from this low-frequency portion of the spectrum amount to less than 1 percent (Farabee and Casarella 1991), the filtered statistics for the present measurements are believed to be accurate. As evidence, the filtered planar boundary layer measurements of Karangelen et al. (1991) revealed a flatness of 4.91—in agreement with the measurements of Schewe (1983).

energy associated with a particular fluctuation level, $(p/p_{rms})^2$, weighted by the likelihood of the fluctuation level occurring, $w(p/p_{rms})$. Since the fraction of energy from $-\infty$ to ∞ must equal one, the area under each curve in Figure 4-2(b) is unity. As can be seen in the figure, the energy density for large-amplitude wall pressure fluctuations, $|p/p_{rms}| > 3$, is considerably larger than that which exists for a Gaussian signal. Consequently, large-amplitude wall pressure fluctuations occur slightly more frequently compared to a Gaussian signal (Figure 4-2a) but contribute a significantly larger fraction to the total mean square energy.

A similar result was found for the planar boundary layer by Schewe (1983) when he computed that the wall pressure fluctuations exceed a threshold of $3p_{rms}$ 1.0 percent of the time but contribute 40 percent to the total rms wall pressure (compared to 0.3 percent of the time and 17 percent of the rms for a Gaussian signal). Performance of a similar computation for the present measurements (i.e., integrating Figures 4-2(a) and 4-2(b) above and below the given threshold level) shows that the fluctuating wall pressure signal in the present investigation exceeds the $|p/p_{rms}| > 3$ threshold 1.1 percent of the time and contributes 39.7 percent to the rms wall pressure. Hence, the overall character of the large-amplitude wall pressure fluctuations in the cylindrical and planar boundary layers appears similar. Even so, for all thresholds greater than 2, the percent-time values for the present measurements are slightly larger than those of Schewe (1983). Although the differences are small (5-10 percent) and could be due to experimental error, the trend is consistent with the larger flatness measured for the present investigation and the notion that large-amplitude fluctuations occur more frequently in the cylindrical boundary layer. Considering the additional fact that wall pressure fluctuations exceeding a threshold of $6p_{rms}$ in the present measurements occur less than 0.01 percent of the time but contribute over 6 percent to the total rms wall pressure level (versus 0.03 percent for the Gaussian

signal), it is clear that the large-amplitude wall pressure fluctuations play a predominant role in the character and overall energy level of the wall pressure signal.

By examining Figure 4-2(b), it can be seen that a slight asymmetry exists in the mean square energy density at large amplitudes with larger values of $(p/p_{rms})^2 w(p/p_{rms})$ occurring for large negative amplitudes. The asymmetry is not as easy to detect in the probability density function itself (Figure 4-2a). Results for the percent-time and percent mean square energy contributions for fluctuations that exceed some positive ($+\kappa$) or negative ($-\kappa$) threshold $\kappa = |p/p_{rms}|$ are shown in Figures 4-3(a) and 4-3(b). Results for a Gaussian signal are also included. These values are obtained by integrating the curves in Figures 4-2(a) and 4-2(b) above (κ to ∞) or below ($-\infty$ to κ) the specific threshold level. Although the asymmetry is more apparent in the mean square wall pressure contributions (Figure 4-3b), negative events occur more frequently and contribute more to the mean square wall pressure than positive events at all threshold levels. The negative skewness value of -0.0843 (-0.0813 without filter) for the present measurements confirms the observed asymmetry.

Schewe (1983) also observed an asymmetry in the percent-time of large-amplitude events in a planar boundary layer, except he found that a greater probability for occurrence of large negative amplitudes begins at a threshold of $2p_{rms}$. His measured skewness was -0.18. Haritonidis et al. (1990) has suggested that positive wall pressures are associated with sweeps while negative pressures are associated with ejections and inward interactions. Consequently, the negative skewness values measured for the wall pressure by Schewe and in the present investigation are consistent with the finding of Tiederman (1990) that multiple ejections can occur during the bursting process. The smaller negative skewness value for the present measurements of -0.08 (equal to -0.1 when transducer resolution is accounted for, see Figure 3-6) indicates that a slightly smaller number of

negative with respect to positive large-amplitude pressure fluctuations are present. Consequently, if the difference is solely a result of transverse curvature, this result suggests that a larger relative number of sweeps to ejections (or inward interactions) occurs in the cylindrical boundary layer.

The rms wall pressure measured in the present investigation and listed in Table 4-1 was 0.679 Pa. Nondimensionalized by the free-stream dynamic pressure and the mean wall shear stress, the rms levels are $p_{rms}/q_\infty = 8.64 \times 10^{-3}$ and $p_{rms}/\tau_w = 1.84$, respectively. Schewe (1983) reported values of $p_{rms}/q_\infty = 9.8 \times 10^{-3}$ and $p_{rms}/\tau_w = 2.48$ for his measurements in a planar boundary layer with $d^+ = 19$. Since the slight difference in transducer spatial resolutions only amounts to a 1- to 2-percent variation in the rms wall pressure level (see Figure 3-4), it would appear that the effect of transverse curvature is to decrease the mean square energy level of the wall pressure fluctuations. Although the Reynolds number of the present investigation is larger than that of Schewe (1983) ($Re_\theta = 2870$ versus 1400), the analyses of Bradshaw (1967) and Panton and Linebarger (1974) along with the accumulative body of experimental and numerical evidence show that the rms wall pressure level increases, not decreases, with Reynolds number. According to the results of Bull and Thomas (1976), the effect of the pinhole used for the present measurements would also serve to increase—not decrease—the rms wall pressure level.

Further support for the observed trend is provided in Figure 4-4, where the rms wall pressure levels from the numerically simulated cylindrical boundary layer results of Neves et al. (1991), the cylindrical boundary layer measurements of Willmarth and Yang (1970), and the present measurements are compared to simulated and experimental planar wall pressure levels. The use of δ^*/a in Figure 4-4 rather than δ/a was motivated by the relative uncertainty in measuring δ. Because the rms wall pressure level must be

interpreted in light of transducer resolution, transducer type, and Reynolds number, curves are drawn connecting data obtained under similar conditions. The results clearly indicate that the rms wall pressure level decreases with increased transverse curvature in all cases. The only exception is for the Willmarth data scaled on q_∞; however, this is, in all likelihood, a result of the larger transducer resolution for the planar measurements of Willmarth and Roos (1965) and the relatively small transverse curvature for the measurements of Willmarth and Yang (1970). The more pronounced decrease in p_{rms}/τ_w with increased δ^*/a compared to p_{rms}/q_∞ is due to the increase in the coefficient of friction that occurs with increased transverse curvature.

4.1.3 Streamwise Turbulent Velocity Statistics

The probability density functions for the streamwise turbulent velocities at the nine wall-normal locations in the cylindrical boundary layer are shown in Figure 4-5. Also included in the figures is the probability density function (PDF) for the Gaussian random process. The probability densities at the first five wall-normal positions ($14 < y^+ < 339$) maintain a relatively Gaussian appearance except that the peak magnitudes are shifted to the positive side of the mean. The PDFs become peaked for the measurements in the range $677 < y^+ < 1355$ ($0.762 < y/\delta < 1.52$) due to the intermittent character of the turbulent potential flow interface, with the largest peak occurring for the measurement at $y/\delta = 1.143$. The probability density function at $y/\delta = 1.91$ regains a relatively Gaussian appearance due to the diminished influence of the turbulent potential flow interface and the relatively homogeneous and therefore Gaussian nature (Hinze 1975) of the free-stream turbulence. These results agree qualitatively with the results of Luxton et al. (1984) for a cylindrical boundary layer with transverse curvatures of $\delta/a = 26$ to 41.6. The present results also appear to agree qualitatively with the probability density functions measured in

a planar boundary layer by Klebanoff (1954) and others.

The statistical moments for the measured streamwise turbulent velocities are shown in Table 4-1 and plotted in Figures 4-6 and 4-7. After examining the unfiltered spectral densities of the streamwise velocity signals (presented in Section 4.2), it was discovered that low-frequency disturbances were not contaminating the velocity measurements made within the boundary layer ($y/\delta < 1$). Thus, the unfiltered turbulent velocity statistics for $y/\delta < 1$ were utilized in Table 4-1 and Figures 4-6 and 4-7 because the results of Lueptow (1986), Lueptow and Haritonidis (1987), and Haritonidis et al. (1990), to which the present measurements are compared, are unfiltered. For $y/\delta > 1$, where the low-frequency spectra were clearly contaminated, the filter was utilized.

The skewness distribution measured for the present investigation is compared to the planar boundary layer measurements of Haritonidis et al. (1990) in Figure 4-6(a). The present measurements have negative skewness throughout most of the boundary layer with a sharp negative peak magnitude of -1.5 occurring near $y^+ = 1000$ due to intermittency near the edge of the boundary layer. The skewness is near the Gaussian value of zero at the farthest position from the wall due to the Gaussian nature of free-stream turbulence. It is also near zero at the closest position to the wall. The measurements are qualitatively similar to the planar boundary layer measurements of Haritonidis et al. (1990), except the present measurements are more negatively skewed throughout the entire boundary layer. The effect is amplified if spatial resolution effects of the hot wire are considered since Johansson and Alfredsson (1983) found that larger probe lengths, such as the one used in the present investigation ($l^+ = 18.5$) compared to that of Haritonidis et al. ($l^+ = 5.1$), cause the skewness to be less, not more, negative. Since negative skewness implies that negative excursions from the mean are more likely, the larger negative values in the present investigation indicate that transverse curvature acts

to increase the relative number of negative streamwise velocity fluctuations throughout the boundary layer. The cylindrical boundary layer measurements of Lueptow (1986) for $\delta/a = 8$ and $l^+ = 7.7$ agree with the present findings. Negative streamwise velocity fluctuations result predominantly from ejections for $y^+ < 100$ and inward interactions for $y^+ > 100$ (Robinson 1990); hence, transverse curvature appears to increase the relative number of these types of motions over those found in a planar boundary layer, at least for $y^+ > 14$.

As the wall is approached, the streamwise velocity skewness becomes positive in a planar boundary layer due to an increase in the number of large-amplitude positive velocity fluctuations resulting from sweep structures in the near-wall region. Brodkey et al. (1974) found that the contributions to the Reynolds stress from ejections and sweeps are nearly equal at $y^+ = 15$. In the previous section, the measured skewness for the wall pressure was less negative than the value measured by Schewe (1983) in a planar boundary layer. If this is a result, as speculated, of an increased number of sweep-motions near the wall over those found in the planar boundary layer, then the near-wall streamwise velocity measurements in the cylindrical boundary layer should be more positively skewed for $y^+ < 15$. Although measurements were not taken close enough to the wall in the present investigation to observe whether this is the case, the measurements of Lueptow (1986) appear to support this conjecture, although not conclusively.

The flatness distribution for the present measurements in Figure 4-6(b) remains very near the Gaussian value of 3 throughout most of the boundary layer, except near $y^+ = 1000$ where a sharp peak occurs. This distribution is very similar in character to the flatness distribution measured by Haritonidis et al. (1990) in a planar boundary layer, also shown in Figure 4-6(b). A similar trend was found for the boundary layer with transverse curvature by Lueptow (1986). A notable difference between the present

measurements and those for the planar boundary layer is that when viewed in coordinates of y/δ, the peak in the flatness distribution (as well as that for the skewness) for the cylindrical boundary layer occurs at a farther distance from the wall ($y/\delta = 1.1$) than observed for the planar boundary layer ($y/\delta \sim 0.7$, Haritonidis et al. 1990; $y/\delta \sim 0.9$, Klebanoff 1954).[3] The cylindrical boundary layer measurements of Lueptow (1986) also support this trend. A monotonic increase in the wall-normal location of the flatness maximum with increasing δ/a is apparent or can be extrapolated from the results of Luxton et al. (1984) for transverse curvatures of $\delta/a = 26$ to 41.6. Because a high flatness is indicative of a highly intermittent signal, this result indicates that the interface between the highly intermittent turbulent and nonturbulent flow is shifted to a larger wall-normal location in the cylindrical boundary layer. This is supported by the direct intermittency measurements of Lueptow and Haritonidis (1987) in a cylindrical boundary layer with $\delta/a \sim 7$, in which they found that the mean location of the turbulent/nonturbulent interface was shifted to $y/\delta = 1.0$ from $y/\delta = 0.8$ for the planar boundary layer.

Very near the wall ($y^+ < 10$), the flatness in the planar boundary layer is larger than the Gaussian level of 3, presumably due to large-amplitude velocity fluctuations resulting from the intermittency of the sweep structures very near the wall. Although the measurements were not taken close enough to the wall in the present investigation to detect this trend, the cylindrical boundary layer measurements of Lueptow (1986) did reveal values similar to the planar boundary layer values for $y^+ < 15$.

The distribution of streamwise turbulence intensity for the present measurements scaled on both inner and outer variables, along with the planar boundary layer measurements of Haritonidis et al. (1990), is shown in Figure 4-7. The turbulence

[3]Haritonidis et al. did not explicitly state values for y/δ. Consequently, the value of $y/\delta = 0.7$ was estimated from $y/\delta = y^+/\delta^+$ with $\delta^+ = 1500$. The value for δ^+ was estimated from the work of Johansson et al. (1987), which was performed in the same wind tunnel under very similar flow conditions.

intensities measured in the present investigation nondimensionalized by the friction velocity in Figure 4-7(a) are less than the planar boundary layer values at all points in the boundary layer. This is consistent with the cylindrical boundary layer measurements of Afzal and Singh (1976), Luxton et al. (1984), and the numerically simulated results of Neves et al. (1991). Neves et al. found a systematic decrease in the peak intensity and a shifting of the peak intensity slightly closer to the wall with increased transverse curvature. The decrease in intensity was attributed to the decreased surface area over which vorticity fluctuations can be generated in the cylindrical boundary layer.

The measurements of Patel et al. (1974) and Lueptow and Haritonidis (1987), however, indicate that u_{rms}/u_τ in the cylindrical boundary layer exceeds the planar boundary layer values very near the wall ($y^+ < 30$-40). The results of Lueptow and Haritonidis (1987) with $\delta/a = 7.2$, $Re_\theta = 3300$ and $l^+ = 14.8$ are included in Figure 4-7(a) for comparison. Although the measurements of Lueptow and Haritonidis (1987) and the present measurements agree reasonably well for $y^+ > 100$, the present measurements have a smaller magnitude near the wall. Considering the difficulty in making accurate wall shear measurements, it is possible that the difference near the wall is a result of inaccuracies in the calculated friction velocity.[4] To assess whether this might be the case, the present measurements, along with those of Lueptow et al., are plotted in Figure 4-7(b) in outer variables that nondimensionalize u_{rms} by the free-stream velocity. The planar boundary layer results of Haritonidis et al. (1990) are also included ($\delta^+ = 1500$ assumed, see footnote 3). Clearly, the disparity between the measurements of Lueptow and Haritonidis (1987) and the present investigation disappears in this scaling, confirming the likelihood that the differences in Figure 4-7(a) are due to the measurement of the wall shear stress.

[4]The difference in the l^+ values is not enough to account for the observed magnitude difference.

Comparison of these sets of measurements to the planar boundary layer values shows that the effect of transverse curvature appears to be a reduction in the turbulence intensities throughout most of the layer ($0.07 < y/\delta < 0.7$) but an increase in the levels very near the wall and at the edge of the boundary layer ($y/\delta > 0.8$). The results for u_{rms}/U_∞ of Afzal and Singh (1976), Luxton et al. (1984), and Neves et al. (1991) also support these trends. A systematic increase in u_{rms}/U_∞ near the wall and systematic decrease in u_{rms}/U_∞ in the outer layer are also apparent in the accumulative body of results, as well as the results in Figure 4-7(b). When u_{rms} is scaled on u_τ, the systematic variation is obscured because u_τ itself is a function of transverse curvature. From the decrease in u_{rms}/u_τ with increased δ/a observed in the numerical results of Neves et al., it appears that u_{rms} near the wall increases at a slower rate than u_τ. Since the wall of the cylindrical boundary layer provides less constraint on the outer flow and motion of eddies in the boundary layer, the increased turbulence intensities near the wall could also be related to the passage of large-scale outer structures (of velocity scale U_∞) very near the wall (Luxton et al. 1984). The larger turbulence intensities observed at $y/\delta > 0.8$ are difficult to interpret.

4.2 Spectral Properties

Because of the random character of turbulence, a broad range of quasi-coherent structures and, hence, quasi-periodic motions are present in any turbulent flow. Although distinct frequencies are not permanently present, an average broadband distribution of turbulent energy across all frequencies present in the flow does exist. Spectral analysis of turbulence quantities provides a means to describe the energy content of the turbulent flow as a function of frequency. It thus provides essential information on the random nature of the turbulent signals and a window by which to view the distribution of scales in the

turbulent flow. As a result, any effect transverse curvature has on the physical structure of the turbulent boundary layer should be revealed through the spectral characteristics of measured turbulence quantities. The spectral analysis entails autospectral densities of the fluctuating wall pressure and streamwise turbulent velocity signals.

4.2.1 Definitions

Although there are several ways to compute spectral density functions for a stationary random process, the most straightforward approach is based on the finite Fourier transform of the data record. The one-sided autospectral density for a stationary random variable x(t) is defined as

$$\begin{aligned}\Phi_{xx}(f) &= 2\lim_{T\to\infty} T\,E\left[X^*(f)X(f)\right] \\ &= 2\lim_{T\to\infty} T\,E\left[|X(f)|^2\right] ,\end{aligned} \tag{4.13}$$

where X(f) is the finite Fourier transform of x(t) defined by equation (2.12). In practice, it is impossible to perform the limiting operation in equation (4.13), and the expected value operation E[ ] must be performed over a finite number of subrecords. Consequently, equation (4.13) is estimated by the ensemble average of the subrecords as

$$\widehat{\Phi}_{xx}(f) = \frac{2T}{n_d}\sum_{i=1}^{n_d} |X_i(f)|^2 , \tag{4.14}$$

where n_d is the number of subrecords, T represents the length of each subrecord, and the hat (^) signifies an estimate of the spectral density. Herein, a single subscript will replace

the repeated subscript in the symbol for the autospectrum. Equation (4.14) is performed computationally in terms of the discrete finite Fourier transform according to the following expression:

$$\widehat{\Phi}_x(f_k) = \frac{2T}{n_d} \sum_{i=1}^{n_d} |X_i(f_k)|^2 \quad , \quad k=0,1,\ldots, N/2 \quad , \tag{4.15}$$

where

$$X_i(f_k) = \frac{1}{N} \sum_{n=0}^{N-1} x_{i_n} e^{\frac{-j2\pi kn}{N}} \quad k=0,1,\ldots, N-1 \tag{4.16}$$

and N represents the number of data points in each subrecord. Equation (4.16) was computed by fast Fourier transform (FFT) procedures. Because $\widehat{\Phi}_x(f_k)$ is a one-sided autospectrum (i.e., $f \geq 0$), only spectral components up to values of $k = N/2$ are computed in equation (4.15). All of the autospectral density results to be presented shortly utilized 512 subrecords of 1024 points each (524288 total points), as shown in Table 2-2. This produced a frequency resolution of $\Delta f = 19.53$ Hz. Digital filtering was not used for the following spectral results.

4.2.2 Fluctuating Wall Pressure Spectrum

<u>Wall Pressure Spectral Scaling</u>

Because the fluctuating wall pressure at a point is associated with velocity fluctuations throughout the entire boundary layer through the Poisson equation for the wall pressure (see Section 1.1.2 and equation 1.7), the power spectral density of the fluctuating wall pressure is established by the turbulence throughout the entire boundary layer being convected past the pressure transducer. As a result, scaling methods (dynamical

similarity) have been effective at identifying the location of the turbulent source regions in the boundary layer that contribute to the various regions of the wall pressure spectrum. These regions are consistent with the spectral regions of the wall pressure field suggested from examining the form of the spectral solution to the Poisson equation for the wall pressure.

Recall from Section 1.1.2 that the solution suggests three separate spectral regions exist for the wall pressure fluctuations corresponding to three separate turbulent source regions in the boundary layer. Turbulent sources in the innermost portions of the boundary layer ($y^+ < 30$) contribute to the high-frequency portion of the wall pressure spectrum and lead to an ω^{-5} frequency dependence for the spectral energy. Sources in the log portions of the boundary layer, including the inner portion of the wake region ($y^+ > 30$ to $y/\delta < 0.6$), contribute to the intermediate spectral frequencies and result in an ω^{-1} frequency dependence for the spectrum. Finally, the solution suggests that sources located in the outermost portions of the boundary layer ($y/\delta > 0.6$), including the turbulent/nonturbulent interface, and the portion of the potential flow outside of the boundary layer that experiences irrotational velocity fluctuations due to the undulating turbulent/nonturbulent interface contribute to the low-frequency portion of the wall pressure spectrum and lead to an ω^2 frequency dependence.

When the experimental wall pressure spectra are scaled on outer variables associated with the global features of the flow (i.e., δ^* and U_∞), the low-frequency portion of the spectra collapse independent of Reynolds number. Hence, it can be assumed that sources contributing to the low-frequency portion of the spectra are located in the outer regions of the boundary layer. When scaled on inner variables associated with the viscous effects at the wall (i.e., ν and u_τ), a universal collapse of the experimental wall pressure spectra is

observed independent of Reynolds number at high frequencies.[5] This indicates that sources that contribute to the high-frequency portions of the spectra are located in the near-wall region of the boundary layer. Intermediate frequencies tend to collapse on inner or outer scales.

The appropriate outer scaling variables required to collapse the low-frequency portions of the spectra with widely varying Reynolds numbers are somewhat unresolved. The two outer scaling laws used most frequently are

(1) Outer Variables $$\frac{\Phi_p(\omega)}{\rho^2\delta^* U_\infty^3} \quad \text{vs.} \quad \frac{\omega\delta^*}{U_\infty},$$

(2) Outer (Mixed) Variables $$\frac{\Phi_p(\omega) U_\infty}{\tau_w^2\delta^*} \quad \text{vs.} \quad \frac{\omega\delta^*}{U_\infty},$$

where $\omega = 2\pi f$ and $\Phi_p(\omega) = \Phi_p(f)/2\pi$. Recently Keith, Hurdis, and Abraham (1991) have concluded that the mixed scaling is more effective for data sets having $Re_\theta < 4500$, while the appropriate scaling for data sets having $Re_\theta > 4500$ remains inconclusive due to conflicting results of different investigators. In either outer scaling, high-frequency spectral energy increases with Reynolds number. If high-frequency spectral attenuation due to transducer spatial resolution is assumed to follow the general form proposed by Corcos (1963), the quantity d/δ^* is the appropriate parameter that determines the spatial resolution for the outer scaling (Keith, Hurdis, and Abraham 1991). The inner scaling law that produces a universal collapse independent of Reynolds number of the high

[5]The collapse at high frequencies only occurs after transducer effects are appropriately accounted for. As discussed in Section 3.2, a pressure transducer cannot resolve turbulent scales smaller than its effective diameter. Consequently, transducer size affects the spatial resolution of the pressure field and leads to an attenuation of the wall pressure spectrum at high frequencies. The use of pinhole microphones has also been associated with increased high-frequency spectral levels (Bull and Thomas 1976).

frequency portions of the wall pressure spectra is given by

(3) Inner Variables $$\frac{\Phi_p(\omega)u_\tau^2}{\tau_w^2\nu} \text{ vs. } \frac{\omega\nu}{u_\tau^2}\,.$$

For this scaling, the quantity d^+ has traditionally been used as the spatial resolution parameter that determines the high-frequency attenuation of the spectra. If the form of the Corcos model is considered, however, dimensional analysis reveals that the appropriate spatial resolution parameter is given by $d^* = d^+(u_\tau/U_\infty)$ (Keith, Hurdis, and Abraham 1991). When spectra are scaled on inner variables, the low-frequency spectral energy increases with Reynolds number.

Comparison of Wall Pressure Spectral Results

Because the wall pressure spectra are established by the convected turbulence throughout the entire boundary layer, any effect that transverse curvature has on the flow field and turbulence structure could be revealed in the wall pressure spectrum. The wall pressure spectrum measured in the present investigation is shown in dimensional coordinates in Figure 4-8. The limits of the bandpass filter indicated in the figure are included for later reference (Chapters 5 and 6). The spectrum clearly exhibits an extended region of ω^{-5} frequency dependence at high frequencies, as predicted by Blake (1986), who considered the form of the spectral solution to the Poisson equation for the wall pressure (equation (1.7)). An extended ω^{-1} region predicted to exist by Blake and others is not apparent. Due to the low-frequency acoustic contamination (see Section 3.1.1), an ω^2 frequency dependence predicted to result at low frequencies from irrotational velocity fluctuations in the undulating turbulent/nonturbulent interface is also not visible in the

present measurements.

To deduce the effect of transverse curvature on the various spectral regions of the boundary layer, the present measurements are compared to the planar boundary layer measurements of Farabee (1986) in the three different scalings in Figures 4-9, 4-10, and 4-11. The data of Farabee were selected for comparison because they were obtained with a transducer resolution, microphone type (i.e., pinhole), and Reynolds number similar to those used in the present investigation. The low-frequency contamination below 78 Hz as well as the high-frequency noise above 6700 Hz in the present measurements, both denoted in Figure 4-8, are ignored in the evaluation. Because $Re_\theta < 4500$ for both sets of measurements, the mixed scaling in Figure 4-10 should be the appropriate outer scaling. Since only the low-frequency portions of the spectra collapse independent of Reynolds number in an outer scaling, the spectra should only be compared at low frequencies in Figure 4-10. As can be seen, the present measurements have lower energy content than the planar boundary layer spectrum at low frequencies. The smaller difference in low-frequency energy in Figure 4-9 may be related to the inappropriateness of this outer scaling for data with $Re_\theta < 4500$.

The wall pressure spectra scaled on inner variables are shown in Figure 4-11. Since only the high-frequency portions of the spectra collapse independent of Reynolds number in an inner scaling, the spectra should only be compared at high frequencies in Figure 4-11. Because of the similar transducer types and the small difference of 5 percent in transducer diameters in terms of the inner scaling spatial resolution parameter, d^*, for the two sets of measurements, the influence of these factors on the high-frequency spectral levels should not be large. As can be seen, at high frequencies the present measurements collapse with the planar boundary layer spectrum of Farabee (1986). That the high-frequency portions of the spectra also collapse in both outer scalings (Figures 4-9 and

4-10) tends to indicate that the small differences in Reynolds number and transducer resolution between the two sets of measurements are negligible.

The reduced low-frequency spectral energy content observed in the present measurements is consistent with the cylindrical boundary layer measurements of Willmarth and Yang (1970).[6] They used this result in part to arrive at the conclusion that the transverse shearing action in a boundary layer with transverse curvature acts to reduce the scale of the larger eddies. The spectral results of Willmarth and Yang and the planar boundary layer spectrum of Bull (1967), to which they compared their results, are included in Figures 4-9 through 4-11. The outer scaling in Figure 4-9 is similar to the scaling used by Willmarth and Yang (1970). Since $Re_\theta > 4500$ for both sets of measurements, it should be the more appropriate outer scaling. With this scaling, Willmarth and Yang (1970) also concluded that the spectral energy content of the cylindrical boundary layer exceeds that of the planar boundary layer at high frequencies. This contributed to their conclusion that the pressure-producing eddies in the cylindrical boundary layer are smaller than in a planar boundary layer. However, since differences in Reynolds number exist between the two sets of measurements, the outer scaling can only be used to compare the low-frequency portions of their wall pressure spectra. The larger high-frequency spectral levels of Willmarth and Yang (1970) in the outer scaling in Figure 4-9 are consistent with the larger Re_θ used for their measurements and the fact that high-frequency energy increases with Reynolds number in this scaling. It is also consistent with the 30-percent smaller pressure transducer diameter (in terms of the outer resolution parameter, d/δ^*) used for their measurements. Because scaling the wall pressure spectra on inner variables collapses the spectra at high frequencies independent of Reynolds

---

[6] Willmarth et al. (1976) also measured the wall pressure spectrum in a cylindrical boundary layer ($\delta/a \sim 4$), except they did not provide sufficient parameters to allow a conversion of their spectra into the form used in the present investigation. Hence, their results are not included in this analysis.

number, an inner scaling is the appropriate way to compare the high-frequency spectra of Willmarth and Yang (1970) and Bull (1967).

The results of Willmarth and Yang (1970) and Bull (1967) scaled on inner variables are included in Figure 4-11. In this scaling, the difference in transducer diameters in terms of the inner spatial resolution parameter d^* is only about 4 percent (9 percent in terms of d^+). Clearly, in this scaling, the difference in spectral energies at high frequencies is greatly diminished. If the data of Bull would have extended to higher frequencies, it seems likely that a collapse of the spectra would have occurred—consistent with the present findings. This indicates that the increase in high-frequency spectral energy with transverse curvature observed earlier was entirely a result of the choice of scaling variables and differences in Reynolds number and transducer resolution and not a result of transverse curvature.

Hence, the effect of transverse curvature is to decrease the low-frequency energy content of the fluctuating wall pressure while leaving the high-frequency content unaffected. This is supported by the reduced rms wall pressure for the boundary layer with transverse curvature. These conclusions are consistent with the idea that transverse curvature should not affect the smallest turbulent scales in the flow that are too near the wall and of too small a scale to be influenced by the transverse shearing action or other factors that result from the curvature of the boundary. Based on the present measurements alone, the conclusion of smaller eddy size in the cylindrical boundary layer made by Willmarth cannot be supported.

4.2.3 Streamwise Turbulent Velocity Spectra

The dimensional power spectra for the streamwise turbulent velocities at the nine wall-normal locations in the cylindrical boundary layer are shown in Figure 4-12. The general

character of the spectra is similar to what is observed in a planar boundary layer (Helal, Casarella, and Farabee 1989). The spectral results for $y/\delta > 1$ are indicative of the band-limited energy content of the turbulent potential-flow interface and the free stream past the edge of the boundary layer. Below approximately 40 Hz, these three spectra measured at $y/\delta > 1$ are contaminated by low-frequency acoustic and large-eddy disturbances in the test section. Because the low-frequency energy content of the spectra measured within the boundary layer ($y/\delta < 1$) are generally at least an order of magnitude larger, they are not affected by these free stream disturbances. The bandpass filter limits are included in Figure 4-12 for later reference (Chapters 5 and 6).

The spectra measured at the first six positions from the wall ($y/\delta < 1$) are presented in Figures 4-13 and 4-14 in a nondimensionalized and normalized wavenumber (k) scaling:

$$\frac{\Phi_u(k)}{u_{rms}^2} \quad \text{vs.} \quad k \ ,$$

where $k = \omega/\overline{U} = 2\pi f/\overline{U}$, $\Phi_u(k) = \overline{U}\Phi_u(\omega) = (\overline{U}/2\pi)\Phi_u(f)$, and $\overline{U} = \overline{U}(y)$ is the local mean velocity at the measurement location. Because this wavenumber representation scales the spectral amplitude and normalizes the frequency axis by the local mean velocity, it imposes a self-similarity on the velocity spectra at different wall-normal positions in the boundary layer. Near the wall and at intermediate wavenumbers (or frequencies), a k^{-1} wavenumber dependence known as the viscous-convective region has been predicted and found to exist in a planar boundary layer due to the interaction of the mean and turbulent flows (Hinze 1975). In the outer regions and at relatively high wavenumber values, a $k^{-5/3}$ wavenumber dependence corresponding to the inertial subrange is predicted for and observed in a planar boundary layer due to the turbulent energy transfer being dominated by the inertial transfer of energy from larger to smaller eddies (Hinze 1975).

The spectra measured in the inner part of the boundary layer ($y^+ \leq 169$) are shown in Figure 4-13. These spectra contain a discernible wavenumber range of k^{-1} dependence characteristic of the viscous-convective region as is also found in a planar boundary layer. The low-wavenumber turbulent energy, which results from larger eddies, decreases as the wall is approached, as is expected and as occurs in a planar boundary layer. At high wavenumbers, the spectral energy in a planar boundary layer uniformly increases as the wall is approached. This is not observed in the present measurements where, instead, a maximum high-wavenumber energy content is observed in the measurement at $y^+ = 85$. A similar effect can be seen in the cylindrical boundary layer spectral measurements of Lueptow and Haritonidis (1987). In their case, the maximum high-wavenumber energy content occurred at $y^+ = 78$. Other than the fact that these wall-normal locations are consistent with the locations at which the turbulence intensities (u_{rms}/U_∞) in the cylindrical boundary layer exceed the planar boundary layer values in Figure 4-7, this trend is difficult to interpret.

The spectra measured in the outer portions of the boundary layer ($y^+ = 339$ and 677) are plotted along with the measurement at $y^+ = 169$ in Figure 4-14. The $k^{-5/3}$ law corresponding to the inertial subrange is followed rather closely for these outer region measurements as is also found for a planar boundary layer. The high-wavenumber spectral energy resulting from the smaller eddies in the flow drops off with increased distance from the wall as expected. The low-wavenumber energy content does not increase significantly with increasing distance from the wall over the level obtained at $y^+ = 169$—similar to what is observed in a planar boundary layer. This is because the flow outside of the near-wall region is less affected by the presence of the wall.

To deduce any possible effect of transverse curvature on the velocity spectra, the present measurements for $y/\delta < 1$ are compared to the planar boundary layer

measurements of Klebanoff (1954) ($Re_\theta \approx 7500$, $l^+ = 18.5$) in Figure 4-15. Although it is difficult to make direct spectrum-to-spectrum comparisons due to differences in the y/δ and y^+ values for the two sets of measurements, the overall trend is clear. The low-wavenumber spectral energy content of the present measurements is less than that observed in the planar boundary layer while the high-wavenumber content is higher. The disparity between the present measurements and those of Klebanoff is approximately constant at low wavenumbers for all positions in the boundary layer but decreases at high wavenumbers as the wall is approached. This is consistent with the trends found for the wall pressure spectrum since it is the high-wavenumber portions of the near-wall velocity spectra that are related to the high-frequency portions of the wall pressure spectrum.

CHAPTER 5

CONDITIONAL SAMPLING OF WALL PRESSURE AND STREAMWISE VELOCITY EVENTS

The relationship between the fluctuating wall pressure and the streamwise velocities in the near-wall region is investigated in this chapter by means of conditional sampling. Conditional sampling procedures have emerged from the belief that coherent structures or repeated sequences of events are responsible for the production of turbulence in the near-wall region and the desire to extract their characteristic signature from the stochastic background. They are based on detection schemes that identify a repeated pattern or salient feature believed to be associated with turbulence production in a turbulent signal. Because the bursting phenomenon is believed to be the mechanism largely responsible for the generation of turbulence in the near-wall region, detection schemes have been developed to detect locally high levels of streamwise velocity fluctuations associated with layers of high shear known to be related to the burst-sweep cycle. The most successful is the variable-interval time averaging (VITA) technique (Blackwelder and Kaplan 1976), which has identified a universal streamwise velocity signature associated with the high shear layer (rapid increase or acceleration in streamwise velocity) that is believed to be related to the bursting process. Because large-amplitude wall pressure fluctuations are believed to be associated with turbulence production in the near-wall region (Schewe

1983, Johansson et al. 1987, Haritonidis et al. 1990), the aim of the present analysis is to relate these wall pressure peaks to flow structures associated with the burst-sweep cycle in the near-wall region.

The analysis entails examining the conditionally averaged pressure and velocities to deduce the character of the streamwise velocity at the time of occurrence of the large-amplitude wall pressure peaks and the character of the fluctuating wall pressure at the time of occurrence of the VITA events. Any similarity between the two sets of conditionally averaged results would indicate a bidirectional (one-to-one) relationship between bursting and large-amplitude wall pressure fluctuations. The conditional averaging procedure consists of three steps:

1.) Apply detection criterion to source (or trigger) signal and establish reference times (t_i) for the occurrence of events.

2.) Sample the source and secondary signals over a prespecified window centered about the event detection times to extract the individual events.

3.) Ensemble average the individual conditionally sampled events for the two signals according to the relation

$$\langle x(\tau)\rangle_g = \frac{1}{N_{events}} \sum_{i=1}^{N_{events}} x(t_i + \tau) \quad , \tag{5.1}$$

where x(t) represents either the wall pressure or streamwise velocity signals, N_{events} is the number of events, t_i is the detection time of event *i*, and τ is the time relative to the detection time in the sampling window of duration T ($-T/2 \le \tau \le T/2$). The subscript *g* denotes the trigger signal (pressure or velocity) used for detection. Because throughout this chapter both the conditionally averaged pressure and velocity signatures are presented simultaneously in the figures, the trigger signal is denoted by a bold symbol rather than a subscript *g* (i.e., <p><u> indicates p(t) is the trigger, <u><p> indicates u(t) is the

trigger). The conditionally averaged curve for the trigger signal is also bold in the figures.

The pressure peak and VITA detection schemes will be described in Section 5.1. The frequency of occurrence and duration of the detected events are examined in Section 5.2. These characteristics are used to establish the appropriate detection parameters for the conditional averaging analysis. Finally, the conditionally averaged wall pressure and velocities are examined in Section 5.3 to deduce the origin of the large-amplitude wall pressure fluctuations. For this analysis, the simultaneously acquired 81920-point pressure and velocity records are used. Because conditional sampling is performed on high-frequency wall pressure activities as a consequence of the window of the detection schemes, the low-frequency cutoff for the bandpass filter (see Section 2.3.3) had a negligible effect on the conditionally averaged results. The analysis of the data was performed with the programs PKDET and VITA in Table 2-2.

5.1 Detection Criteria

5.1.1 Pressure Peak Detection

A peak detection method (Her 1986, Johansson et al. 1987) was utilized to identify large-amplitude wall pressure events. When the wall pressure signal amplitudes relative to the rms level exceed some pre-established threshold level κ, an event was said to exist. A positive pressure event was declared to be present when the amplitude exceeded κp_{rms} and a negative pressure event was declared to be present when the amplitude fell below $-\kappa p_{rms}$.

Her (1986) and Johansson et al. (1987) defined the detection time of the event as the midpoint of the portion of the event that exceeds the threshold. If the large-amplitude pressure events are not symmetric about the peaks, this procedure will generate detection

times that do not align with the time of maximum wall pressure activity. Karangelen et al. (1991) resolved this potential problem by setting the reference time at the maximum peak magnitude between two threshold crossings (i.e., maximum amplitude for positive events and minimum amplitude for negative events). This procedure has the problem, however, of registering subtle oscillations in the wall pressure signals about the threshold level as multiple events. Because these oscillations were observed in the pressure signals in the present measurements, the detection time for the present investigation was set at the maximum peak magnitude between the initial threshold crossing and subsequent zero-crossing (i.e., once signal crosses threshold, the event is not declared over until the signal crosses zero). Although this procedure will count positive (or negative) peaks that occur successively without crossing zero as one event, these types of fluctuations occurred far less frequently in the pressure signals. This is because large-amplitude wall pressure fluctuations are generally characterized by two or more extremes of alternating signs (Schewe 1983). Although the total number of events detected with the present scheme was slightly less (2-3 percent) than that detected using the detection scheme used by Karangelen et al. (1991), the relative number of positive to negative events was independent of the scheme used.

5.1.2 VITA Detection

Variable-interval time averaging (Blackwelder and Kaplan 1976), or VITA, can be used to detect layers of high shear (rapid changes in streamwise velocity) associated with the bursting process in the near-wall region of the boundary layer. The technique searches for portions of the velocity signal that contain a sharply changing velocity associated with turbulence activity related to a burst by examining the magnitude of the short-time variance of the signal. The short-time variance of the streamwise velocity is

defined by

$$\mathrm{var}(t,T) = \frac{1}{T}\int_{t-T/2}^{t+T/2} u^2(s)\,ds - \left(\frac{1}{T}\int_{t-T/2}^{t+T/2} u(s)\,ds\right)^2 , \tag{5.2}$$

where the first and second terms are short ('variable-interval') time averages of $u^2(t)$ and $u(t)$, respectively, and T is the averaging time.

A high-shear layer event is declared to exist when this local short-time variance of the streamwise velocity signal relative to the total long-time variance (obtained from equation (5.2) as T becomes large) exceeds a pre-established threshold level κ. For the zero-mean velocity signal the long-time variance is equivalent to the mean square value of the total record of the signal, u_{rms}^2 ; hence, the detection criterion is expressed as

$$\mathrm{var}(t,T) > \kappa u_{rms}^2 , \tag{5.3}$$

If equation (5.3) is satisfied over a consecutive number of points, the time of occurrence or detection time of the event is set at the short-time variance of maximum amplitude.[1]

Two types of VITA events can be distinguished: accelerating velocity events ($\partial u/\partial t > 0$) associated with the passage of a shear layer associated with the burst-sweep cycle and decelerating velocity events ($\partial u/\partial t < 0$) of unknown origin. Because both events appear to be at least indirectly related to the fluctuating pressure at the wall (Haritonidis et al. 1990), the slope of the velocity signal at the detection time was checked so that the event could be classified as accelerating or decelerating.

---

[1]Some investigators have defined the detection time as the midpoint of the VITA event. Because the short-time variance exceeds the threshold level for only very short durations (typically 1 to 3 points), the two approaches differ by an inconsequential amount in this investigation. The present technique, however, ensures that the detection time is co-located with the time of maximum turbulence activity.

5.2 Frequency of Occurrence and Duration of Detected Events

If the pressure peak and VITA detection schemes are to be used to study the relationship between bursting events and large-amplitude wall pressure events, it is necessary for both detection schemes to trigger on the same flow disturbances. This is accomplished by attempting to match the frequency of occurrence of events and event duration from the two detection schemes. The VITA-detected events depend on both the threshold level κ and the averaging time T. Because a threshold of $\kappa = 1.0$ has been found to produce the smallest overall variation in the frequency of occurrence of VITA events with variations in averaging time, this threshold value will be used for all VITA results presented herein. The VITA technique requires that the averaging time correspond closely with the time scale of the flow structure under investigation. For events related to the burst-sweep cycle, the most probable event duration corresponds to the averaging time at which the highest frequency of occurrence of accelerating VITA events is found in the buffer layer (Johansson and Alfredsson 1982).

The frequency of occurrence of both accelerating and decelerating VITA events for the present measurements at $y^+ = 14$, detected with a threshold of $\kappa = 1.0$, is shown in Figure 5-1. The frequency of occurrence is computed as the inverse of the average time between events, where the time between two events is defined as the elapsed time between the two consecutive detection times.[2] The longer independently acquired 524,288-point records from Chapter 4 are used for the computed frequencies to provide more statistically reliable results by increasing the number of realizations. The maximum frequency of occurrence for the accelerating events occurs at an averaging time in wall units of

[2]Although the frequency of occurrence can also be defined as the number of detected events per unit time (i.e., T_{total}/N_{events}), the present method does not count the ends of the signal where no events occur and thus provides a more accurate estimate of the true frequency of occurrence. The difference between the two methods was less than 5 percent.

$T^+ = T\nu/u_\tau^2 = 18.4$. This event duration and associated event frequency are similar to those measured by Lueptow and Haritonidis (1987) in a cylindrical boundary layer at a similar Reynolds number, as noted in Figure 5-1. They are also consistent with those measured in a planar boundary layer (Blackwelder and Haritonidis 1983). The maximum frequency for the decelerating events occurs at a larger averaging time than for the accelerating events, as is also found in a planar boundary layer. This is consistent with the cylindrical boundary layer results of Lueptow and Haritonidis (1987), except the maximum frequency in their case was approximately 40 percent lower. This discrepancy cannot be related to probe resolution because their hot wire was shorter, and the frequency of VITA events increases as hot wire length decreases (Johansson and Alfredsson 1983). It also cannot be related to errors in the measurement of u_τ because $f^+ = fu_\tau^2/\nu$, and, if anything, their value for u_τ was too low as evidenced by larger values of u_{rms}/u_τ in Section 4.1.3.

The frequency of occurrence for the positive and negative large-amplitude wall pressure events is presented in Figure 5-2(a) as a function of threshold level κ. The long 524,288 data were also used for these computed values. Results are only presented for values of κ for which greater than 50 events were detected. The frequency of occurrence of both positive and negative events decreases logarithmically with increased threshold. This is consistent with the logarithmic relationship found for the frequency of wall pressure peaks in a planar boundary layer (Johansson et al. 1987, Karangelen et al. 1991). A similar decrease is also found for the frequency of VITA events in a planar boundary layer (Johansson and Alfredsson 1982). The planar boundary layer measurements of Karangelen et al. (1991) are included in the figure for comparison. Indicated in the figure is the burst frequency associated with the maximum frequency of occurrence of accelerating VITA events in Figure 5-1. The frequency of occurrence of the

positive large-amplitude wall pressure events is equivalent to the VITA frequency at a threshold level of approximately 2.3. This suggests that large-amplitude wall pressure fluctuations at and above this threshold could be associated with the near-wall bursting process.

The average event duration for both the positive and negative wall pressure events as a function of threshold is shown in Figure 5-2(b). The average event duration for the large-amplitude wall pressure peaks was computed as the average time interval between the pre- and post-threshold zerocrossings for all of the events. A maximum occurs in the event duration distribution in Figure 5-2(b) at or very near the threshold value of $\kappa = 2.3$ at which the frequencies of the pressure peak and VITA events are the same. This maximum pressure peak event duration of 15.7 t_v is comparable to the VITA event duration (optimum averaging time) of 18.4. The variation in event duration with threshold in Figure 5-2(b) of approximately 10-16 t_v is very similar to the range of values given by Johansson et al. (1987) and Karangelen et al. (1991) for large-amplitude wall pressure events in a planar boundary layer. The duration of negative wall pressure events in the present measurements is smaller than the positive wall pressure events at all threshold levels. This result has not been previously reported in the literature. A possible explanation for this phenomenon is revealed in Section 5.3.1.

From the results in Figures 5-1 and 5-2 it can be concluded that for a meaningful comparison to be made between the large-amplitude pressure fluctuations at the wall detected with the peak detection method and bursting events in the near-wall region detected with VITA, a threshold of approximately 2.3 should be used for the pressure peak criterion. In this way, the two detection schemes yield similar event frequencies and event durations. Conditionally averaged pressure and velocity signatures typical of those measured in the near-wall region in this investigation are shown in Figure 5-3 for peak

detection thresholds of 2 and 3. Clearly, a variation in κ about this optimum threshold level does not have much of an effect on the relationship between <p> and <u>. Consequently, to facilitate comparison of the results to the planar boundary layer measurements of Johansson et al. (1987) and Haritonidis et al. (1990), a threshold level of 2.5 is utilized for the conditionally averaged results in the next section.

The logarithmic decrease of event frequencies measured in the present investigation with increasing threshold level is consistent with the planar boundary layer measurements of Karangelen et al. (1991), as shown in Figure 5-2(a). Figure 5-4 compares the ratios of positive-to-negative event frequencies from Figure 5-2(a) for the cylindrical and planar boundary layer measurements. Both sets of measurements have ratios less than one since for either set of measurements the frequency of occurrence for large-amplitude negative events exceeds that for large-amplitude positive events—consistent with the negative skewness measured for the wall pressure in either boundary layer (see Section 4.1.2). However, the ratios for the present measurements are larger than those of Karangelen et al. (1991) for all threshold levels greater than $\kappa = 2$. If this trend is solely due to the transverse wall curvature in the present measurements, these results indicate that positive events occur more frequently with respect to negative events in a cylindrical boundary layer than they do in the planar boundary layer—consistent with the wall pressure skewness findings in Chapter 4.

5.3 Conditionally Averaged Pressure-Velocity Results

The conditionally averaged pressure and velocity signatures obtained with the hot-wire probe immediately above the pressure transducer ($x^+ = 0$, $y^+ = 14$, $\emptyset = 0°$) are presented

in Figure 5-5.[3] The p and u signatures obtained using pressure peak detection ($\kappa = 2.5$) are shown in Figures 5-5(a) and 5-5(b), while those obtained using VITA ($\kappa = 1.0$, $T^+ = 18.4$) are shown in Figures 5-5(c) and 5-5(d). The conditional averages are normalized according to the usual conventions—$\langle p\rangle/\kappa p_{rms}$ and $\langle u\rangle/u_{rms}$ for the pressure peak results and $\langle u\rangle\kappa^{1/2}u_{rms}$ and $\langle p\rangle/p_{rms}$ for the VITA results.

The conditionally averaged pressure and velocity signatures obtained from the two detection schemes are qualitatively similar. Positive large-amplitude wall pressure events in Figure 5-5(a) are associated with local increases or accelerations in streamwise velocity, while negative large-amplitude pressure peaks (Figure 5-5(b)) are associated with local decreases in streamwise velocity. Correspondingly, streamwise velocity accelerations detected with VITA (Figure 5-5(c)) are associated with positive peaks in the wall pressure, while decelerations (Figure 5-5(d)) are associated with negative pressure peaks. This bidirectional relationship between pressure peak and VITA events illustrates that a coupling exists between both positive and negative large-amplitude wall pressure peaks and streamwise velocity fluctuations in the near-wall region. The relationship between decelerations and negative pressure peaks is not as strong as for the positive pressure peaks and accelerations as can be seen by the lower overall similarity in the magnitudes of the conditionally averaged signatures between the two detection schemes (i.e., smaller velocity magnitudes are associated with the negative peak detection results than with the positive peak results, and smaller pressure amplitudes are associated with the decelerating VITA results than with the accelerating VITA results). These results are consistent with

---

[3]The conditionally averaged wall pressure peaks in Figures 5-5(a) and 5-5(b) with the hot-wire probe located at $x^+ = 0$, $y^+ = 14$, and $\emptyset = 0°$ are slightly affected by the presence of the probe (see Section 3.1.3). The primary effect is a larger number of positive events than would be otherwise present due to the flow field around the hot wire impinging upon the wall/pressure-transducer (the skewness for the wall pressure was also slightly positive at this hot wire location). This results in a slightly distorted shape of the conditionally averaged pressure pattern due to the presence of these extraneous nonturbulence related 'events'. The effect, however, is small (see Figure 5-8).

those reported for measurements in a pipe flow at $y^+ = 16$ (Dinkelacker 1990). Very similar relationships can also be detected in the planar boundary layer measurements of Haritonidis et al. (1990) at $y^+ = 15$.

This bidirectional relationship is also demonstrated in Figure 5-6(a), where the amplitude for each detected pressure event is plotted against the slope of the streamwise velocity signal ($\partial u/\partial t$) at the time of detection, and in Figure 5-6(b), where the slope ($\partial u/\partial t$) for each detected VITA event amplitude is plotted against the pressure amplitude at the time of detection. The gap in the data points in Figure 5-6(a) is a result of the pressure threshold used for the pressure peak detection scheme. The vast majority of the events fall in either the first or third quadrants (i.e., positive pressure peaks with accelerating velocities and negative pressure peaks with decelerating velocities)—consistent with the conditionally averaged results.

From simultaneous measurement of wall pressure and both the streamwise and wall-normal component of velocity at $y^+ = 15$ in a planar boundary layer, Haritonidis et al. (1990) found that positive pressures were associated with sweeps ($u > 0$, $v < 0$), while negative wall pressures were primarily distinguished by negative streamwise velocities ($u < 0$) with no preferential sign for v. This conclusion is not supported by the present measurements, as shown in Figure 5-7(a), where the amplitude of each detected pressure peak is plotted against the streamwise velocity at the time of detection. Although the present measurements do show a slight tendency for positive pressures to be associated with positive values of u, the trend is nowhere near as strong as that indicated by Haritonidis et al. Furthermore, negative pressures show no greater tendency to be associated with positive or negative values of u. When the streamwise velocity and pressure at the time of detected VITA events are plotted in a similar fashion, as shown in Figure 5-7(b), neither positive nor negative pressures show any tendency to be associated

with a particular sign of u. Although the cause for the difference between the present measurements and those of Haritonidis et al. (1990) is difficult to interpret, the results of Haritonidis et al. (1990) contradict some of their earlier results (Johansson, Her, and Haritonidis 1987) in which it was reported that negative wall pressure events were associated with predominantly positive values for u (i.e., sweeps).

From the results presented in Figures 5-5, 5-6, and 5-7, the correct interpretation of the large-amplitude wall pressure peaks appears to be that their sign is directly related to the sign of the temporal derivative of u(t) and not the sign of u(t) itself. Positive pressure peaks are associated with local accelerations of fluid ($\partial u/\partial t > 0$) and are thus associated with shear-layer structures as initially deduced by Johansson et al. (1987). Negative wall pressure peaks, on the other hand, are associated with local decelerations of fluid ($\partial u/\partial t < 0$). Because the sign of p is only related to the slope of u, there is no explicit link to the sign of u(t) since the magnitude of the streamwise velocity at the time of the acceleration or deceleration can be of either sign, depending upon the form of large-scale influences at the time. This explains the contradiction between the results of Haritonidis et al. (1990), Johansson et al. (1987), and the present measurements with regard to the sign of u. The conclusion by Haritonidis et al. (1990) that the pressure and buffer layer flow structures are coupled through the normal velocity component is not necessarily contradictory since the u and v velocity components are likely coupled themselves.

This bidirectional relationship for both positive and negative pressure peaks indicates that both types of large-amplitude wall pressure fluctuations are directly linked to flow structures in the near-wall region. Considering that both positive and negative events occur with similar frequency, it would appear that both types of 'events' (i.e., positive-p/accelerating-u, negative-p/decelerating-u) are equally important to the physics of the near-wall flow. If Taylor's hypothesis, $\partial/\partial t = -U_c\partial/\partial x$, is assumed for the small-scale,

near-wall structure generating the pressure fluctuations, the interpretation is that the sign of p is directly related to the sign of the spatial derivative of u(x). Although it is clear that local accelerations ($\partial u/\partial t > 0$, $\partial u/\partial x < 0$) result from near-wall shear layers, which have low-speed fluid in front and high-speed fluid behind, the question that remains is what sort of near-wall flow structure generates a local deceleration in streamwise velocity ($\partial u/\partial t < 0$, $\partial u/\partial x > 0$) such that the streamwise velocity is high in front and then goes low with the passage of the structure. A possibie answer to this question is revealed in Section 6.2.2 with respect to the pressure-velocity cross-spectral and cross-correlation results.

5.3.1 Wall-Normal Dependence of Conditionally Averaged Signals

The conditionally averaged wall pressure and velocity signatures obtained immediately above the pressure transducer ($x^+ = 0$, $\varnothing = 0°$), but at various distances above the wall, are examined in Figures 5-8 and 5-9. In Figure 5-8, the velocity signatures at each wall-normal location are obtained by conditional sampling the velocity signals at the detection times established by the pressure peak detection method for the associated pressure signal. The pressure signatures are nearly identical in each plot, except for small variations from one data set to another. Although the form of the pressure signature at the closest position to the wall ($y^+ = 14$) is affected somewhat by the presence of the hot-wire probe, the effect is small (see footnote 3). In Figure 5-9, the pressure signals are conditionally sampled at the detection times set by the VITA technique at the various distances from the wall. Here, the separate velocity signatures are different since they are associated with different regions of the flow.

For either detection scheme, the relationship between the conditionally averaged pressure and velocities weakens considerably with increased y. The bidirectional

relationship between positive large-amplitude wall pressure peaks and shear layer structures observed at $y^+ = 14$ is nearly as strong at $y^+ = 28$, as evidenced by the qualitative similarity still present between the conditional averages obtained with the two detection techniques shown in Figures 5-8 and 5-9. The relationship between negative pressures and decelerating velocities, although still present, has diminished from what it was at $y^+ = 14$. By $y^+ = 85$, the association between both positive-pressures/accelerations and negative-pressures/decelerations has diminished. By $y+ = 169$, nearly all the observed associations are gone. A similar trend has been found for the positive large-amplitude wall pressure peaks at a very similar value of y^+ in a planar boundary layer (Johansson et al. 1987). Johansson et al. did not examine decelerating VITA-on-u events.

The diminished bidirectional relationship observed at $y+ = 169$ in the present measurements is further illustrated in Figure 5-10, where the pressure amplitudes and velocity derivatives at the detection times for each event are plotted against one another for both detection schemes. This figure should be compared to Figure 5-6, which was constructed in the same fashion but at $y^+ = 14$. The events in either Figure 5-10(a) (pressure peak detection) or 5-10(b) (VITA-on-u detection) are distributed in all four quadrants equally, indicating that no preferred associations exist between the sign of p and $\partial u/\partial t$ and that the bidirectional relationship between $\langle p \rangle$ and $\langle u \rangle$ disappears.

The results in Figures 5-8, 5-9, and 5-10 indicate that large-amplitude wall pressure fluctuations are primarily associated with flow structures in and beneath the buffer layer ($y^+ \leq 28$), although there is some relation to flow structures throughout the near-wall region ($y^+ \leq 85$). In addition, flow structures generating the negative pressures appear to be concentrated somewhat closer to the wall than those that generate the positive pressures, as indicated by the more rapid decay of the conditional averages with distance

from the wall. From the observed trend with increasing y^+ in Figures 5-8 and 5-9, it appears that a strong negative pressure peak may be associated with a strong decelerating velocity in the figures if measurements were made closer to the wall than $y^+ = 14$. If the sources for the negative pressure peaks are located closer to the wall, the smaller associated length scales might explain the shorter average event duration observed for the negative pressure peaks than for the positive pressure peaks (see Section 5.2 and Figure 5-2(b)).

5.3.2 Streamwise Dependence of Conditionally Averaged Signals

The convective behavior of the flow structures responsible for the large-amplitude wall pressure fluctuations is examined in Figures 5-11 and 5-12 through comparisons of conditionally averaged velocity and wall pressure signatures at various streamwise separation distances between the hot wire and pressure transducer ($\emptyset = 0°$). The relationships at both $y^+ = 14$ and 28 are examined since these are the locations at which the greatest relationship was observed between the large-amplitude wall pressure fluctuations and near-wall velocity events. The positive and negative pressure peak results are presented in Figure 5-11. Because the trigger signal (pressure) is located upstream of the secondary signal (velocity), these results examine the convective behavior of shear layer structures in the downstream direction that produced a pressure peak at $x^+ = 0$. Since the conditionally averaged pressure is the same at each position of the probe, only the pressure signature at $x^+ = 0$ is included. The accelerating and decelerating VITA-on-u results are presented in Figure 5-12. Because in this case the trigger signal (velocity) is located downstream of the secondary signal (wall pressure), these results examine the character of the wall pressure (at $x^+ = 0$) associated with a shear layer structure located at successively further downstream locations. Each of the two pressure

patterns shown at each x^+ is obtained by triggering at the two different wall-normal positions of the velocity probe. Because the conditionally averaged velocity patterns at any given y are the same at each streamwise position of the probe, only the velocity signatures at $x^+ = 0$ are included.

With increasing streamwise separation of the pressure transducer and hot-wire probe, the velocity signatures at both $y^+ = 14$ and 28 associated with the large-amplitude wall pressure fluctuations in Figure 5-11 show the expected convection as indicated by the successively larger time shift for the centroid of the velocity pattern. The differences in time shifts between the velocity patterns at $y^+ = 14$ and 28 are primarily due to differences in convection velocities at the two probe positions. The pressure patterns associated with the accelerating and decelerating VITA events in Figure 5-12 also show the expected convection effects but because the pressure transducer is located upstream of the hot wire (negative x^+ with respect to trigger signal), the pressure signatures shift to negative time delays with increasing spanwise separation. The differences in convection velocity for the pressure patterns associated with the probe at $y^+ = 14$ and 28 are also apparent.

No appreciable change in the magnitude or duration (width) of either the shear layer patterns (Figure 5-11) or the pressure patterns (Figure 5-12) occurs until a streamwise separation distance of $x^+ = 339$. This indicates that the pressure-producing structures in the near-wall flow remain fairly coherent and experience little convective decay over this streamwise extent. By $x^+ = 677$ (not shown) the patterns have decayed considerably and by $x^+ = 1355$ no correlated pattern remains. This indicates that the near-wall structure responsible for the large-amplitude wall pressure fluctuations remains intact for a streamwise extent between $677 < x^+ < 1355$ or $0.76 < x/\delta < 1.52$. This is comparable to the convective behavior of the characteristic pressure pattern in a planar boundary layer measured by Schewe (1983) using streamwise-separated pressure transducers and to the

convective behavior of the near-wall quasi-streamwise vortex structure believed to be associated with the burst-sweep cycle in a planar boundary layer (Kline and Robinson 1990, Robinson 1990). Willmarth and Yang (1970) found that the decay of pressure-producing structures was more rapid in the boundary layer with transverse curvature due to the presence of smaller eddies. However, this result pertained primarily to the larger scales in the flow since their pressure transducer was too large ($d^+ = 158$) to detect the characteristic large-amplitude fluctuations associated with small scales near the wall (see Section 3.2.1).

From the streamwise separation distance and the time shift of the pressure or velocity patterns in Figures 5-11 and 5-12, an average convection velocity for the pressure-producing structure at the two wall-normal locations can be computed. The convection velocities for the positive-pressures/accelerating-velocity events at $y^+ = 14$ and 28 are $10.7u_\tau$ and $12.1u_\tau$, respectively. The convection velocities for the negative-pressures/decelerating-velocity events at $y^+ = 14$ and 28 are $9.6u_\tau$ and $10.6u_\tau$, respectively. These values are comparable to the convection velocity of $11.9u_\tau$ computed by Schewe (1983) for the characteristic pressure-producing structure in a planar boundary layer; however, he did not specify the sign of the wall pressure associated with the computed value. The lower convection velocity for the negative wall pressure peaks and decelerating velocity patterns has not been previously reported. The trend is consistent, however, with the results in Section 5.3.1, which appeared to indicate that the sources for the negative pressure peaks are concentrated closer to the wall.

5.3.3 Circumferential Dependence of Conditionally Averaged Signals

The circumferential extent of the near-wall shear layer structure responsible for the large-amplitude wall pressure fluctuations is examined in Figures 5-13 and 5-14, which

compare conditionally averaged pressure and velocity signatures at various spanwise or circumferential separated positions ($x^+ = 0$). The relationships at both $y^+ = 14$ and 28 are examined. The positive and negative pressure peak results are presented in Figure 5-13, while the accelerating and decelerating VITA-on-u events are presented in Figure 5-14. The conditionally averaged pressure and velocity signatures at the circumferentially separated positions bear no resemblance to the form of the conditional averages immediately above the pressure transducer ($\varnothing = 0°$) in either Figure 5-13 or 5-14. Even so, a consistent variation in $<p>$ and $<u>$ between the two detection schemes from those at $\varnothing = 0°$ can be detected. At $\varnothing = 20°$, the conditionally averaged velocity and pressure signatures are inverted forms from what they were at $\varnothing = 0°$. The effect is generally more apparent at $y+ = 14$. By $\varnothing = 40°$, no appreciable relationship exists between the pressure and velocity for either detection scheme.

Considering the fact that the spanwise (arclength) separation distances at $\varnothing = 20°$ of $s^+ = 67$ and 71 at $y^+ = 14$ and 28, respectively, are very near the average spanwise separation distance of $z^+ = 50$ for the low- and high-speed streaks, the observed inversion in the relationship between $<p>$ and $<u>$ is consistent with character of the flow in the near-wall region. The inverted relationship is not as strong at $y^+ = 28$ because the larger spanwise separation is not as near the characteristic spanwise scale for the streaky structure. By $\varnothing = 40°$ the spanwise separations of $s+ = 133$ and 143 at $y+ = 14$ and 28, respectively, are larger than the spanwise scale over which the near-wall structure remains correlated. Dinkelacker (1990) performed similar measurements in a pipe flow and found that the inversion of the pressure and velocity signatures occurred very systematically with small increments in the spanwise direction ($\Delta z^+ = 19$)—as would be expected from the character of the near-wall flow.

CHAPTER 6

SPECTRAL AND CORRELATION RELATIONS BETWEEN THE PRESSURE AND VELOCITY FLUCTUATIONS

The flow processes throughout the cylindrical boundary layer that give rise to the fluctuating pressure at the wall are investigated in this chapter. This is done by means of pressure-velocity cross-spectral densities and cross correlations. Because cross spectra and cross correlations are Fourier transform pairs (see Section 6.2.1), both sets of measurements provide related information on the relationship between the wall pressure and the turbulent velocities in the flow. Even so, each set of results has particular advantages. The cross-spectral density provides the desired results as a function of frequency and is useful for examining contributions to the wall pressure from specific turbulent structures in the flow. The cross correlation on the other hand represents an averaging over all frequencies present in the signals and thus characterizes the dominant temporal relationship between the wall pressure and the turbulent velocity at any given point in the flow field.

The contributions to the fluctuating wall pressure from turbulent sources located across the boundary layer are investigated by examination of the pressure-velocity cross spectra and cross correlations from the near-wall region ($y^+ = 14$) to the outer edge of the turbulent/nonturbulent interface ($y/\delta = 1.91$). Information about the evolution and decay

of these pressure-producing structures across the boundary layer as they convect downstream is provided from cross spectra and correlation measurements made with the hot-wire probe located at various distances downstream of the wall pressure transducer ($x/\delta \leq 1.52$). Finally, by examination of the pressure-velocity relationships resulting from the hot-wire probe located at various circumferential positions, the spanwise character and scale of the pressure-producing flow structures are identified.

The pressure-velocity cross-specral density and cross-correlation coefficient results are presented in Sections 6.1 and 6.2, respectively. Both sets of results used the 81920-point simultaneous pressure-velocity data records. The data analysis parameters used in the computer codes PUSPEC and PUCORR that were used for these analyses are summarized in Table 2-2.

6.1 Pressure-Velocity Cross Spectra

6.1.1 Definition of the Cross Spectrum

The cross-spectral density provides a measure of the degree to which two temporal records are related as a function of frequency. The method used to compute the cross spectrum for the present investigation is based on the finite Fourier transform. The one-sided cross-spectral density function between the temporal records of two stationary random processes p(t) and u(t) is given by

$$\Phi_{pu}(f) = 2 \lim_{T \to \infty} T\, E\left[P^*(f)U(f)\right] \, , \qquad (6.1)$$

where P(f) and U(f) are the finite Fourier transforms of p(t) and u(t), respectively, defined

by equation (2.12). The cross-spectral density is estimated by ensemble averaging over a finite number of subrecords according to the relation

$$\widehat{\Phi}_{pu}(f) = \frac{2T}{n_d} \sum_{i=1}^{n_d} P^*(f)U(f) \ , \tag{6.2}$$

where n_d is the number of subrecords and T is the length of each subrecord. Equation (6.2) is evaluated computationally by the expression

$$\widehat{\Phi}_{pu}(f_k) = \frac{2T}{n_d} \sum_{i=1}^{n_d} P_i^*(f_k)U_i(f_k) \ , \quad k=0,1,\ldots, N/2 \ , \tag{6.3}$$

where

$$P_i(f_k) = \frac{1}{N} \sum_{n=0}^{N-1} p_{i_n} e^{\frac{-j2\pi kn}{N}} \quad k=0,1,\ldots, N-1 \ , \tag{6.4a}$$

$$U_i(f_k) = \frac{1}{N} \sum_{n=0}^{N-1} u_{i_n} e^{\frac{-j2\pi kn}{N}} \quad k=0,1,\ldots, N-1 \ , \tag{6.4b}$$

and N represents the number of data points in each subrecord.

Equation (6.3) was computed by fast Fourier transform (FFT) methods. Because cross spectra are complex quantities, it is convenient to present them in terms of magnitude and an associated phase angle:

$$\Phi_{pu}(f) = |\Phi_{pu}(f)| e^{j\varnothing_{pu}(f)} \ , \tag{6.5}$$

where

$$|\Phi_{pu}(f)| = \sqrt{Re^2\{\Phi_{pu}(f)\} + Im^2\{\Phi_{pu}(f)\}} \ , \tag{6.6a}$$

$$\varnothing_{pu}(f) = \tan^{-1}\left[\frac{Im\{\Phi_{pu}(f)\}}{Re\{\Phi_{pu}(f)\}}\right] \ , \tag{6.6b}$$

and $\text{Ø}_{pu}(f) < 0$ implies that p(t) leads u(t) at the frequency f. Because $\tan^{-1}$ in equation (6.6b) is bounded by ±90° (i.e., the first and third quadrants of the real and imaginary plane), a phase unwrapping algorithm was employed that corrected the phase if the real component of $\Phi_{pu}(f)$ was negative by adding or subtracting 180°, depending upon whether the imaginary component was positive or negative, respectively. In this way, the phase was bounded by $-180° \leq \text{Ø}_{pu}(f) \leq 180°$. Because the magnitude of the cross spectrum is bounded by the relation (Bendat and Piersol 1980)

$$|\Phi_{pu}(f)|^2 \leq \Phi_p(f)\Phi_u(f) \ , \tag{6.7}$$

where $\Phi_p(f)$ and $\Phi_u(f)$ are the single-sided autospectral densities for p(t) and u(t), respectively, given by equation (4.13), it is common to normalize the cross-spectral magnitude in terms of the coherence function as

$$\Gamma_{pu}(f) \equiv \gamma^2_{pu}(f) = \frac{|\Phi_{pu}(f)|^2}{\Phi_p(f)\Phi_u(f)} \ , \tag{6.8}$$

so that $0 \leq \Gamma_{pu}(f) \leq 1$. The value of $\Gamma_{pu}(f)$ indicates how much one record is related to the other at a particular frequency. A value of $\Gamma_{pu}(f) = 1$ implies that the signals p(t) and u(t) are linearly related at the frequency f, while a value of $\Gamma_{pu}(f) = 0$ indicates that the two signals are totally unrelated.

The statistical error for both the magnitude and phase of the cross spectrum are both increasing functions of frequency since both are proportional to the inverse of the coherence (Bendat and Piersol 1986) and because coherence decreases as frequency increases for these results. Consequently, smoothing of the coherence and phase

functions was performed according to

$$\Gamma_{pu}(f_k) = \frac{1}{2m_s+1}\sum_{j=k-m_s}^{k+m_s} \Gamma_{pu}(f_j) \ , \qquad (6.9a)$$

$$\O_{pu}(f_k) = \frac{1}{2m_s+1}\sum_{j=k-m_s}^{k+m_s} \O_{pu}(f_j) \ , \qquad (6.9b)$$

where m_s is an integer that defines the smoothing window. Because of the logarithmic scaling customarily used to present these results and the greater statistical error at large frequencies, a propensity of points containing large statistical scatter occurs at high frequencies. As a result, m_s was increased logarithmically with frequency. Through trial and error, the smoothing function that generated the best curve without distorting the information in the original results was

$$m_s \sim \frac{1}{2}(\log f_k)^{\log(f_k)} \ . \qquad (6.10)$$

The proportional symbol '~' is used in equation (6.10) because m_s was an integer obtained by truncating the fractional part of the expression. A maximum value of $m_s = 51$ was used at frequencies above 4000 Hz since larger values tended to oversmooth.

Shown in Figure 6-1 is a typical set of coherence and phase results in their original form and after smoothing. Clearly, the smoothed curves eliminate all the random statistical fluctuations without distorting the character of the results. This was true for the coherence results at all measurement points in the flow. The phase results, however, were only effectively smoothed in the streamwise vicinity ($x/\delta = 0.016$, $x^+ \leq 14$) and circumferential plane ($\O = 0°$) of the pressure transducer. At all other positions in the

boundary layer, they retained substantial scatter, even after the smoothing operation. The reason for this is related to the fact that time delays between p(t) and u(t) associated with spatial separations are reflected directly in the phase function. Because of the circular nature of the phase and the form of the phase unwrapping algorithm, the phase is folded back if large phase shifts due to spatial separations are present. Because of the changing character of the phase with frequency due to the physics of the flow, other phase unwrapping schemes that utilized a different modulus for the phase did not correct the problem. Consequently, the phase results are only discussed in Section 6.1.2 for the hot-wire probe positions directly above the pressure transducer.

All the pressure-velocity cross-spectral results presented in the following sections were computed from the ensemble average of 80 subrecords of 1024 points each (81920 total points), resulting in a frequency resolution of Δf=19.53 Hz (see Table 2-2). Results are presented for the frequency range of 59 to 5332, Hz as described in Section 2.3.3. The frequency in all the cross-specral results to follow is scaled on outer variables according to $\omega\delta^*/U_\infty$. The low-frequency and high-frequency filter cutoffs are $\omega\delta^*/U_\infty$=0.13 and $\omega\delta^*/U_\infty$=12.5, respectively.

6.1.2 Wall-Normal Dependence of Coherence and Phase

The coherence and phase distributions between the fluctuating wall pressure and streamwise turbulent velocity at various wall-normal locations immediately above the pressure transducer (x = 0, Ø = 0°) are shown in Figure 6-2. Although the results at all nine positions in the boundary layer are not included in the figure for purposes of clarity, they reinforce the trends apparent in the figures in all cases. The maximum overall coherence values in Figure 6-2(a) occur at the closest position to the wall (y^+ = 14) and decrease in magnitude as the hot-wire probe is moved away from the wall and towards the

edge of the boundary layer for $y/\delta \le 0.76$. This is consistent with the r^{-1} dependence for the turbulent source contributions to the fluctuating wall pressure (equation (1.7)). By $y/\delta = 0.76$, nearly all coherence between the pressure and velocity has disappeared. As the hot-wire probe moves past the edge of the boundary layer, the coherence values increase again reaching a maximum value for the measurement made at $y/\delta = 1.52$ shown in the figure. Russell and Farabee (1991) measured the coherence between the wall pressure and streamwise turbulent velocity in the range $0.13 \le y/\delta \le 2.0$ in a planar boundary layer and reported coherence values of similar magnitude distributed over a nearly identical nondimensional band of frequencies. Although their spectra also exhibited a decrease in magnitude with increased y, their coherence values past the edge of the boundary layer ($y/\delta \ge 1.25$) exceeded those near the wall (at low frequencies) and no region of zero coherence was observed near $y/\delta = 0.75$, as in the present measurements. Their coherence at $y/\delta = 1.5$ was also the largest for positions measured outside of the boundary layer.

Near the wall ($y^+ \le 28$), the coherence function in Figure 6-2(a) exhibits a double-humped structure with a peak of maximum magnitude near $0.2 < \omega\delta^*/U_\infty < 0.3$ and a smaller hump near $1 < \omega\delta^*/U_\infty < 3$. The third hump centered about $8 < \omega\delta^*/U_\infty < 10$, which exists for $y^+ \le 85$ ($y^+ = 85$ not shown), may be related to correlated electrical noise.[1] The large-amplitude hump at low frequencies diminishes rapidly with increasing hot wire distance from the wall, disappearing almost entirely by $y^+ = 85$. As the coherence value for the second hump decreases with increased distance from the wall, the frequency at which it occurs also decreases. Since the frequency of a convected eddy

[1]This is not conclusive, however, considering that (1) it exists only in the measurements at $y^+=14$ and 28 at this and other streamwise positions in the boundary layer, (2) the humps exhibit a decrease in amplitude with streamwise separation reminiscent of convective decay, and (3) the frequencies over which this hump exists are considerably lower than obvious noise-related coherence for $\omega\delta^*/U_\infty > 12.5$.

goes as $\omega = kU_c = 2\pi U_c/\lambda_e$, this is consistent with the notion that the average eddy size, λ_e, is proportional to y. A similar trend of decreasing frequency for the maximum coherence level was found by Russell and Farabee (1991) in a planar boundary layer. However, even if small scales exist at the hot-wire probe, they will not appear in the coherence function if their scale is much less than y/δ, since a coherence can only exist between the pressure transducer and hot-wire probe for eddies whose average scale is greater than or comparable to the hot-wire/microphone separation distance ($\lambda_e \geq y$).

The frequency of $\omega\delta^*/U_\infty \approx 0.2$ at which the coherence reappears at the edge of the boundary layer is comparable to the frequency at which the large peaks are observed in the coherence at $y^+ = 14$ and 28. If this low-frequency coherence observed very near the wall is related to the corresponding low-frequency coherence at the edge of the boundary layer, then the large-scale outer flow structures that contribute to the wall pressure extend from the turbulent/potential flow interface all the way down to the wall. That a coherence peak at $\omega\delta^*/U_\infty \approx 0.2$ does not exist at intermediate y/δ locations may be related to the character of the flow associated with the large-scale structure in this intermediate region of the boundary layer. This low-frequency hump is not apparent in the near-wall planar boundary layer measurements of Russell and Farabee (1991). Although they only measured as close to the wall as $y/\delta = 0.13$, their coherence curves show no hint of coherent energy at the low-frequency region. If this difference is related to transverse curvature, it would imply that the large-scale structure has a larger role on the flow near the wall in the cylindrical boundary layer than in the planar boundary layer. However, without more extensive measurements in a planar boundary layer closer to the wall, it is not possible to make any conclusive statements.

The phase between the pressure and velocity, shown in Figure 6-2(b), provides insight into the character of the relationships between the pressure and velocity at

frequencies observed to contain coherent energy in Figure 6-2(a). At all frequencies and for all hot-wire probe positions above the pressure transducer, the phase is negative, $\O_{pu} < 0$, indicating that the pressure leads the velocity. Within the boundary layer ($y/\delta \leq 0.76$), the values range from approximately 0° to -90°. At $y^+ = 14$, the phase associated with the smaller high-frequency hump in the coherence is associated with a minimum in the phase function very near -90°. This -90° phase relationship between p and u is consistent with the form of conditionally averaged large-amplitude wall pressure peak and VITA results at $y^+ = 14$ associated with the bursting process, as shown in Figure 5-5. In all cases, the peak in the wall pressure leads the velocity by approximately 90°. This suggests that this high-frequency region is related to the burst-sweep cycle. The phase associated with the larger low-frequency hump at $y^+ = 14$ is near -30°. The significance of this is addressed in Section 6.2.2.

As y increases and the energy of the "high-frequency hump" shifts to lower frequencies, the minimum in the phase function decreases in magnitude and shifts to a corresponding lower frequency. This causes the magnitude of the phase at the high-frequency region to steadily decrease and the magnitude of the phase at the low-frequency region to steadily increase. By $y/\delta = 0.38$ (not shown), the phase at high frequencies becomes undefined, as evidenced by a random fluctuation between ±180° due to the loss of coherence, while at low frequencies the phase becomes very nearly -90°. At $y/\delta = 0.76$, the phase is indeterminate due to the near-zero coherence at nearly all frequencies. Then with further increases in y into the turbulent/potential-flow interface ($y/\delta = 1.14, 1.52, 1.91$), a considerably more negative phase near -180° emerges at low frequencies. This phase relationship between p and u has been observed in correlation measurements in a planar boundary layer and has been shown to be consistent with a potential flow over a wavy 'wall' or wavy turbulent/potential-flow interface (Panton et al.

1980). However, as y increases in this region, the phase is not constant but decreases gradually from approximately -135° to -175° over the range of measurements. This indicates that the wavy wall model is only consistent with the pressure-velocity relationships at the very edge of the turbulent/potential-flow interface and that some other flow mechanism is responsible for the observed relationships between p and u at positions deeper inside this region.

The double-humped structure (bimodal character) of the coherence function between the pressure and velocity near the wall ($y^+ \leq 28$) in Figure 6-2(a) results from the presence of correlated turbulent energy at two distinct (not necessarily separate) frequency bands. The frequencies at which the coherence is concentrated are notably similar to the frequencies at which a maximum concentration of energy exists in the streamwise velocity and wall pressure spectra. This is shown in Figure 6-3, where the spectral densities are plotted in the form $\omega\Phi(\omega)$ versus ω such that the area under the spectrum in a particular frequency range is equivalent to the turbulent energy in that frequency range. After division by the mean-square level, the area under the curve is unity.[2] This format enables a direct examination of the frequency band at which the greatest contribution to the turbulent energy occurs.

The maximum concentration of energy for the wall pressure in Figure 6-3(a) occurs in the frequency range $1.5 < \omega\delta^*/U_\infty < 3$. This range of frequencies is consistent with the frequency at which the smaller hump occurs in the coherence distributions near the wall in Figure 6-2(a). Because a very large portion of the total rms wall pressure level results from the large-amplitude wall pressure fluctuations related to the bursting process (see

---

2 $$\int_0^\infty \frac{\omega\Phi_x(\omega)}{x_{rms}^2}\, d(\ln \omega) = 1$$

Chapter 4), the frequency of the wall pressure spectral peak in Figure 6-3(a) and corresponding small hump in the coherence function appear to be associated with the burst-sweep cycle. This is corroborated by the similar phase relation found for this hump and the conditionally averaged large-amplitude wall pressure peak and VITA results in Chapter 5. Even further support is provided when the characteristic frequency of the large-amplitude wall pressure peaks associated with the burst-sweep cycle is considered. Since the characteristic frequency of the pressure peaks is related to the inverse of their average duration (see Section 5.2) and the average event duration was found to be $\Delta T^+ = \Delta T u_\tau^2/\nu \sim 16$, the associated frequency is $\omega\nu/u_\tau^2 = 0.39$ or $\omega\delta^*/U_\infty = 3.0$—commensurate with the value of $\omega\delta^*/U_\infty = 2\text{-}3$ of the hump in the coherence near the wall.

The frequencies at which the maximum concentration of turbulent energy occurs for the streamwise velocities in Figure 6-3(b) are distributed in the range $0.2 < \omega\delta^*/U_\infty < 0.9$. The velocity spectra and the frequencies at which the peaks occur are comparable to the cylindrical boundary layer measurements of Lueptow and Haritonidis (1987) presented in a similar format. Subtle differences can be detected in the distribution of energy at the various wall-normal positions, but they are not large enough to allow for any conclusive statements to be made. Very near the wall and in the turbulent/nonturbulent region at the edge of the boundary layer, the spectra have distinct corresponding peaks at $\omega\delta^*/U_\infty \approx 0.25$. This is consistent with the frequency at which the large hump at low frequencies occurs in both the coherence function near the wall and in the turbulent/nonturbulent region. This trend appears to support the idea that the large hump in the coherence near the wall is in fact associated with the low-frequency coherent energy past the edge of the boundary layer and that these large-scale flow structures extend from the turbulent/potential-flow interface all the way down to the wall.

The very large-amplitude, low-frequency spectral peak measured for the streamwise

velocity at $y/\delta = 1.52$ in Figure 6-3(b) indicates that at this wall-normal position nearly all the turbulent energy is confined to a very small band of frequencies, suggesting the presence of a single large-scale flow disturbance. This wall-normal location is consistent with the wall-normal position at which a maximum coherence between the pressure and velocity is observed past the edge of the boundary layer at low frequencies. Because this low-frequency energy also shows up in the pressure-velocity measurements very near the wall, this suggests that the large-scale structure takes the form of a large rotating conglomeration of fluid particles in close contact with the wall and with an average wall-normal extent of approximately 1.5δ. At the top and bottom of the rotating structure where the streamwise velocity due to the rotation of the structure is a maximum, a strong relationship is observed between the pressure and velocity. Because the measurements at $y/\delta=0.76$ correspond to the wall-normal position of the center of the structure where the streamwise velocity induced by the rotating structure is a minimum, very little coherence between the pressure and velocity is observed. Large rotating coherent fluid motions have also been reported for planar boundary layers; however, the precise form of these large-scale structures is a subject of controversy (see Section 1.1.1).

6.1.3 Streamwise Dependence of Coherence

The convective behavior of the flow structures responsible for the pressure-velocity coherence across the boundary layer is investigated in Figure 6-4 by examining how the character of the coherence functions changes with increasing hot-wire/pressure-transducer streamwise separation distance ($x/\delta \leq 1.52$). For clarity, the same wall-normal hot-wire probe positions used in Figure 6-2 are used in Figure 6-4, and only five of the eight different streamwise separations are plotted. The coherence functions at all intermediate locations support the observed trends.

With increasing streamwise separation between the hot wire and pressure transducer, a large decrease occurs in the coherence levels near the wall ($y/\delta \leq 0.032$, $y^+ \leq 28$). At $y/\delta = 0.095$ (not shown) and throughout the outer portions of the boundary layer, the level of the coherence functions remains nearly the same. These different behaviors in the inner and outer regions are expected since the smaller scales near the wall should decay more rapidly than the large-scale outer flow structures. That very little decay occurs at $y/\delta = 0.095$ ($y^+ = 85$) indicates that most of the very small turbulent scales are concentrated nearer to the wall than this point. This is consistent with the findings in Chapter 5 that the association between large-amplitude wall pressure peaks and VITA events related to the bursting phenomena only exists for $y^+ \leq 28$. At all streamwise positions measured, very little coherence exists between the pressure and velocity at $y/\delta = 0.76$.[3]

Very near the wall ($y^+ \leq 28$) the decrease in coherence level with increased streamwise separation is accompanied by a distinct variation in the form of the coherence function. This is because both small and large scales exist near the wall as evidenced by the double-humped character of the coherence function at $x = 0$. A systematic variation in the form of $\Gamma_{pu}(\omega)$ with increasing x can be seen at $y/\delta=0.016$ ($y^+ = 14$). For $x/\delta \leq 0.38$ ($x^+ \leq 339$), an increase in streamwise separation results in a much larger decrease in the coherence level of the low frequency hump than for the high frequency hump. Then for $x/\delta \geq 0.38$, the reverse situation occurs with the high-frequency hump dropping off in amplitude much more rapidly than the low-frequency hump. A similar trend exists at $y/\delta = 0.032$ ($y^+ = 28$) but it is not as systematic. Because the frequency associated with the low-

[3]Data sets were taken by traversing the hot-wire probe in the wall-normal direction at any given x and Ø. Consequently, the zero coherence measured at y/δ=0.76 at all measurement locations is not the result of one bad set of measurements. The data were obtained at separate times and in some cases on separate days.

frequency hump does not change with x, the average size of the large-scale structure does not change with x over the domain measured (assuming a constant propagation velocity). Consequently, the decrease in magnitude of the low-frequency coherence is likely due to the increased distance between the hot wire and pressure transducer and not to a decay of the large-scale structure. The decrease in frequency of the high-frequency hump with x is a result of both the decay and resulting disappearance of the smaller scales and the fact that a coherence can only exist for eddy scales comparable to or greater than the separation distance. In the outer portions of the boundary layer ($y/\delta \geq 0.76$), the general form of the coherence function and frequency of maximum coherence does not change with x. This lends support to the notion that the low-frequency hump near the wall is related to the low-frequency coherent energy observed at the edge of the boundary layer.

These general trends are summarized in contour plots of the coherence at two different frequencies in Figure 6-5. Because the coherence functions are characterized by two distinct behaviors at two different bands of frequencies, the coherence levels at two frequencies representative of the two bands of coherent activity are plotted for all 72 points in the x-y plane containing the pressure transducer ($\emptyset = 0°$). The upper figure shows isocoherence lines for the pressure and velocity at a frequency of $\omega\delta^*/U_\infty = 0.23$, associated with the low-frequency hump, while the bottom figure shows the isocontours at a frequency of $\omega\delta^*/U_\infty = 1.42$, associated with the high-frequency hump. These two frequencies are marked in Figure 6-4 with small arrows at the top and the bottom of the figure. The low-frequency pressure-velocity coherence in the upper figure is distributed in two bands ($y/\delta < 0.6$ and $y/\delta > 1$) across the entire streamwise extent of the measurements. The largest coherence levels in the figure occur in the vicinity of the pressure transducer (the origin) due to the close proximity of the hot wire. They decay rapidly in either direction (x or y) but retain a level throughout the full streamwise extent

that is very similar to that which exists in the band outside of the boundary layer. The downstream decay is minimal as evidenced by the nearly horizontal (streamwise-oriented) contour lines indicating that the coherence levels remain very nearly constant throughout the full streamwise extent of the measurements. This suggests that the large-scale flow structures associated with the turbulent/potential-flow interface that have convected downstream a distance $x/\delta = 1.52$ are correlated with the wall pressure nearly as strongly as they were when they were positioned immediately above the wall pressure transducer and, as a result, experience little decay.

Upon closer examination, the coherence levels within the outer band at any particular x have their maximum values along a line near $y/\delta = 1.5$ and decrease gradually with either increases or decreases in y. The coherence levels within the inner band are largest at the wall and decrease gradually as y increases (at larger x values, the maximum values actually occur slightly above the wall). Between these two bands exists a region nearly devoid of any coherent energy due to the lack of any sort of relationship between the pressure and velocity for the measurements at $y/\delta = 0.76$. This 'valley' of very low coherence, reaching from nearly $y/\delta = 0.6$ to 1.0, that extends throughout the entire streamwise domain suggests one of two things. Either the turbulent scales in this region have an upper size limit that is less than this distance to the wall or they exceed this wall-normal distance but their average configuration takes the form of a large spanwise-oriented rotating fluid mass centered about this distance from the wall. As stated in Section 6.1.2., this is because the streamwise velocities resulting from such a structure are a minimum at wall-normal positions near the center of rotation.

Although both cases likely coexist, the second explanation provides a mechanism by which the low-frequency coherence near the wall could be related to the corresponding low-frequency coherence at the edge of the boundary layer. This is because a large-scale

rotating structure would generate high streamwise velocities and, hence, lead to large low-frequency coherence values for hot-wire probe positions near the wall and in the turbulent/nonturbulent interface, but not in between. This large-scale structure would also be consistent with the gradual increase in coherence levels that are observed as the hot-wire probe moves away from the center of the structure since the magnitude of the streamwise velocities associated with the structure would increase in a similar fashion with increased distance from the center of rotation. If the 'edge' of the rotating structure resides near $y/\delta = 1.5$, a decrease in coherence beyond this point would also be experienced due to the 1/r dependence of u.

In the lower contour plot in Figure 6-5 associated with the high-frequency region of coherent activity between the pressure and velocity, the coherent energy is confined to a thin region very near the wall ($y/\delta \leq 0.2$). The region has a streamwise extent on the order of δ. This is consistent with the streamwise extent over which the large-amplitude wall pressure fluctuations remained correlated with high shear layers in Chapter 5. This again suggests that the high-frequency coherent energy is related to the burst-sweep cycle. Because of the overlap in space of the large-scale structure in the upper figure with this small-scale structure near the wall, it seems likely that these two scales interact. The underlying mechanisms, however, will require more in-depth analysis of the data.

6.1.4 Circumferential Dependence of Coherence

The circumferential or spanwise extent of the pressure-producing flow structures is examined in Figure 6-6 through comparisons of pressure-velocity coherence functions with the hot-wire probe located at various circumferential positions (x = 0). Near the wall ($y/\delta \leq 0.095$, $y^+ \leq 85$), the coherence magnitudes at both circumferential separations ($\emptyset = 20°$ and $40°$) are considerably less than those measured above the pressure transducer

($\emptyset = 0°$). At the edge of the boundary layer ($y/\delta \geq 0.76$), the coherence magnitudes are similar at all three spanwise separations. At intermediate wall-normal locations, only the coherence at $\emptyset = 20°$ has a magnitude similar to that at $\emptyset = 0°$. This trend is a consequence of the uniformly increasing size of the pressure-producing eddies at increasing distances from the wall. The pressure and velocity relationships in circumferentially separated planes is examined more thoroughly in Section 6.2.4.

6.2 Pressure-Velocity Cross Correlations

6.2.1 Definition of the Cross Correlation

The cross correlation provides a measure of the degree to which two temporal records are related as a function of the time delay between the two signals. Although there are several ways to compute the cross-correlation function, $R_{pu}(\tau)$, the most computationally efficient utilizes the Fourier relationship that exists between the cross correlation and the cross-spectral density (Wiener-Khinchine relations):

$$R_{pu}(\tau) = \int_{-\infty}^{\infty} S_{pu}(f) e^{j2\pi f\tau} df \ , \qquad (6.11)$$

where the quantity $S_{pu}(f) = \Phi_{pu}(f)/2$ is the double-sided cross-specral density defined for $-\infty < f < \infty$. Equation (6.11) illustrates how the correlation incorporates the cross-spectral information at all frequencies into a single temporal function. Because the cross-spectral density in equation (6.11) is computed by FFT methods and these techniques require an assumption that p(t) and u(t) are cyclic with period T, the cross correlation that results is

circular. Consequently, zero padding of the data records p(t) and u(t) is necessary such that the number of data points in each subrecord after zero padding, N_z, satisfies the relation $N_z \geq 2N$, where N is the number of actual data points in each subrecord (Bendat and Piersol 1986). The resulting estimate for the cross-correlation function is given by

$$\hat{R}_{pu}(r\Delta t) = \frac{N}{|N-r|} \Delta f_z \sum_{k=0}^{N_z-1} \hat{S}_{pu}(f_k) e^{\frac{j2\pi kr}{N_z}} \ , \ \ r=0,1,\dots, N_z-1 \ , \tag{6.12}$$

where

$$\hat{S}_{pu}(f_k) = \frac{N_z}{N} \frac{T_z}{n_d} \sum_{i=1}^{n_d} P_i^*(f_k) U_i(f_k), \ \ k=0,1,\dots,N_z-1 \ . \tag{6.13}$$

The discrete finite Fourier transforms $P_i(f_k)$ and $U_i(f_k)$ are defined by equations (6.4a) and (6.4b), respectively, with N replaced by N_z. The quantities Δf_z and T_z are the zero-padded frequency resolution ($\Delta f_z = f_s/N_z$) and zero-padded subrecord length ($T_z = N_z \Delta t$).

For a zero-mean random process, the magnitude of the cross-correlation function is bounded by the relation (Bendat and Piersol 1986)

$$|R_{pu}(\tau)|^2 \leq \sigma_p \sigma_u \ , \tag{6.14}$$

where σ_p and σ_u are the standard deviations of p(t) and u(t), respectively. Consequently, it is common to normalize the cross-correlation magnitude according to

$$\rho_{pu}(\tau) = \frac{|R_{pu}(\tau)|^2}{\sigma_p \sigma_u} \tag{6.15}$$

so that $-1 \leq \rho_{pu}(\tau) \leq 1$. This cross-correlation coefficient, as it is called, measures the degree of linear dependence between p(t) and u(t) for a time delay τ between the two

temporal records.

All the pressure-velocity cross-correlation results presented in the following sections were computed from the ensemble average of 80 subrecords of 1024 points each (81920 total points), padded with 1024 zeros (see Table 2-2). Digital bandpass filtering ($59 \leq f \leq 5332$ Hz) was utilized for these results. Because the cross correlations are an averaging over all frequencies, the removal of both the low and high frequencies had some effect on the correlation results. This is shown in Figure 6-7 at three different wall-normal positions of the hot-wire probe. Although the overall character of the correlations did not change, three subtle effects of filtering can be observed:

(1) the filter removes very small-scale, small-amplitude oscillations near $\tau = 0$ for hot wire positions at the edge of the boundary layer, presumably resulting from correlated electrical noise in the microphone and hot wire signals and a relatively low signal-to-noise ratio;

(2) the filter removes large time-scale (~0.05 s) undulations in the correlations for hot wire positions at the edge of the boundary layer, presumably due to large-eddy disturbances in the test section; and

(3) the filter causes the correlations to shift down slightly with respect to the zero-correlation line—the general trend being to decrease slightly (≤ 10-15 percent) the magnitude of positive peak values and increase slightly the magnitude of negative peak values. This results from the removal of low-frequency, in-phase pressure-velocity relationships from the correlations possibly caused by an acoustic plane wave propagating in the streamwise direction in the test section (see Section 3.1.1).

6.2.2 Wall-Normal Dependence of the Cross Correlations

The cross correlations between the fluctuating wall pressure and streamwise turbulent velocities immediately above the pressure transducer ($x = 0$, $\varnothing = 0°$) and at various wall-normal positions of the hot-wire probe are shown in Figure 6-8. A correlation, although considerably stronger at the wall, exists all the way out into the turbulent/nonturbulent interface. The general decrease in correlation amplitude with increased distance from the wall is a consequence of the r^{-1} dependence of the turbulent source contributions to the wall pressure. The general character of the correlations is consistent with what has been observed in a planar boundary layer (Willmarth and Wooldridge 1963, Panton et al. 1980, Kobashi and Ichijo 1986).

Near the wall ($y/\delta \leq 0.032$, $y^+ \leq 28$), the correlations exhibit two distinct length or time scales; a small-scale motion contributes to the rapidly decreasing part and a large-scale motion contributes to the slowly decreasing part. These two time scales are evidently associated with the double-humped structure observed in the coherence function near the wall. These two contributions to the pressure-velocity correlation can be separated by highpass and lowpass filtering the pressure and velocity data prior to the calculation of the correlation. The results of this filtering with a cutoff frequency of $\omega\delta^*/U_\infty = 0.73$ are plotted along with the full correlation at $y^+ = 14$ in Figure 6-8.[4] The high-frequency portion shows a form characteristic of the -90° phase, which was revealed in the cross-spectral results associated with the high-frequency hump in the coherence function. This form is also consistent with what can be deduced from the conditionally averaged pressure-velocity results in Figure 5-5 associated with the burst-sweep cycle near the wall. The low-frequency portion of the correlation exhibits an almost in-phase

---

[4]This filter is implemented in addition to the bandpass filtering operation $0.13 \leq \omega\delta^*/U_\infty < 12.5$ already utilized.

relationship with a time scale comparable to that observed in the correlations past the edge of the boundary layer. This appeared in the cross-spectral results as a low-frequency hump in the coherence function near the wall, with an almost in-phase phase angle of -30° and a frequency coincident with the frequency at which the coherent energy existed past the edge of the boundary layer. These highpass and lowpass filtered results are very similar to the correlation results of Kobashi and Ichijo (1986) obtained with a similar nondimensional cutoff frequency at $y/\delta = 0.1$ in a planar boundary layer.

Although not shown in Figure 6-8, the amplitude of the high-frequency correlation diminishes rapidly with increased distance from the wall, such that by $y/\delta = 0.19$ it is nearly zero. This is also consistent with the high-frequency correlation results of Kobashi and Ichijo (1986) in a planar boundary layer. This trend was revealed in the cross-spectral results as a decrease in the amplitude of the coherence at high frequencies with increased distance from the wall. The form of the low-frequency correlation also changes with increased distance from the wall. Since all the high-frequency correlation is gone by $y/\delta = 0.19$, the full correlations shown in Figure 6-8 are nearly identical to the lowpass results at and above this point. As y increases, a general decrease in the overall magnitude of the correlations occurs up to the measurement made at $y/\delta = 0.76$ where the correlation disappears. As y increases further, the correlation magnitude increases again with its largest amplitude occurring for the measurement made at $y/\delta = 1.52$, as shown in the figure. This is precisely the form of the variation in the low-frequency coherence levels. This gradual variation in correlation magnitude is accompanied by a gradual transition in the overall character of the correlation from the nearly in-phase relationship near the wall (-30°) to a nearly -180° out-of-phase relation at the farthest position measured from the wall. This variation proceeds systematically for all the wall-normal positions at which measurements were made, except at $y/\delta = 0.76$ where the correlation is zero and, hence,

the phase of the correlation is undefined. The low-frequency correlations of Kobashi and Ichijo (1986) are qualitatively similar to the present measurements except fewer hot wire positions were used, such that the full range of behavior observed in the present measurements cannot be detected in their results.

This change in character of the low-frequency correlation is apparent in the p-u phase results in Figure 6-2(b). At the position of the low-frequency coherence hump, the magnitude of the phase steadily increases with increasing y from -30° near the wall to nearly -180° at the edge of the boundary layer, except at the point $y/\delta = 0.76$ where the coherence is zero and the phase, as a result, is randomly distributed about 0°. As pointed out in Section 6.1.2, a -180° phase relationship between p and u past the edge of the boundary layer and in the wavy turbulent/potential-flow interface has been deduced by consideration of a potential flow over a wavy 'wall' (Panton et al. 1980). However, because the phase between p and u in the present measurements decreases gradually from -135° to -175° throughout this region, the wavy wall model is not entirely consistent with the observed behavior outside of the boundary layer. A similar variation in phase as found for $y/\delta > 1$ in the present investigation can be detected in the measurements of Panton et al. (1980) performed in the noise-free boundary layer on the surface of a sailplane.

Willmarth (1975) proposed a rotating vortex model to predict the pressure-velocity relationships in the boundary layer due to the large-scale structure in which a two-dimensional vortex (with solid body core) moves adjacent to a nearby wall. The passage of the vortex was assumed to produce a reduced pressure at the wall. Although his computed correlation for R_{pv} was qualitatively consistent with the measurements, Willmarth did not consider the streamwise velocity component. Kobashi and Ichijo (1986) presented computed pressure-velocity correlations for a vortex model of a

turbulent boundary layer for both u and v components of velocity. Although their results for R_{pv} were also qualitatively comparable to their measurements, only two phase relationships between the wall pressure and the streamwise velocity appear in their solution; 0° below the center of the vortex and -180° above the center. Although these phase relations appear consistent with the asymptotic behavior of the relationship between p and u in the flow, the model does not predict the distinct systematic variation in phase between these two limits observed across the boundary layer in the present measurements. Although they did not state the assumptions behind their model, it is clear from the form of their solution that the streamwise velocity field they computed changed sign across a horizontal plane through the center of the vortex (above the plane, $u > 0$, while below it, $u < 0$) since the passage of the structure produces a particular pressure pattern at the wall. To arrive at a phase of 0° at the wall, a negative wall pressure was present.

From a purely physical standpoint, however, the full range of phase relationships observed in the present measurements can be understood. Downstream of the vortex, a flow of high-speed fluid ($u > 0$) towards the wall beneath the centerline of the structure can occur. Similarly, behind the vortex a flow of low-speed fluid ($u < 0$) away from the wall above the centerline of the structure can occur. These two effects cause a clockwise rotation (about the center of the vortex) of the $u = 0$ plane across which u changes sign from the horizontal orientation present in the model of Kobashi and Ichijo (1986). As the vortex moves past a fixed probe, both positive and negative streamwise velocities are experienced at any given y. Because the $u = 0$ plane is at an angle to the wall, the spatial location at which $u(x) = 0$ steadily decreases with increasing y. From the point of view of a fixed probe, the time at which $u(t) = 0$ steadily increases with increasing y. The net effect is a phase between the pressure and velocity that varies gradually from 0° at the wall (if the passage of the structure is assumed to produce a reduced pressure at the wall)

through -90° at the centerline of the vortex (where p leads u) to -180° at the outer edge of the vortex.

This behavior of the rotating vortex model qualitatively predicts the low-frequency correlation and phase relationship between p and u observed in the present measurements. If the vortex is assumed to be centered at $y/\delta \approx 0.75$ with a scale twice its distance from the wall of $\sim 1.5\delta$, a single large rotating vortex structure is sufficient to predict all the observed low-frequency behavior in the boundary layer. The largest correlation and coherence levels and maximum peak in the streamwise velocity spectra for $y/\delta > 1$ occurring at $y/\delta = 1.52$ are consistent with this being the location of the outer 'edge' of the vortex where the streamwise velocity of the structure is greatest. The absence of any relationship between the pressure and velocity at $y/\delta = 0.76$ is consistent with this being the centerline of the structure where its u component of velocity is at a minimum. The emergence of a strong low-frequency relationship very near the wall is a consequence of this being the location where the streamwise velocity fluctuations reach a maximum magnitude again (combined with the close proximity of the hot wire and pressure transducer). The wavy wall model, although consistent with the rotating vortex at large y, is only a consequence of the large rotating vortex and not the cause of the out-of-phase p-u relationship. This is evident by the fact that the viscous vortex predicts the variation in phase from -135° to -175° past the edge of the boundary layer observed in the present measurements and the measurements of Panton et al. (1980) while the wavy wall does not.

It is interesting to point out that in front of the spanwise vortex structure $u > 0$, while behind it $u < 0$; hence, the passage of the vortex past a fixed probe will produce a positive streamwise velocity followed rapidly by a negative streamwise velocity. This is precisely the form of the velocity during the decelerating VITA events ($\partial u/\partial t < 0$) observed near the

wall. Because decelerating VITA events are linked to negative large-amplitude wall pressure peaks (see Section 5.3), this suggests that both the decelerating VITA events and the negative pressure peaks may be related to the passage of a small-scale mass of fluid particles rotating in the direction of the mean shear analogous to a small spanwise vortex structure near the wall. This result also provides evidence that the passage of a spanwise vortex structure does in fact produce a reduced pressure at the wall, as initially speculated by Willmarth (1975).

6.2.3 Streamwise Dependence of the Cross Correlations

The streamwise evolution and decay of the pressure-velocity correlations over a streamwise extent of $x/\delta = 1.52$ is shown in Figure 6-9 for three wall-normal positions of the hot-wire probe ($y/\delta = 0.016, 0.19, 1.52$). With increasing streamwise separation between the hot wire and pressure transducer, the correlations show the expected convective behavior as evidenced by the successively larger time shifts of the patterns. Near the wall ($y/\delta \leq 0.032$, $y^+ \leq 28$), the amplitude of the correlation decreases rapidly with increased streamwise extent due to the decay of small-scale structures close to the wall. At farther distances from the wall ($y^+ \geq 85$), a decrease in overall amplitude is not present. This is consistent with previous findings that most of the small-scale structure is concentrated very close to the wall and that the large-scale structure does not decay much over the domain of measurements.

These trends are illustrated more clearly in Figure 6-10(a), where the maximum amplitude of the correlation at each streamwise position is plotted as a function of x/δ for the three wall-normal positions plotted in Figure 6-9. Only the curves for $y^+ \leq 28$ ($y^+ = 28$ not shown) exhibit any appreciable decrease in amplitude over the streamwise extent of the measurements. The very rapid decrease in magnitude for $x/\delta < 0.1$ at

$y^+ = 14$ is most likely associated with the very high-frequency hump observed in the coherence functions near the wall near $\omega\delta^*/U_\infty = 8\text{-}10$. Whether this is associated with correlated noise or the presence of some extremely small scale in the flow is difficult to say. The small hump in the decay curves near $x/\delta = 0.2$, which exists in all measurements for $y/\delta \leq 0.19$, indicates that the relationship between the pressure and velocity is stronger at this particular downstream location. More will be said about this shortly. The correlation that still remains at $x/\delta = 1.52$ for the measurement near the wall is probably associated with the large-scale structure.

The convection velocity of the pressure-producing structures contributing to the correlation are examined in Figure 6-10(b) for the three wall-normal positions in Figures 6-9 and 6-10(a). Convection velocities can be computed for the average pressure producing structure from the time shifts associated with the maximum correlation amplitudes, τ_c, at each streamwise separation in Figure 6-9 according to $U_c = x/\tau_c$.[5] The convection velocity at the closest position to the wall is less than that in the outer portions of the boundary layer, as would be expected. This can also be seen in Figure 6-9 since the time shift for the measurement at $y/\delta = 0.016$ is the largest at any x/δ. Near the wall ($y/\delta \leq 0.095$, $y^+ \leq 85$), the convection velocities increase appreciably with increased streamwise separation presumably because of the decay of smaller, slower eddies near the wall that contribute to the correlation. For the measurements outside of the boundary layer ($y/\delta \geq 1.14$), the convection velocities decrease with increased streamwise separation, presumably due to the loss of momentum to the boundary layer of large-scale structures associated with the turbulent/potential flow interface. In an intermediate region

[5] Convection velocities can be computed from space-time correlations in a number of different ways according to what feature of the correlation is followed through space and time (Hinze 1975). The method used for the present investigation was chosen because it is the most intuitive. Differences between the various techniques amounted to less than 5 percent for the present measurements.

($0.19 \leq y/\delta \leq 0.38$), very little change in convection velocity occurs over the full streamwise extent of the measurements. Because no correlation exists at $y/\delta = 0.76$, it was not possible to compute a convection velocity at this point.

At $y^+ = 14$, the convection velocity varies from $U_c = 0.40U_\infty$ ($= 8.3u_\tau$) for small streamwise separations to an asymptotic value of $U_c = 0.60U_\infty$ ($= 12.4u_\tau$) at large separations. These convection velocities are consistent with those found in Chapter 5 for the large-amplitude wall pressure peaks and near-wall shear layer structure associated with bursting. They are also consistent with measurements of the convection velocity for the fluctuating wall pressure in a planar boundary layer of $U_c = 0.39U_\infty$ reported by Emmerling (1973) and $U_c = 11.9u_\tau$ reported by Schewe (1983). The convection velocities at all points $y/\delta \geq 0.19$ asymptote to a value of $0.83U_\infty$ by $x/\delta \approx 1$, indicating that this is the mean convection velocity for the large-scale structure. Willmarth and Wooldridge (1962) computed the convection velocity between streamwise separated pressure transducers in a planar boundary layer and found an identical result for the convection velocity of the fluctuating wall pressure for the frequency range $0.13 \leq \omega\delta^*/U_\infty \leq 12.5$. If the mean position of the average large-scale structure is centered near $y/\delta \approx 0.76$, then the convection velocity at this distance from the wall should not change with streamwise position since the large-scale structure is always at its convection velocity and is a constant over the domain of these measurements. Since, for these measurements, $U(y) = 0.97U_\infty$ at $y/\delta = 0.76$, the mean convection velocity of the large-scale structure is less than the local mean velocity and, hence, does not obey Taylor's hypothesis. The convection velocity near the wall at large x/δ is smaller than that of the mean convection velocity for the large-scale structure even though all the small scales have decayed. This suggests that the large-scale structure may be distorted by the mean velocity gradient and, as a result, be inclined to the wall.

The pressure-velocity correlation measurements in the x-y plane containing the microphone ($\emptyset = 0°$) are summarized by means of a contour plot, as shown in Figure 6-11. At all 72 points in the plane at which the correlation was measured, the magnitude at zero time delay ($\tau = 0$) was used to construct isocorrelation contours. Because the cross correlation is the integral of the cross spectrum over frequency, the isocorrelation contour plot incorporates the coherence and phase information at all frequencies and all positions in the plane into a single plot. Because the isocontours are constructed at a single (zero) time delay, they depict an instant in time and thus represent a 'snapshot' of the average eddy structure throughout the boundary layer that contributes to the fluctuating wall pressure. The sign of the correlation in the isocontour plot is a direct indication of the average sign of the pressure relative to that of the streamwise velocity. Thus, $\rho_{pu}(0) > 0$ means p and u are of the same sign, while $\rho_{pu}(0) < 0$ means p and u are of opposite sign.

The isocorrelation contours reveal a band of positive correlation that extends out from the wall past the edge of the boundary layer, suggesting the presence of a large-scale flow structure at an angle of inclination to the wall as was suggested by the convection velocities for the correlations. The band has an angle of inclination to the wall of 45°, presumably a result of distortion from the mean velocity gradient. This angle of inclination is consistent with that reported by some investigators for the average large-scale eddy structure in a planar boundary layer (see Section 1.1.1). If the average sign of the pressure is assumed to be negative at this instant in time, the structure of the isocorrelation indicates that the 45° band is associated with low-speed fluid ($u < 0$). This is qualitatively consistent with the character of the large-scale structure found thus far. Near the wall and downstream of the pressure transducer, the contours are negative and exhibit a sweptback character with an average inclination to the wall of 18°. This angle is consistent with the angle of inclination observed for the near-wall shear layers and quasi-

streamwise vortex structures in a planar boundary layer (Robinson et al. 1990). With the average sign of the pressure being negative during the correlation, this region of negative correlation represents high-speed fluid near the wall. This is consistent with sweeps observed near the wall beneath inclined shear-layer structures, which the line of zero correlation constitutes. The pocket of negative correlation (high-speed fluid) above the pressure transducer at the edge of the boundary layer may be related to fluid from the free stream entering the boundary layer via a bulge. It appears from the isocorrelation contours that the large-scale structure, turbulent/potential-flow interface, and near-wall flow structures are interrelated.

Willmarth and Wooldridge (1963) constructed similar contours in a planar boundary layer with a nearly identical nondimensional bandpass filter. Their results are similar to the present results near the wall ($y/\delta < 0.2$) and beyond the edge of the boundary layer ($y/\delta > 1$). In the outer portion of the boundary layer, however, their isocorrelation contours do not show a band of positive correlation extending out from the wall. Although their transducer was an order of magnitude larger than the one used here, this should only have an effect on the smaller scales near the wall. The difference is consistent, however, with what was found for the fluctuating wall pressure spectra in chapter 4. Namely, if the smallest scales in the flow near the wall are not affected by transverse curvature, the planar and cylindrical boundary layer contours should agree as they do. As y increases and the scales of the eddies increase, they begin to be affected by transverse curvature, as evidenced by the lower wall pressure spectral energies than found in a planar boundary layer, and differences can be expected to develop between the planar and cylindrical boundary layer contours. Finally, for $y/\delta > 1$, the flow is governed by parameters associated with the potential flow and not the wall. Thus, it is reasonable to expect that the planar and cylindrical boundary layers and, hence, the contours would

become similar again as the edge of the boundary layer is approached.

Since the positive correlation region exists at the edge of both the planar and cylindrical boundary layers, the band of positive correlation observed in the present measurements can be interpreted as the outer flow structure present in both boundary layers, extending all the way down to the wall in the cylindrical boundary layer. This might explain the double-humped structure observed in the coherence function very near the wall for the present measurements that does not appear in the planar boundary layer measurements of Russell and Farabee (1991). However, cross-spectral p-u measurements closer to the wall in a planar boundary layer are necessary to resolve this issue. If it is a result of transverse curvature, however, it would suggest that the outer flow interacts more strongly with the flow in the near-wall region in the cylindrical boundary layer.

6.2.4 Circumferential Dependence of the Cross Correlations

The form of the pressure-velocity correlations that result from a circumferential separation between the pressure transducer and hot-wire probe are examined in Figure 6-12. Near the wall ($y/\delta \leq 0.095$), the correlations at all three spanwise separations exhibit a different character. At the outer portions of the boundary layer ($y/\delta \geq 0.76$), all three correlations are similar. This is a result of the increasing scales of the structures in the boundary layer with increasing distance from the wall. A similar effect was observed in the magnitudes of the coherence in Section 6.1.4. At intermediate points in the boundary layer, only the correlation at $\varnothing = 20°$ is similar to that at $\varnothing = 0°$. This spanwise scale is examined more closely in Figure 6-13, where zero-time-delay pressure-velocity isocorrelation contours are constructed in streamwise-spanwise (x-$\varnothing$ or x-s) lamina at various distances from the wall. Near the wall, the isocorrelation lines are elongated in

the streamwise direction, indicating a rapid change in the character of the flow in the spanwise direction. These large spanwise gradients are indicative of the highly three-dimensional nature of the turbulence near the wall. At the edge of the boundary layer, the isocorrelation lines take on an entirely different form with a nearly spanwise orientation. This indicates that the character of the flow does not change very much in the spanwise direction. This is expected since the scales in the outer portion of the flow are large. A gradual transition with increasing wall-normal distance is observed in the form of the isocorrelation contours between these two cases.

The isocorrelation contour nearest the wall at $y^+ = 14$ illustrates the streaky structure associated with the flow in this region, as evidenced by successive regions of high- and low-speed fluid with a spanwise separation of $s^+ \sim 50$. This is consistent the character of the streaky structure observed in a planar boundary layer. The form of the isocorrelation is entirely consistent with the character of the quasi-streamwise vortex structure if it is assumed that the lower loop of the hairpin structure is situated over the pressure transducer (the position for which an optimum correlation would result). With the vortex in this position, the wall pressure would be negative, and the negative correlation region downstream of the pressure transducer represents high-speed fluid ($u > 0$), presumably associated with a sweep (if $v < 0$). The region of positive correlation to the side and downstream of the pressure transducer represents low-speed fluid ($u < 0$), presumably related to the ejection of low-speed fluid between the legs of the inclined vortex structure. The angle of the zero correlation line associated with the location of the stretched vortex element of approximately 10° with respect to the streamwise direction is consistent with the findings of Wallace (1982, 1985) for the angle associated with the leg of the quasi-streamwise vortex structure in a planar boundary layer. The streamwise extent of the near-wall structure of $x/\delta \sim 1$ is also consistent with that observed for the quasi-

streamwise vortex structure in a planar boundary layer. This streamwise extent also being consistent with the extent over which the wall pressure peaks were related to VITA events associated with the bursting process supports the idea that this correlation structure near the wall is a depiction of the burst-sweep cycle.

The general character of the contours at $y^+ = 28$ is the same as that at $y^+ = 14$, except that the region of large negative correlation is shifted downstream due to the inclination to the wall of this structure. By $y^+ = 85$ (not shown), the large spanwise gradients begin to disappear. This is consistent with all previous findings indicating that the small-scale structure near the wall is concentrated in the region $y^+ \leq 28$. By $y^+ = 169$ in Figure 6-13, the region of negative correlation presumably associated with high-speed fluid ($u > 0$) has moved even farther downstream due to the inclination to the wall and has spread considerably in the spanwise direction with a spanwise scale that appears even larger than the wall-normal position.

The character of the isocorrelations for $y/\delta > 1$ is reminiscent of an undulating turbulent/potential-flow interface, as evidenced by large regions of high-speed fluid (dips in the interface that bring in higher speed free-stream fluid) or large regions of low-speed fluid (bulges in the interface associated with lower speed fluid from within the boundary layer). The regions have a spanwise and streamwise scale of $\sim\delta$. However, because of the poor spatial resolution resulting from the large distance between the circumferentially separated planes at these large streamwise distances, it is not possible to detect any small-scale details at this large distance from the wall.

CHAPTER 7

SUMMARY AND CONCLUSIONS

The relationship between the fluctuating wall pressure and streamwise turbulent velocities within a turbulent boundary layer on a cylinder in axial flow has been examined. The aim has been to relate the unsteady pressure at the wall to turbulent structures in the flow and thus deduce the sources of the fluctuating wall pressure in the cylindrical boundary layer. The major results and conclusions will be summarized in three sections. Section 7.1 addresses features of the cylindrical boundary layer flow that are similar to those found in planar boundary layer flows. Section 7.2 discusses features that are distinctly different. Finally, Section 7.3 summarizes findings that are new with respect to wall pressure in a turbulent boundary layer and consequently involve ambiguity as to whether they are related to transverse wall curvature or are characteristic of wall-bounded flows in general.

7.1 Similarities Between Cylindrical and Planar Boundary Layers

The accumulative body of results presented in this thesis suggests that the overall character of the turbulent structures that contribute to the fluctuating wall pressure in the cylindrical boundary layer is similar to that observed in planar boundary layers.

Flow disturbances that were found to contribute to the wall pressure take two forms: a small-scale, high-frequency disturbance near the wall and a large-scale, low-frequency disturbance associated with the 'global' boundary layer—similar to that reported for wall pressure fluctuations in a planar boundary layer (Kobashi and Ichijo 1986). Evidence for this two-scale-behavior is provided by pressure-velocity cross spectra that exhibit concentrations of coherent energy in two distinct frequency bands. Low-frequency concentrations of energy are observed throughout and beyond the boundary layer, while high-frequency coherent energy is confined to a thin region near the wall ($y/\delta < 0.2$). The high-frequency coherent energy is consistent with the characteristic frequency of the large-amplitude wall pressure fluctuations associated with bursting in the near-wall region. The low-frequency concentration of energy is consistent with the frequency of the organized irrotational motion of the turbulent/potential-flow interface. Similar effects can be seen in the pressure-velocity cross correlations but in the form of short and long time scales.

The high-frequency, small-scale structure contributing to the wall pressure appears to be associated with the burst-sweep cycle, which is believed to be the mechanism responsible for the generation of turbulence near the wall in planar boundary layers. This is consistent with previous measurements in a cylindrical boundary layer that have indicated that the flow near the wall is similar to that in other wall-bounded flows (Lueptow and Haritonidis 1987). Evidence for this is provided by several different results. Large-amplitude pressure peaks in the cylindrical boundary layer produce a probability density function and contribution to the rms wall pressure level that are similar to those measured in a planar boundary layer with similar transducer resolution (Schewe 1983). The high-frequency portion of the wall pressure spectrum collapses with planar boundary layer spectra (on inner variables) at similar Re_θ and with similar transducer type and resolution. This indicates that the small scales very near the wall are not affected by

transverse curvature as would be expected. The form of the conditionally averaged pressure and velocity signatures near the wall is very similar to that measured in planar boundary layers. A strong association between large-amplitude wall pressure peaks and shear layer structures near the wall is observed, as has been found in planar boundary layers (Johansson et al. 1987, Haritonidis et al. 1990). The character of this relationship will be discussed in Section 7.3. Convection velocities for the near-wall structures contributing to the wall pressure are very similar to those reported for planar boundary layers. The iso-correlation pressure-velocity contours in the x-y plane through the pressure transducer have a sweptback appearance near the wall with an angle of inclination to the wall of 18°—consistent with that for near-wall shear layers and quasi-streamwise hairpin vortex structures believed to be associated with turbulence production in planar boundary layers (see Section 1.1.1). The isocorrelation contours in x-s lamina ($s = r\varnothing$) also exhibit a spanwise streaky structure characterized by alternating regions of high- and low-speed fluid with a spanwise spacing of $s^+ \sim 50$, as has been observed in planar boundary layers.

The overall character of the low-frequency, large-scale motion that contributes to the fluctuating pressure at the wall appears consistent with features reported for the large-scale structure in a planar boundary layer. Evidence for this is provided by several different results. The pressure-velocity correlations, although considerably stronger at the wall, extend well outside the edge of the boundary layer and into the turbulent/nonturbulent region consistent with measurements in a planar boundary layer (Kobashi and Ichijo 1986). The correlations also exhibit an overall appearance that is similar to that observed in planar boundary layers. A phase difference between p and u near 180° emerges outside of the boundary layer, as has been previously shown to be consistent with the contributions to the wall pressure that would result from a potential flow over the wavy

turbulent/nonturbulent interface (Panton et al. 1980). The form of the correlation, coherence, and phase functions across the boundary layer suggest that the large-scale motion takes the form of a large conglomeration of fluid particles that rotates in the direction of rotation expected from the mean shear. Similar flow patterns have been reported in planar boundary layers (see Section 1.1.1) and have been used to describe observed pressure-velocity relationships in the boundary layer (although not effectively). The character of this large-scale structure will be described in Section 7.3. The convection velocity for the large-scale, low-frequency correlation is nearly identical to that reported for the large-scale structure in a planar boundary layer, while the isocorrelation contours reveal a band of positive correlation extending out from the wall throughout the entire domain of measurements ($y/\delta \leq 1.91$, $x/\delta \leq 1.52$) at an angle of about 45° to the wall. Similar large-scale inclined flow structures have been reported to exist in planar boundary layers (see Section 1 1.1). Outside of the boundary layer, the spanwise and streamwise extent of the bulges in the turbulent/potential-flow interface is on the order of δ—consistent with that found in this region of the flow for planar boundary layers.

7.2 Effects of Transverse Wall Curvature

Even though the mechanisms for the generation of turbulence near the wall and the large-scale motion in the cylindrical boundary layer appear similar to those for the planar boundary layer, some clear differences exist.

Through comparisons of wall pressure spectra measured in cylindrical and planar boundary layers at similar Re_θ, transducer resolution, and transducer type, the effect of transverse curvature is to reduce the low-frequency spectral energy content of the fluctuating wall pressure (scaled on outer variables) while leaving the high-frequency

spectral content unchanged (scaled on inner variables). Earlier measurements of wall pressure spectra in a cylindrical boundary layer (Willmarth and Yang 1970) using an inappropriate scaling led to the conclusion that transverse curvature causes a decrease in low-frequency spectral energy and an *increase* in high-frequency energy and, as a result, a concentration of energy at higher frequencies. This result contributed to the conclusion that the eddies in a cylindrical boundary layer are smaller. Although the present measurements show that the net effect of transverse curvature is a larger concentration of energy at higher frequencies, this result is produced entirely from less energy at low frequencies and not more energy at high frequencies. Further support for this can be found by comparisons of rms wall pressure levels measured in cylindrical and planar boundary layers at similar Re_θ and with similar transducer resolutions and transducer types. Nondimensionalized by either q_∞ or τ_w, a clear decrease in rms wall pressure level with increased transverse curvature occurs. Based on the present measurements alone, the conclusion of smaller eddy size in the cylindrical boundary layer made by Willmarth cannot be supported.

Transverse curvature alters the statistical characteristics of the fluctuating wall pressure and streamwise velocities compared to those measured in a planar boundary layer. Differences in the wall pressure skewness and flatness factors as well as the frequency of occurrence of large-amplitude wall pressure events were found to exist, which suggest that large-amplitude wall pressure fluctuations may occur more frequently in the cylindrical boundary layer with a relative increase in the number of positive-to-negative fluctuations. Streamwise turbulence intensities u_{rms}/U_∞ are lower than those measured in a planar boundary layer throughout the bulk of the boundary layer, except very near the wall ($y/\delta < 0.07$), and at the edge of the boundary layer ($y/\delta > 0.8$) where they are larger. Skewness for the streamwise velocity is more negative throughout the boundary layer,

and the peaks in the flatness and skewness distributions for the streamwise velocity occur at a farther distance from the wall than for a planar boundary layer. These trends suggest that more energy in the cylindrical boundary layer is concentrated near the wall and at the edge of the boundary layer, with a resulting shift in the mean position of the turbulent/nonturbulent interface to a farther distance from the wall.

7.3 New Findings on the Structure of Boundary Layer Turbulence

Certain similarities and differences can be identified between the turbulent structures responsible for the fluctuating pressure at the wall in cylindrical and planar boundary layers. Even so, the lack of consensus on the exact character of the coherent motions in a planar boundary layer makes it difficult to ascertain whether new information observed in the present measurements concerning the structure of turbulence is an effect of δ/a or a characteristic of wall-bounded flows in general. As a result, several interesting findings will be presented in the general context of wall-bounded turbulence. However, where effects of transverse curvature appear pertinent, statements on its possible influence will be made.

A distinct bidirectional relationship exists between both positive and negative large-amplitude wall pressure fluctuations and the time derivative of the streamwise velocity in the near-wall region ($y^+ \leq 85$). Large-amplitude positive wall pressure peaks are associated with local accelerations in streamwise velocity ($\partial u/\partial t > 0$), while large-amplitude negative wall pressure peaks are associated with local decelerations in streamwise velocity ($\partial u/\partial t < 0$). Although a similar result was reported by Dinkelacker (1990) for a turbulent pipe flow, only the relationship between positive pressures and accelerating streamwise velocities has been reported in the planar boundary layer

literature. It is not possible to deduce whether this observed relationship between both positive and negative pressure peaks and the time derivative of u is a general relationship for all wall-bounded flows or a feature related to the curved walls of both the cylindrical boundary layer and pipe flows without more extensive planar boundary layer measurements. However, considering the overall similarity between the near-wall structure of the planar and cylindrical boundary layers, it seems likely that it is a general characteristic of turbulent boundary layers. Nevertheless, this bidirectional relationship for both positive and negative pressure peaks indicates that both types of large-amplitude wall pressure fluctuations are directly linked to flow structures in the near-wall region. Considering that both positive and negative events occur with similar frequency, it would appear that both types of 'events' (i.e., positive-p/accelerating-u, negative-p/decelerating-u) are equally important to the physics of the near-wall flow.

Differences that exist between the character of the positive and negative large-amplitude wall pressure peaks provide some insight into the nature of the responsible flow structures. With increased distance from the wall ($14 \leq y^+ \leq 85$), a more rapid decrease in the bidirectional relationship between negative pressure peaks and decelerating velocity events occurs than for the positive pressure peaks and accelerating events. In addition, the convection velocity and event duration of the negative wall pressure peaks are less than for the positive pressure peaks. These results suggest that the near-wall turbulent sources that generate the large-amplitude negative pressure peaks are concentrated closer to the wall than the flow structures that generate the positive pressure peaks. If the sources for the negative pressures are concentrated beneath $y^+=14$, as the present measurements suggest, this may be the reason that a universal relationship between negative-p and decelerating-u has not been revealed in the literature (i.e., negative pressure peaks have not been examined this close to the wall).

Finally, because p is only related to the slope of u, no explicit relationship exists between the sign of p and the sign of u—contrary to already conflicting information that has been presented recently in the literature on this point (Johansson et al. 1987, Haritonidis et al. 1990). Conclusions drawn in these earlier studies concerning the relationship between the sign of p and the sign of u appear to be a result of large-scale, low-frequency disturbances superimposed over the small-scale streamwise velocity gradients.

The coherence functions exhibit a low-frequency concentration of energy both near the wall ($y^+ = 14$) and in the turbulent/potential-flow interface that appears at the same frequency. This suggests that a single large-scale flow disturbance, which extends from very near the wall to the turbulent/potential-flow interface, is responsible for the measured low-frequency p-u relationships. Between these two wall normal extremes, a systematic variation occurs in the form of the low-frequency coherence level and phase (or correlation) with increasing distance from the wall across the entire flow field. If the large-scale structure is assumed to take the form of a large spanwise-oriented conglomeration of fluid particles rotating in the direction of the mean shear (a 'rotating vortex') centered at $y/\delta \sim 0.75$ with a wall-normal extent of $\sim 1.5\delta$, a single large-scale spanwise vortex structure is sufficient to predict the low-frequency behavior of the pressure and velocity throughout the entire flow. Although the wavy wall model produces a phase relation between p and u that is consistent with that obtained from the spanwise vortex structure at large y, it cannot predict the variation in phase that exists even in the turbulent/nonturbulent region.

Although similar large-scale structures have been reported to exist in planar boundary layers, the distinct change in the phase relationship between p and u from the wall to regions outside of the boundary layer has not been explicitly reported and, consequently,

not accurately modeled. This variation with distance from the wall, however, should be a common feature of any wall-bounded flow possessing a large-scale structure that rotates in the direction of the mean shear. However, the relatively large wall-normal extent of $y/\delta \sim 1.5$ and streamwise band of virtually zero coherence (or correlation) in the region $0.6 < y/\delta < 1.0$ observed in the present measurements may be a consequence of transverse curvature. This could explain some of the differences observed in the streamwise velocity statistics throughout the boundary layer. However, without more extensive measurements in a planar boundary layer, this remains inconclusive.

Because the large-scale structure extends all the way down to the closest measurements made to the wall where high-frequency coherent energy exists due to the bursting events, the near-wall coherence functions exhibit a bimodal character with elevated coherence levels at two distinct (not necessarily separate) frequencies over nearly the entire streamwise extent of the measurements. The overlap in space of the large-scale and small-scale structures in the near-wall region as well as the overlap in the bands of frequencies at which coherent energy exists strongly suggest that the two motions are somehow interrelated.

TABLES

Table 2-1

Separation Distances Between Hot-wire Probe and Wall Pressure Transducer Used in This Investigation

Wall Normal:	Position	y(in)	y^+	y/δ	y/δ^*
	1	0.015	14	0.016	0.089
	2	0.030	28	0.032	0.179
	3	0.090	85	0.095	0.536
	4	0.180	169	0.191	1.073
	5	0.360	339	0.381	2.146
	6	0.720	677	0.762	4.292
	7	1.080	1016	1.143	6.438
	8	1.440	1355	1.524	8.584
	9	1.800	1693	1.905	10.73
Axial:	**Position**	**x(in)**	x^+	x/δ	x/δ^*
	1	0.000	0	0	0
	2	0.015	14	0.016	0.089
	3	0.030	28	0.032	0.179
	4	0.090	85	0.095	0.536
	5	0.180	169	0.191	1.073
	6	0.360	339	0.381	2.146
	7	0.720	677	0.762	4.292
	8	1.440	1355	1.143	8.584

Circumferential:	Position	Ø(deg)	s(in)
	1	0	0
	2	20	(y+a)Ø
	3	40	(y+a)Ø

Table 2-2
Data Analysis Procedures

Chapter	Data Analysis	Program	Output	$N(=2^n)$#	n_d##	$N_r=Nn_d$†	N_z††	Window	Δf (Hz)*
4	PDF & Statistics	PSTATS	$w(p/p_{rms}), p_{rms}, S, K$	524288	1	524288	0	Rectangular	0.038
		USTATS	$w(u/u_{rms}), u_{rms}, S, K$	524288	1	524288	0	Rectangular	0.038
4	Autospectra	PSPEC	$\Phi_p(f)$	1024	512	524288	0	Hanning	19.53
		USPEC	$\Phi_u(f)$	1024	512	524288	0	Hanning	19.53
5	Conditional Sampling: p trigger	PKDET	event statistics	524288	1	1	0	Rectangular	0.038
			$<p><u>$	65536	1	1	0	Rectangular	0.305
5	Conditional Sampling: u trigger	VITA	event statistics	524288	1	524288	0	Rectangular	0.038
			$<u><p>$	65536	1	65536	0	Rectangular	0.305
6	Cross Spectra	PUSPEC	$\Gamma_{pu}(f)$, $\O_{pu}(f)$	1024	80	81920	0	Hanning	19.53
6	Cross Correlations	PUCORR	$\rho_{pu}(t)$	1024	80	81920	1024	Rectangular	9.77

number of data points per subrecord
number of subrecords
† number of data points in total record
†† number of zero-padded points
* frequency resolution

Table 3-1

Experimental and Flow Parameters

Experimental Parameters	Boundary Layer Parameters	Wall Shear Parameters
f_s=20,000 Hz (Δt=50 μs)	δ =0.024 m	τ_w=0.369 Pa
f_c=10,000 Hz	δ^*= 4.26x10^{-3} m	u_τ=0.552 m/s
U_∞=11.4 m/s	θ = 3.75x10^{-3} m	u_τ/U_∞=0.0484
ρ=1.21 kg/m^3 (18°C)	δ/δ^*=5.63	$l_v=\nu/u_\tau$=26.9 μm
ν=14.9x10^{-6}m^2/s (18°C)	δ^*/θ =1.14	$t_v=\nu/u_\tau^2$=48.9 μs
q_∞=78.6 Pa	δ/a =5.04	a^+=177
a=4.76x10^{-3} m	δ^*/a=0.895	Re_τ=892
X_p=2.48 m (1950 trip heights)	Re_δ=18362	Resolution Parameters
Re_x=1.90x10^6 (tripped)	Re_{δ^*}=3259	d^+=25.9 (microphone)
Re_a=3644	Re_θ=2869	d/δ^*=0.164
		$d^*=d^+(u_\tau/U_\infty)$=1.25
		l^+=18.5 (hot wire)

Table 4-1

Statistical Properties of the Fluctuating Wall Pressure and the Streamwise Turbulent Velocities Across the Boundary Layer.

	(y/δ)	y^+	Mean[a]	RMS	Skewness	Flatness	min/rms	max/rms
pressure	0	0	0.000 Pa	0.679 Pa	-0.084	5.054	-7.321	6.731
velocity	0.016	14	5.93 m/s	1.430 m/s	-0.170	2.367	-3.015	3.196
	0.032	28	7.40 m/s	1.207 m/s	-0.403	2.771	-3.806	2.864
	0.095	85	8.79 m/s	0.836 m/s	-0.273	2.854	-4.570	3.121
	0.191	169	9.52 m/s	0.676 m/s	-0.274	2.868	-4.833	3.711
	0.381	339	10.26 m/s	0.505 m/s	-0.401	3.126	-5.390	3.333
unfiltered ↑	0.762	677	10.92 m/s	0.302 m/s	-0.646	3.770	-6.647	3.870
filtered ↓	1.143	1016	11.19 m/s	0.095 m/s	-1.514	11.31	-10.93	6.699
	1.524	1355	11.21 m/s	0.039 m/s	-0.534	8.976	-10.69	8.387
	1.905	1693	11.17 m/s	0.013 m/s	0.084	3.832	-5.997	9.056

[a] The mean velocity in the freestream for this data is $U(y/\delta \geq 1) = U_\infty = 11.2$ m/s. The freestream velocity for the mean velocity profile presented in Figure 3-8 as well as the average freestream velocity for all the simultaneous pressure-velocity data examined in chapters 5 and 6 is $U_\infty = 11.4$ m/s (a 2% difference).

ILLUSTRATIONS

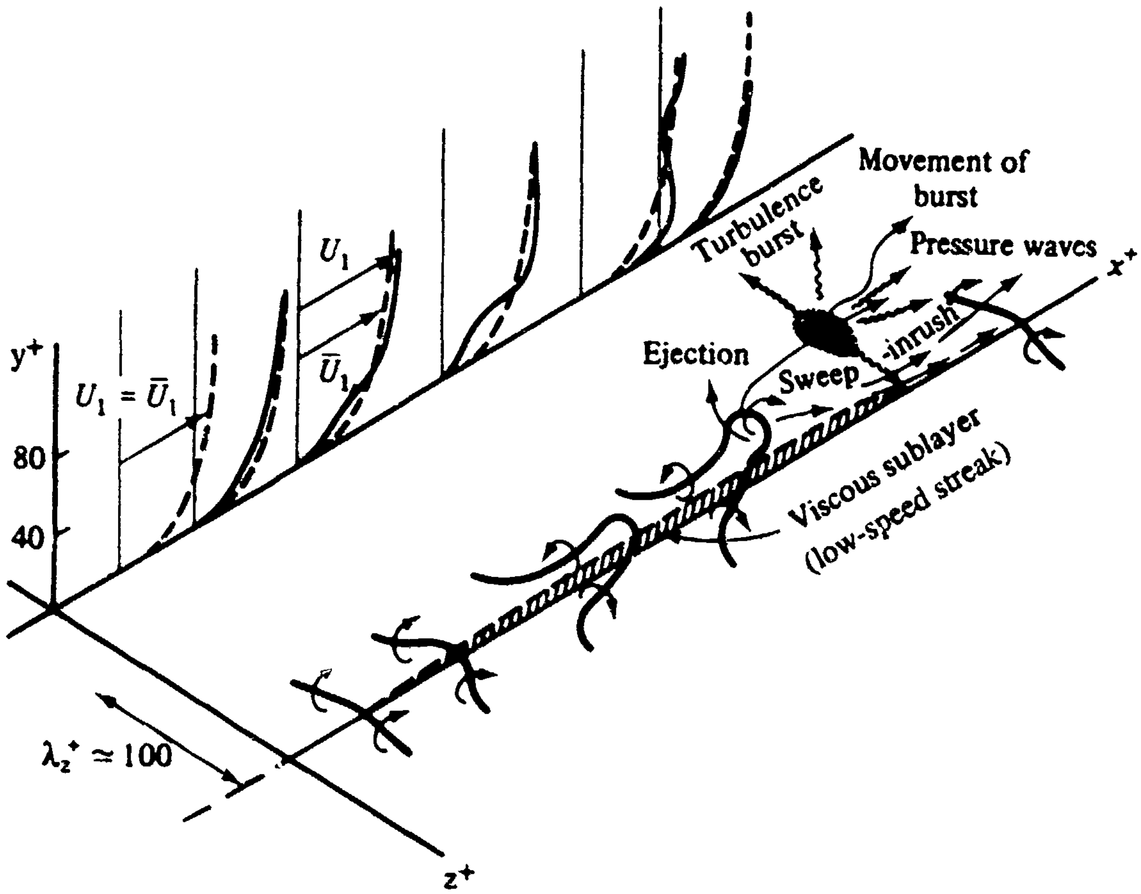

Figure 1-1. Quasi-streamwise vortex structure in near-wall region ($y^+ \lesssim 100$) and its relationship to the burst-sweep cycle. Dashed line represents mean velocity profile. Solid line represents instantaneous streamwise velocity profile (Hinze 1975).

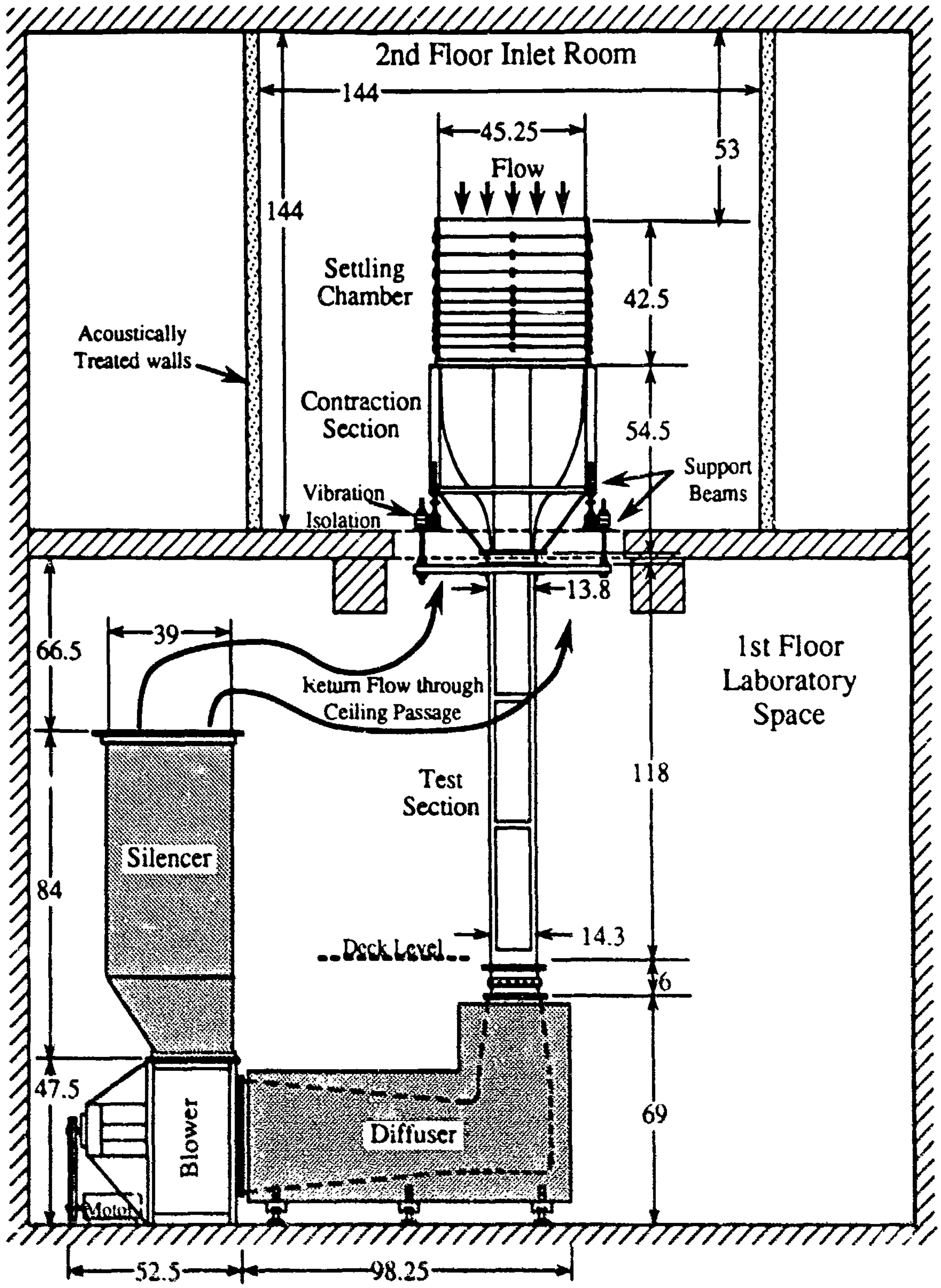

Figure 2-1. Schematic of vertical wind tunnel facility (all dimensions in inches).

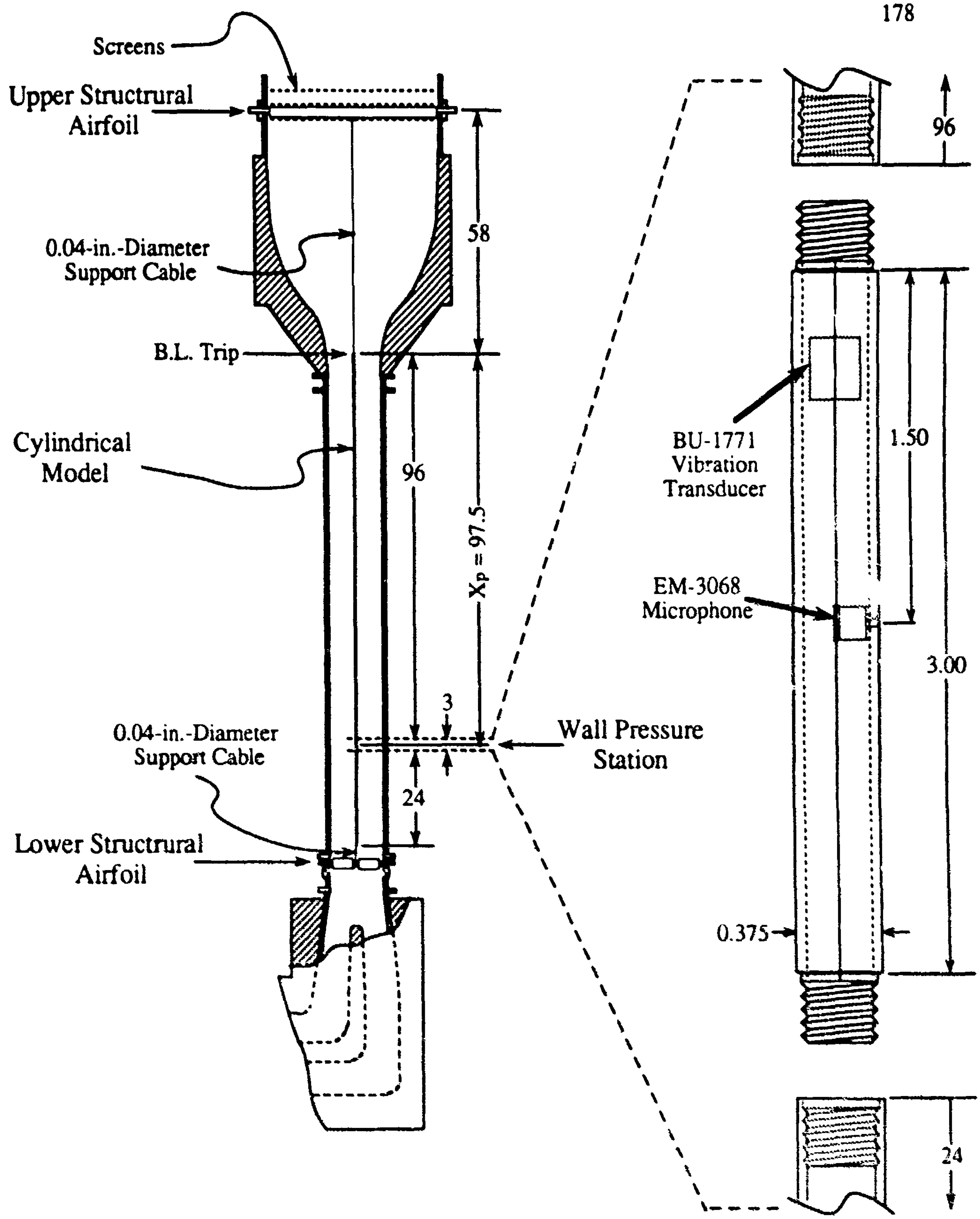

Figure 2-2. Cut-away view of wind tunnel illustrating cylindrical model, model suspension system, and position of wall pressure instrumentation section (all dimensions in inches).

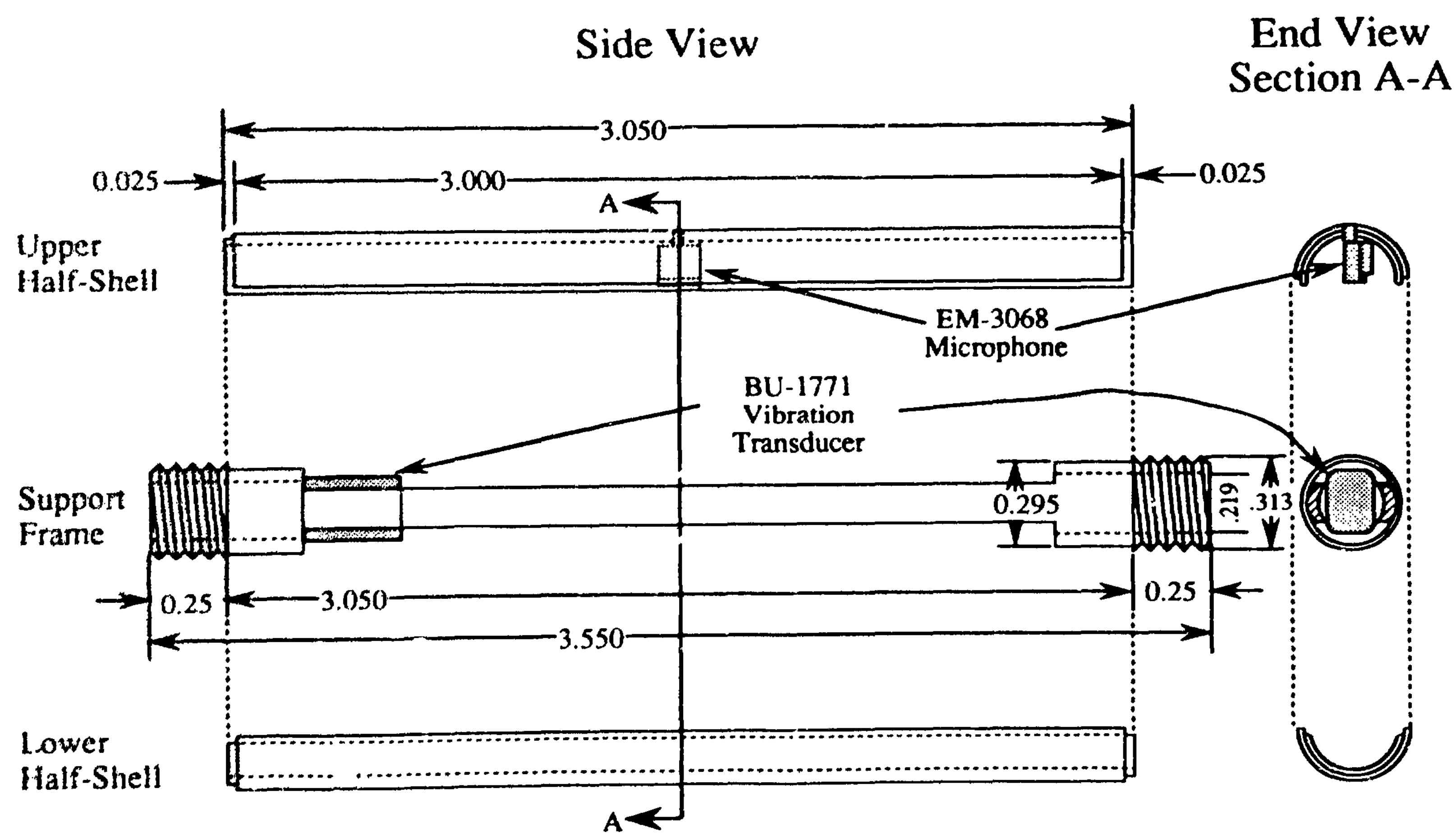

Figure 2-3. Exploded view of cylinder wall pressure instrumentation section (all dimensions in inches).

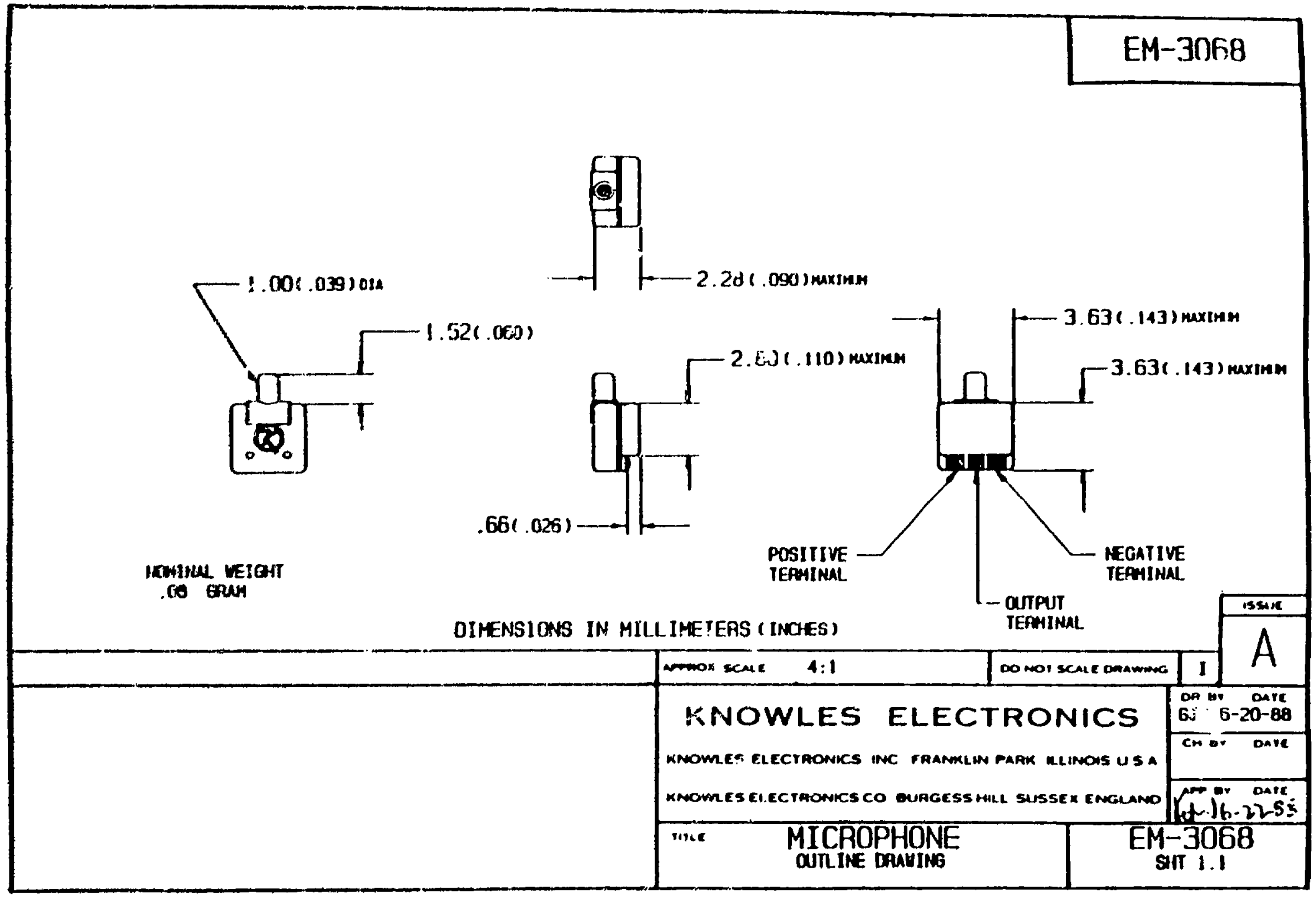

Figure 2-4. Schematic of the EM-3068 subminiature electret condenser microphone used for fluctuating wall pressure measurements. Knowles Electronics outline drawing.

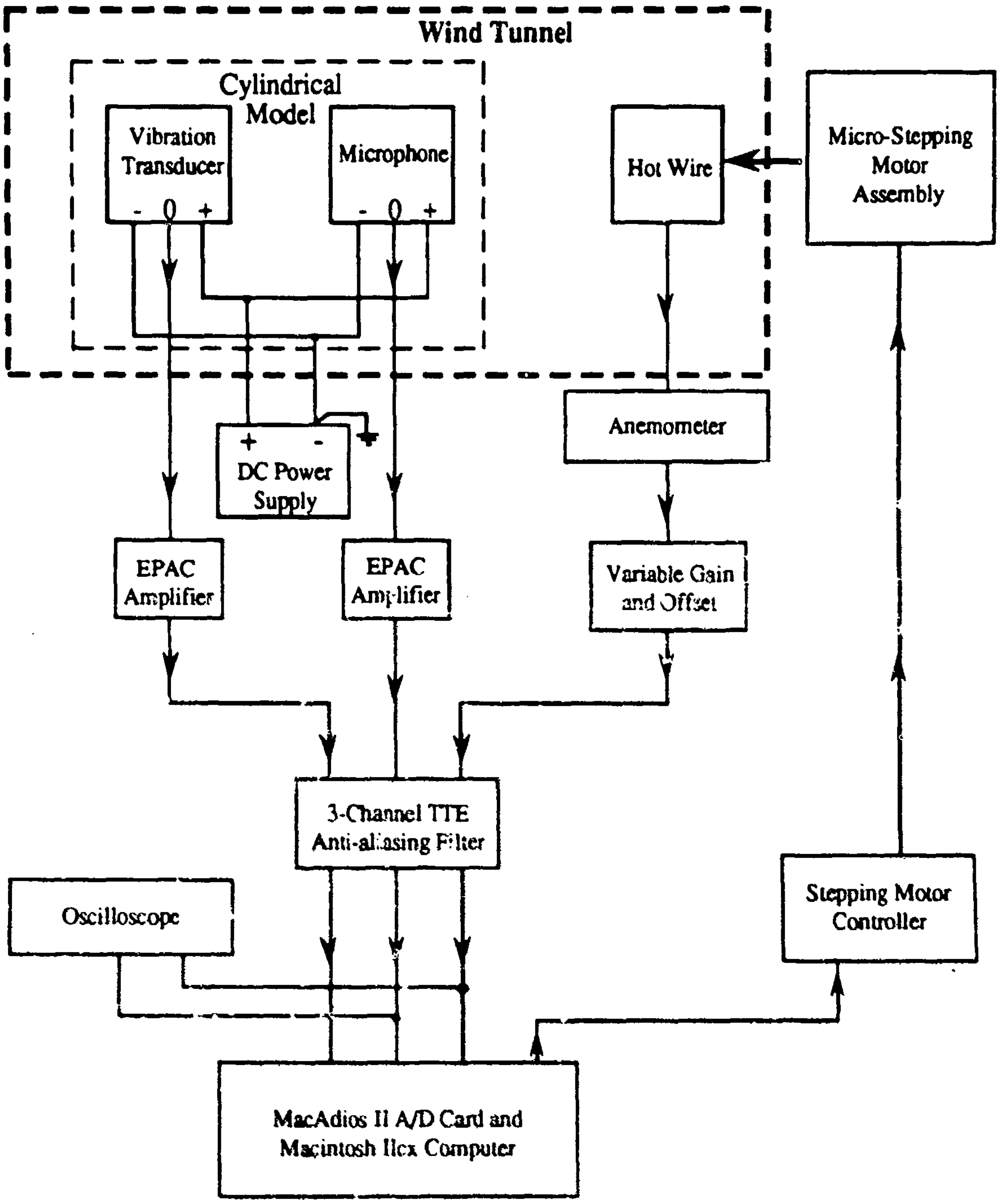

Figure 2-5. Schematic of electronic circuitry and instrumentation for simultaneous microphone, vibration transducer, and hot wire measurements.

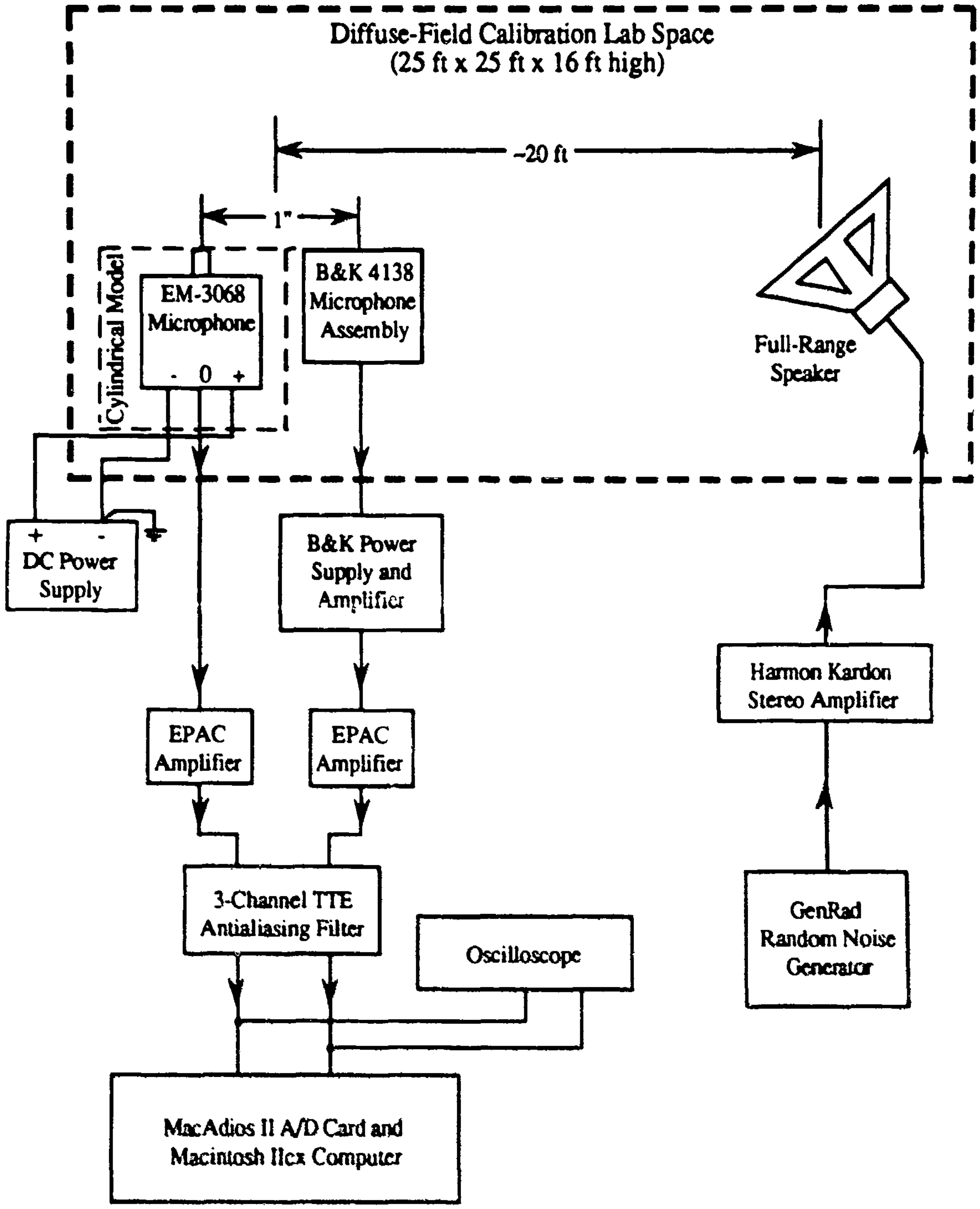

Figure 2-6. Schematic of electronic circuitry and instrumentation for diffuse field comparison calibration for the EM-3068 microphone.

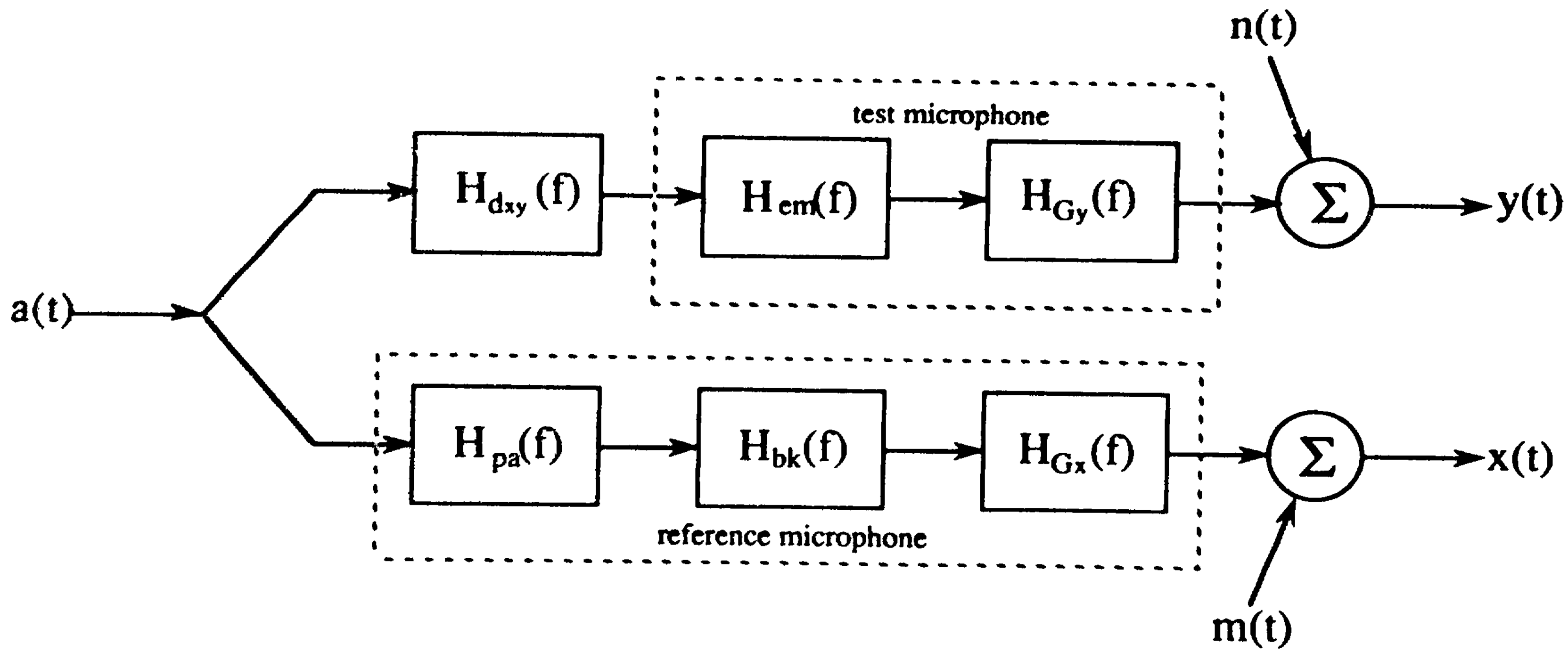

Figure 2-7. Single-input/two-output constant parameter linear system model of the diffuse-field comparison calibration between EM-3068 elecret 'test' microphone and Bruel and Kjaer reference microphone.

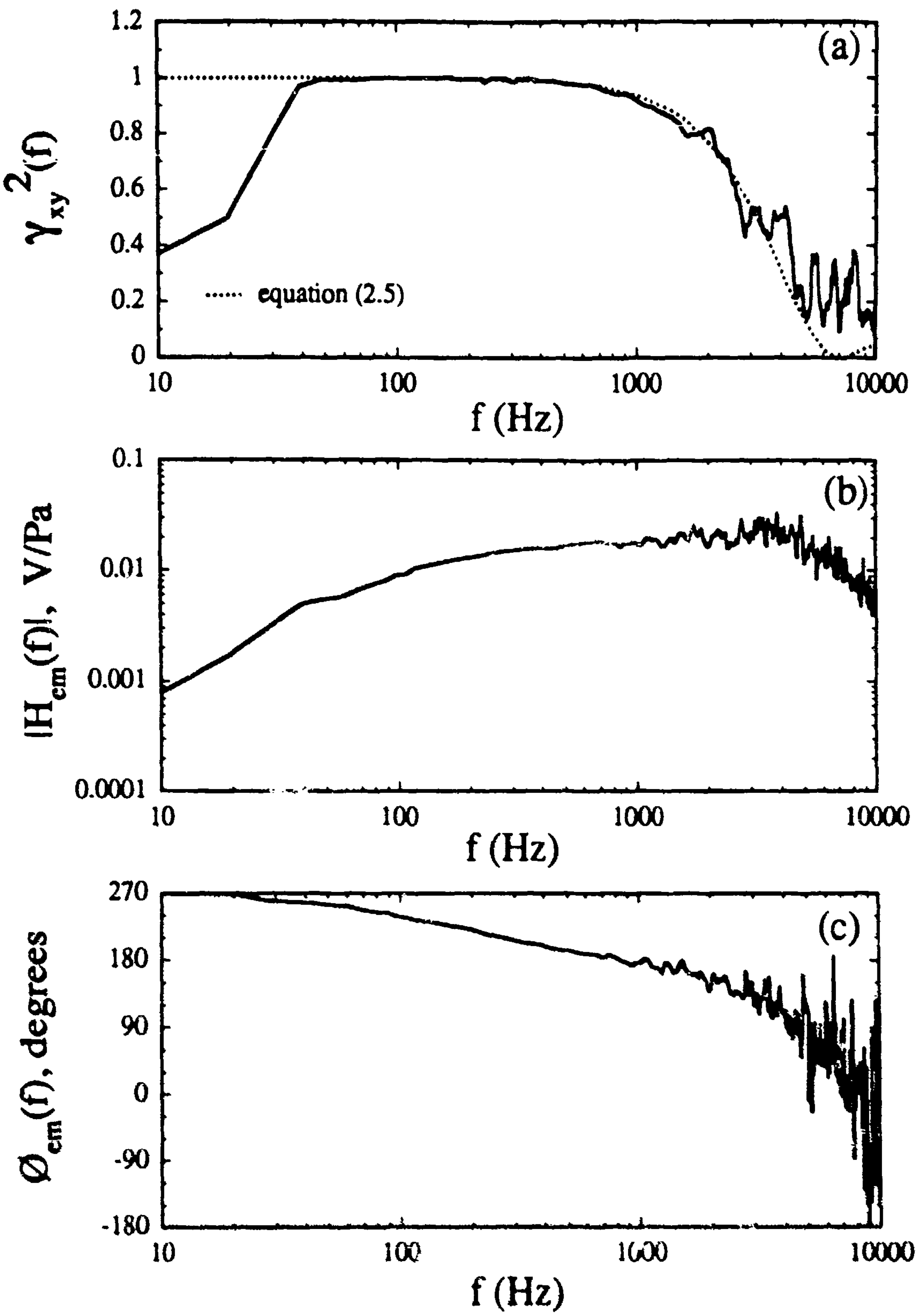

Figure 2-8. Typical diffuse-field comparison calibration results between EM-3068 test and Bruel and Kjaer reference microphones: (a), coherence between test and reference microphones compared to that for a purely diffuse sound field; (b) EM-3068 microphone sensitivity; (c), EM-3068 microphone phase.

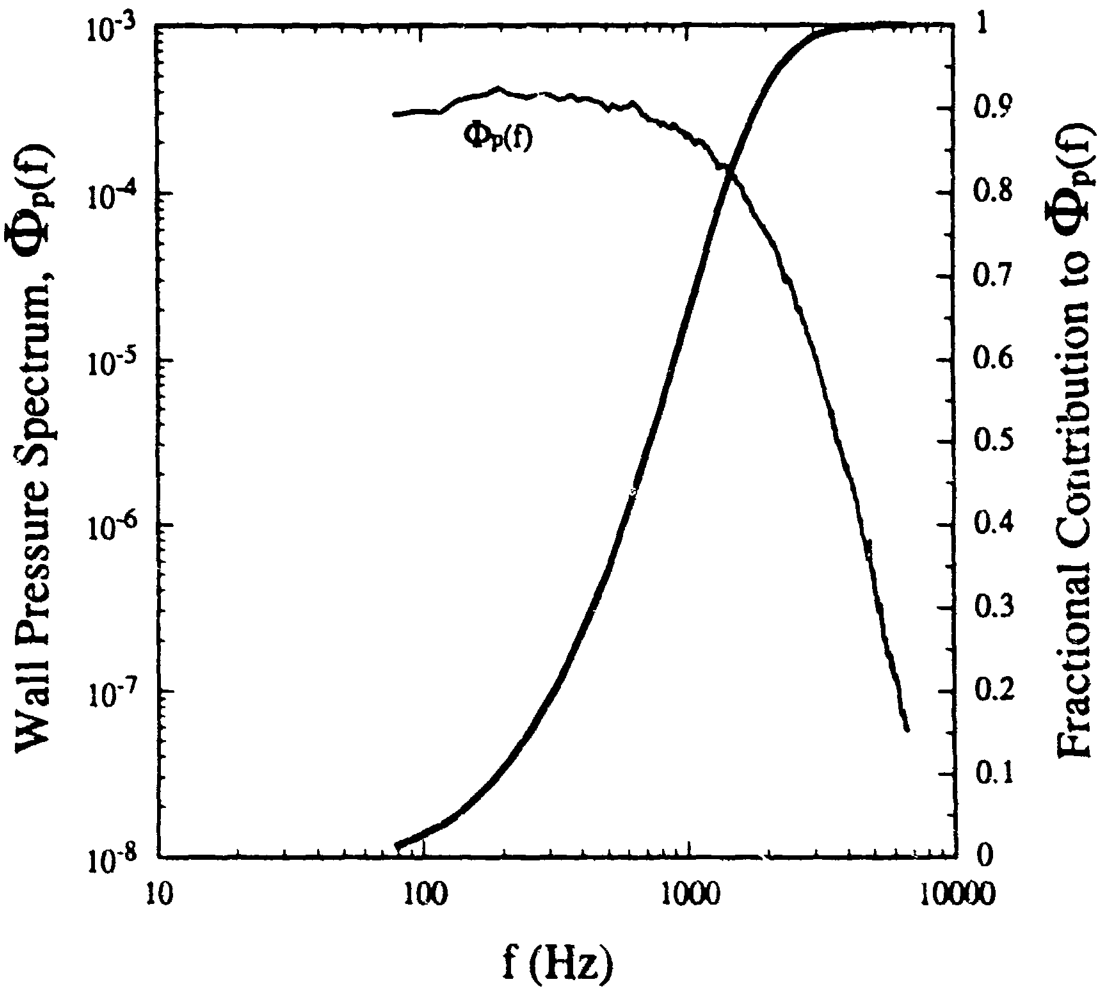

Figure 2-9. Frequency range over which fluctuating wall pressure energy is distributed and accurate sensitivity and phase calibrations are required: plain line, power spectral density of the fluctuating wall pressure on the cylinder; bold line, fractional contribution to the total wall pressure energy as a function of frequency.

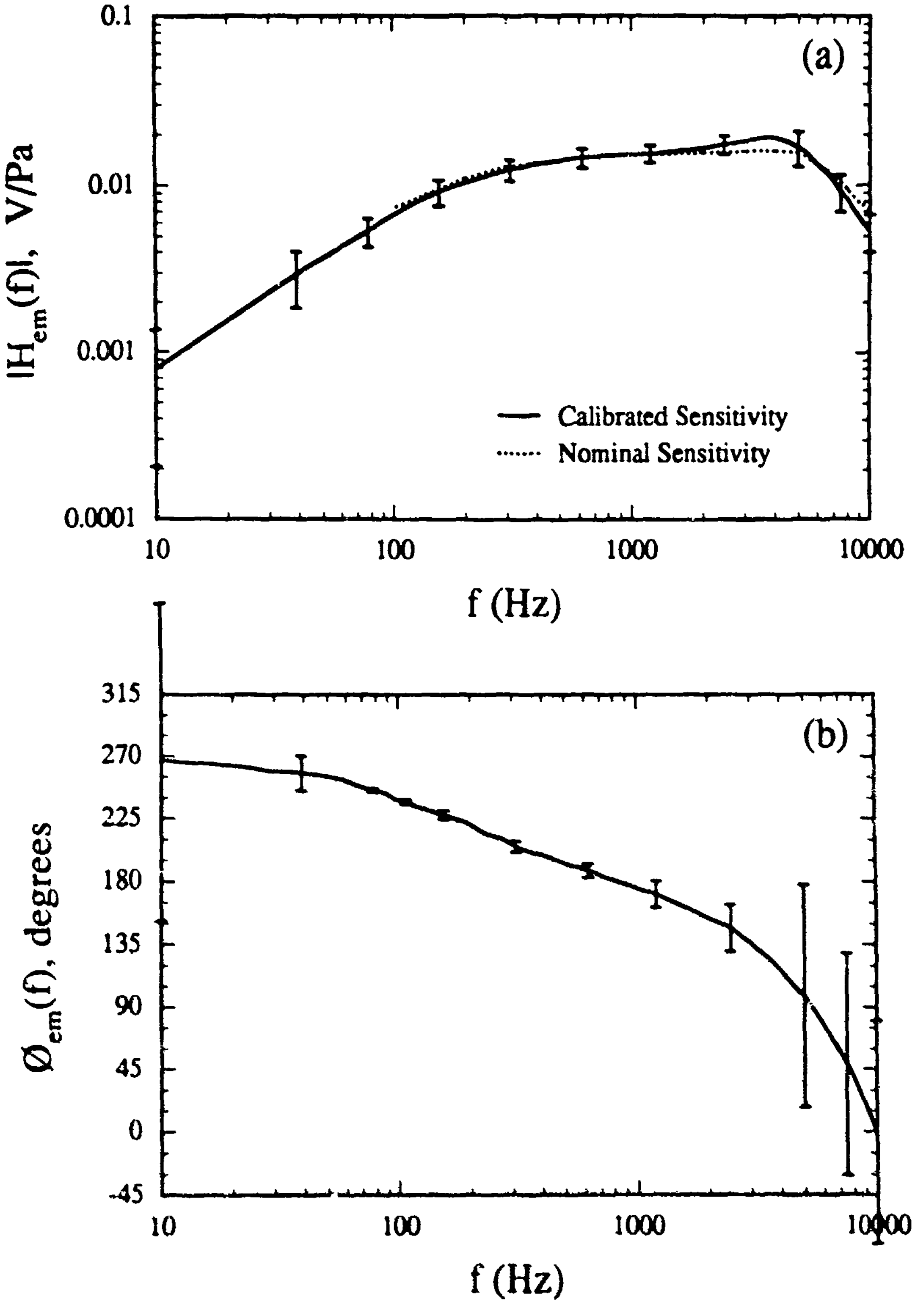

Figure 2-10. Calibrated frequency response curves for the Knowles EM-3068 electret microphone: (a), sensitivity; (b), phase. Error bars represent $\pm\sigma$.

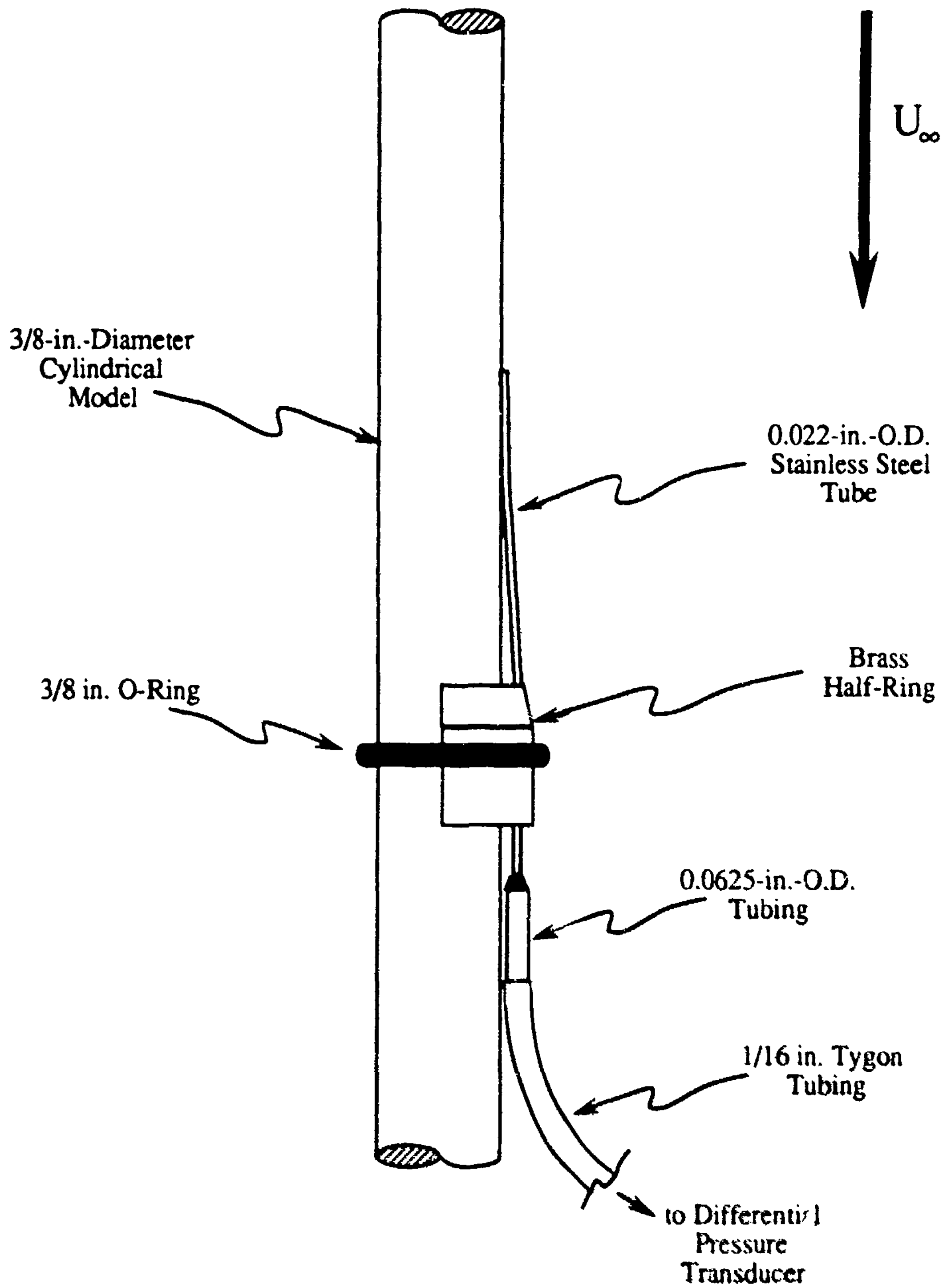

Figure 2-11. Schematic of Preston tube used to measure wall shear stress on cylinder.

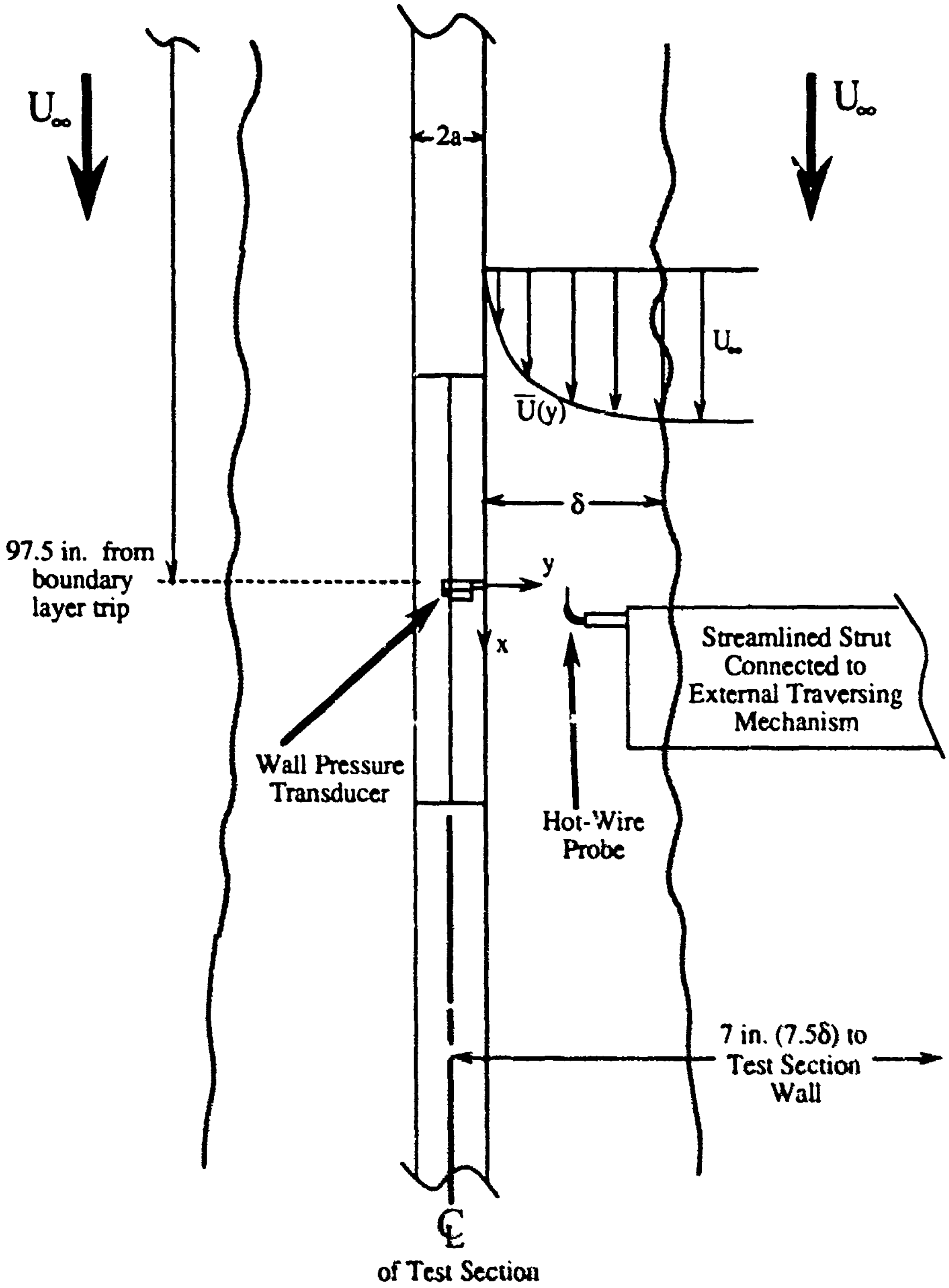

Figure 2-12. Schematic illustrating flow geometry and typical measurement configuration of wall pressure transducer and hot-wire probe, $\delta/a=5.04$.

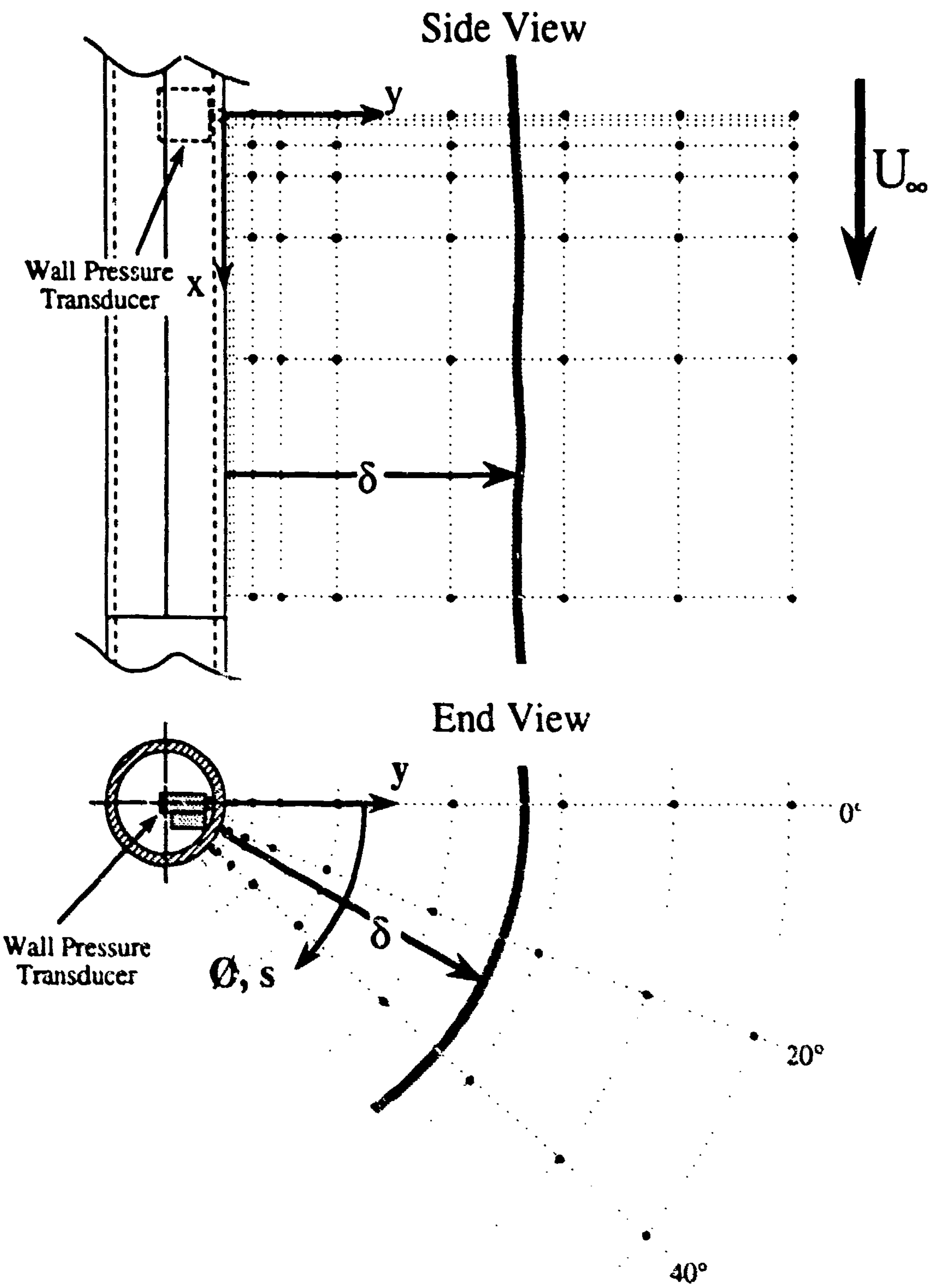

Figure 2-13. Schematic illustrating measurement locations of hot-wire probe in relation to wall pressure transducer. See Table 2-1 for separation distances of measurement points.

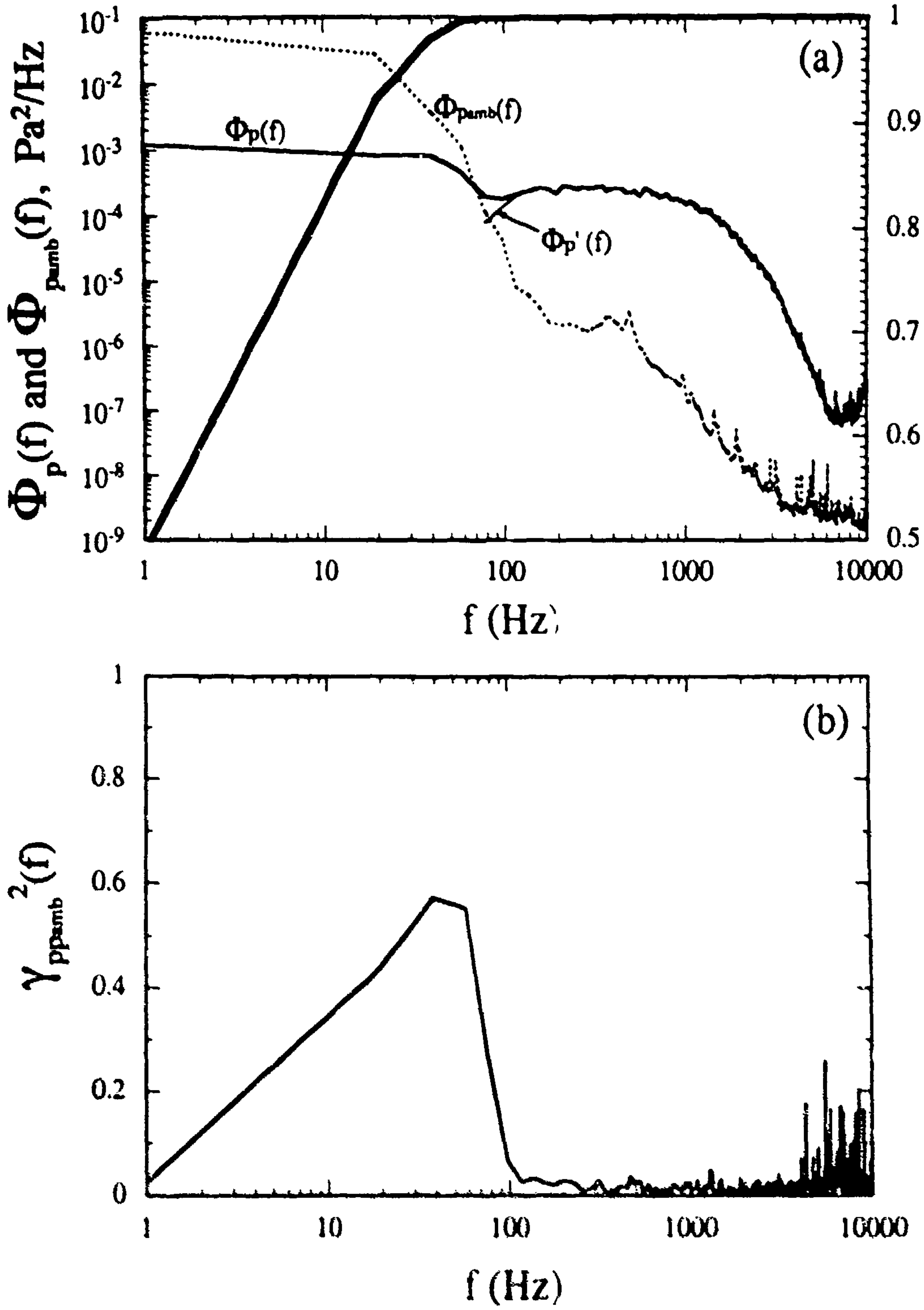

Figure 3-1. Ambient sound field in test section (U_∞=11.4 m/s): (a), power spectral density relative to that for fluctuating wall pressure on cylinder (bold line, fractional contribution to total ambient sound energy); (b), coherence between ambient sound and wall pressure.

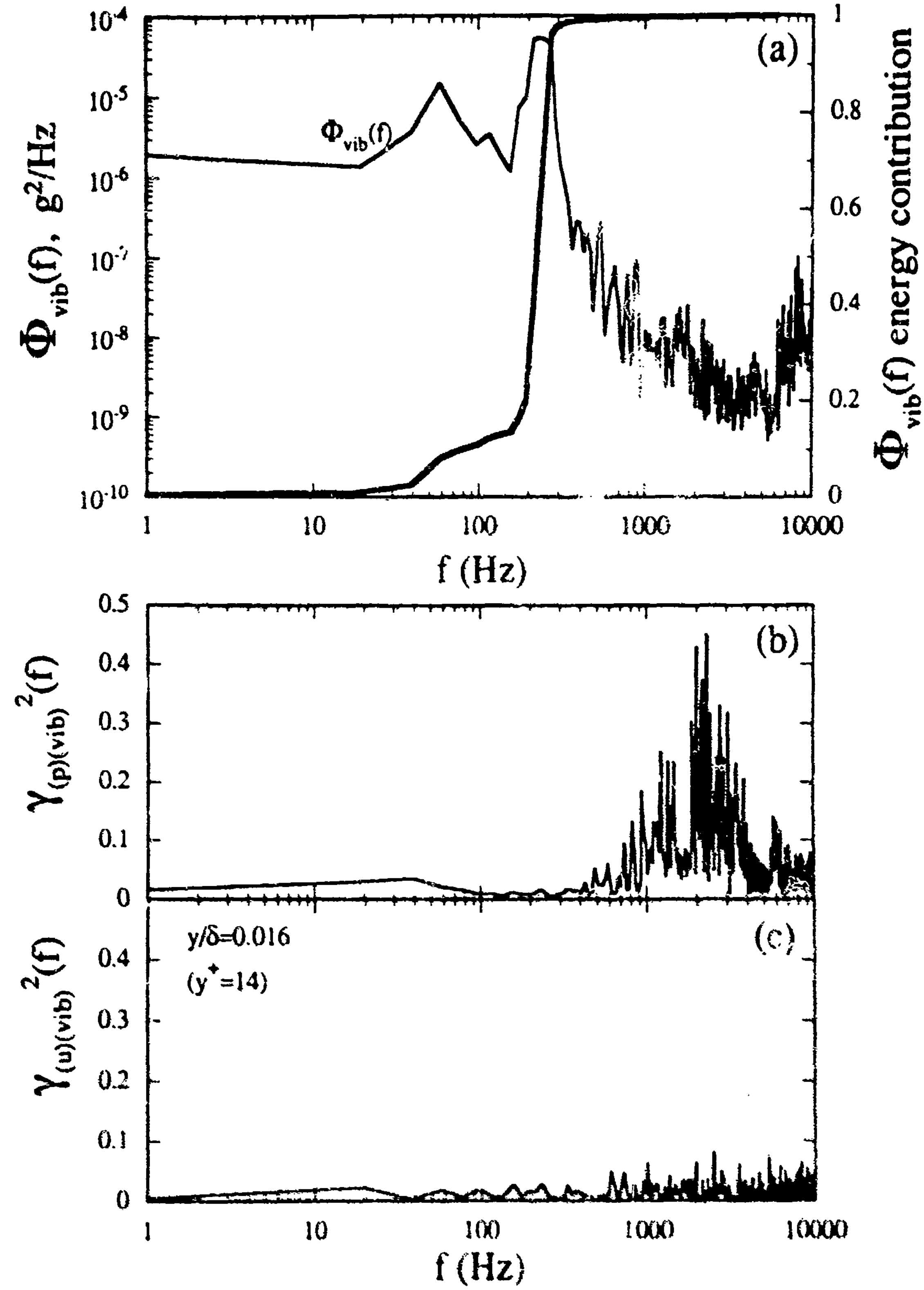

Figure 3-2. Cylinder vibration (U_∞=11.4 m/s): (a), power spectral density (bold line, fractional contribution to total vibrational energy); (b), coherence between wall pressure and cylinder vibration; (c), coherence between near-wall velocity and cylinder vibration.

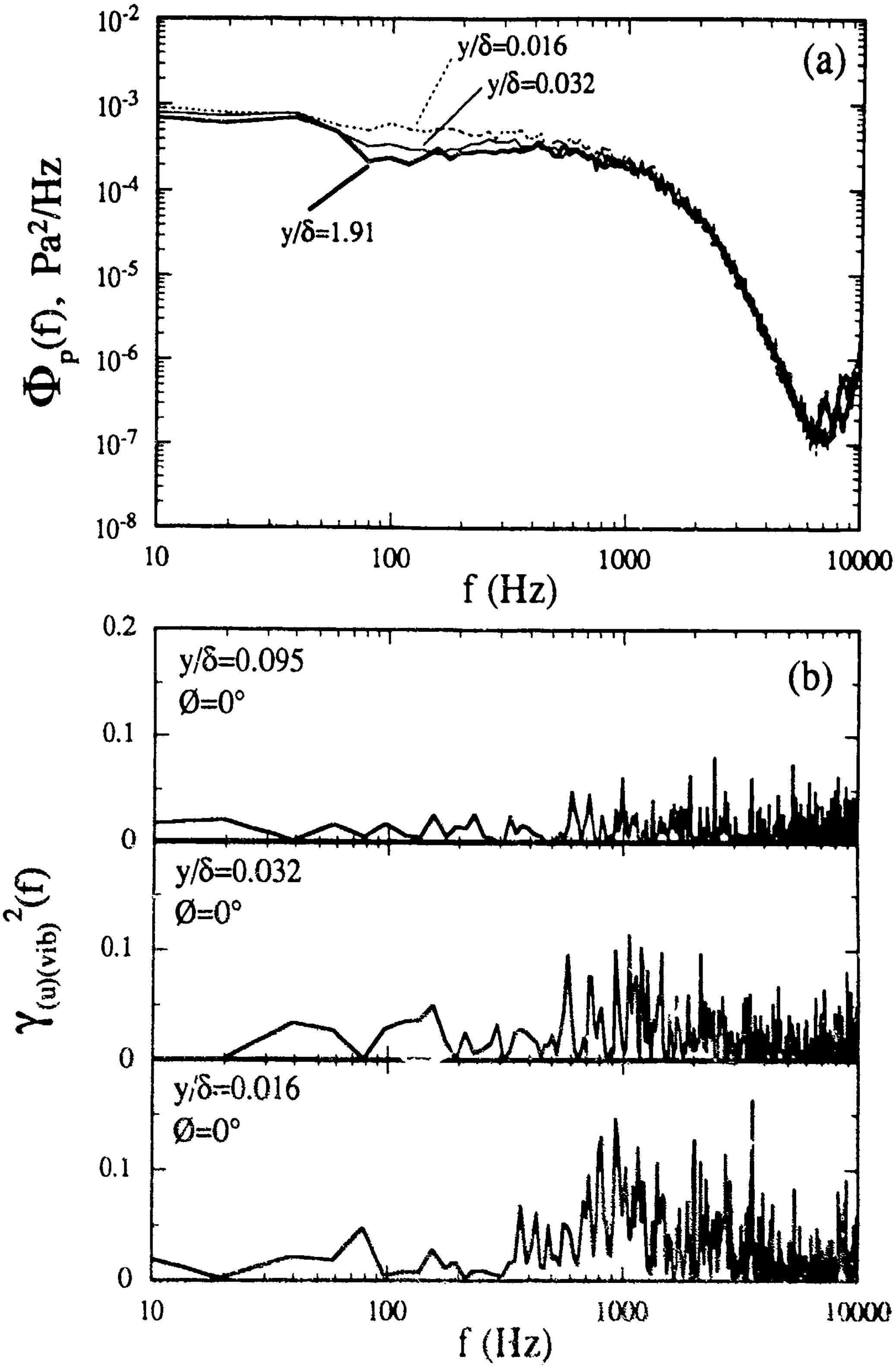

Figure 3-3. Hot-wire/microphone interference with hot wire at various positions above microphone: (a), wall pressure spectra; (b), velocity-vibration coherence.

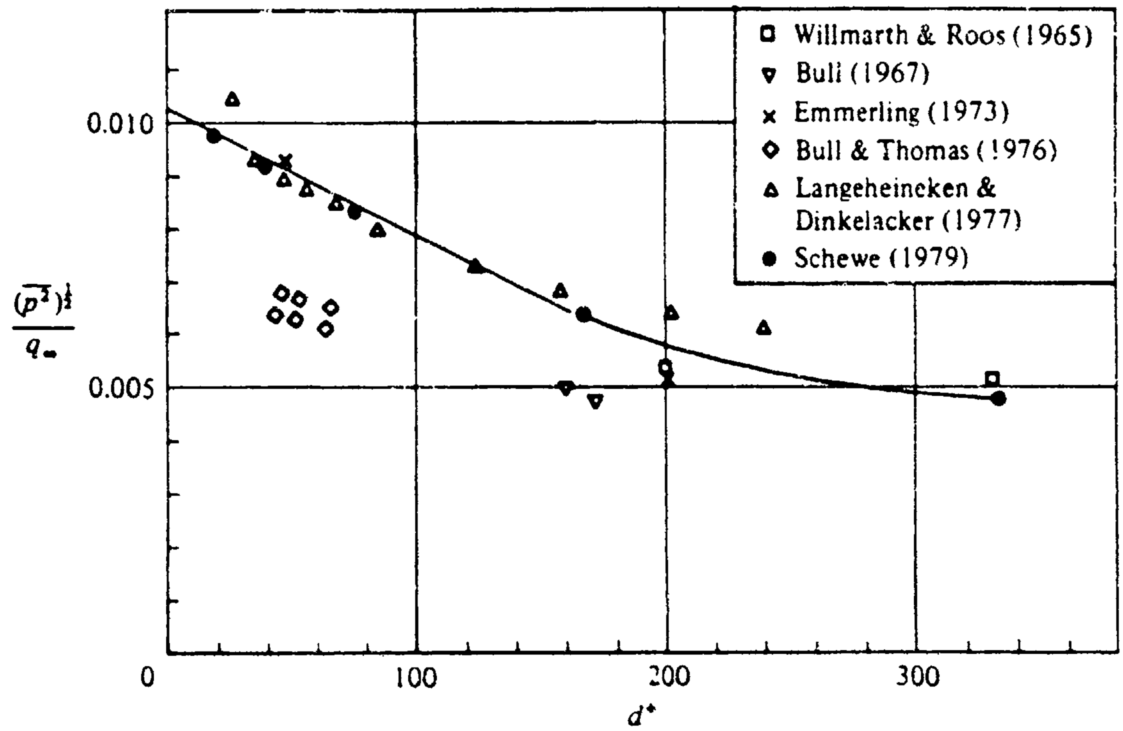

Figure 3-4. Dependence of rms wall pressure on transducer diameter scaled on inner variables (planar boundary layer). From Schewe (1983).

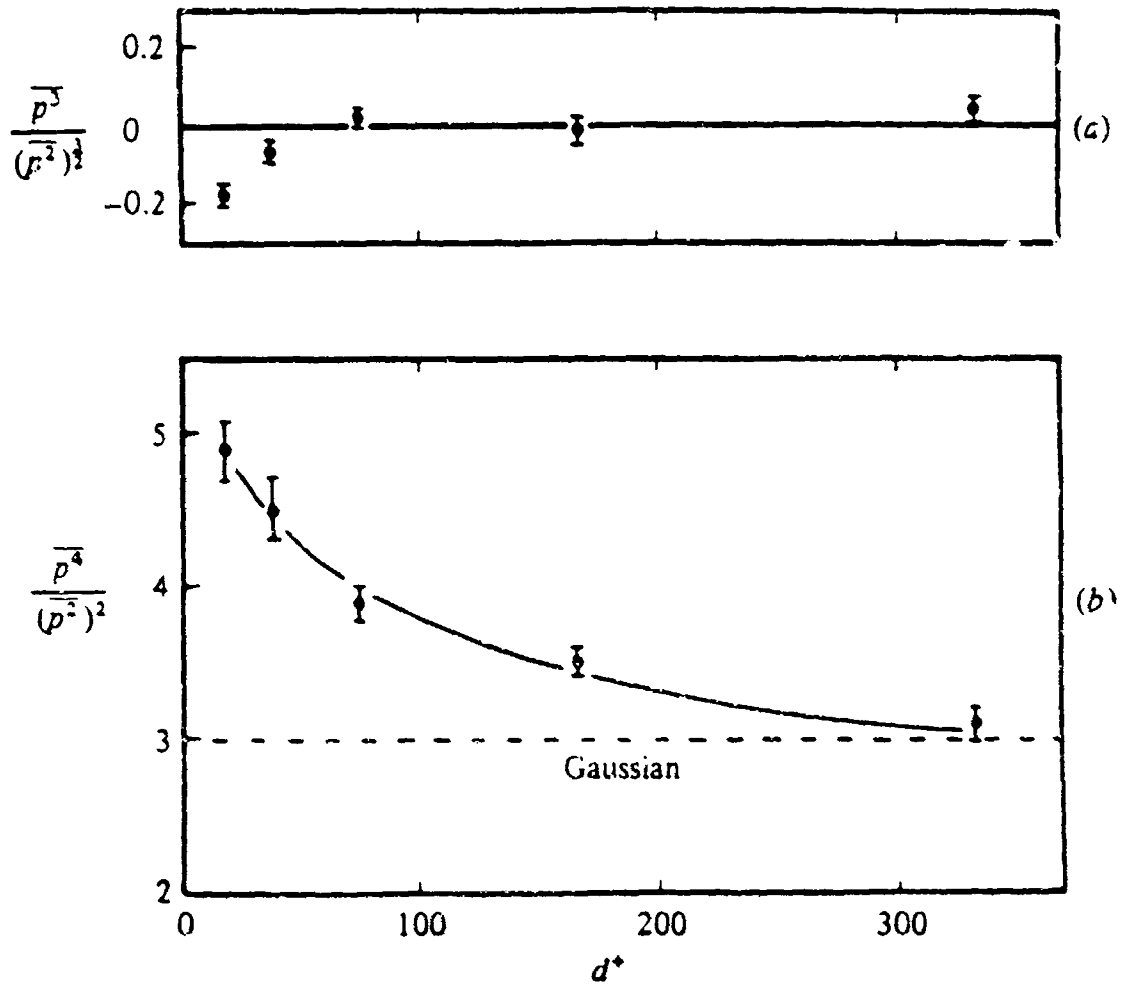

Figure 3-5. Dependence of fluctuating wall pressure (a) skewness and (b) flatness on transducer diameter scaled on inner variables (planar boundary layer). From Schewe (1983).

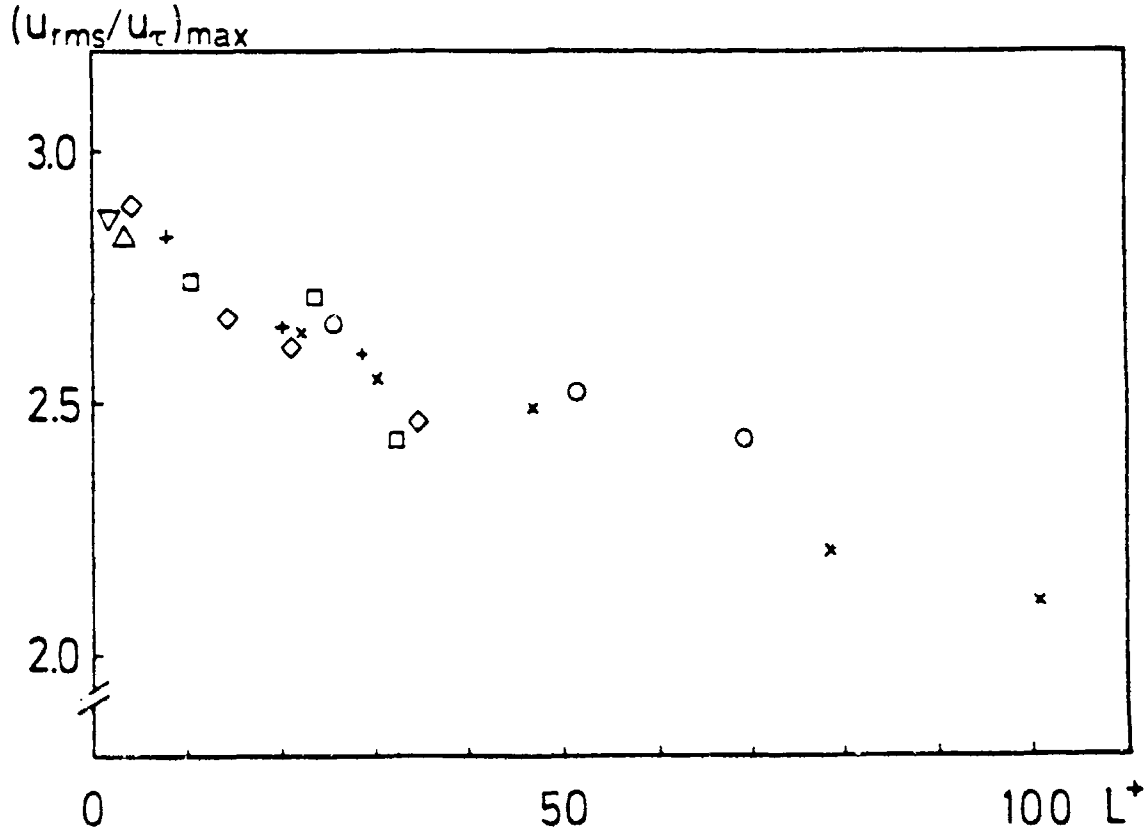

Figure 3-6. Dependence of maximum turbulence intensity on hot-wire probe length scaled on inner variables (planar boundary layer). From Johansson and Alfredsson (1983).

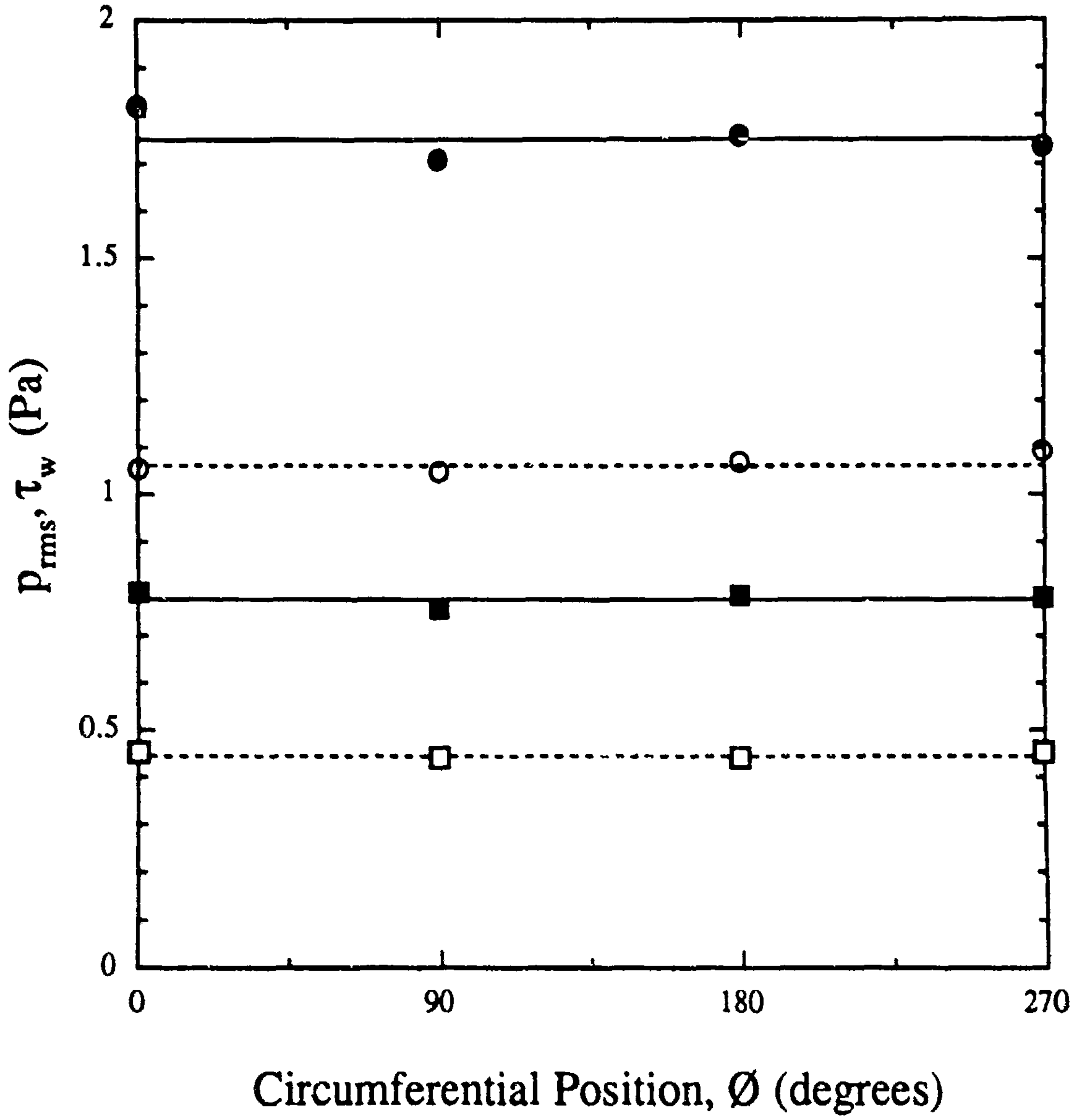

Figure 3-7. Boundary layer axisymmetry as measured by symmetry of wall shear stress and wall pressure around cylinder. U_∞=14.4 m/s: ○, p_{rms}; □, τ_w. U_∞=18.5 m/s: ●, p_{rms}; ■, τ_w.

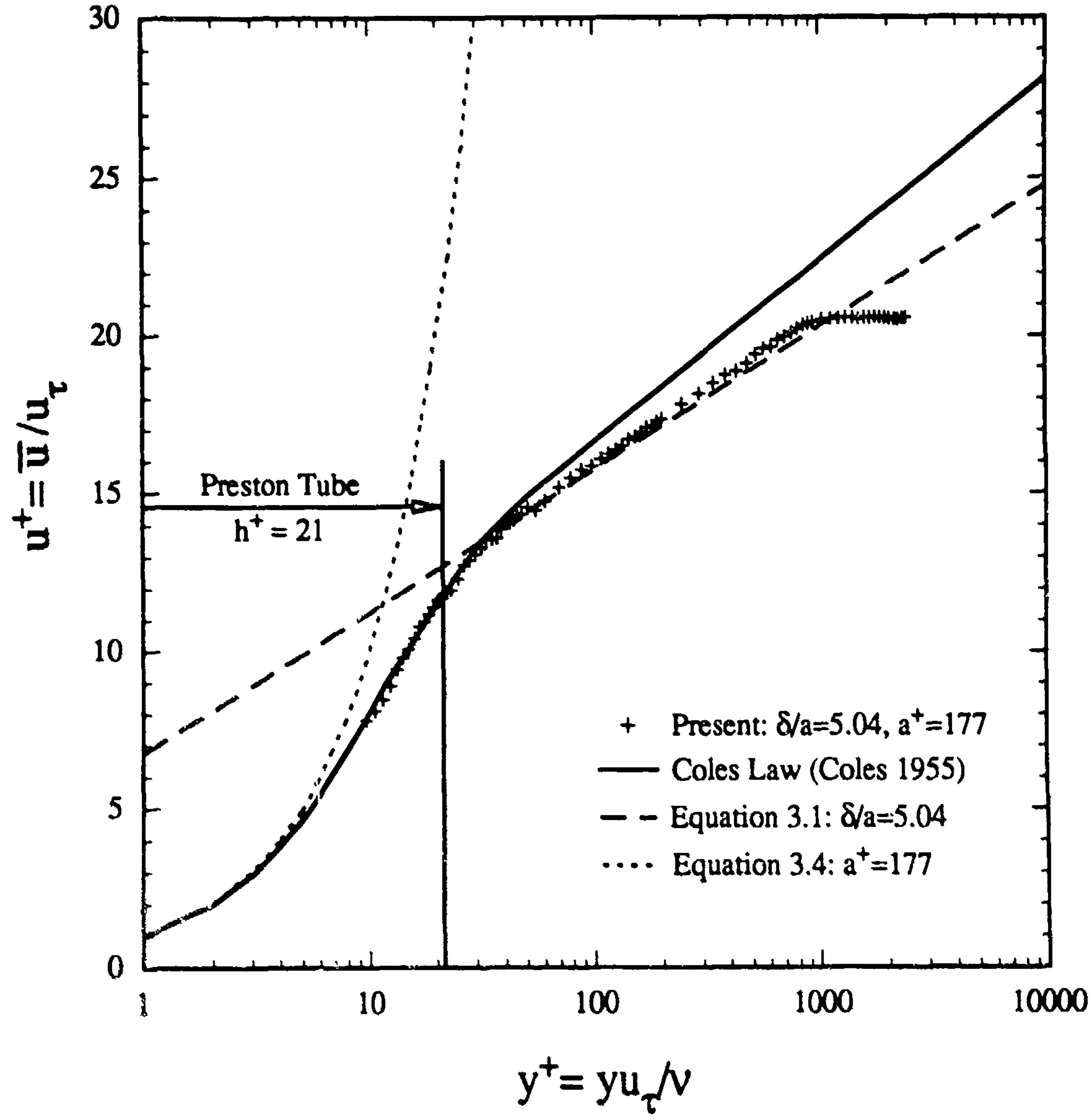

Figure 3-8. Mean velocity profile for the cylindrical boundary layer used in this investigation scaled on inner variables, U_∞=11.4 m/s. Relative height of Preston tube (h^+=21) used for wall shear stress measurements is indicated.

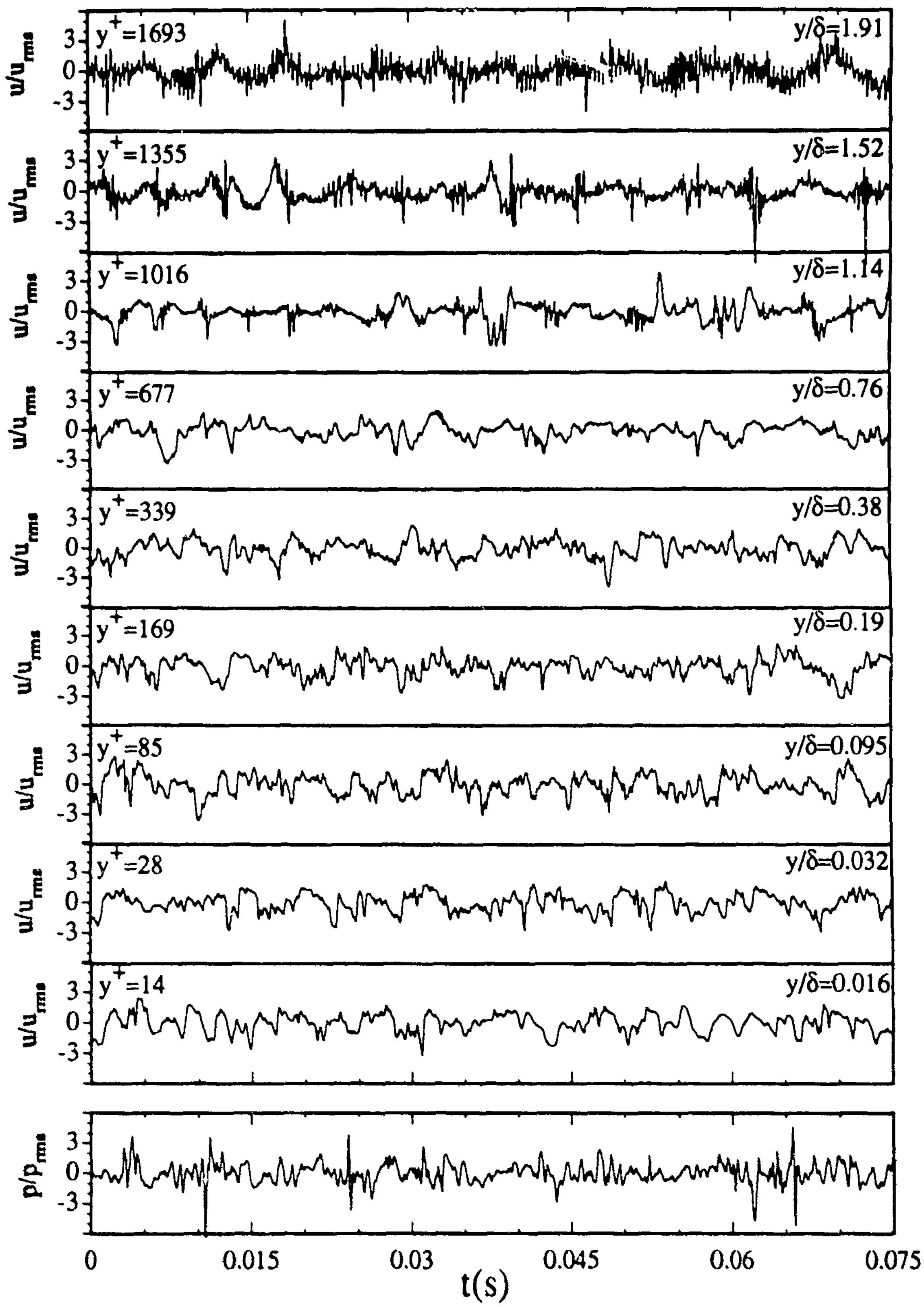

Figure 4-1. Segments of temporal records for fluctuating wall pressure and streamwise velocities at nine wall-normal positions measured. Data records are digitally band pass filtered ($59 \leq f \leq 5332$ Hz). None of the data sets are synchronized.

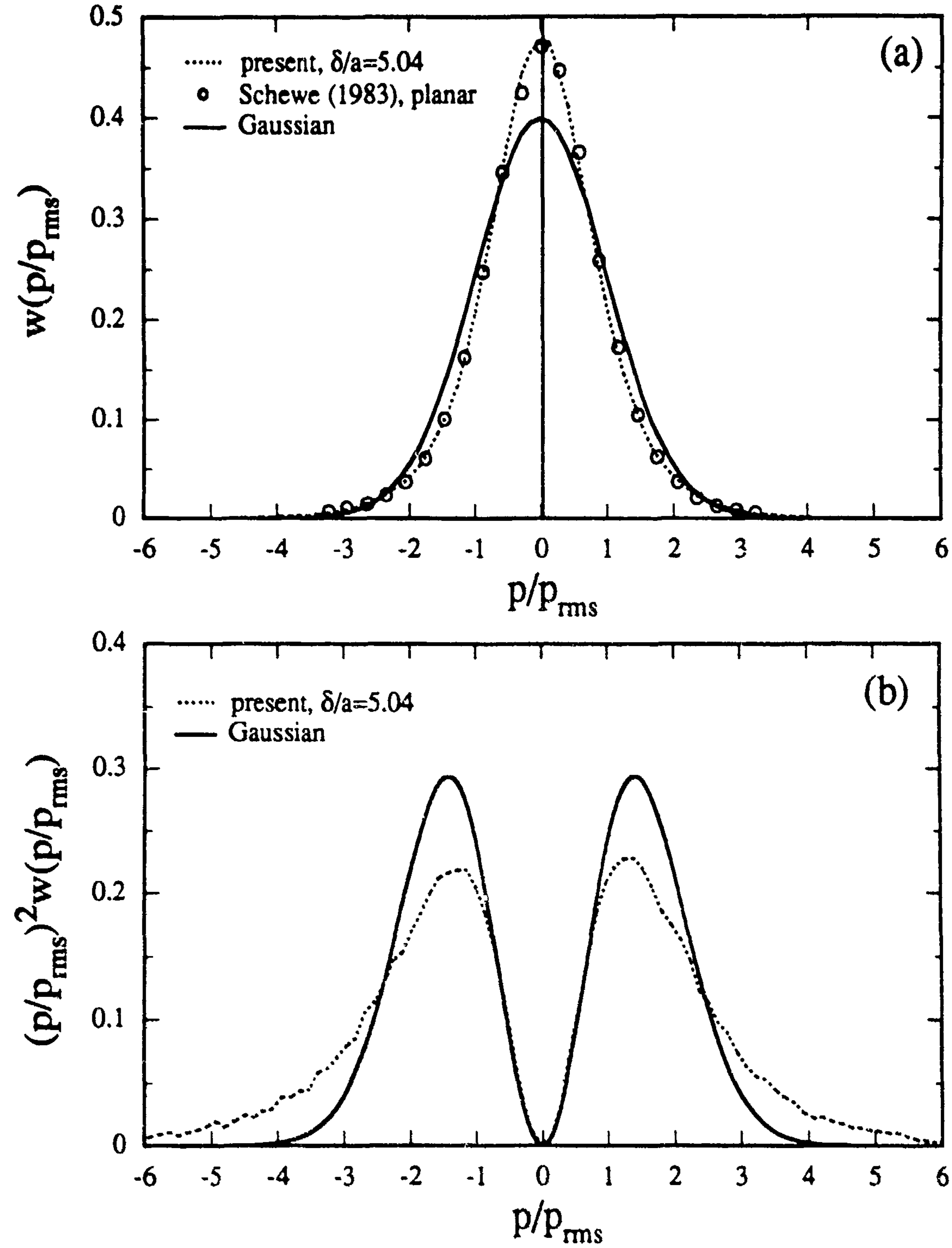

Figure 4-2. Probability density of wall pressure fluctuations: (a), compared to planar boundary layer; (b), weighted by mean square energy level of fluctuation amplitude giving fractional contribution to the mean square energy for a particular fluctuation level.

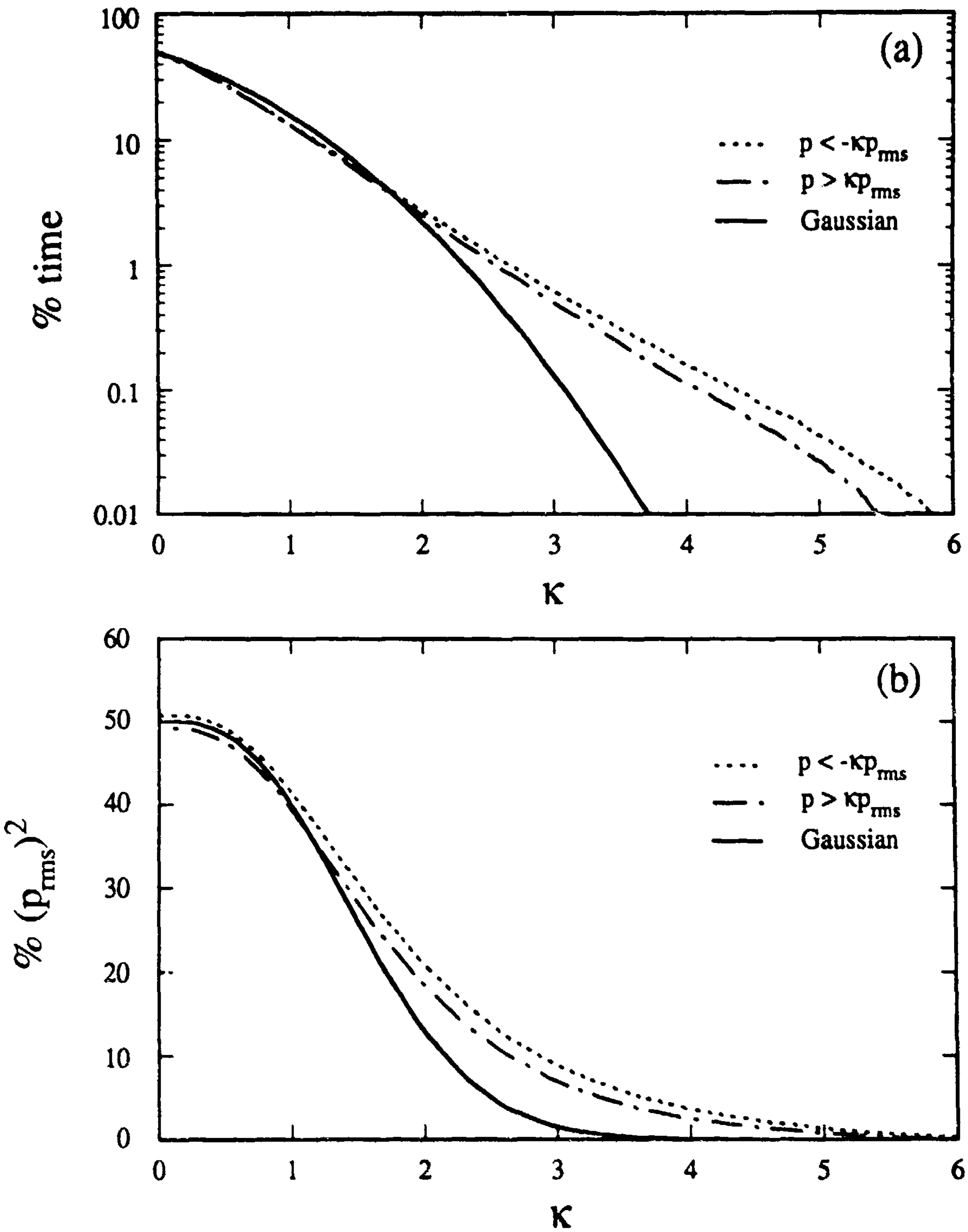

Figure 4-3. Percent contribution of positive and negative wall pressure fluctuations that exceed a threshold level $|\kappa p_{rms}|$ to (a) total time of signal and (b) total mean square energy.

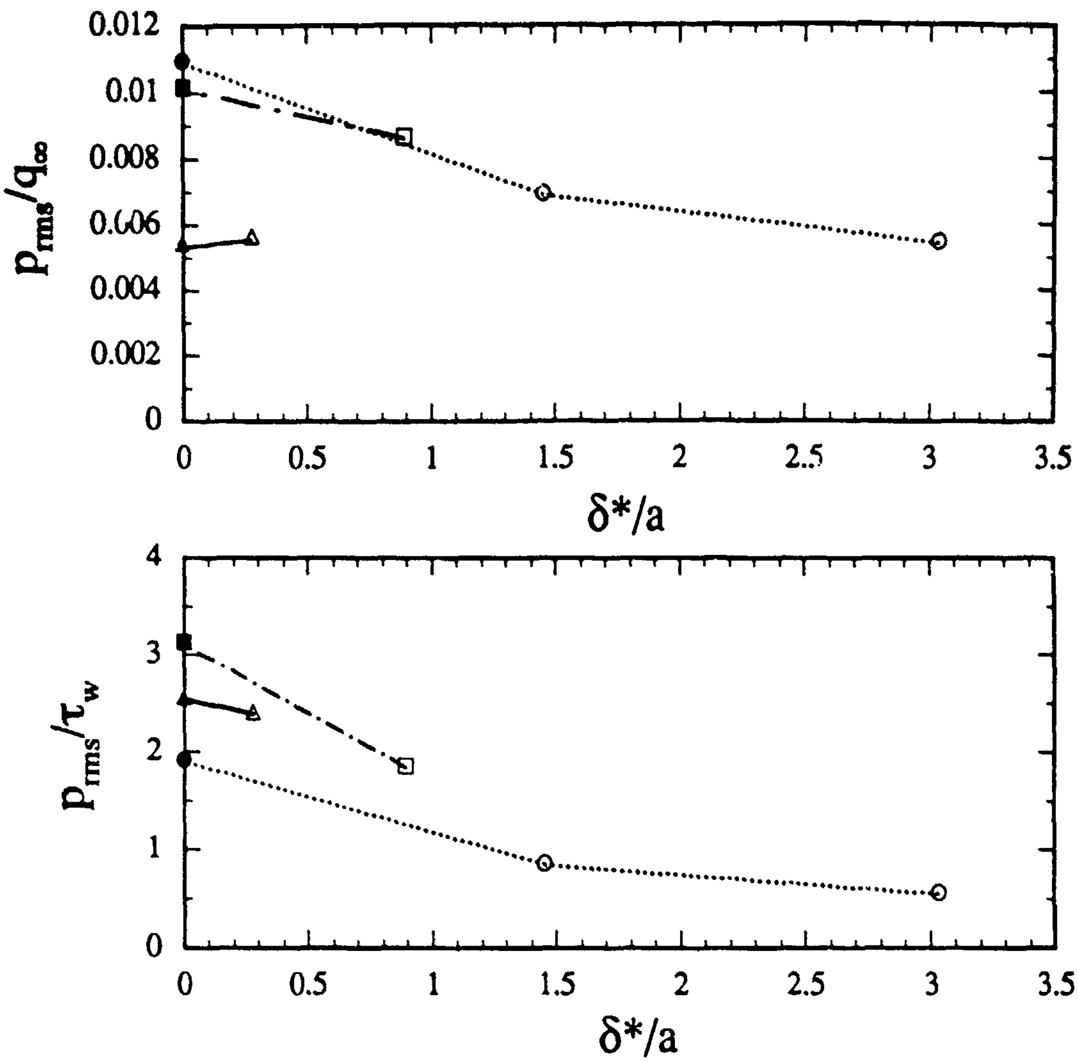

	Investigation	Reθ	d/δ*	d+	d*	mic type
—·—·	□ present	2870	0.164	25.9	1.25	pinhole
	■ Farabee (1986)	3400	0.177	32.8	1.32	pinhole
——	△ Willmarth & Yang (1970)	26200	0.143	158	5.42	flush
	▲ Willmarth & Roos (1965)	38000	0.122	203	6.62	flush
·······	○ Neves et al. (1991)	425	~0.17	~11	~0.57	numerical
	● Spalart (1988)	300	—	~13	—	numerical

Figure 4-4. Effect of transverse wall curvature on the rms wall pressure level: upper, nondimensionalized on free-stream dynamic pressure; lower, nondimensionalized on mean wall shear stress.

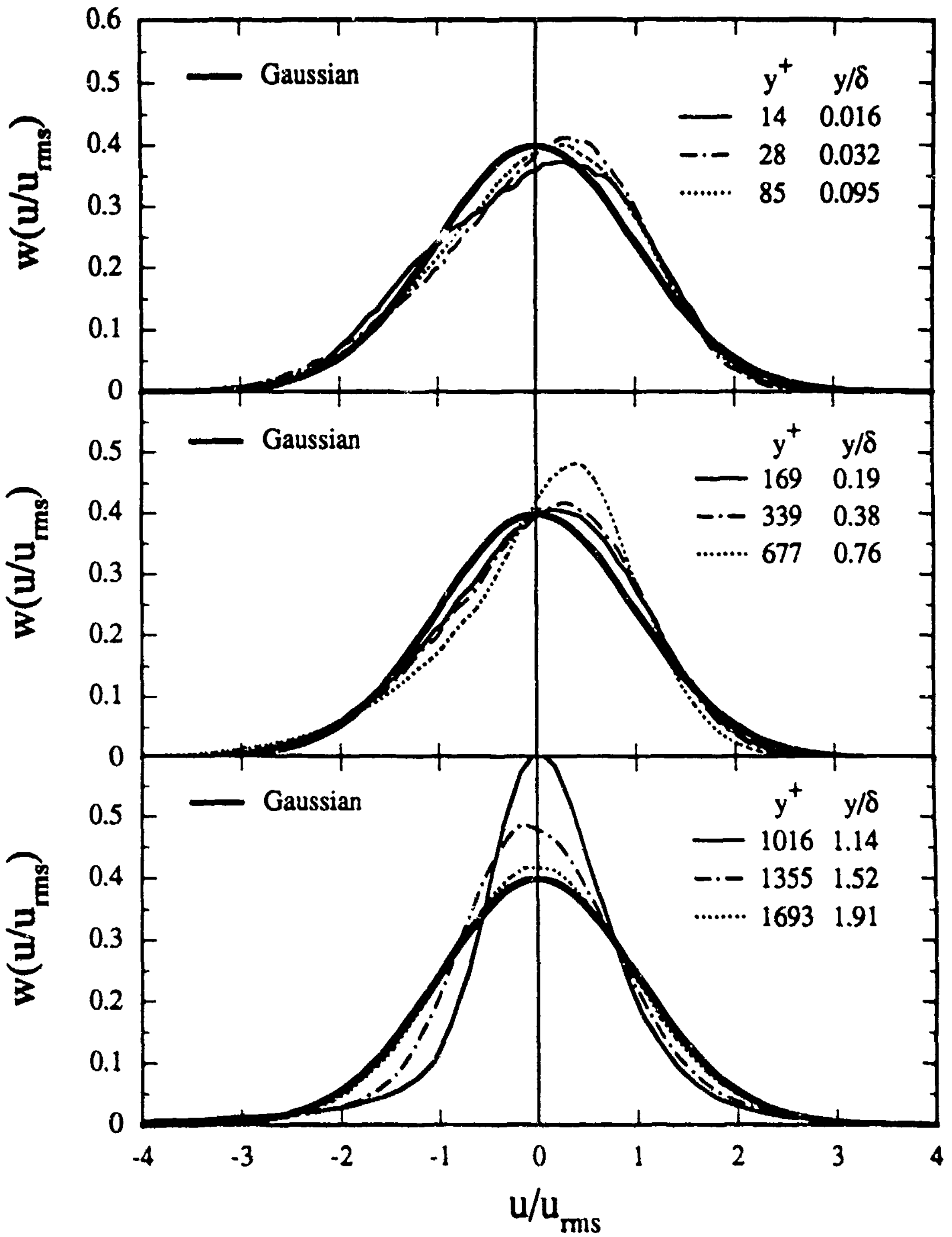

Figure 4-5. Probability density of the streamwise velocity fluctuations at the nine wall-normal positions of hot-wire probe used for this investigation.

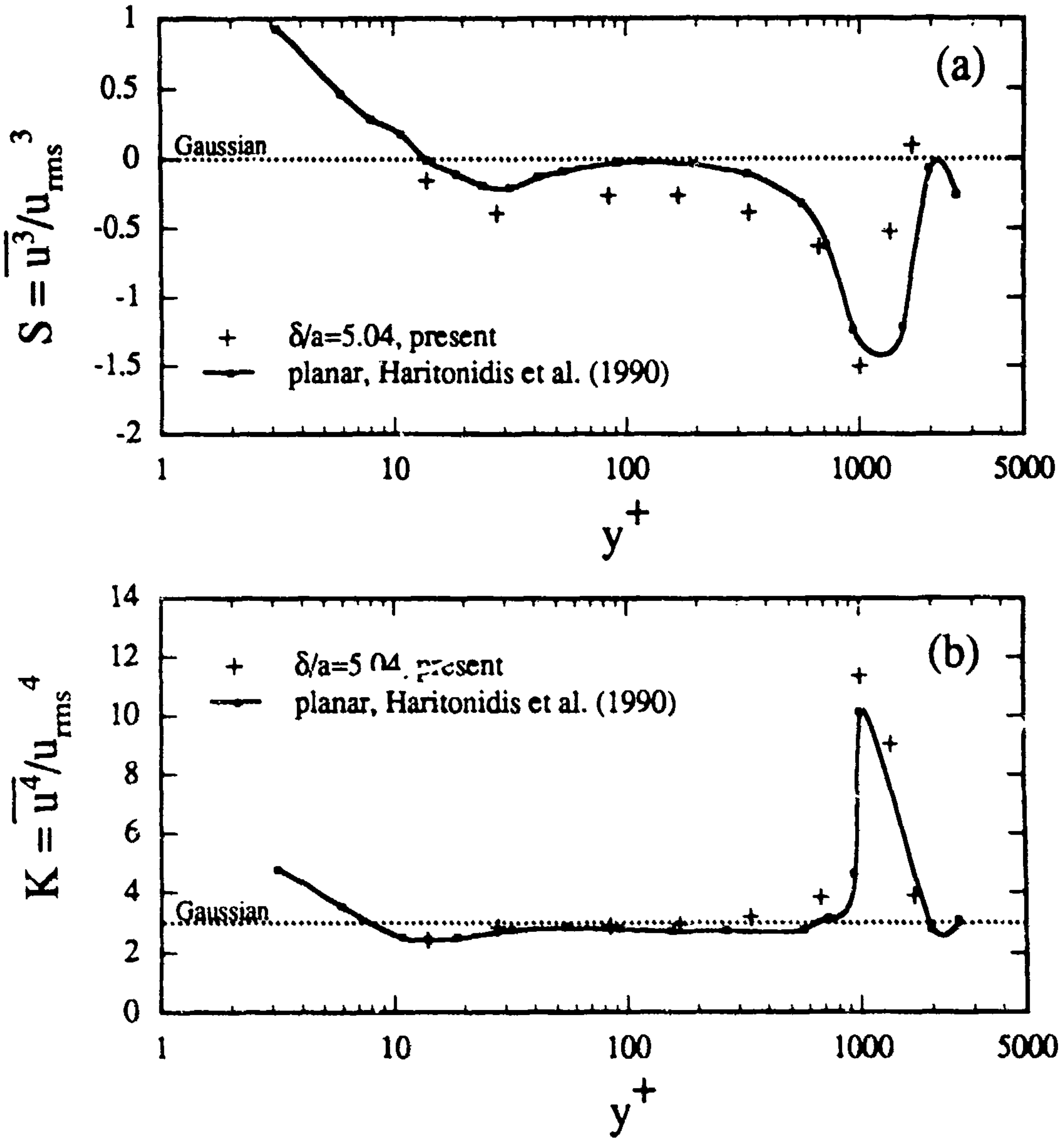

Figure 4-6. Comparison of streamwise velocity statistics across boundary layer in a cylindrical and planar boundary layer: (a), skewness; (b), flatness.

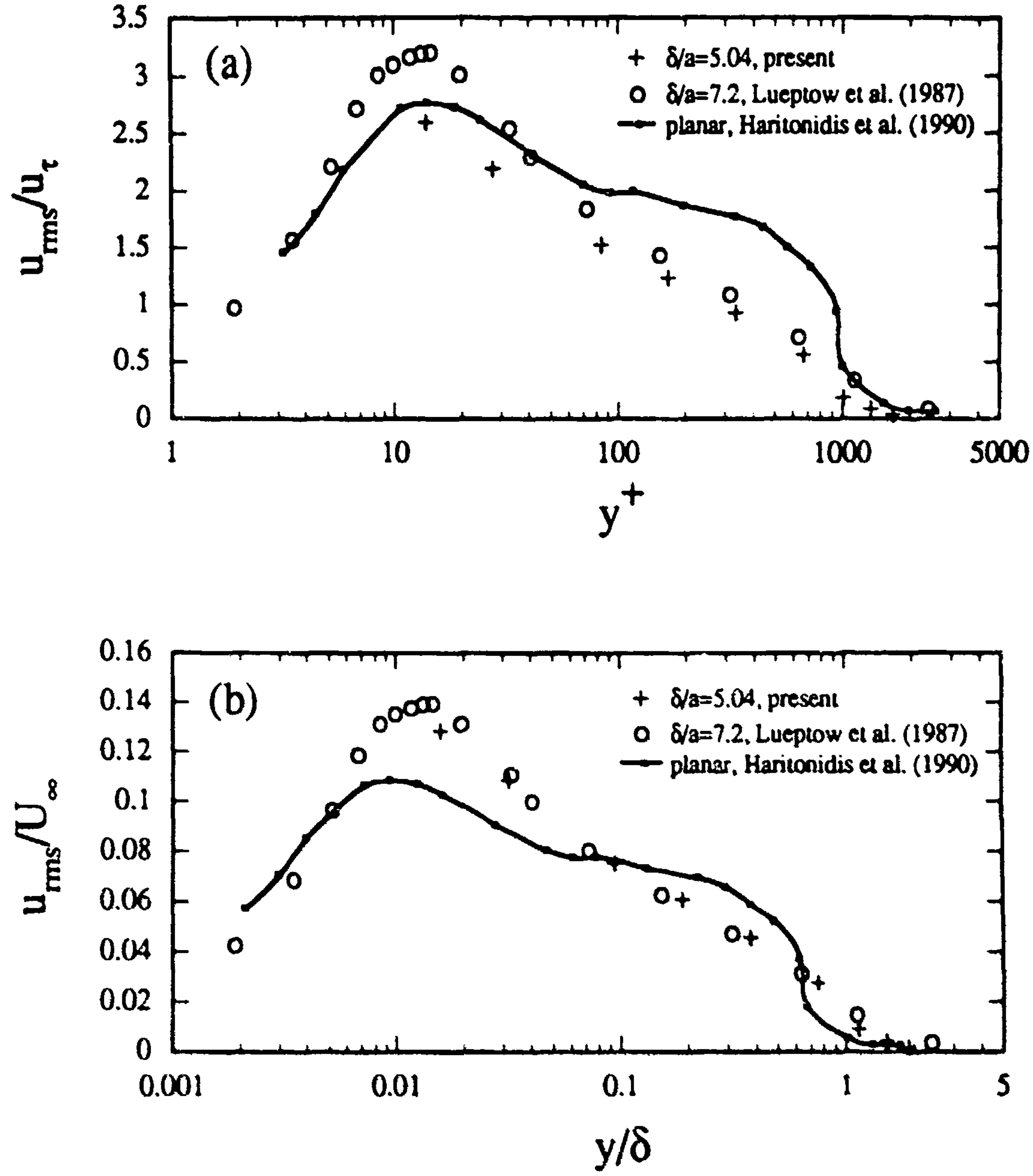

Figure 4-7. Comparison of streamwise turbulence intensities across boundary layer in a cylindrical and planar boundary layer: (a), inner variable scaling; (b), outer variable scaling.

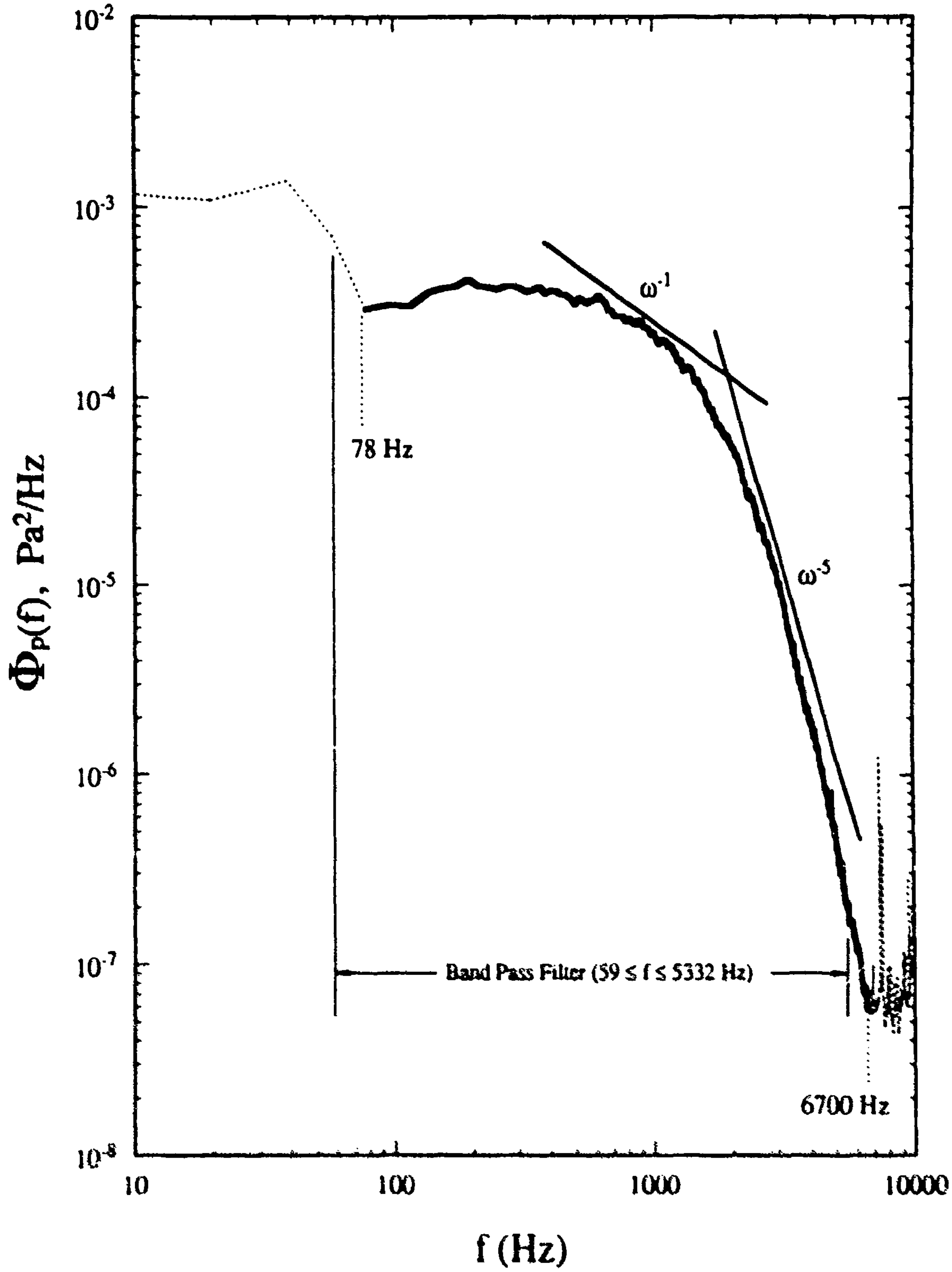

Figure 4-8. Power spectral density of the fluctuating wall pressure on cylinder. Dimensional coordinates.

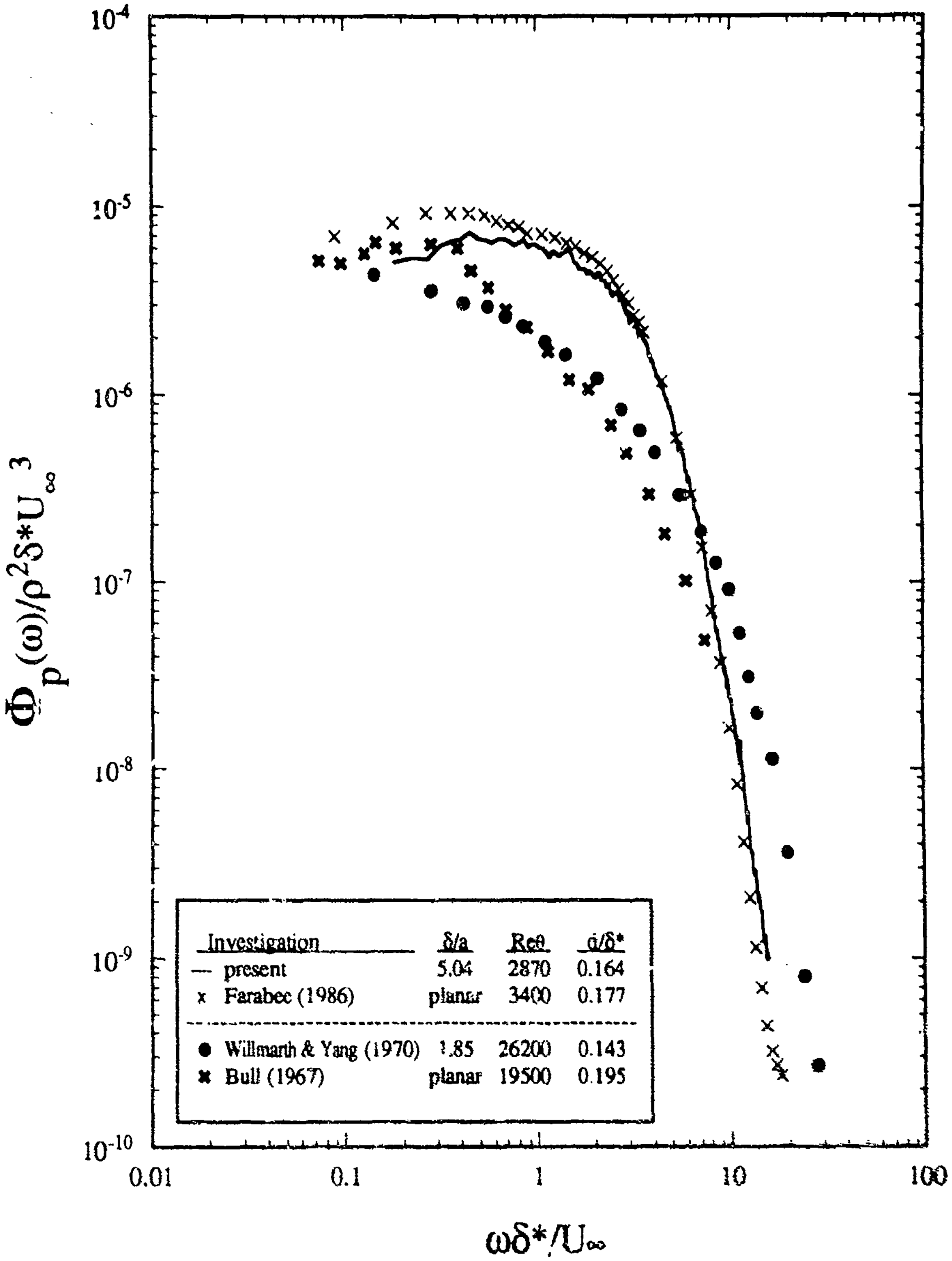

Figure 4-9. Comparison of fluctuating wall pressure spectra in cylindrical and planar boundary layers. Outer variable scaling.

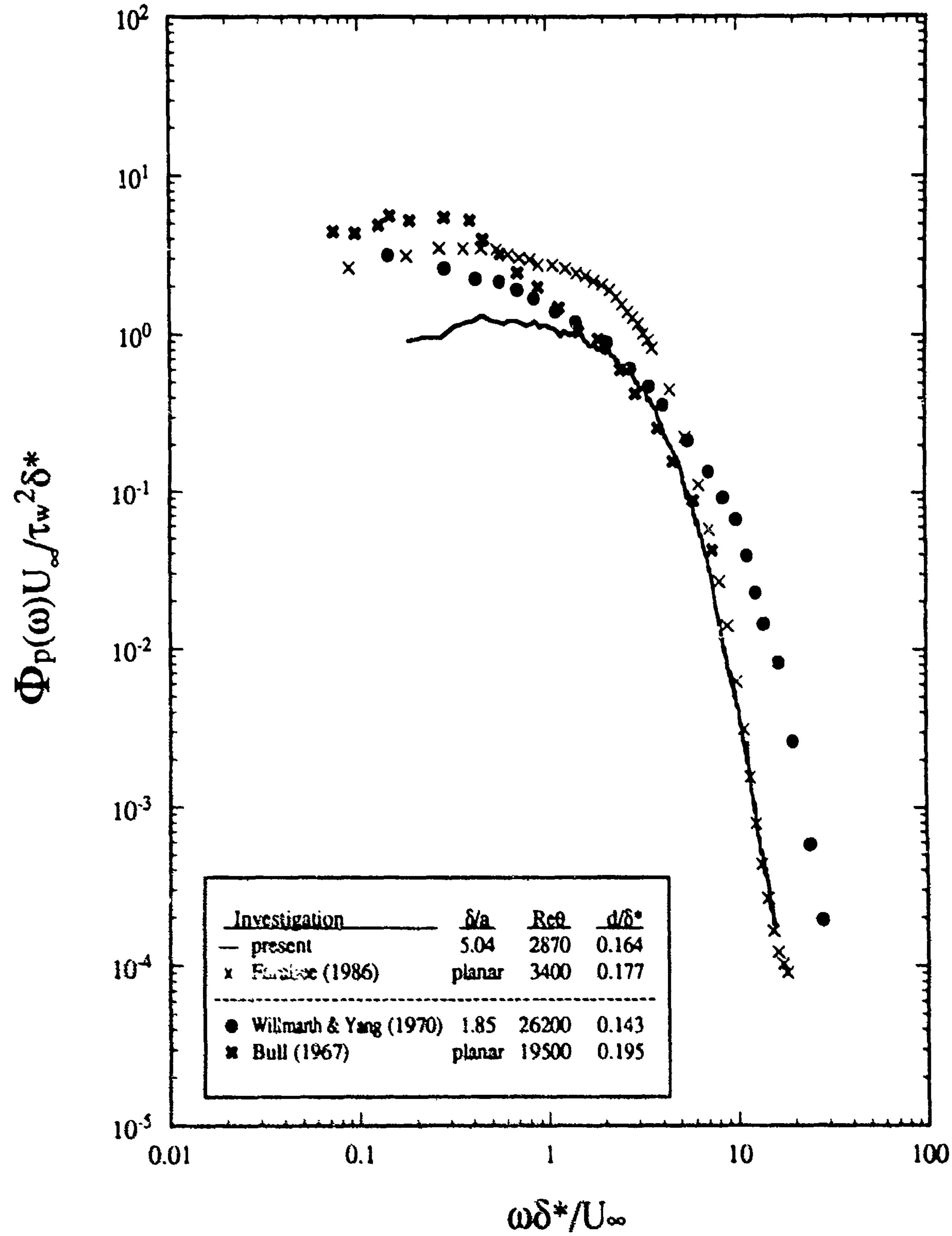

Figure 4-10. Comparison of fluctuating wall pressure spectra in cylindrical and planar boundary layers. Outer (mixed) variable scaling.

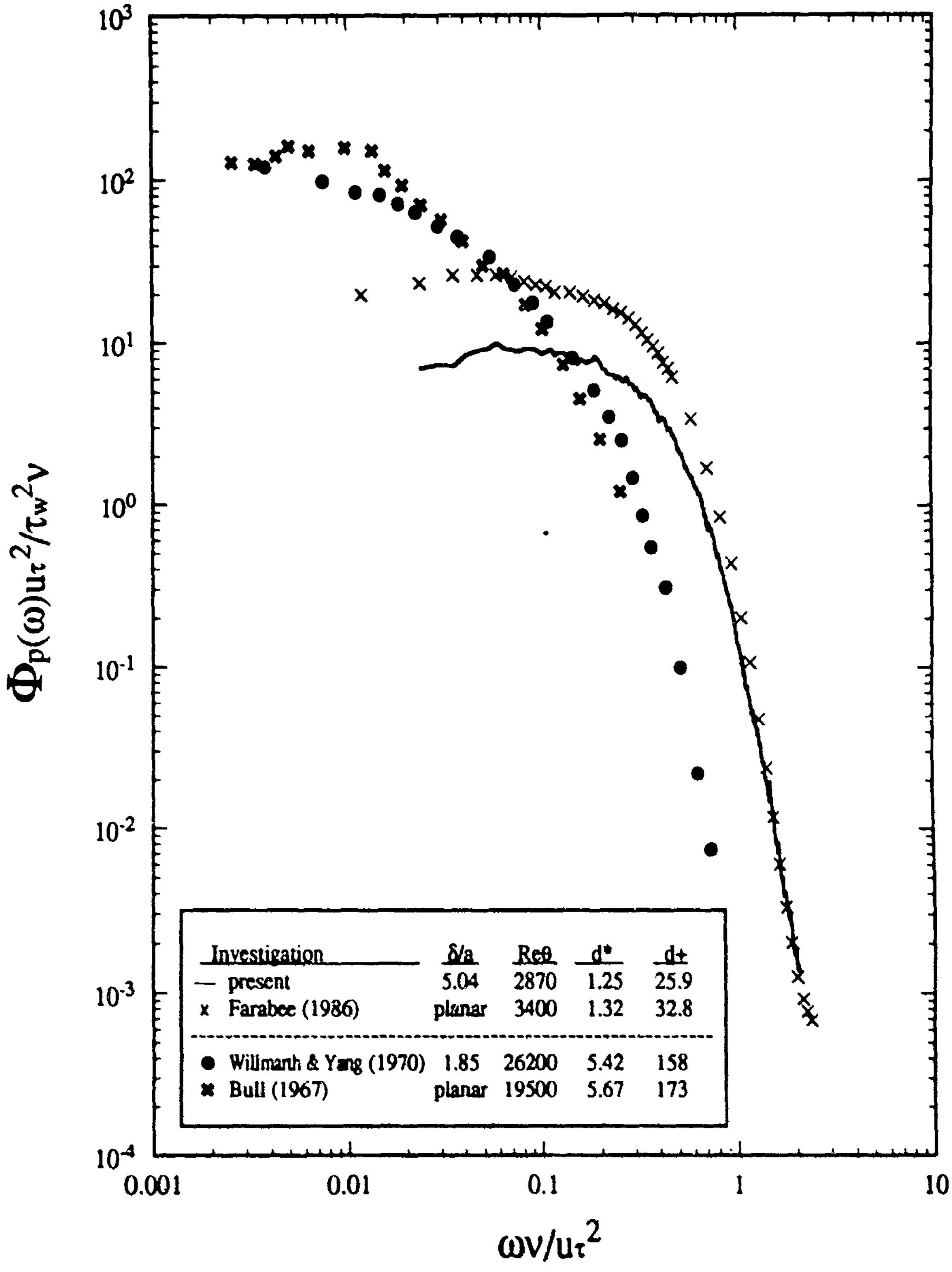

Figure 4-11. Comparison of fluctuating wall pressure spectra in cylindrical and planar boundary layers. Inner variable scaling.

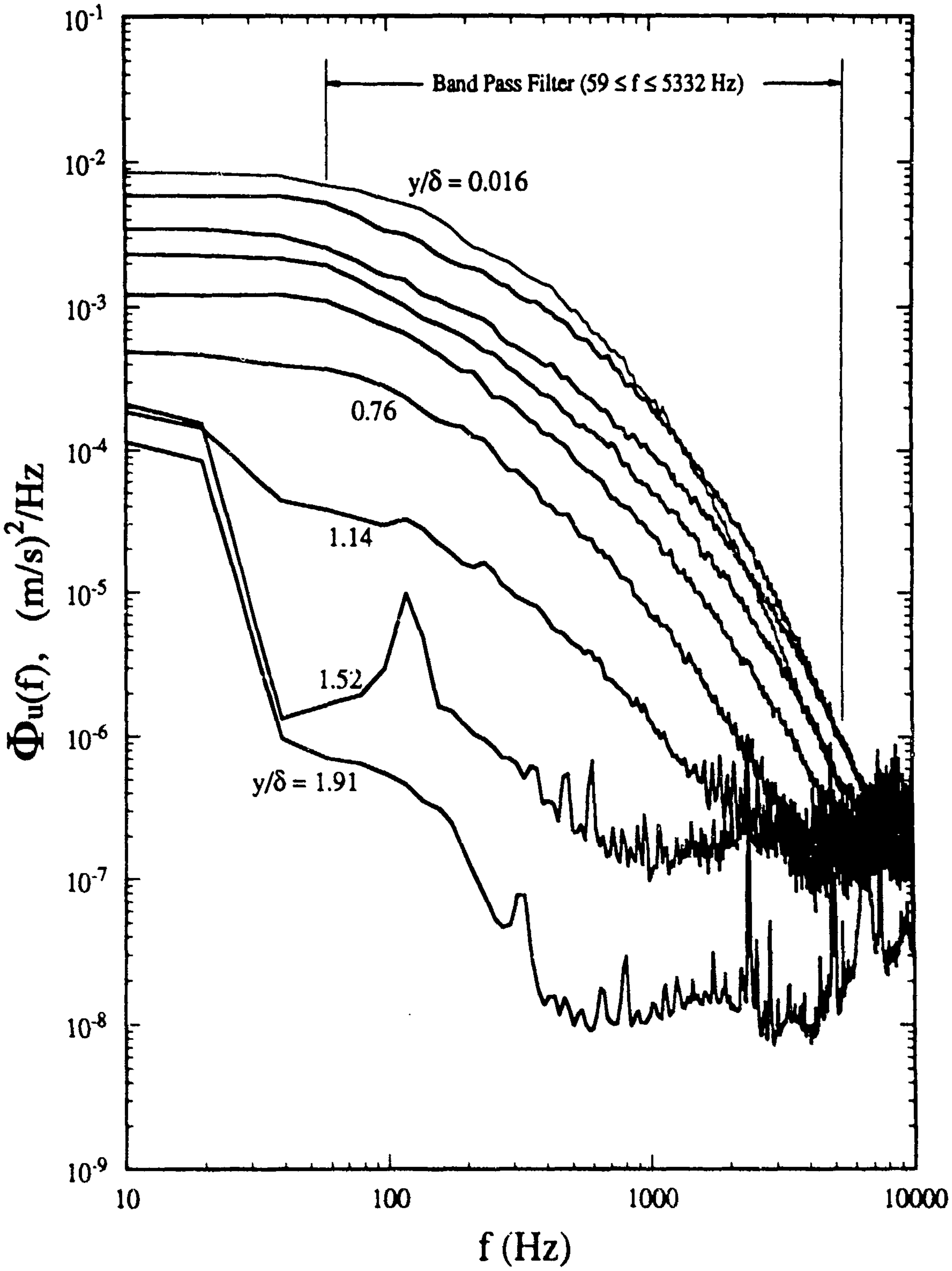

Figure 4-12. Power spectral densities of the streamwise velocity fluctuations at nine wall-normal positions of hot-wire probe used for this investigation. Dimensional coordinates.

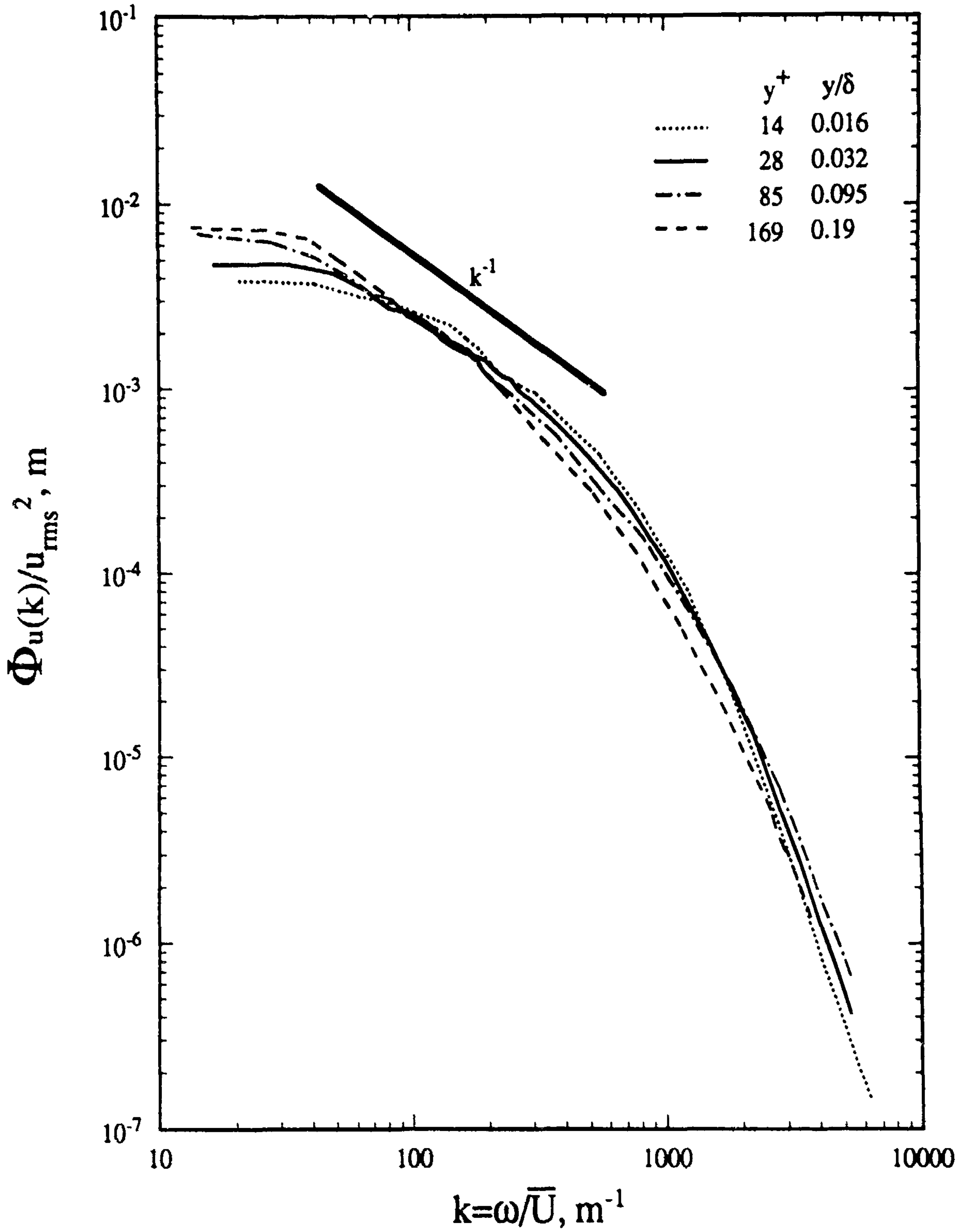

Figure 4-13. Streamwise velocity spectra in inner portion of cylindrical boundary layer. Wavenumber scaling.

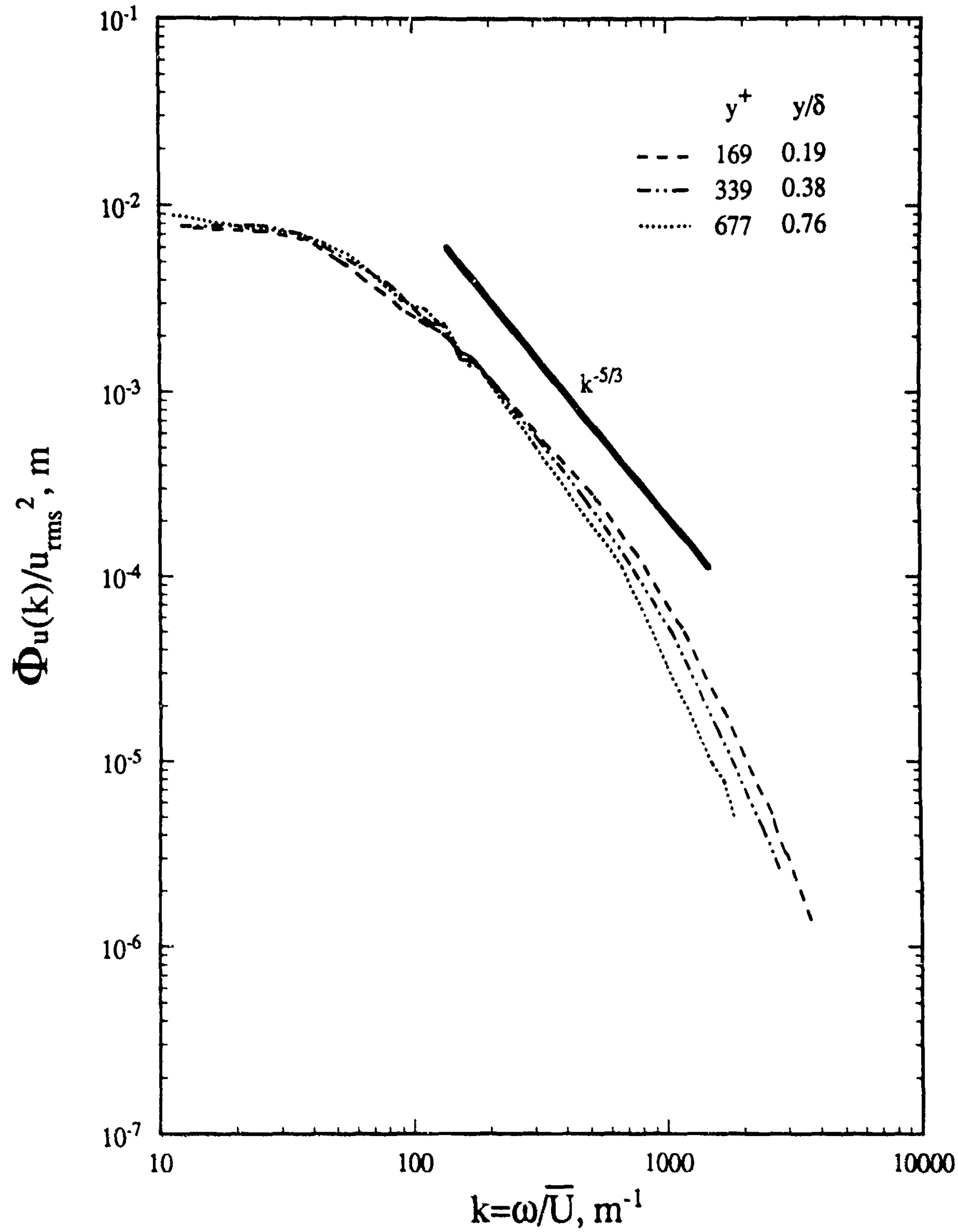

Figure 4-14. Streamwise velocity spectra in outer portion of cylindrical boundary layer. Wavenumber scaling.

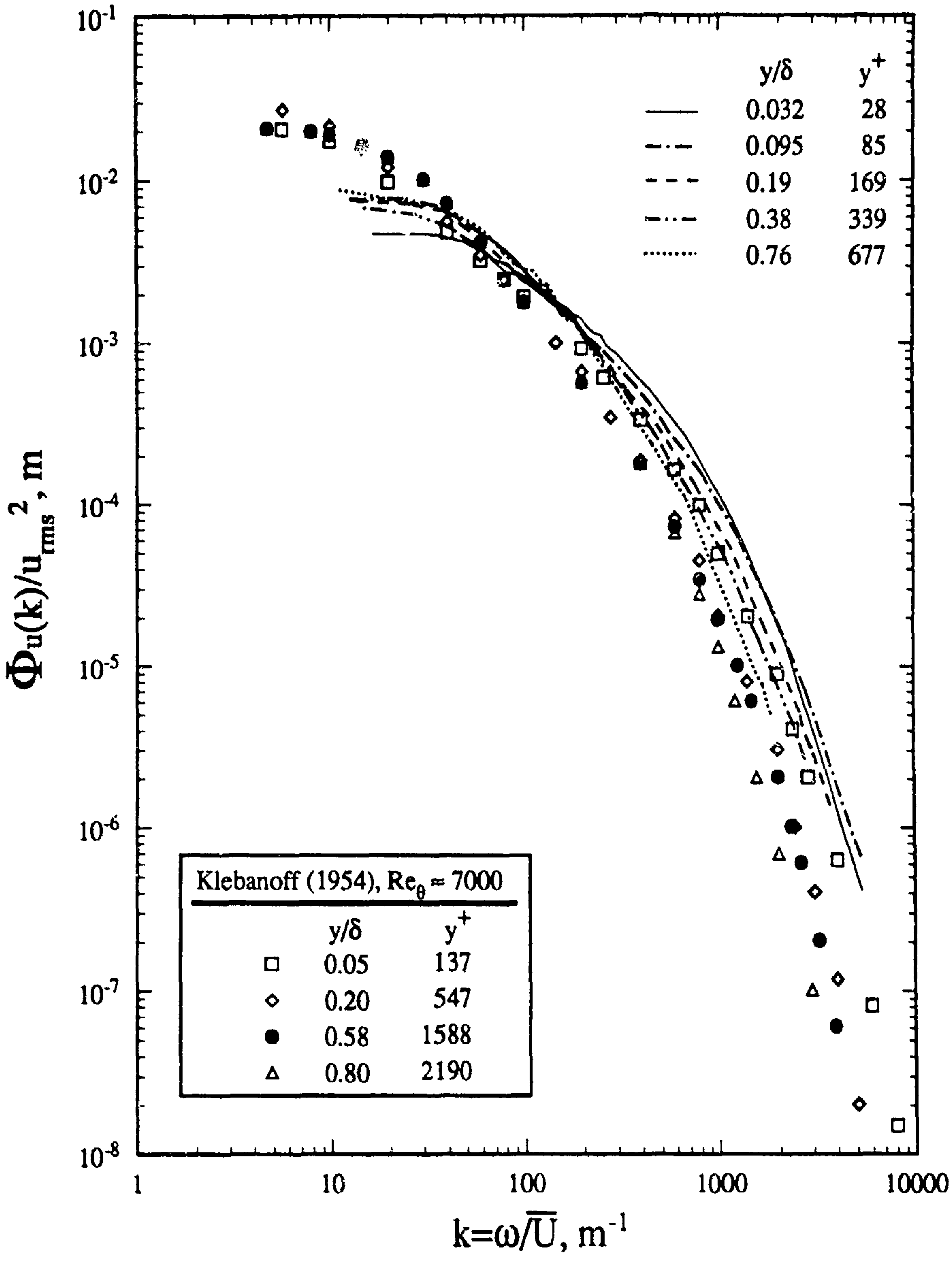

Figure 4-15. Comparison of streamwise velocity spectra in cylindrical and planar boundary layers. Wavenumber scaling.

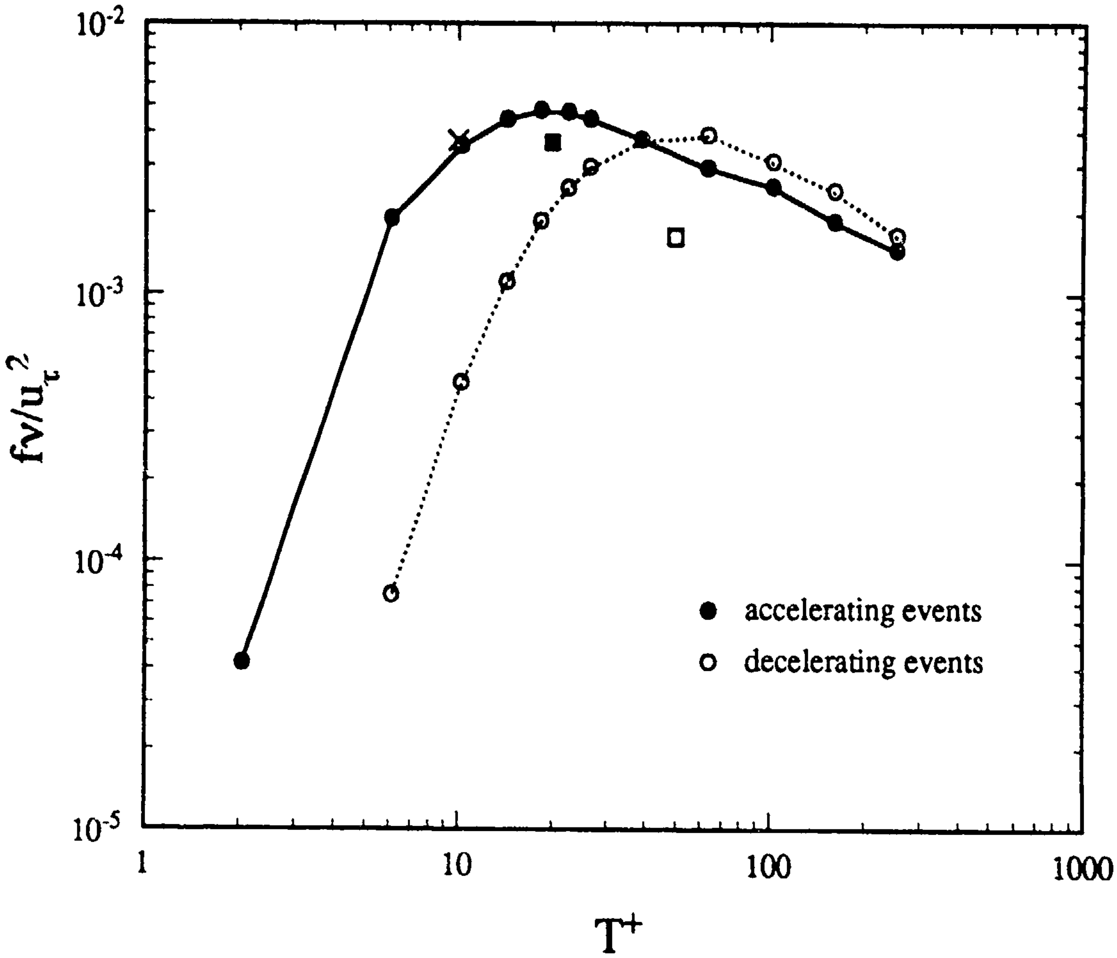

Figure 5-1. Frequency of occurrence for accelerating and decelerating VITA events at $y^+=14$ as a function of averaging time in wall units ($\kappa=1.0$). Also indicated: ■, Lueptow et al. (1987), $y^+=33$, $Re_\theta=3300$, $\delta/a=7.2$, $\partial u/\partial t>0$; □, Lueptow et al., $\partial u/\partial t<0$; ×, Blackwelder et al. (1983), $y^+=15$, $Re_\theta=3000$, $\delta/a=0$, $\partial u/\partial t>0$.

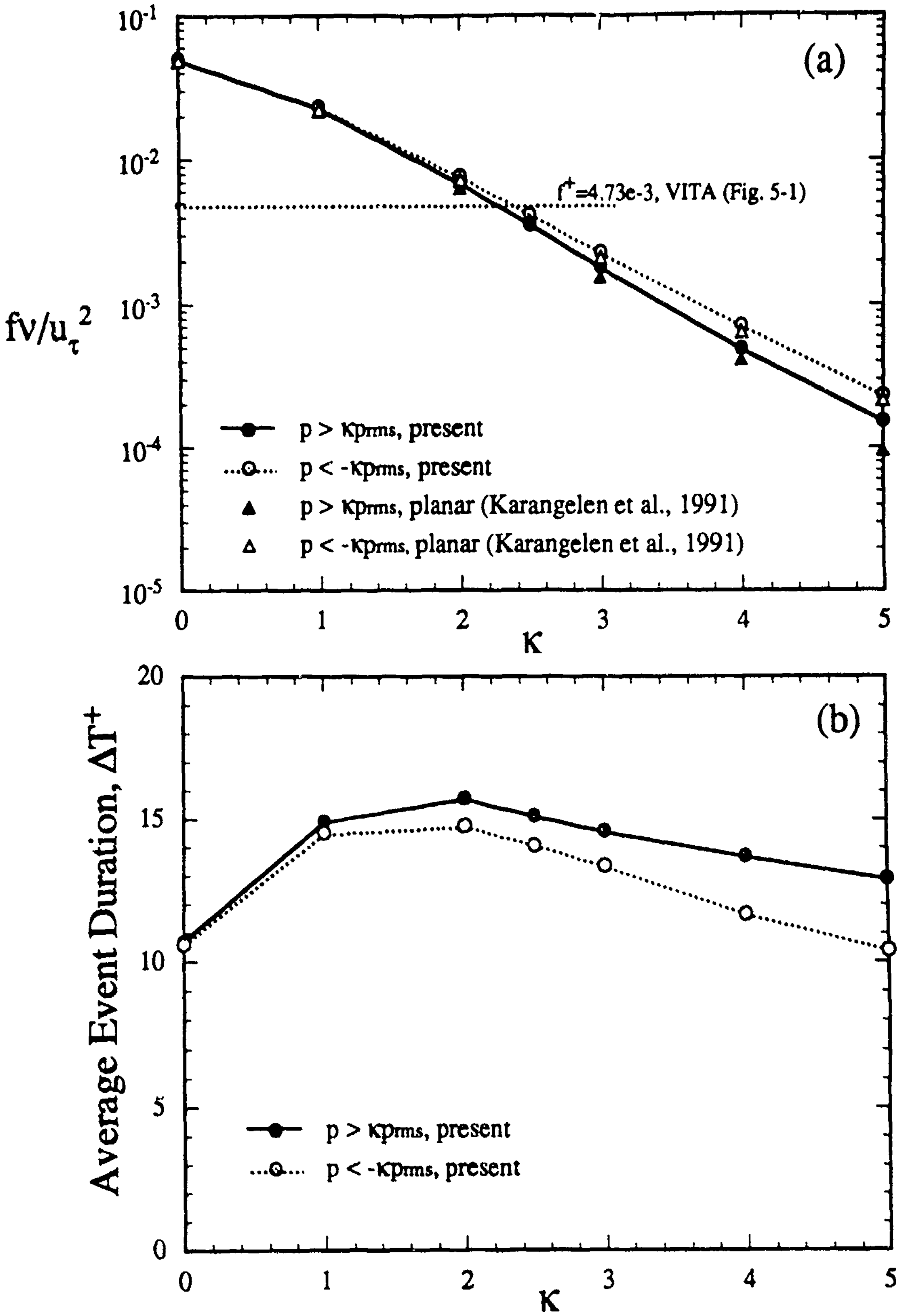

Figure 5-2. Positive and negative pressure event statistics as a function of pressure peak threshold level: (a), frequency of occurrence (inner variables) for cylindrical and planar boundary layers; (b), average duration in wall units.

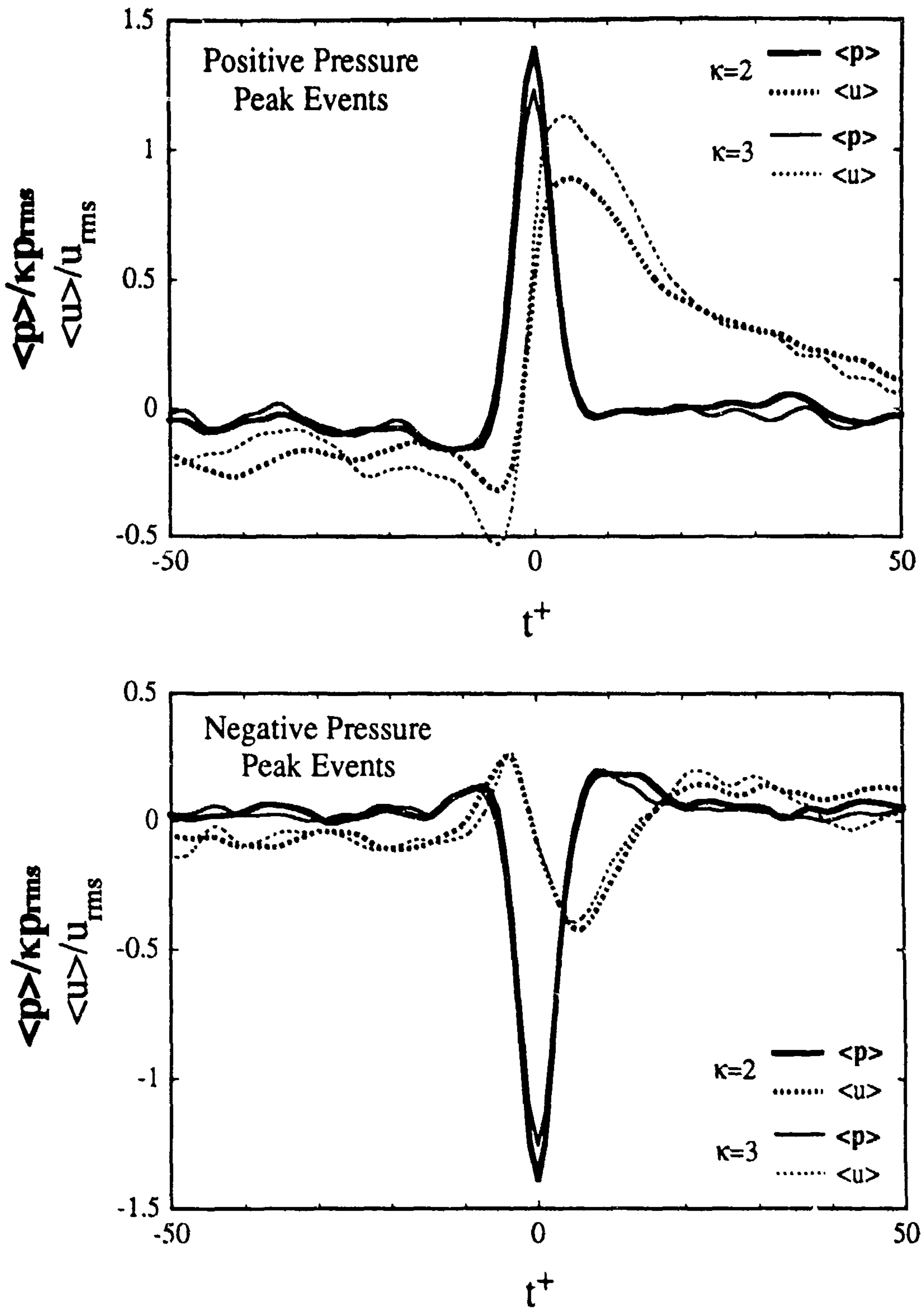

Figure 5-3. Effect of pressure peak detection threshold level on conditionally averaged pressure and velocity signals ($y^+=14$): upper, positive pressure peak events; lower, negative pressure peak events.

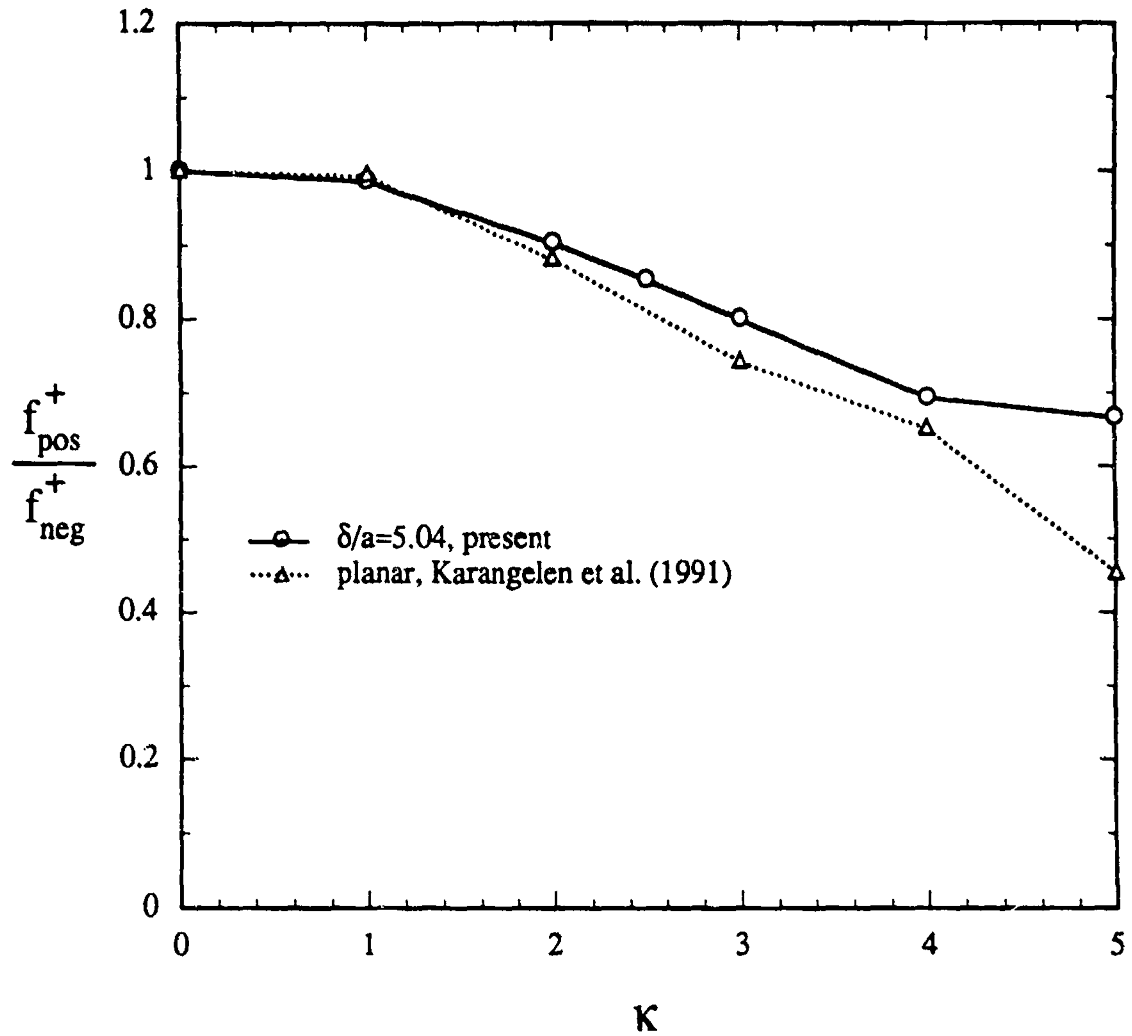

Figure 5-4. Comparison of frequency of occurrence for positive and negative pressure peak events in cylindrical and planar boundary layers as a function of pressure peak threshold level.

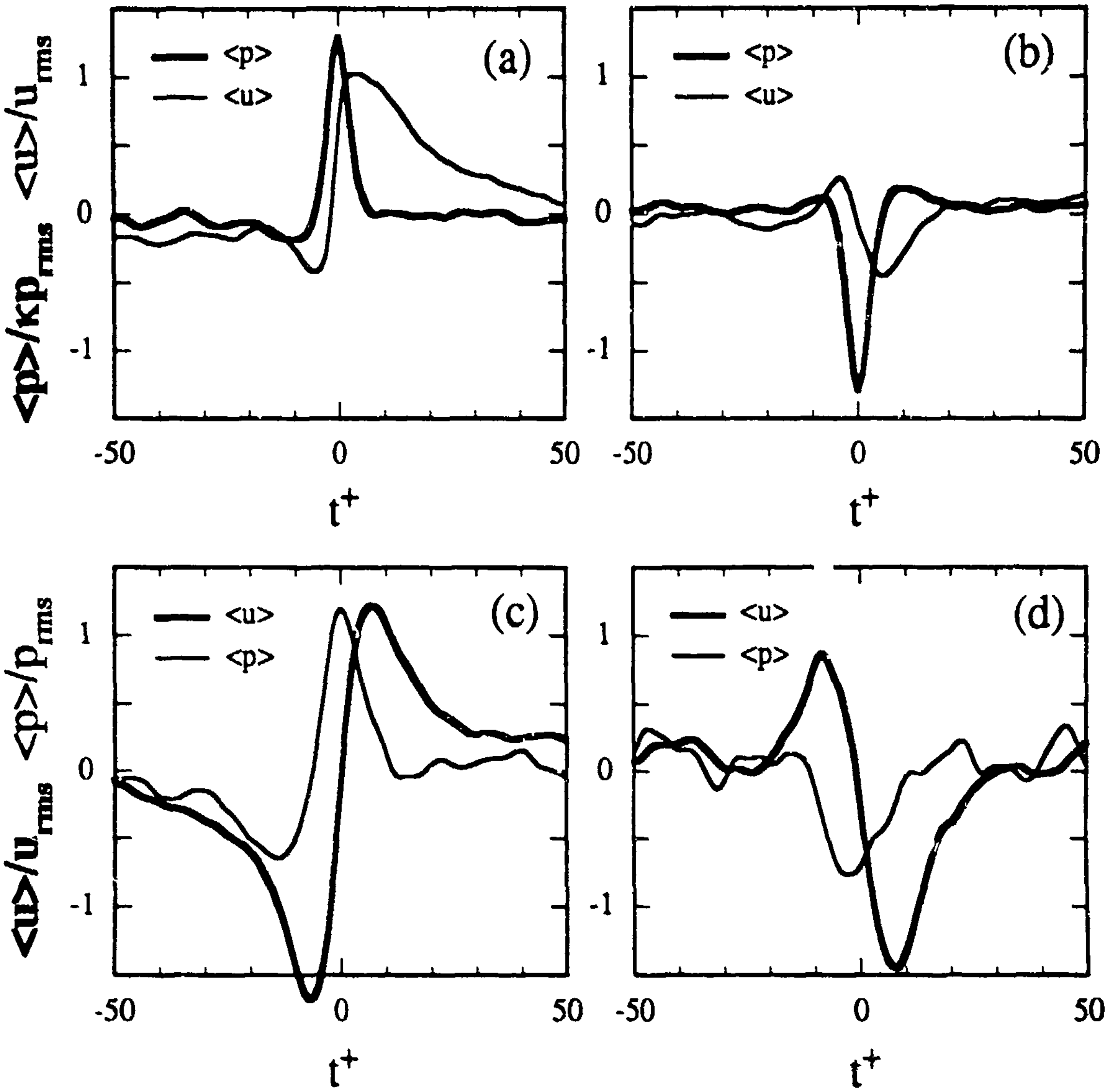

Figure 5-5. Conditionally averaged pressure and velocity signals with hot-wire probe immediately above pressure transducer ($x^+=0$, $y^+=14$, $\emptyset=0°$). Pressure peak detection ($\kappa=2.5$): (a), positive pressure peak events; (b), negative pressure peak events. VITA-on-u detection ($\kappa=1.0$, $T^+=18.4$): (c), accelerating-u events; (b), decelerating-u events.

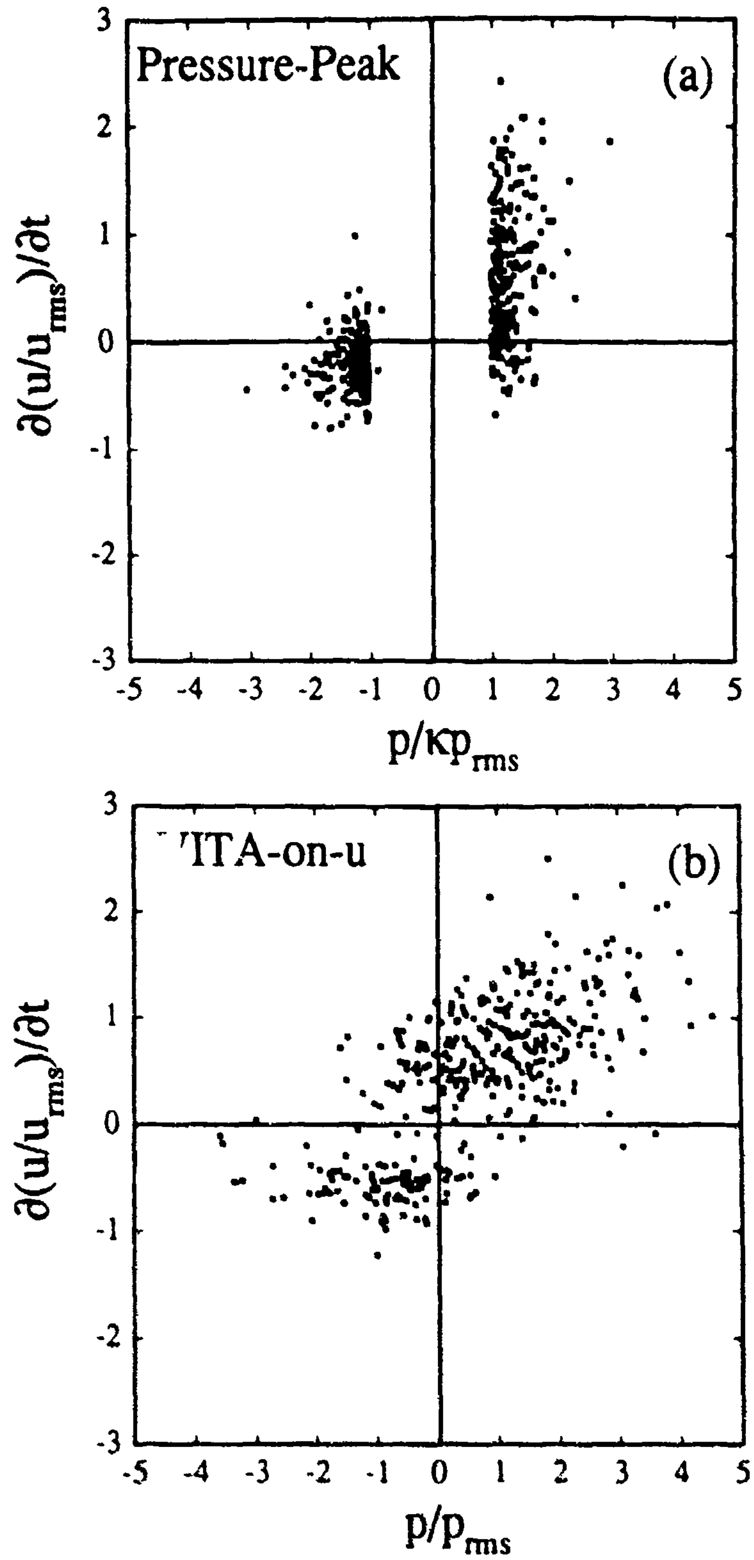

Figure 5-6. Slope of streamwise velocity versus amplitude of wall pressure at time of detection (hot-wire probe at $x^+=0$, $y^+=14$, $\varnothing=0°$): (a), pressure peak events ($\kappa=2.5$); (b), VITA-on-u events ($\kappa=1.0$, $T^+=18.4$).

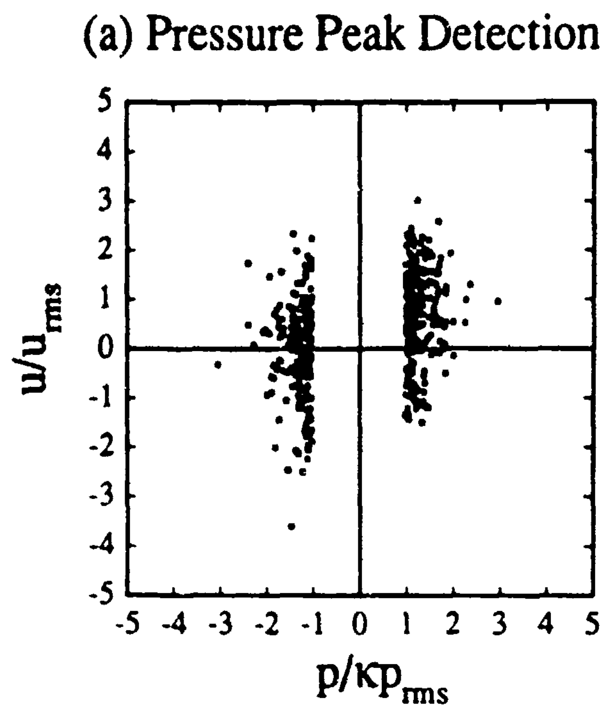

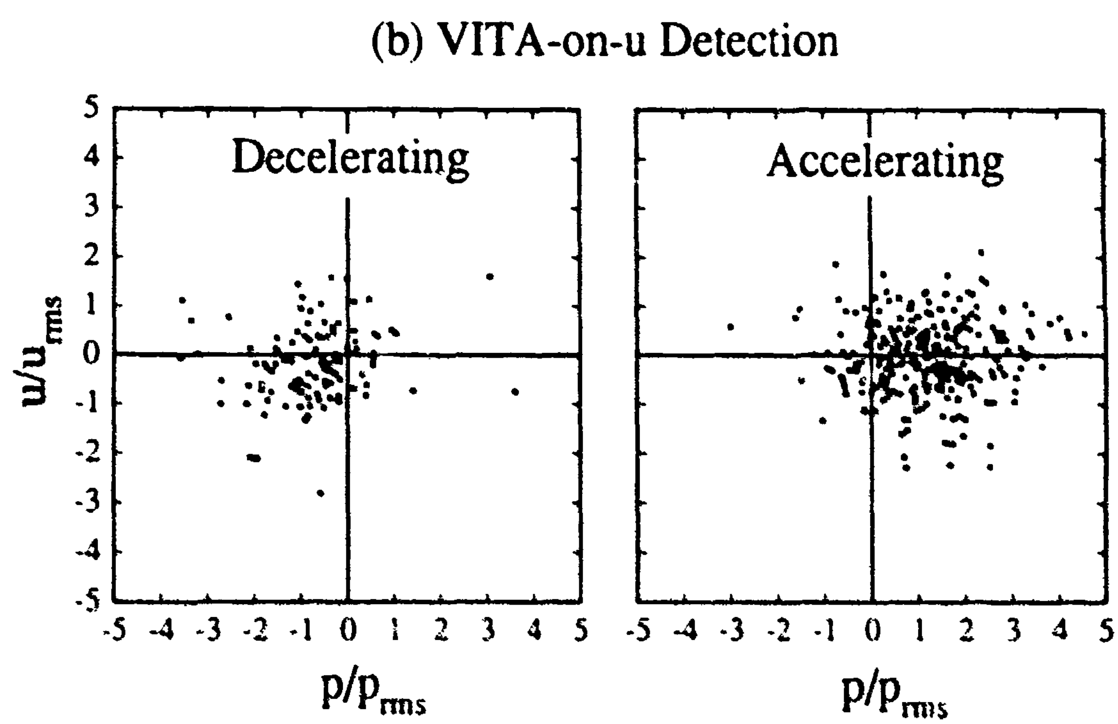

Figure 5-7. Amplitude of streamwise velocity versus amplitude of wall pressure at time of detection (hot-wire probe at $x^+=0$, $y^+=14$, $\varnothing=0°$): (a), pressure peak events ($\kappa=2.5$); (b), VITA-on-u events ($\kappa=1.0$, $T^+=18.4$).

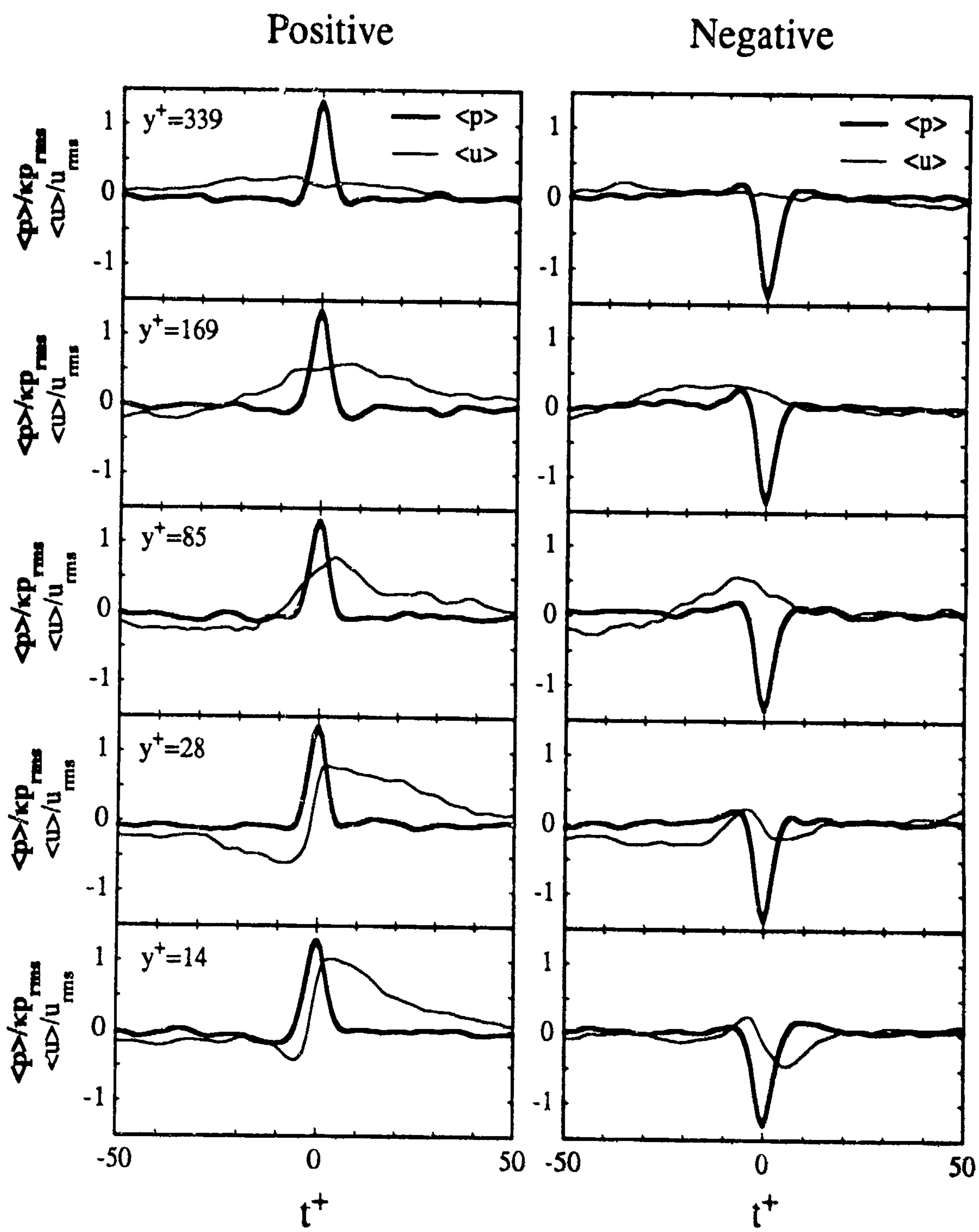

Figure 5-8. Dependence of conditionally averaged pressure and velocity signals based on pressure peak detection (κ=2.5) on wall-normal position of hot-wire probe (x^+=0, y^+=..., Ø=0°): left, positive pressure peak events; right, negative pressure peak events.

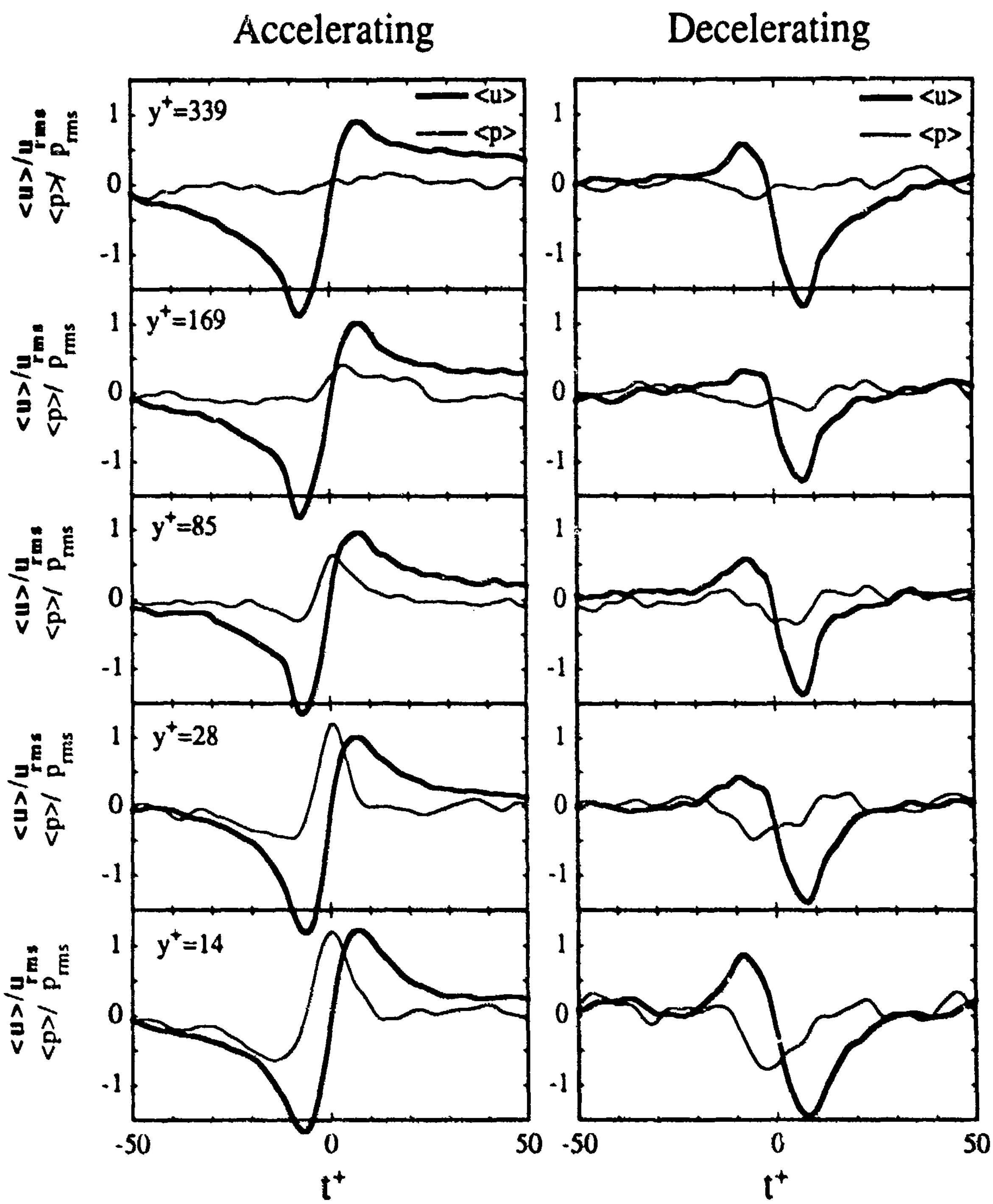

Figure 5-9. Dependence of conditionally averaged pressure and velocity signals based on VITA-on-u detection (κ=1.0, T^+=18.4) on wall-normal position of hot-wire probe (x^+=0, y^+=..., Ø=0°): left, accelerating-u events; right, decelerating-u events.

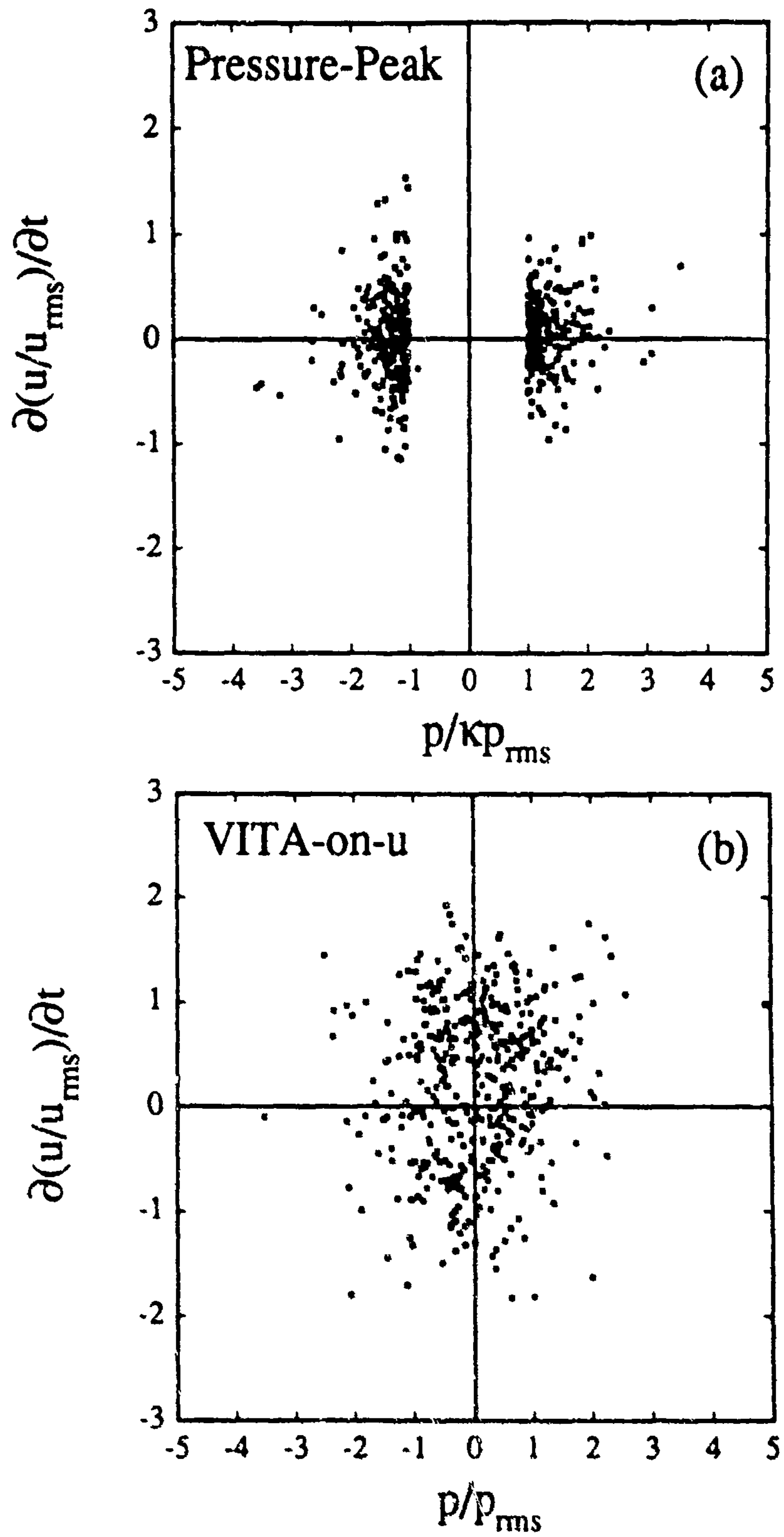

Figure 5-10. Slope of streamwise velocity versus amplitude of wall pressure at time of detection (hot-wire probe at $x^+=0$, $y^+=169$, $\emptyset=0°$): (a), pressure peak events ($\kappa=2.5$); (b), VITA-on-u events ($\kappa=1.0$, $T^+=18.4$).

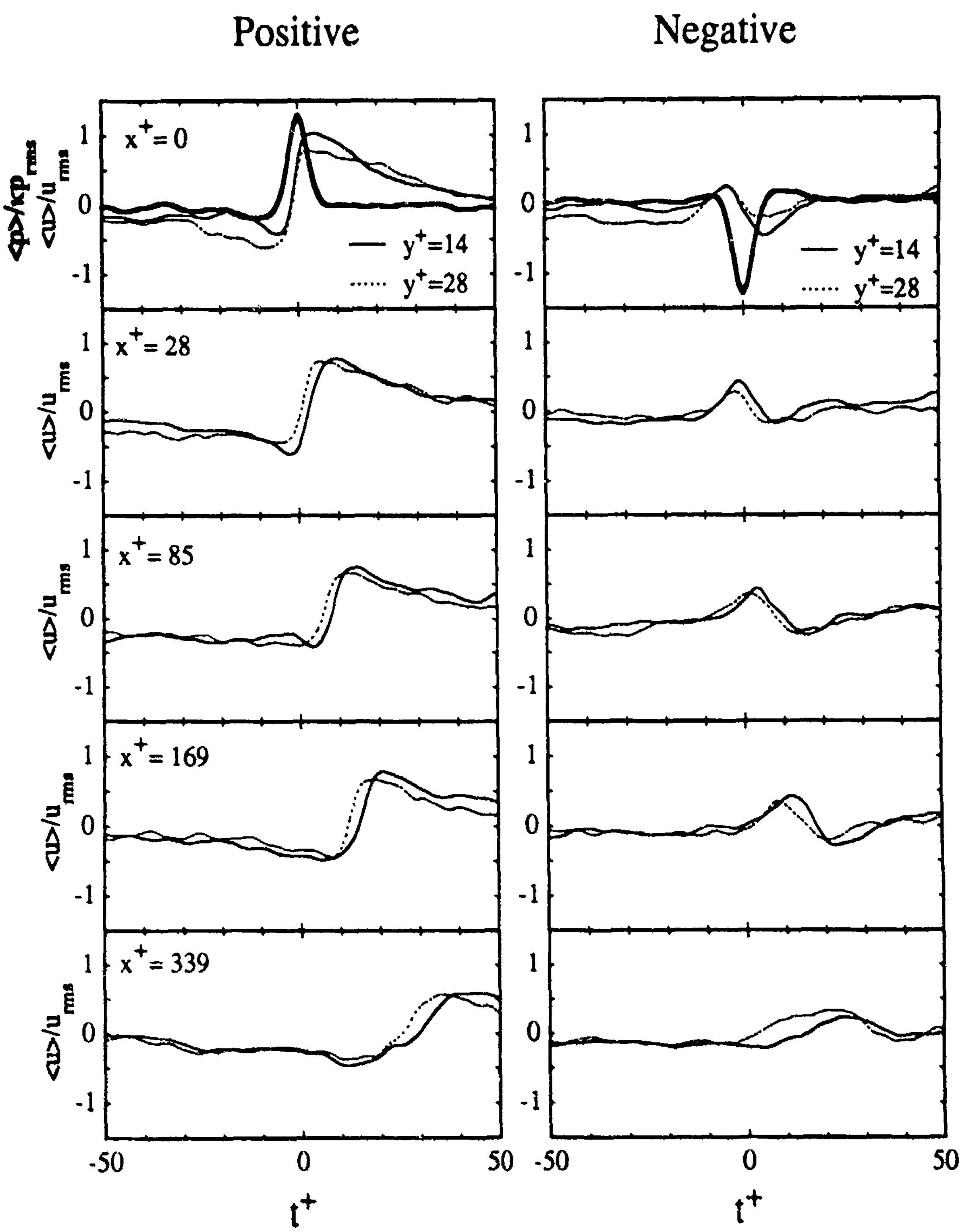

Figure 5-11. Dependence of conditionally averaged velocity signals at $y^+=14$ and 28 based upon pressure peak detection ($\kappa=2.5$) on streamwise position of hot-wire probe ($x^+=...$, $\varnothing=0°$): left, positive pressure peak events; right, negative pressure peak events.

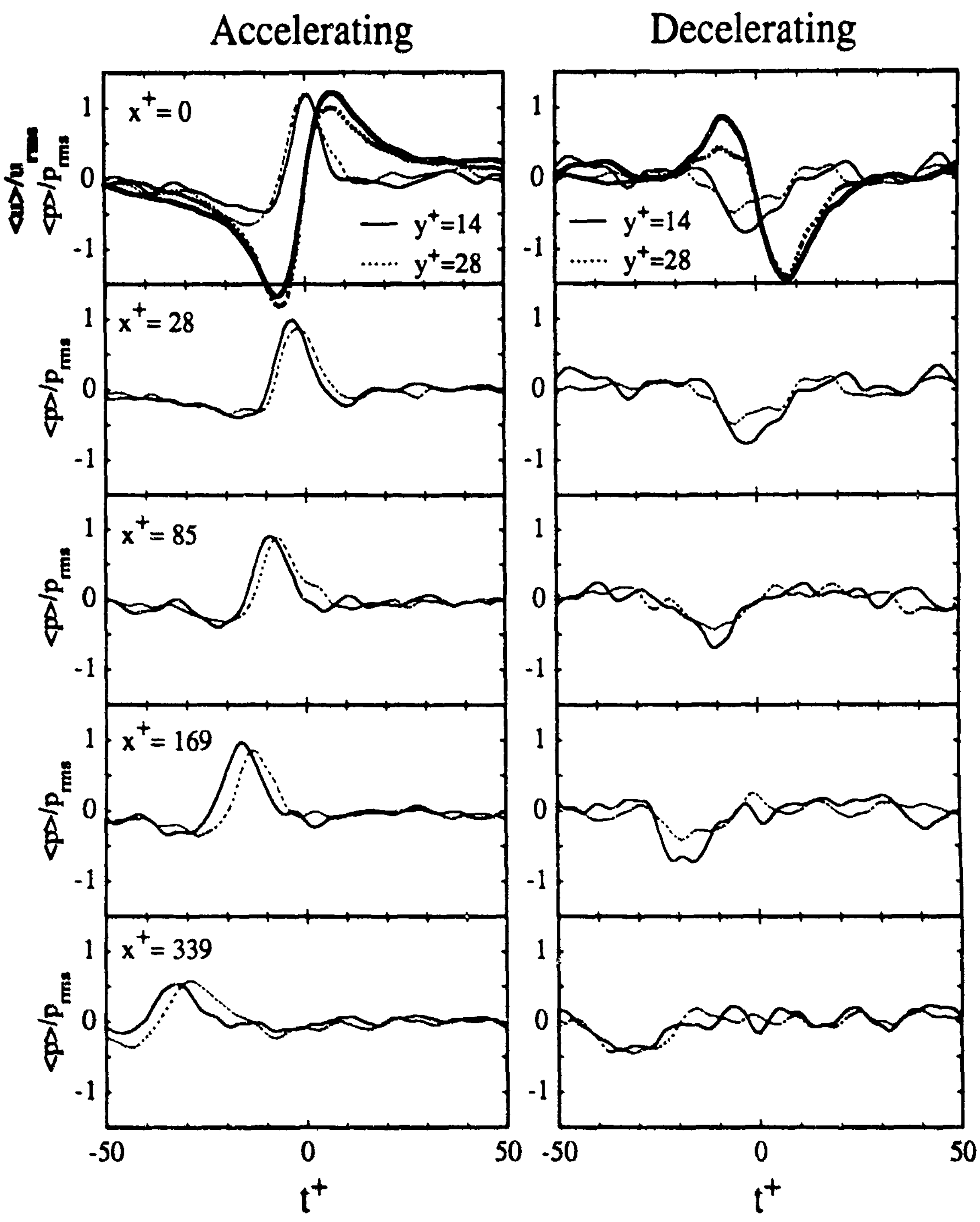

Figure 5-12. Dependence of conditionally averaged pressure signals based upon VITA-on-u detection applied at $y^+=14$ and 28 ($\kappa=1.0$, $T^+=18.4$) on streamwise position of hot-wire probe ($x^+=...$, $\varnothing=0°$): <u>left</u>, accelerating-u events; <u>right</u>, decelerating-u events.

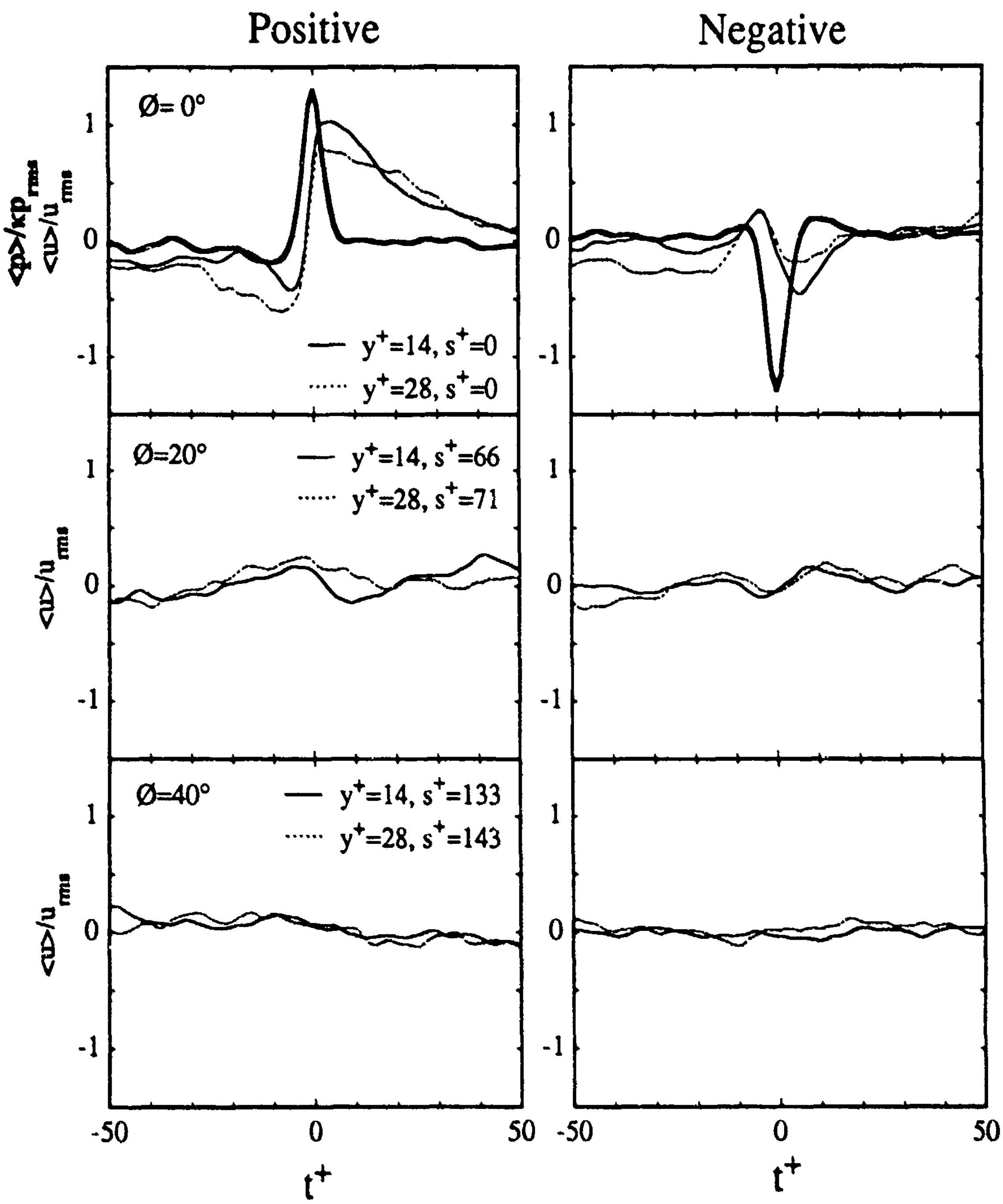

Figure 5-13. Dependence of conditionally averaged velocity signals at $y^+=14$ and 28 based upon pressure peak detection ($\kappa=2.5$) on circumferential position of hot-wire probe ($x^+=0$, $\emptyset=...$): left, positive pressure peak events; right, negative pressure peak events.

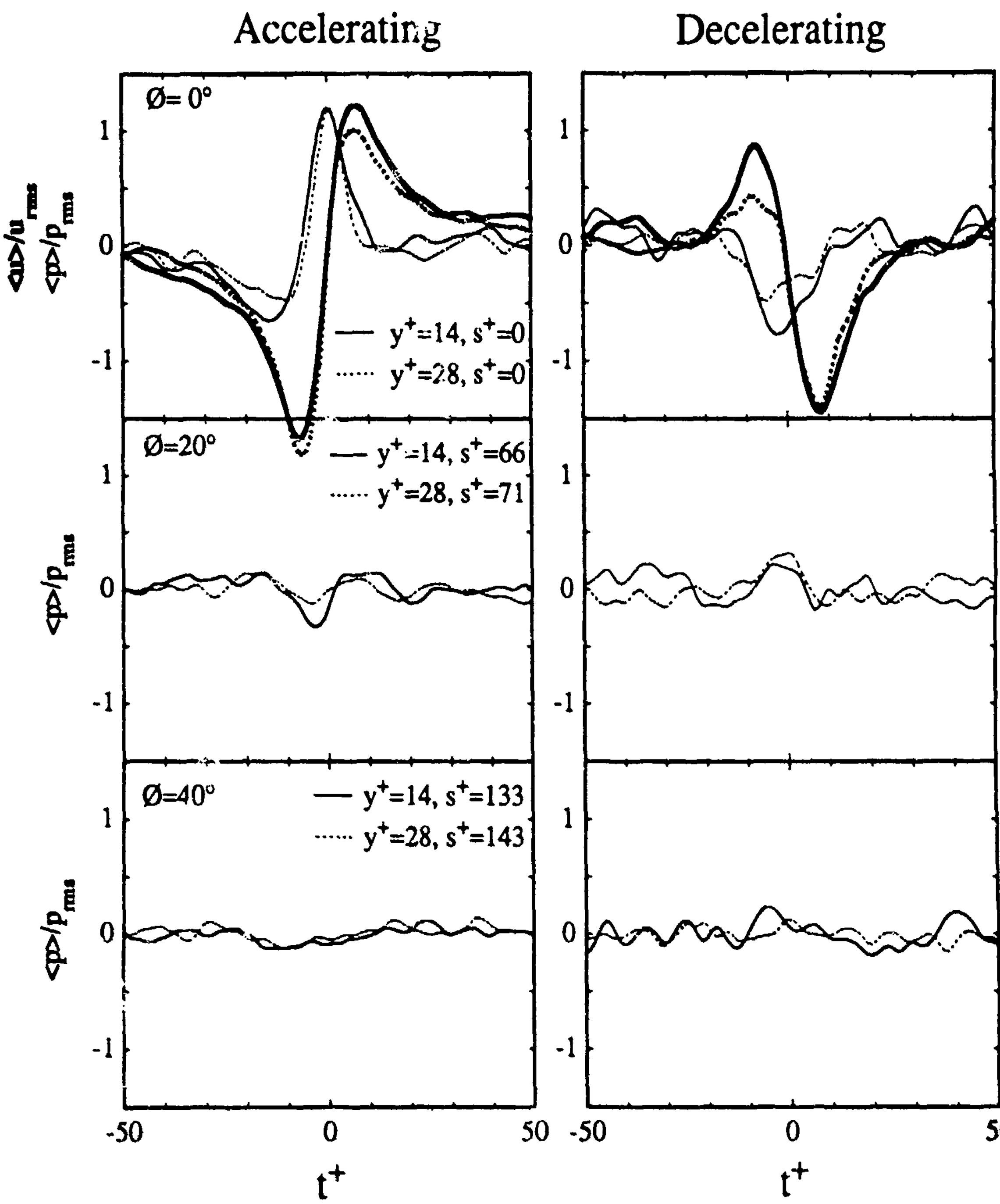

Figure 5-14. Dependence of conditionally averaged pressure signals based upon VITA-on-u detection applied at $y^+=14$ and 28 ($\kappa=1.0$, $T^+=18.4$) on circumferential position of hot-wire probe ($x^+=0$, $Ø=...$): left, accelerating-u events; right, decelerating-u events.

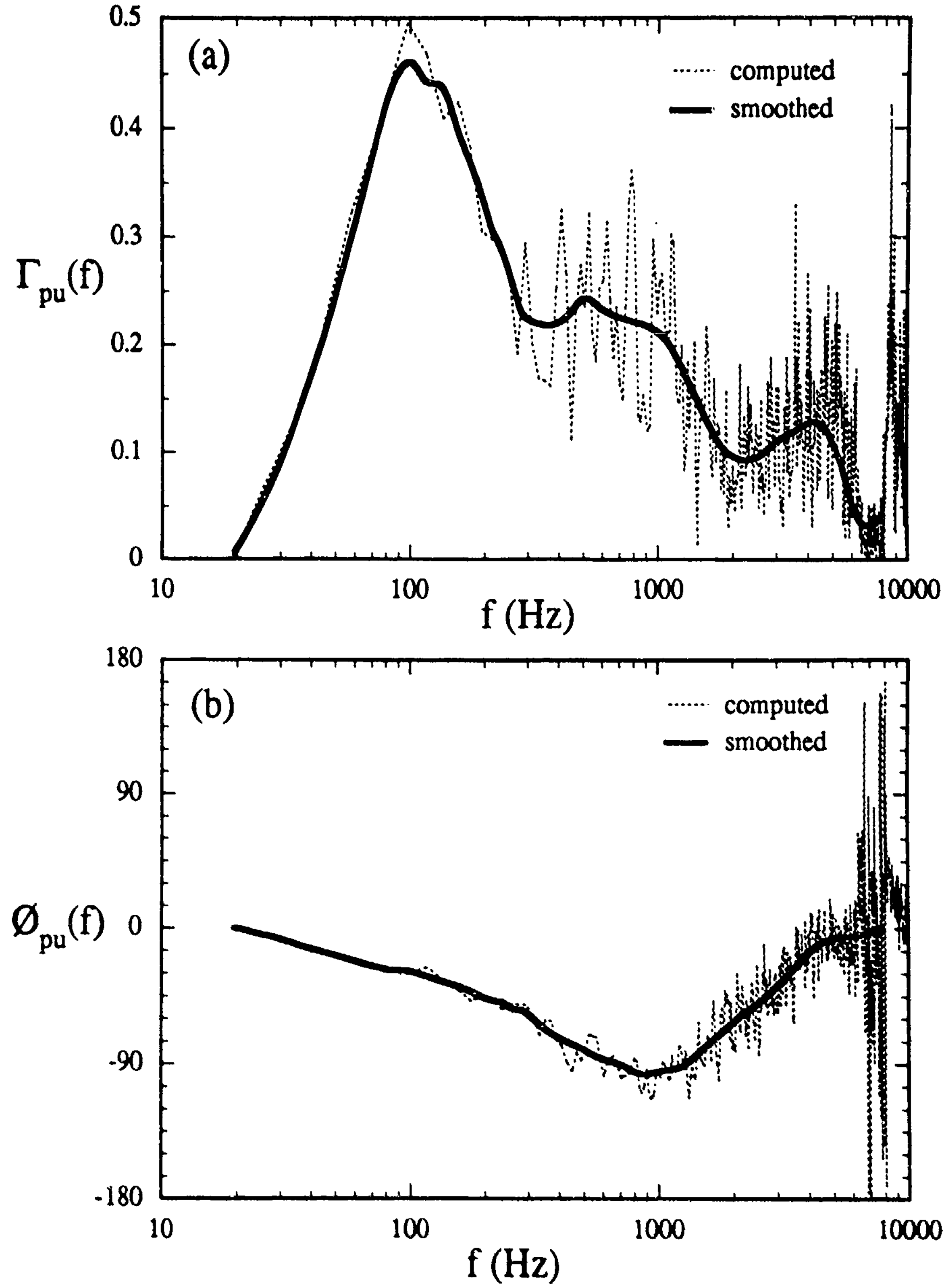

Figure 6-1. Test of smoothing procedure for (a) coherence and (b) phase.

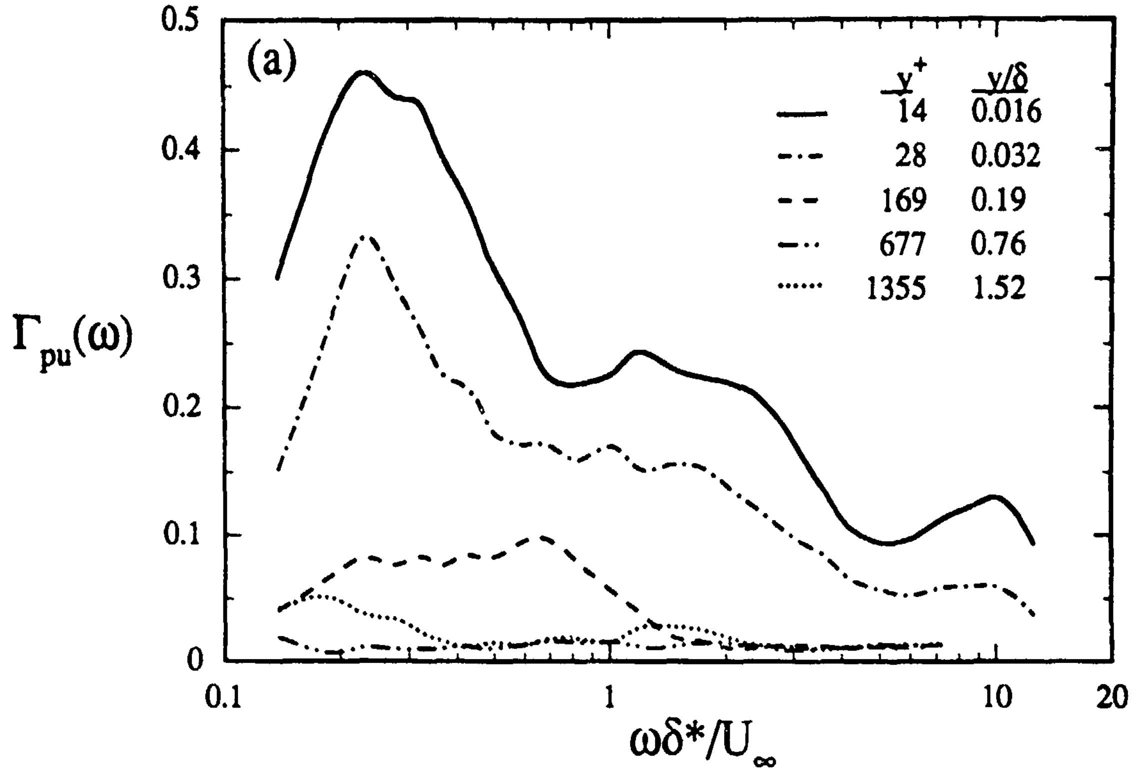

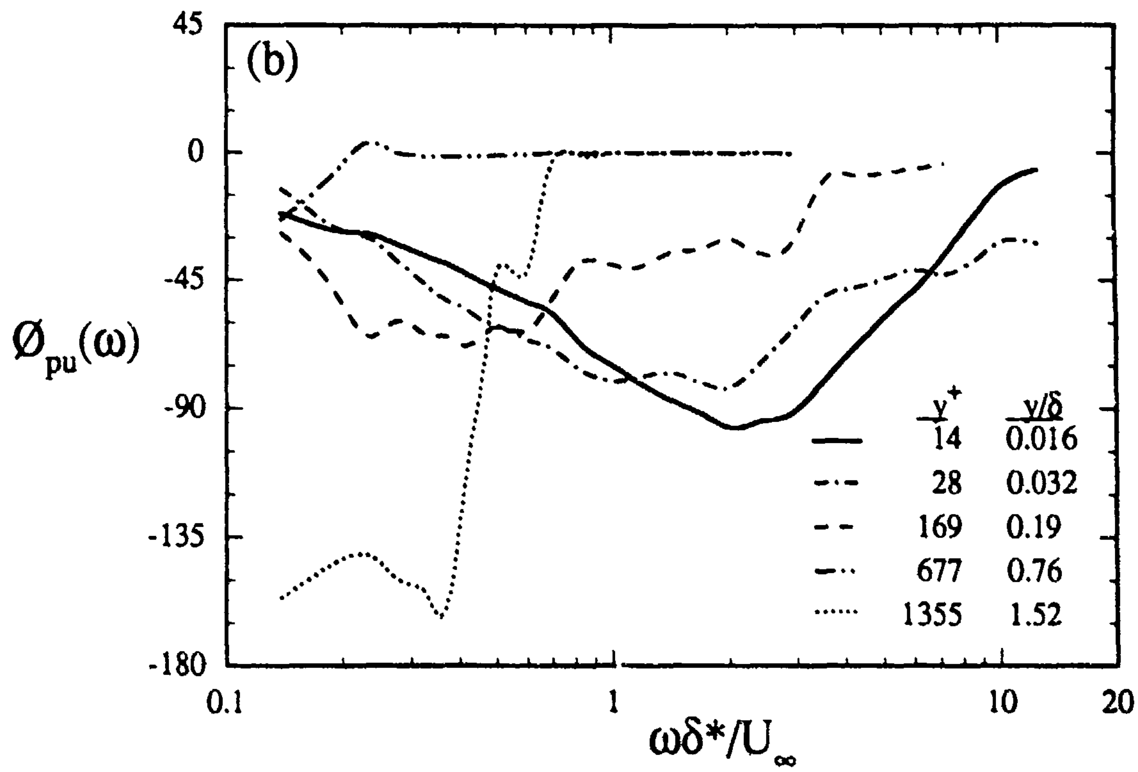

Figure 6-2. Dependence of (a) coherence and (b) phase between wall pressure and streamwise velocity on wall-normal position of hot-wire probe (x=0, y=..., Ø=0°).

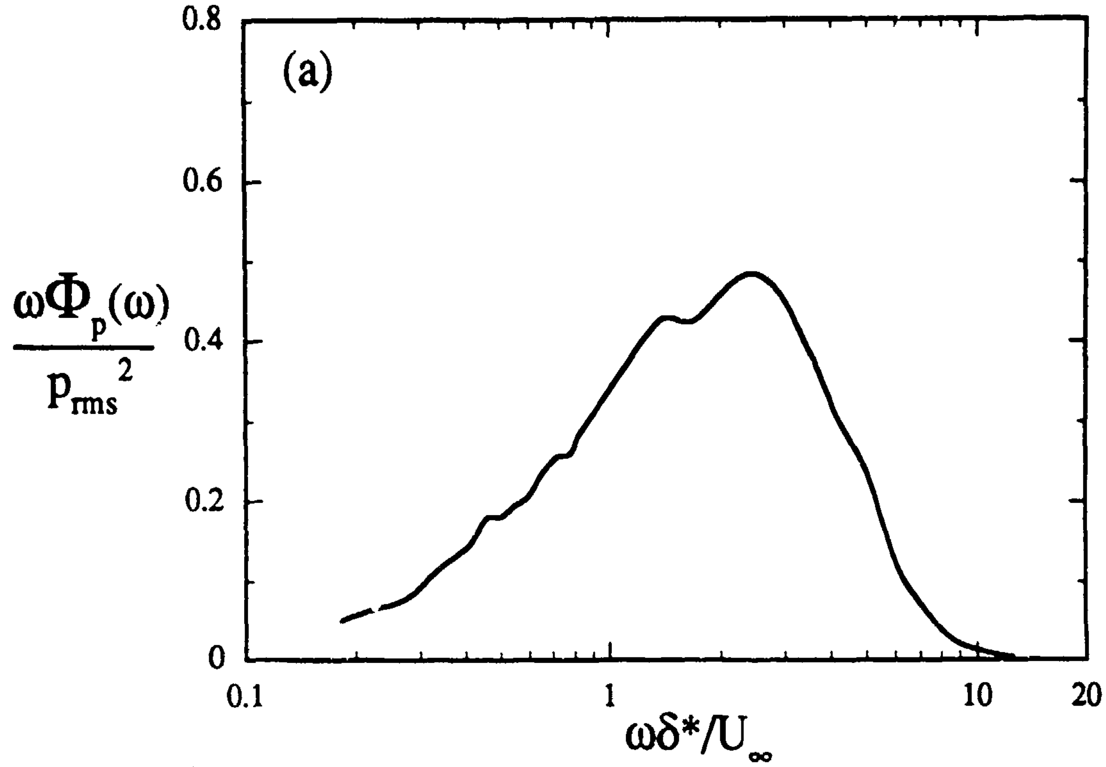

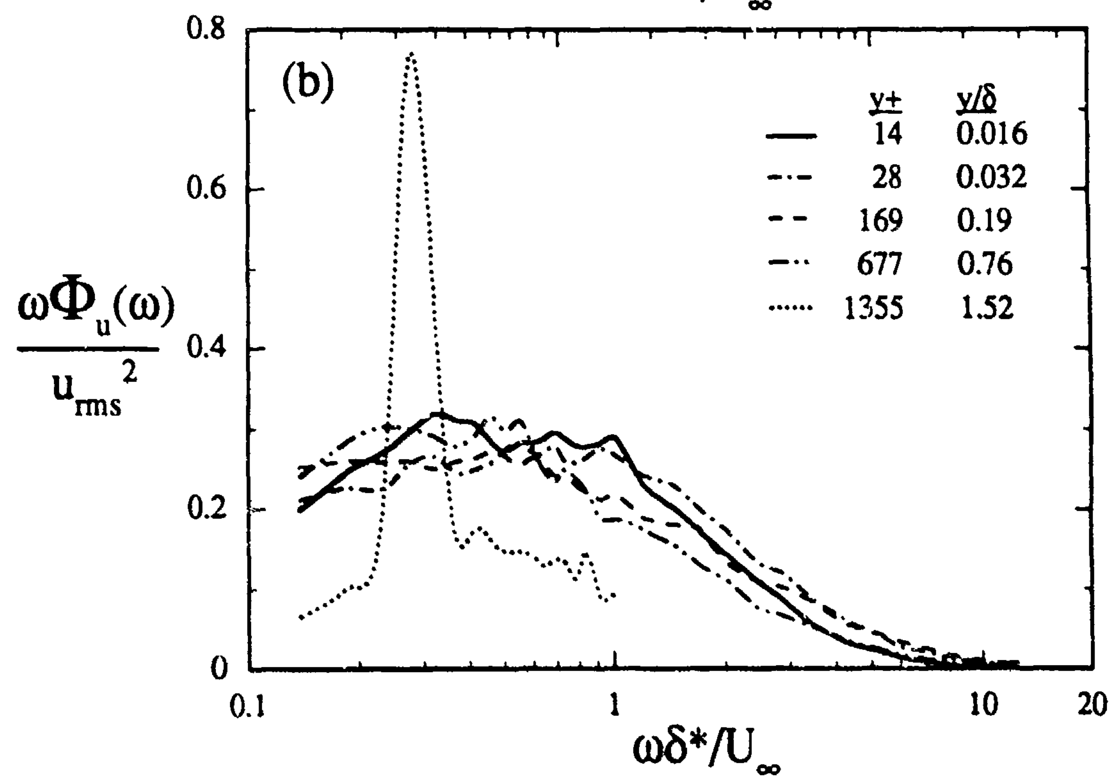

Figure 6-3. Normalized fluctuating (a) wall pressure and (b) streamwise velocity spectra.

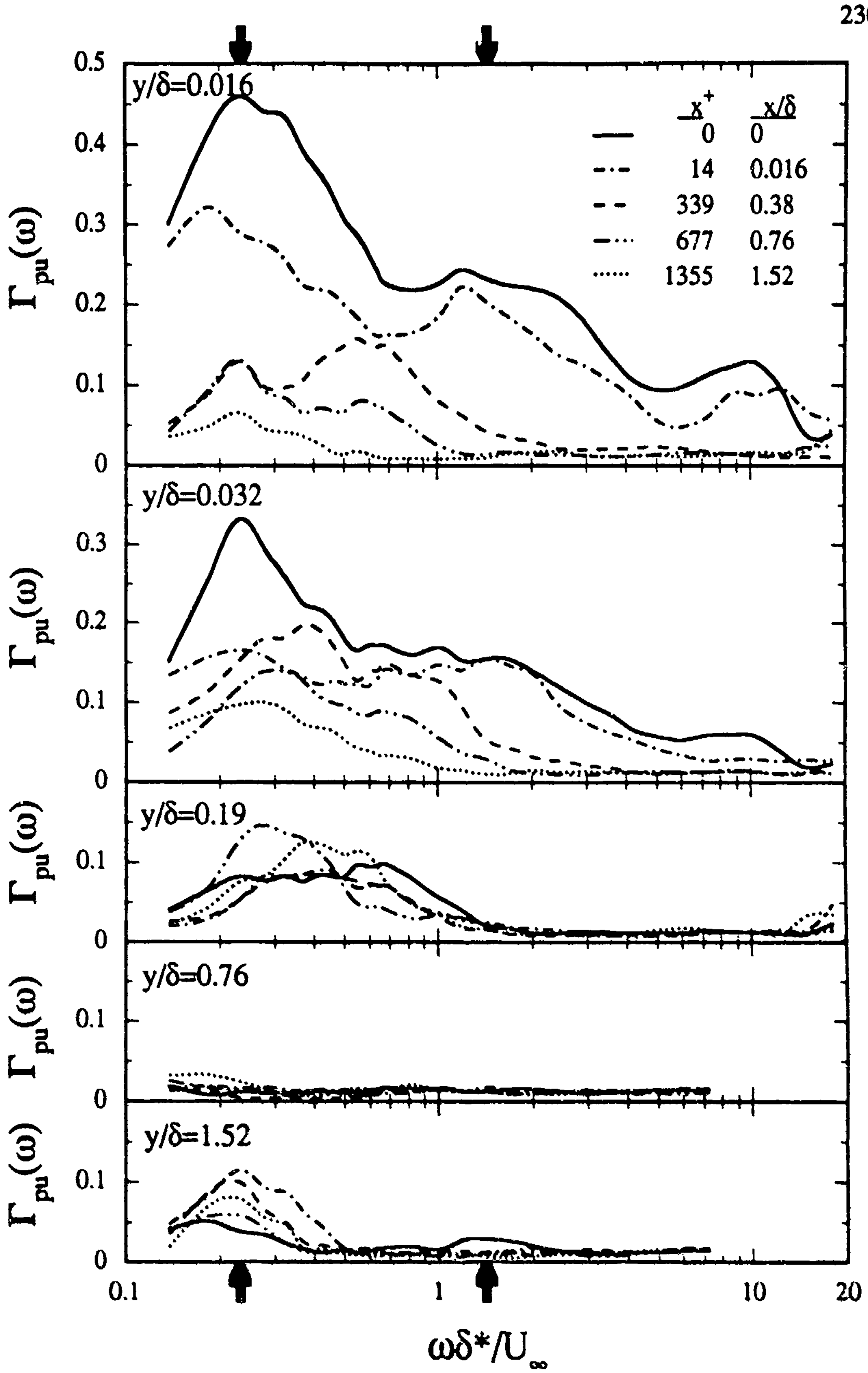

Figure 6-4. Dependence of coherence between wall pressure and streamwise velocity at various wall-normal positions on streamwise position of hot-wire probe (x=..., Ø=0°).

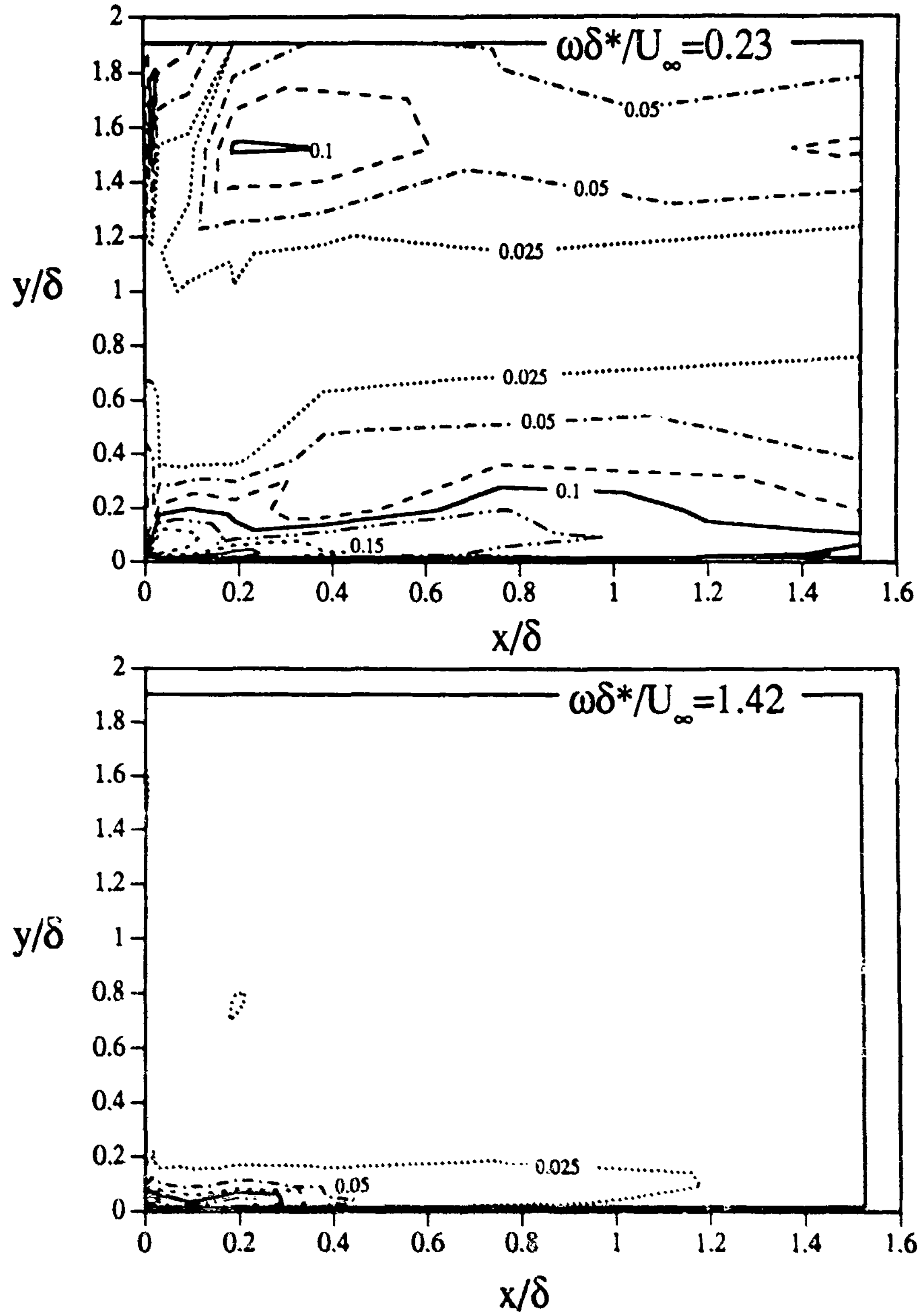

Figure 6-5. Contour plots of coherence between wall pressure and streamwise velocity at a single frequency in x-y plane containing microphone (Ø=0°): upper, coherence levels at $\omega\delta^*/U_\infty$=0.23; lower, coherence levels at $\omega\delta^*/U_\infty$=1.42.

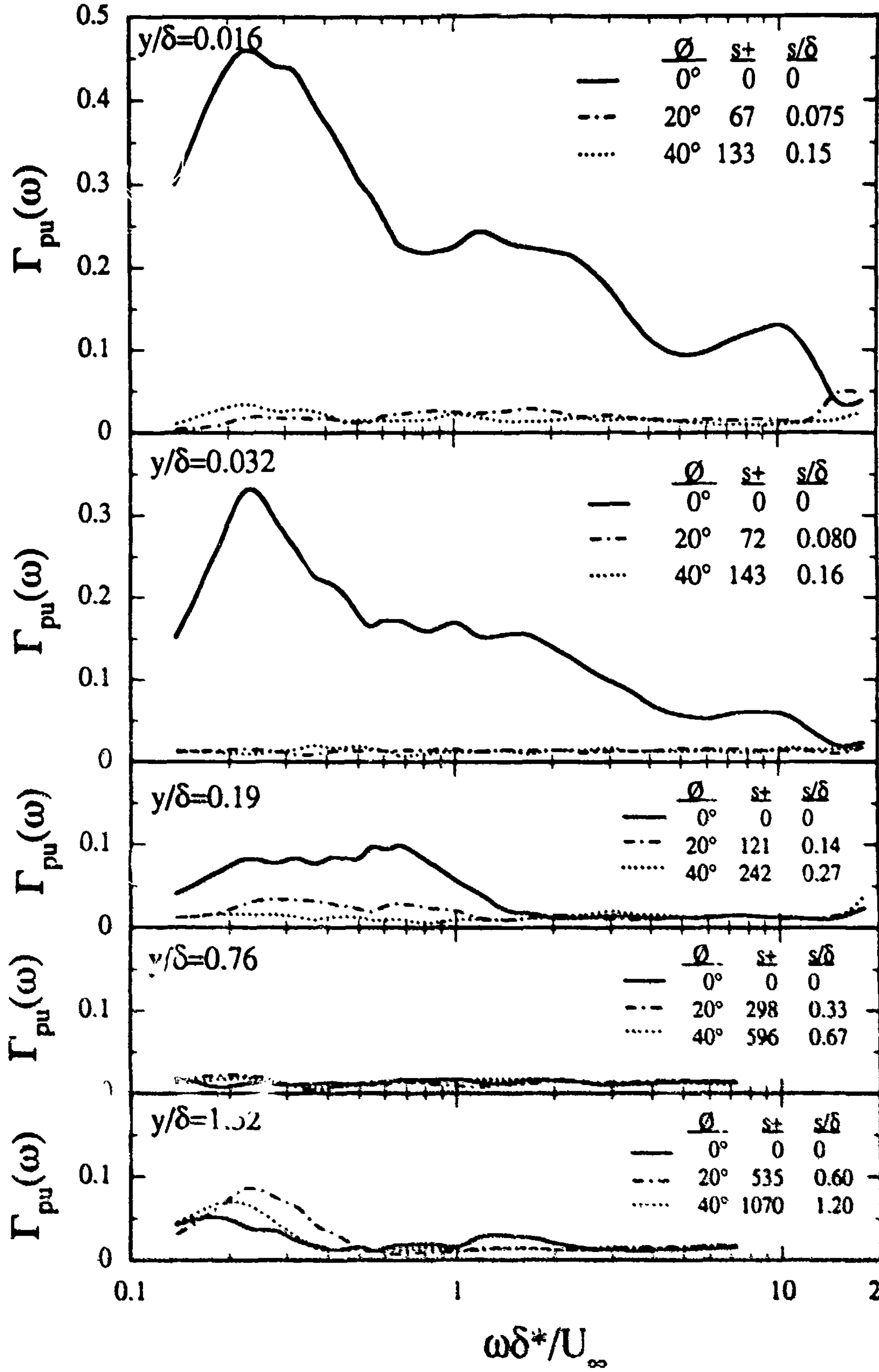

Figure 6-6. Dependence of coherence between wall pressure and streamwise velocity at various wall-normal positions on circumferential position of hot-wire probe (x=0, Ø=...).

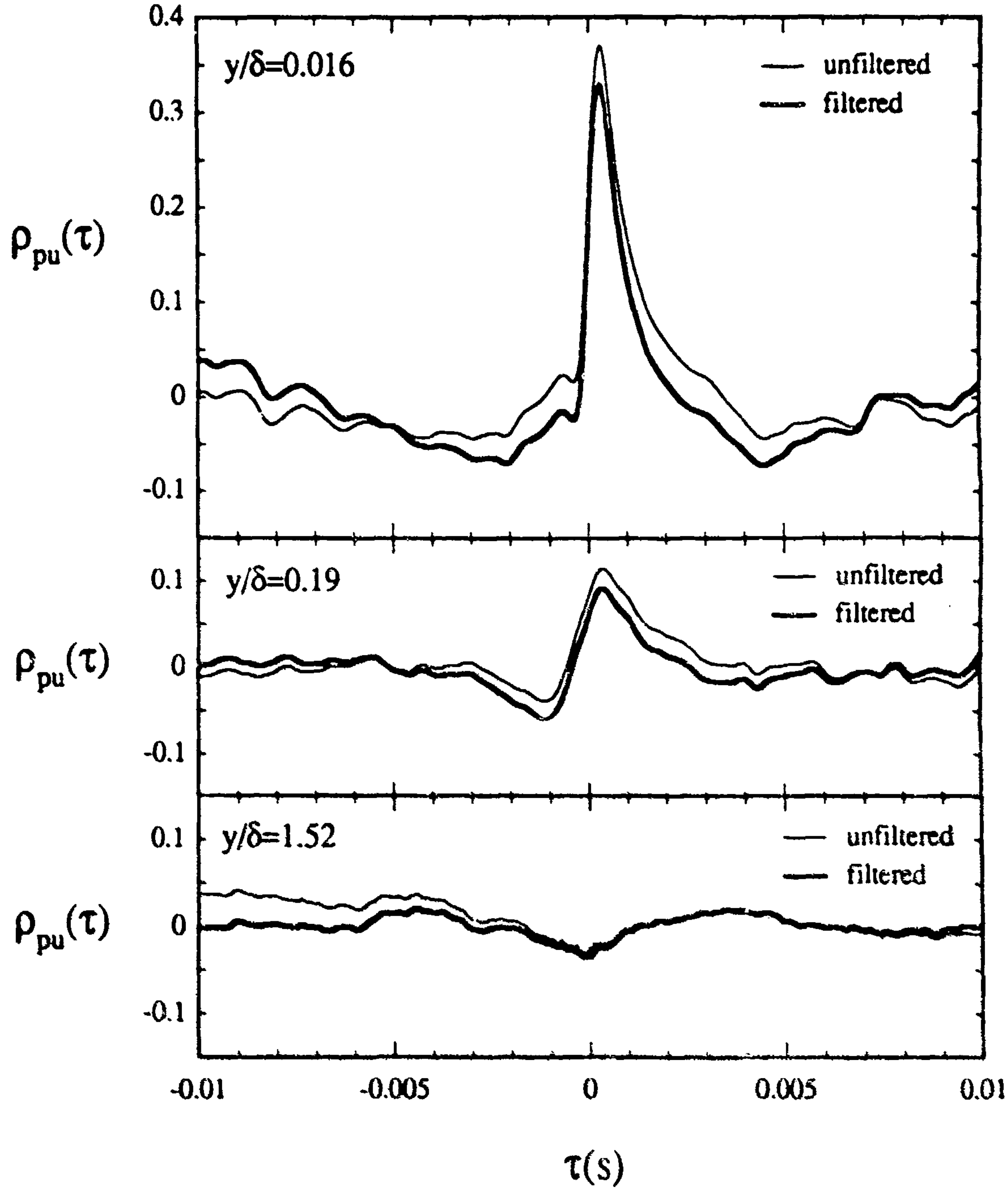

Figure 6-7. Effect of digital bandpass filter ($59 \leq f \leq 5332$ Hz) on pressure-velocity correlation at three positions in boundary layer.

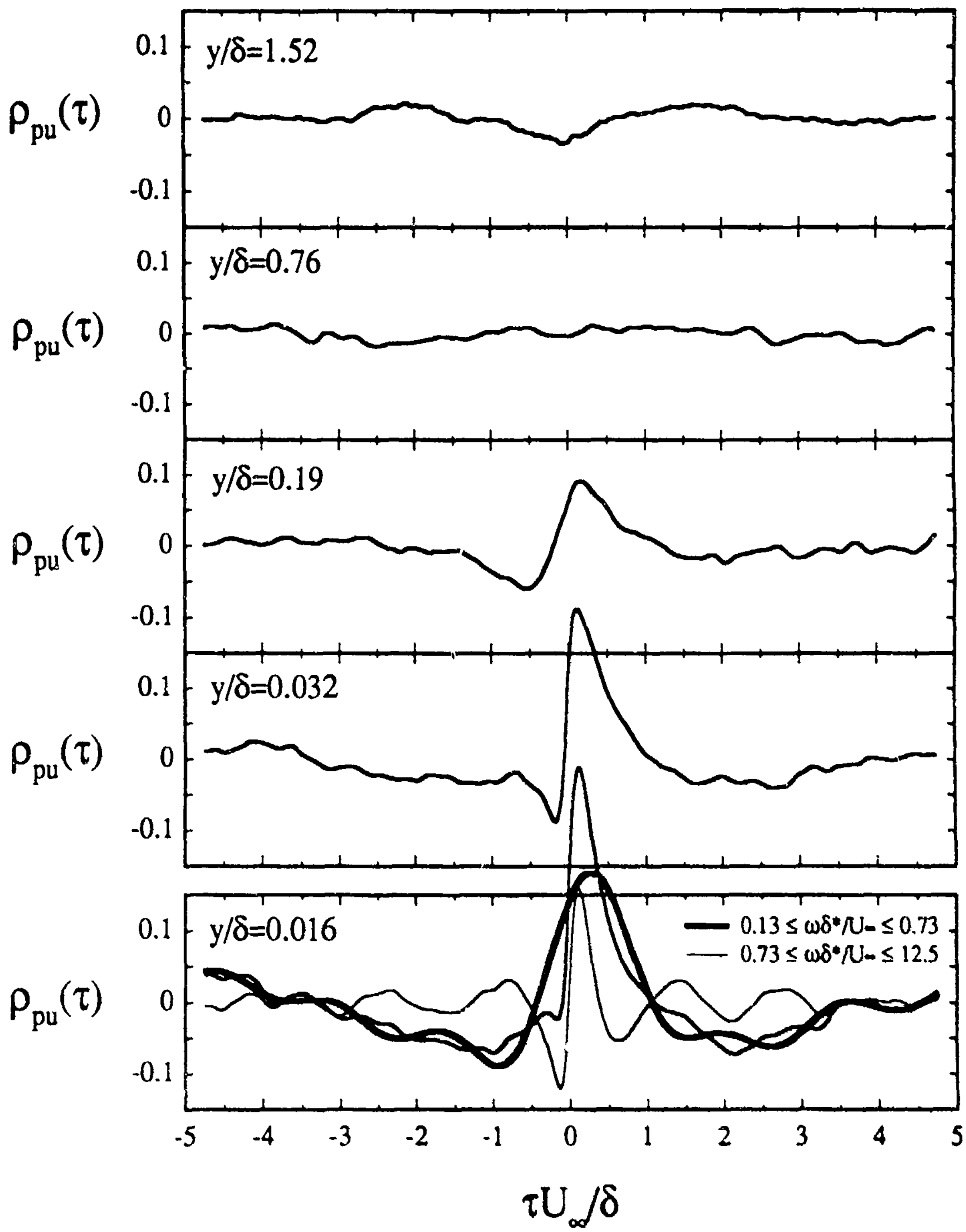

Figure 6-8. Dependence of cross correlation between wall pressure and streamwise velocity on wall-normal position of hot-wire probe (x=0, y=..., Ø=0°). Lower figure (y/δ=0.016) shows lowpass (bold) and highpass (dashed) correlations.

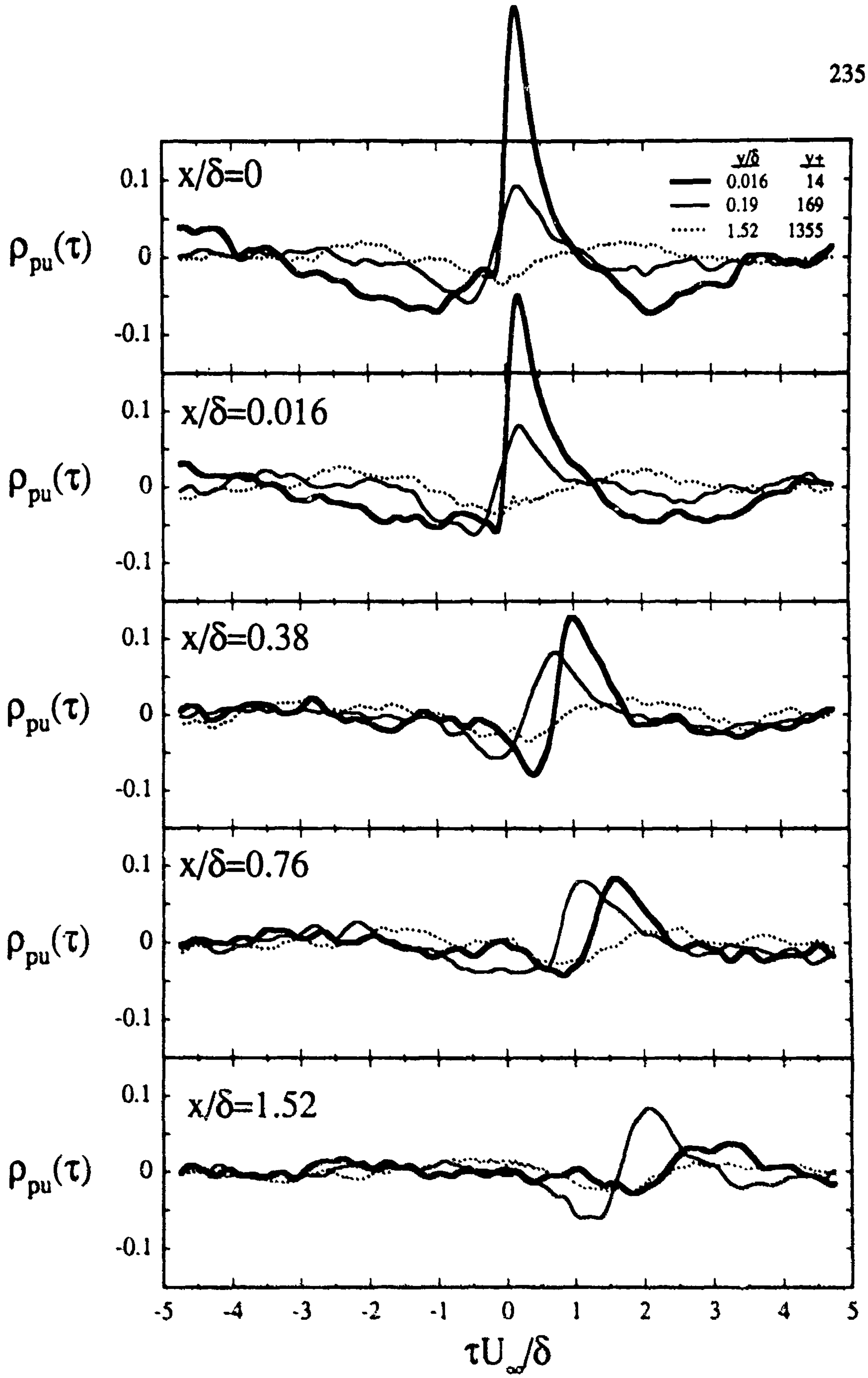

Figure 6-9. Dependence of cross correlation between pressure and streamwise velocity on streamwise position of hot-wire probe at various wall normal locations (x=..., Ø=0°).

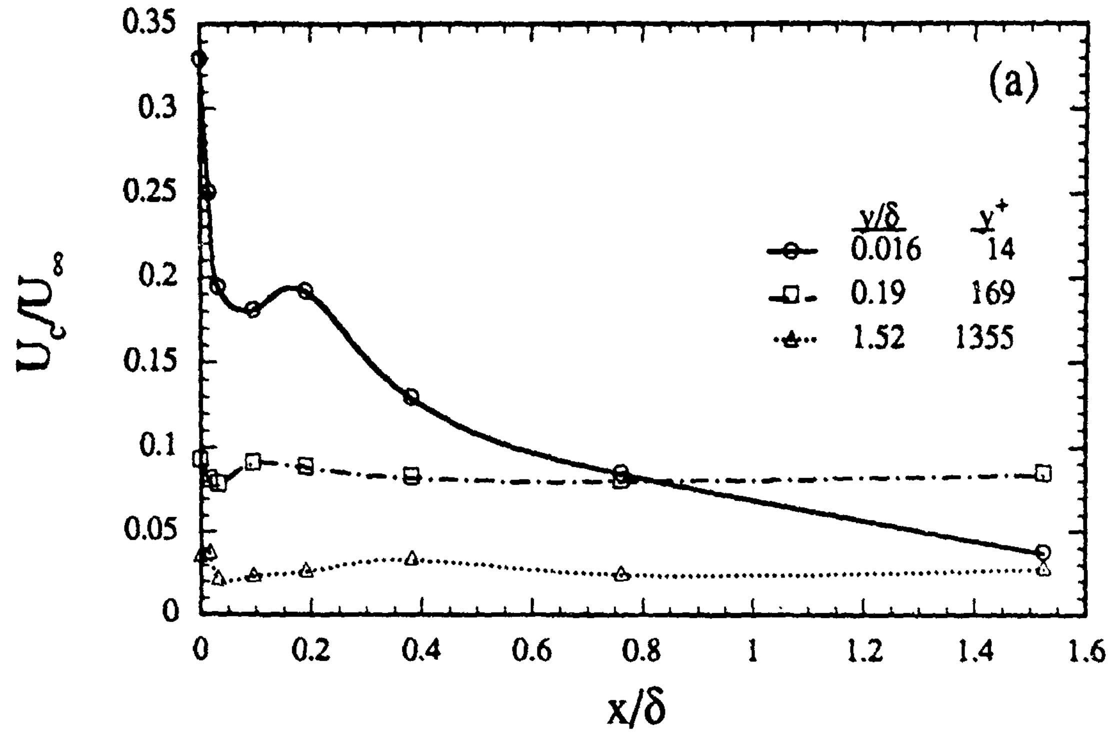

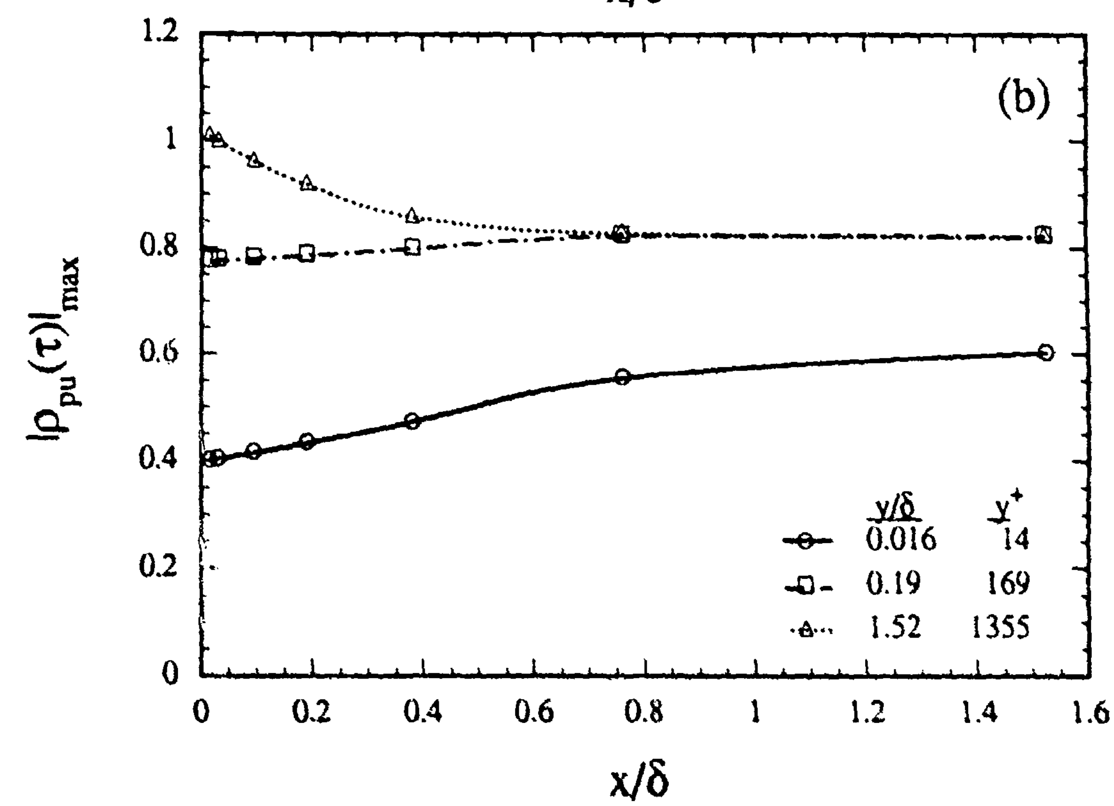

Figure 6-10. Streamwise dependence of pressure-velocity cross correlation: (a), decay of maximum of correlation; (b), local convection velocity of correlation.

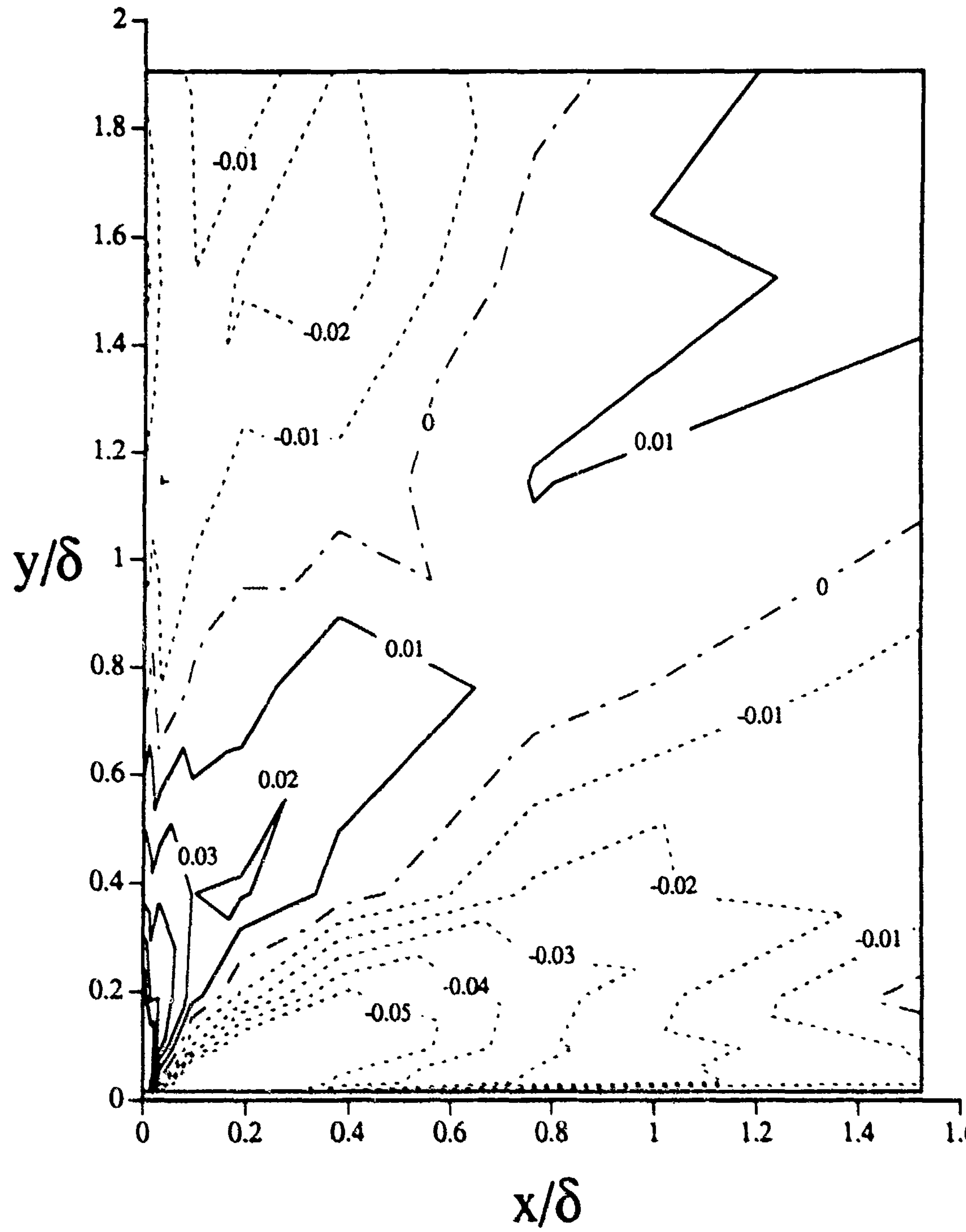

Figure 6-11. Contour plot of cross correlation between wall pressure and streamwise velocity for zero-time delay (τ=0) in x-y plane containing microphone (Ø=0°).

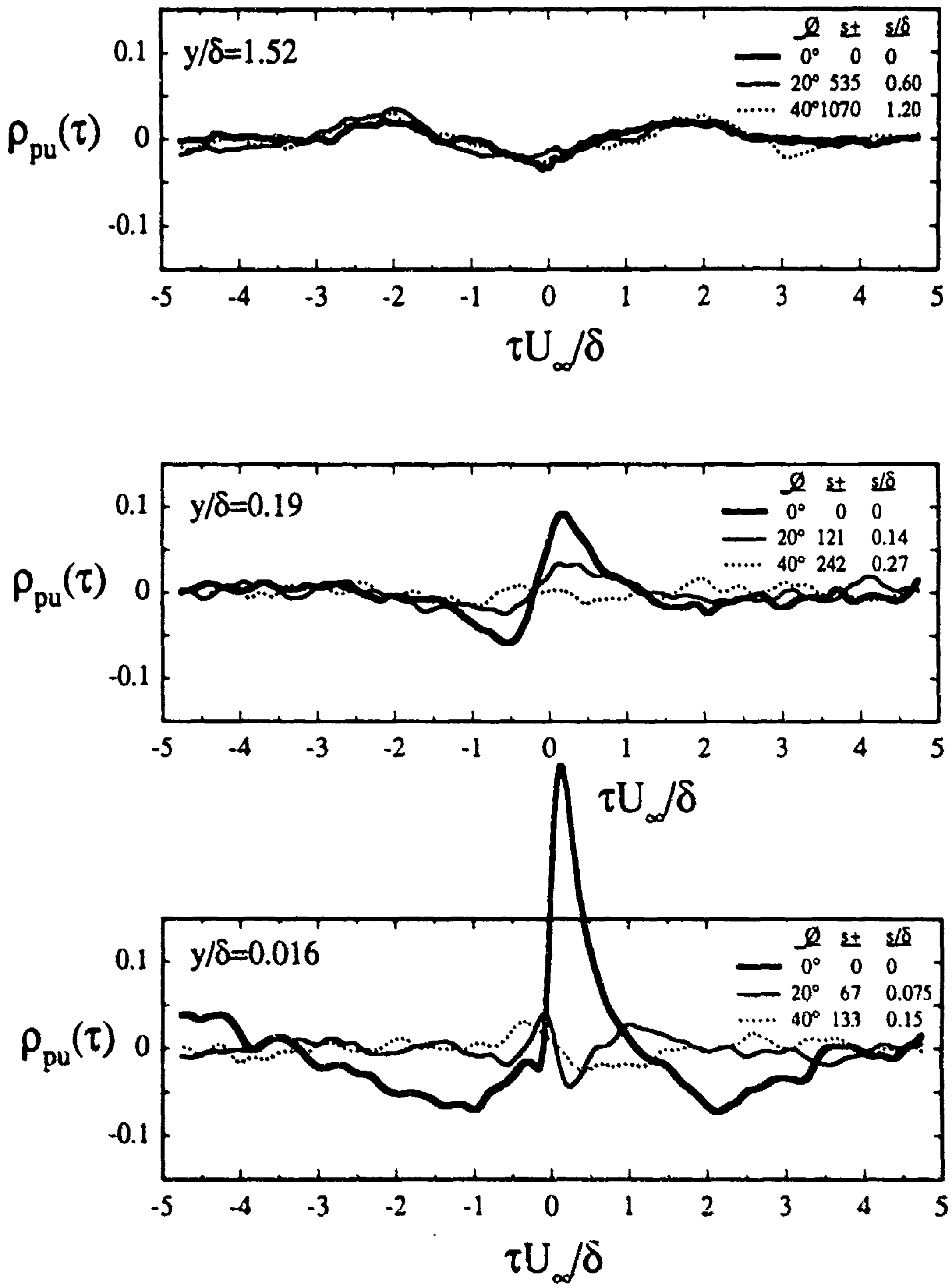

Figure 6-12. Dependence of cross correlation between pressure and streamwise velocity at various wall-normal locations on circumferential position of hot-wire probe (x=0, Ø=...).

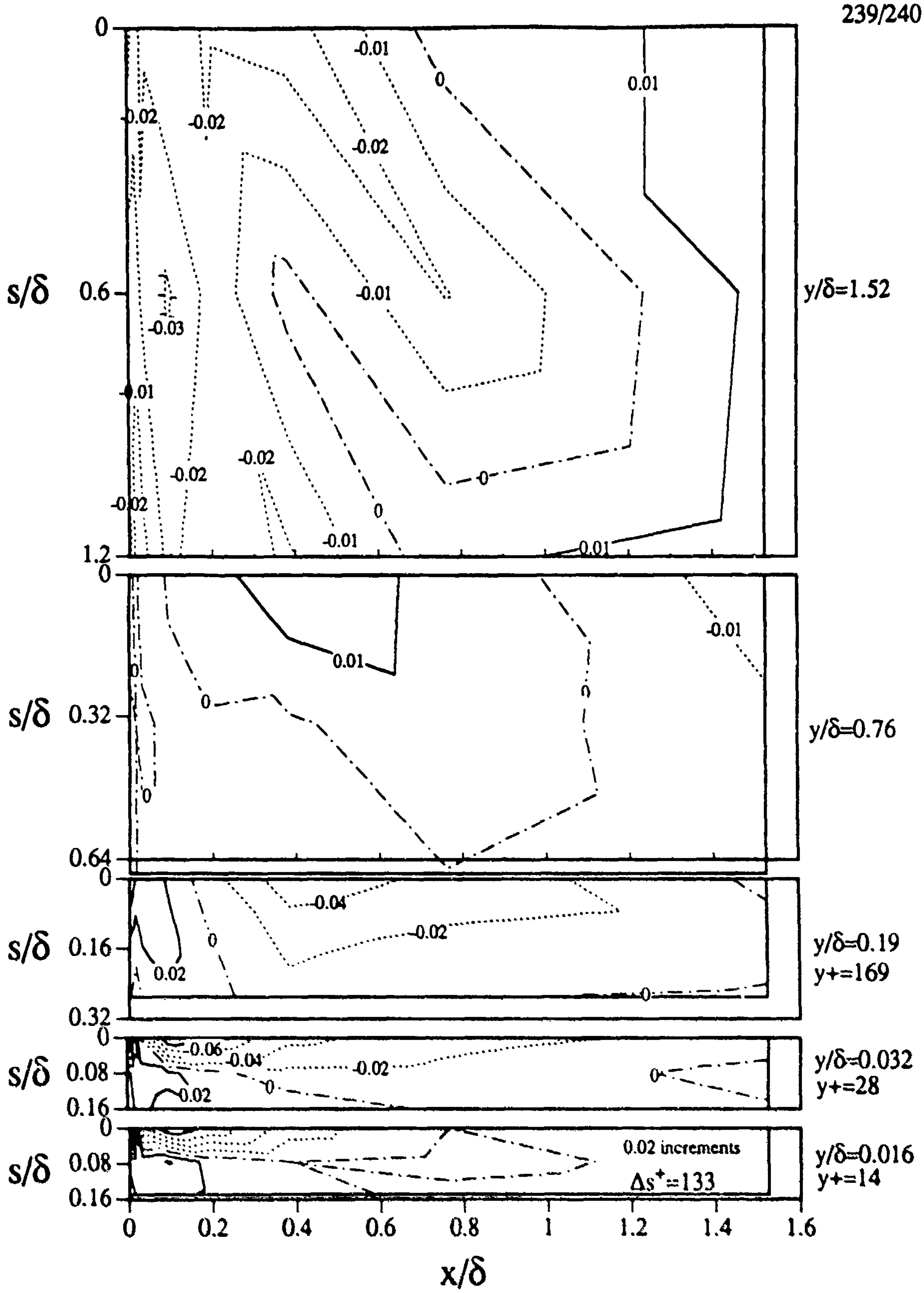

Figure 6-13. Contour plot of cross correlation between wall pressure and streamwise velocity for zero-time delay (τ=0) in x-s lamina at various wall-normal positions.

REFERENCES

Afzal, N., and K.P. Singh. 1976. Measurements in an axisymmetric turbulent boundary layer along a circular cylinder. Aeronautical Quarterly 27: 217.

Batill, S.M., M.J. Caylor, and J.J. Hoffman. 1983. An experimental and analytical study of the flow in subsonic wind tunnel inlets. Air Force Wright Aeronautical Laboratories Report No. AFWAL-TR-83-3109 (October).

Batill, S.M., and R.C. Nelson. 1989. Low speed, indraft wind tunnels. In Frontiers in Experimental Fluid Mechanics, ed. M. Gad-el-Hak. Springer-Verlag: Lecture Notes in Engineering.

Bendat J.S., and A.G. Piersol. 1980. Engineering applications of correlation and spectral analysis. New York, NY: John Wiley & Sons.

Bendat J.S., and A.G. Piersol. 1986. Random data analysis and measurement procedures. New York, NY: John Wiley & Sons.

Beranek, L.L. 1988. Acoustical measurements. Published for the Acoustical Society of America by the American Institute of Physics.

Blackwelder, R.F., and J.H. Haritonidis. 1983. Scaling of the bursting frequency in turbulent boundary layers. J. Fluid Mech. 132: 87-103.

Blackwelder, R.F., and R.E. Kaplan. 1976. On the wall structure of the turbulent boundary layer. J. Fluid Mech. 76, part 1: 89-112.

Blake, W.K. 1970. Turbulent boundary-layer wall-pressure fluctuations on smooth and rough walls. J. Fluid Mech. 44, part 4: 637-660.

Blake, W.K. 1986. Essentials of turbulent wall pressure fluctuations. Chapter 8 of Mechanics of flow-induced sound and vibration, vol. II: Complex flow-structure interactions. Orlando, FL: Academic Press, Inc.

Bradshaw, P. 1967. 'Inactive' motion and pressure fluctuations in turbulent boundary layers. J. Fluid Mech. 30: 241.

Brodkey, R.S., J.M. Wallace, and H. Eckelmann. 1974. Some properties of truncated signals in bounded shear flows. J. Fluid Mech. 63, part 2: 209.

Brodkey, R.S., J.M. Wallace, and J. Lewalle. 1984. The delta conferences: A discussion of coherent structures in bounded shear flows. Research Foundation Project 761061/711063 Report. Ohio State University Research Foundation.

Brown, G.L., and A.S.W. Thomas. 1977. Large structure in a turbulent boundary layer. Phys. Fluids 20, no. 10, part 2 (October): S243-S252.

Bruel and Kjaer. 1982. Condenser microphone and microphone preamplifiers for acoustic measurements: Bruel & Kjaer data handbook. Denmark: Nærum Offset.

Bull, M.K. 1967. Wall-pressure fluctuations associated with subsonic turbulent boundary layer flow. J. Fluid Mech. 28, part 4: 719-754.

Bull, M.K., and S.W. Thomas. 1976. High frequency wall-pressure fluctuations in turbulent boundary layers. Phys. Fluids 19, no. 4 (April): 597-599.

Chin, Y.T., J. Hulsebos, and G.H. Hunnicut. 1967. Effect of lateral curvature on the characteristics and skin friction of a turbulent boundary layer with and without helium addition. In Proceedings of 1967 Heat Transfer and Fluid Mechanics Institute, 394. Stanford: Stanford Univ. Press

Choi, H., and P. Moin. 1990. On the space-time characteristics of wall-pressure fluctuations. Phys. Fluids A 2, no. 8: 1450-1460.

Coles, D. 1955. The law of the wall in turbulent shear flow. In 50 Jahre Grenzschicht-forschung. ed. H. Gortler and W. Tollmien, 153. Braunschweig: Vieweg & Sohn.

Corcos, G.M. 1963. Resolution of pressure in turbulence. J. Acous. Soc. Amer. 35, no. 2: 192-199.

Corino, E.R., and R.S. Brodkey. 1969. A visual inspection of the wall region in turbulent flow. J. Fluid Mech. 37, part 1: 1-30.

Corrsin, S., and A.L. Kistler. 1955. Free-stream boundaries of turbulent flows. NACA Report 1244.

Denli, N., and L. Landweber. 1978. Thick axisymmetric turbulent boundary layer on a circular cylinder. J. Hydronautics. 13: 92.

Dinkelacker, A. 1990. Relations between wall pressure fluctuations and velocity fluctuations in turbulent pipe flow. In Near-wall turbulence: Proceedings of the 1988 Zoran Zaric Memorial Conference. ed. S.J. Kline and N.H. Afgan, 348-360. New York, NY: Hemisphere Publishing Corporation.

Doeblin, E.O. 1983. Measurement systems: Application and design. New York, NY: McGraw-Hill Book Company.

Emmerling, R. 1973. Die momentane Struktur des Wanddruckes einer turbulenten Grenzschichtströmung. Mitt. Max-Planck-Institut fur Strömungsforschung, u. Aerodyn. Vers., no. 56, Göttingen.

Falco, R.E. 1974. Some comments on turbulent boundary layer structure inferred from the movements of a passive contaminant. AIAA 12th Annual Aerospace Science Meeting 1974: AIAA paper no. 74-99.

Falco, R.E. 1983. New results, a review and synthesis of the mechanism of turbulence production in boundary layers and its modification. AIAA paper no. 83-0377.

Farabee, T.M. 1986. An experimental investigation of wall pressure fluctuations beneath non-equilibrium turbulent flows. DTNSRDC Technical Report No. 86/047.

Farabee, T.M., and M.J. Casarella. 1991. Spectral features of wall pressure fluctuations beneath turbulent boundary layers. Phys. Fluids A 3, no. 10 (October): 2410-2420.

Favre, A., J. Gaviglio, and R. Dumas. 1957. Space-time double correlations and spectra in a turbulent boundary layer. J. Fluid Mech. 2: 313.

Favre, A., J. Gaviglio, and R. Dumas. 1958. Further space-time correlations of velocity in a turbulent boundary layer. J. Fluid Mech. 3: 344.

Fiedler, H.E. 1986. Coherent structures. In Advances in Turbulence, 320. Berlin: Springer-Verlag.

Haritonidis, J.H., L.S. Gresko, and K.S. Breuer. 1990. Wall pressure peaks and waves. In Near-wall turbulence: Proceedings of the 1988 Zoran Zaric Memorial Conference. ed. S.J. Kline and N.H. Afgan, 397-417. New York, NY: Hemisphere.

Head, M.R., and V.V. Ram. 1971. Simplified presentation of Preston tube calibration. Aeronautical Quarterly (August): 295-300.

Helal, H., M.J. Casarella, and T.M. Farabee. 1989. An application of noise cancellation techniques to the measurement of wall pressure fluctuations in a wind tunnel. In Flow-induced noise due to laminar-turbulence transition process: Winter Annual Meeting of ASME in San Francisco, CA, Dec. 10-15, 1989. NCA-Vol. 5: 49-59.

Her, J. 1986. The relation between wall pressure and the flow field in the wall region of a turbulent boundary layer. Ph.D. diss., Department of Ocean Engineering, MIT.

Hinze, J.O. 1975. Turbulence, 2nd edition. New York, NY: McGraw-Hill Publishing Company.

Johansson, A.V., and H.P. Alfredsson. 1982. On the structure of turbulent channel flow. J. Fluid Mech. 122: 295-314.

Johansson, A.V., and H.P. Alfredsson. 1983. Effects of imperfect spatial resolution on measurements of wall bounded turbulent shear flows. J. Fluid Mech. 137: 409-421.

Johansson, A.V., J. Her, and J.H. Haritonidis. 1987. On the generation of high-amplitude wall-pressure peaks in turbulent boundary layers and spots. J. Fluid Mech. 175: 119-142.

Karangelen, C.C., V. Wilczynski, and M.J. Casarella. 1991. Large amplitude wall pressure events beneath a turbulent boundary layer. In Flow Noise Modeling, Measurement and Control: Winter Annual Meeting of ASME in Atlanta, Georgia, December 1-6, 1991. NCA-Vol.11, FED-Vol.130: 45-53.

Keith, W.L., and J.C. Bennett. 1991. Correction of wall pressure fluctuation measurements with a view to hydrodynamic applications. NUSC Reprint Report 8889 .

Keith, W.L., D.A. Hurdis, and B.M. Abraham. 1991. A comparison of turbulent boundary layer wall-pressure spectra. In Flow Noise Modeling, Measurement and Control: Winter Annual Meeting of ASME in Atlanta, Georgia, December 1-6, 1991. NCA-Vol.11, FED-Vol.130: 1-19.

Kim, J. 1989. On the structure of pressure fluctuations in simulated turbulent channel flow. J. Fluid Mech. 205: 421-451.

Klebanoff, P.S. 1954. Characteristics of turbulence in a boundary layer with zero pressure gradient. NACA Technical Note 3178.

Kline, S.J., W.C. Reynolds, F.A. Schraub, and P.W. Runstadler. 1967. The structure of turbulent boundary layers. J. Fluid Mech. 30, part 4: 741-773.

Kline, S.J. and S.K. Robinson. 1990. Quasi-coherent structures in the turbulent boundary layer: Part I. Status report on a community-wide summary of the data. Summary lecture in Near-wall turbulence: Proceedings of the 1988 Zoran Zaric Memorial Conference. ed. S.J. Kline and N.H. Afgan, 200-217. New York, NY: Hemisphere Publish. Co.

Kobashi, Y., and M. Ichijo. 1986. Wall pressure and its relation to turbulence structure of a boundary layer. Exp. in Fluids 4: 49-55.

Kovasznay, L.S.G., V. Kibens, and R.F. Blackwelder. 1970. Large-scale motion in the intermittent region of a turbulent boundary layer. J. Fluid Mech. 41: 283-325.

Kraichnan, R.H. 1956. Pressure fluctuations in turbulent flow over a flat plate. J. Acous. Soc. Amer. 28, no. 3: 378-390.

Lauchle, G.C., and M.A. Daniels. 1987. Wall-pressure fluctuations in a turbulent pipe flow. Phys. Fluids 30, no. 10 (October): 3019-3024.

Leehey, P. 1988. Dynamic wall pressure measurements. MIT Acoustics and Vibration Laboratory Report No. 97457-2 (August).

Lilley, G.M., and T.H. Hodgson 1960. On surface pressure fluctuations in turbulent boundary layers. AGARD Report No. 276.

Loehrke, R.I., and H.M. Nagib. 1976. Control of free-stream turbulence by means of honeycombs: A balance between suppression and generation. Trans. ASME J. Fluids Eng. 981: 342-353.

Lueptow, R.M. 1986. The turbulent boundary layer on a cylinder in axial flow. Sc.D. diss., Department of Mechanical Engineering, MIT.

Lueptow, R.M. 1988. Turbulent Boundary Layer on a Cylinder in Axial Flow. NUSC Tech. Report No. 8389 (29 September). (See also Lueptow, R.M. 1990. Turbulent boundary layer on a cylinder in axial flow. AIAA Journal, 28, no. 10: 1705-1706.)

Lueptow, R.M. and J.H. Haritonidis. 1987. The structure of the turbulent boundary layer on a cylinder in axial flow. Phys.Fluids 30, no. 10: 2993-3005.

Lueptow, R.M. and C.P. Jackson. 1991. Near-wall streaky structure in a turbulent boundary layer on a cylinder. Phys. Fluids A 3, no. 11: 2822-2824.

Lueptow R.M., P. Leehey, and T. Stellinger. 1985. The thick, turbulent boundary layer on a cylinder: Mean and fluctuating velocities. Phys.Fluids 28, no. 12: 3495-3505.

Luxton, R.E., M.K. Bull, and S. Rajagopalan. 1984. The thick turbulent boundary layer on a long fine cylinder in axial flow. Aeronautical J. 88: 186-199.

Mehta, R.D. and P. Bradshaw. 1979. Design rules for small low speed wind tunnels. Aeronautical J. Technical Notes Paper No. 718 (November): 443-449.

Nagib, H.M., A. Marion, and J. Tan-atichat. 1984. On the design of contractions and settling chambers for optimal turbulence manipulation in wind tunnels. AIAA 22nd Aerospace Science Meeting (January 9-12), Report No. 84-0536.

Neves, J.C., P. Moin, and R.D. Moser. 1991. Numerical study of axial turbulent flow over a long cylinder. 8th symposium on Turbulent Shear Flows, Munich, Germany (September 9-11), 1-6.

Panton, R.L., A.L. Goldman, R.L. Lowery, and M.M. Reischman. 1980. Low-frequency pressure fluctuations in axisymmetric turbulent boundary layers. J. Fluid Mech. 97, part 2: 299-319.

Panton, R.L. and J.H. Linebarger. 1974. Wall pressure spectra calculations for equilibrium boundary layers. J. Fluid Mech. 65, part 2: 261-287.

Patel, V.C. 1965. Calibration of a preston tube and limitations on its use in pressure gradients. J. Fluid Mech. 23: 185.

Patel, V.C, A. Nakayama, and R. Damian. 1974. Measurements in the thick axisymmetric turbulent boundary layer near the tail of a body of revolution. J. Fluid Mech. 63, part 2: 345-367.

Praturi, A.K., and R.S. Brodkey. 1978. A stereoscopic visual study of coherent structures in turbulent shear flow. J. Fluid Mech. 89, part 2: 251.

Preston, J.H. 1954. The determination of turbulent skin friction by means of pitot tubes. J. Roy. Aero. Soc. 58: 109.

Rae, W.H., and A. Pope. 1984. Low-speed wind tunnel testing. 2nd edition. New York, NY: John Wiley & Sons.

Rao, G.N.V., and N.R. Keshavan 1972. Axisymmetric turbulent boundary layers in zero pressure-gradient flows. J. Appl. Mech. 39: 25-32.

Richmond, R.L. 1957. Experimental investigation of thick, axially symmetric layers on cylinders at subsonic and hypersonic speeds. Hypersonic Research Proj. Memo No. 39, California Institute of Technology.

Robinson, R.L. 1990. A review of vortex structures and associated coherent motions in turbulent boundary layers. In Structure of Turbulence and Drag Reduction IUTAM Symposium, Zurich, Switzerland, 1989, 23-50. Berlin: Springer-Verlag.

Robinson, S.K., S.J. Kline, and P.R. Spalart. 1990. Quasi-coherent structures in the turbulent boundary layer: Part II. Verification and new information from a numerically simulated flat-plate layer. In Near-wall turbulence: Proceedings of the 1988 Zoran Zaric Memorial Conference. ed. S.J. Kline and N.H. Afgan, 218-247. New York, NY: Hemisphere Publishing Corporation.

Russell, S.J., and T.M. Farabee. 1991. The wall pressure field due to a wing-body flow. In Flow Noise Modeling, Measurement and Control: Winter Annual Meeting of ASME in Atlanta, Georgia, December 1-6, 1991. NCA-Vol.11, FED-Vol.130: 85-94.

Schewe, G. 1983. On the structure and resolution of wall-pressure fluctuations associated with turbulent boundary-layer flow. J. Fluid Mech. 134: 311-328.

Schlicting, H. 1979. Boundary-layer theory, 7th edition. New York, NY: McGraw-Hill Book Company.

Schloemer, H. 1967. Effects of pressure gradients on turbulent boundary layer wall pressure fluctuations. J. Acous. Soc. Amer. 42: 93.

Schweppe, J.L. 1963. Methods for the dynamic calibration of pressure transducers. Natl. Bur. Std. (U.S.), Monograph 67.

Spalart, P.R. 1988. Direct simulation of a turbulent boundary layer up to Re_θ=1410. J. Fluid Mech. 187: 61-98.

Tan-Atichat, J., H.M. Nagib, and R.I. Loehrke. 1982. Interaction of free-stream turbulence with screens and grids: a balance between turbulence scales. J. Fluid Mech. 114: 501-528.

Theodorsen, T. 1952. Mechanism of turbulence. In Proceedings of 2nd Midwestern Conference on Fluid Mechanics, Ohio State University. Columbus, OH.

Thomas, A.S.W., and M.K. Bull. 1983. On the role of wall-pressure fluctuations in deterministic motions in the turbulent boundary layer. J. Fluid Mech. 128: 283-322.

Tiederman, W.G. 1990. Eulerian detection of bursts. Summary lecture in Near-wall turbulence: Proceedings of the 1988 Zoran Zaric Memorial Conference. ed. S.J. Kline and N.H. Afgan, 874-887. New York, N.Y.: Hemisphere Publishing Corporation.

Townsend, A.A. 1951. The structure of the turbulent boundary layer. Proc. Cambridge Phil. Soc. 47: 375.

Townsend, A.A. 1976. The structure of turbulent shear flow, 2nd edition. Cambridge: Cambridge University Press.

Wallace, J.M. 1982. On the structure of bounded turbulent shear flow: A personal view. In Developments in Theoretical and Applied Mechanics, XI, 509. University of Alabama, Huntsville.

Wallace, J.M. 1985. The vortical structure of bounded turbulent shear flow. In Lecture Notes in Physics 235, p. 253. Berlin: Springer-Verlag.

White, F.M. 1974. Viscous fluid flow. New York, NY: McGraw Hill Publishing Company: 436-439.

Wieghardt, K.E.G. 1953. On the resistance of screens. Aero. Quarterly 4: 186-192.

Willmarth, W.W. 1975. Structure of turbulence in boundary layers. Adv. Appl. Mech. 15: 159-254.

Willmarth, W.W., and S.S. Lu. 1972. Structure of the Reynolds stress near the wall. J. Fluid Mech. 55, part 1: 65.

Willmarth, W.W., and F.W. Roos. 1965. Resolution and structure of the wall pressure field beneath a turbulent boundary layer. J. Fluid Mech. 22, part 1: 81-94.

Willmarth, W.W., and B.J. Tu. 1967. Structure of turbulence in the boundary layer near the wall. Phys.Fluids Suppl. 10: S134-S137.

Willmarth, W.W.. R.E. Winkel, L.K. Sharma, and T.J. Bogar. 1976. Axially symmetric turbulent boundary layers on cylinders: mean velocity profiles and wall pressure fluctuations. J. Fluid Mech. 76, part 1: 35-64.

Willmarth, W.W., and C.E.Wooldridge. 1962. Measurements of the fluctuating pressure at the wall beneath a thick turbulent boundary layer. J. Fluid Mech. 14: 187-210.

Willmarth, W.W. and C.E. Wooldridge. 1963. Measurements of the correlation between the fluctuating velocities and the fluctuating wall pressure in a thick turbulent boundary layer. AGARD Report 456.

Willmarth, W.W., and C.S. Yang. 1970. Wall-pressure fluctuations beneath turbulent boundary layers on a flat plate and a cylinder. J. Fluid Mech. 41, part 1: 47-80.

Winter, K.G. 1977. An outline of the techniques for the measurement of skin friction in turbulent boundary layers. Prog. Aerospace Sci. 18: 1-57.

Yu, Y.S. 1958. Effect of transverse curvature on turbulent boundary layer characteristics. J. Ship Res. 2: 33.

INITIAL DISTRIBUTION LIST

Addressee	No. of Copies
CDNSWC [T. Farabee (Code 1942)]	1
Northwestern University [R. Lueptow]	2
DTIC	12
Coast Guard Academy [V. Wilczynski]	1